PROBING THE ULTRAFAST DYNAMICS OF THE MAGNETIC PHASE TRANSITION IN FeRh NANOSTRUCTURES

A THESIS SUBMITTED TO THE UNIVERSITY OF MANCHESTER
FOR THE DEGREE OF DOCTOR OF PHILOSOPHY
IN THE FACULTY OF SCIENCE AND ENGINEERING

2022

By
Michael Tomás Grimes
School of Computer Science

Contents

Word Count: 56,875

List of Tables

List of Figures

Acronyms

AF Anti-Ferromagnetic
BAM Beam Arrival Monitor
BCC Body Centred Cubic
COM Centre Of Mass
DFT Density Functional Theory
DWF Debye-Waller Factor
EBL Electron Beam Lithography
EDS Energy-Dispersive x-ray Spectroscopy
FCC Face Centred Cubic
FEM Finite-Element Modelling
FM FerroMagnetic
FWHM Full-Width Half Maximum
HAMR Heat Assisted Magnetic Recording
IP In-Plane
IPA Iso-Propyl Alcohol
LINAC LINear ACcelerator
MFM Magnetic Force Microscopy
MOKE Magneto-Optical Kerr Effect
MPCCD Multi-Port Charge-Coupled Device
MPT Magnetic Phase Transition
NLO Non-Linear Optics
ODE Ordinary Differential Equation
OOP Out-Of-Plane
PEEK Poly-Ether Ether Ketone
PEEM PhotoEmission Electron Microscopy
PMMA PolyMethyl MethAcrylate
ROI Region Of Interest

RT Room Temperature
SACLA Spring-8 Angstrom Compact free electron LAser
SASE Self-Amplified Spontaneous Emission
SC Simple Cubic
SEM Scanning Electron Microscopy
SHG Second-Harmonic Generation
SLD Scattering Length Density
TER Total External Reflection
$\mathbf{T_T}$ Transition Temperature
x-FEL x-ray Free Electron Laser
VSM Vibrating Sample Magnetometry
XMCD X-ray Magnetic Circular Dichroism
XMLD X-ray Magnetic Linear Dichroism
XRD X-Ray Diffraction
XRR X-Ray Reflectivity
ZF Zero Field

List of Physical Constants

Symbol	Quantity	Value[†]	Uncertainty
c	speed of light	$2.9979 \times 10^{-8}\,\mathrm{m\,s^{-1}}$	0
h	Planck's constant	$6.6261 \times 10^{-34}\,\mathrm{J\,Hz^{-1}}$	0
$\hbar$	reduced Planck's constant	$1.0546 \times 10^{-34}\,\mathrm{Hz^{-1}}$	0
ε_0	vacuum electric permittivity	$8.854 \times 10^{-12}\,\mathrm{F\,m^{-1}}$	1.5×10^{-10}
μ_0	vacuum magnetic permeability	$1.2566 \times 10^{-6}\,\mathrm{N\,A^{-2}}$	1.5×10^{-10}
e	elementary charge	$-1.6201 \times 10^{-19}\,\mathrm{C}$	0
k_B	Boltzmann constant	$1.3806 \times 10^{23}\,\mathrm{J\,K^{-1}}$	0
μ_B	Bohr magneton	$9.2740 \times 10^{-24}\,\mathrm{J\,T^{-1}}$	3.0×10^{-10}
m_e	electron mass	$9.1094 \times 10^{-31}\,\mathrm{kg}$	3.0×10^{-10}
g_e	electron g-factor	2.002319	1.7×10^{-13}

[†]The NIST Reference on Constants, Units, and Uncertainty

Abstract

Materials that undergo a coupled phase transition offer a window into the relationship between electrons, nuclei, and magnetic spins in condensed matter. The development of ultrafast techniques where materials can be probed in the sub-ps time regime have provided the means to provide new insights into the exchanges of energy that occur between these systems. This can be applied to magnetocaloric, memory storage, and spintronics devices. This work investigated the dynamics of the FeRh coupled phase transition, where the magnetic ordering change from Anti-Ferromagnetic (AF) to FerroMagnetic (FM) at temperatures moderately above room temperature. The specific focus of this work is on the structural transformations and the effects of lateral confinement on the transition.

An x-ray based probe of anti-parallel Fe spin lattice in the AF phase of FeRh is demonstrated experimentally. Non-resonant x-ray magnetic scattering relies upon long-range spin order being established. We demonstrate the temperature dependence of the long-range ordering and confirm that this order only disappears following complete establishment of the FM moment. As a consequence, it allows for a probe of the mixed AF/FM phase of FeRh. This technique allowed for an estimation of the AF domain size suggesting dimensions are limited by the microstructure of the thin film (≈ 40 nm).

Time-resolved X-Ray Diffraction (XRD) studies were carried out at the x-ray Free Electron Laser (x-FEL) at SACLA, Japan. We observed structural changes through the phase transition on a timescale not previously reported and show a fluence dependence that indicates the importance of considering non-equilibrated states in the growth and relaxation dynamics of FeRh. A model is presented which demonstrates that such non-equilibria states can be explained using non-trivial electron-phonon coupling. Complementary heated XRD measurements are consistent with the hypothesis that the paramagnetic phase of FeRh is accessed on ps timescales.

The effects of lateral confinement were examined in FeRh nanowire arrays to determine if mesoscale magnetic interactions affect magnetisation dynamics. In order to understand the results obtained, heat dissipation was modelled using finite-element software so as to separate magnetic and thermal contributions. Pump-probe Magneto-Optical Kerr Effect (MOKE) investigations alongside static electrical measurements demonstrate that the orientation of external magnetic fields influences the transition behaviour in FeRh wires. FM stabilisation is observed when the external field is applied along the nanowire length. This orientation dependence was not observed in thin films and is ascribed to the shape anisotropy which may influence the FM domain growth mechanism - shifting the phase transition temperature by up to 10 K at applied magnetic fields of 1 T.

Declaration

No portion of the work referred to in this thesis has been submitted in support of an application for another degree or qualification of this or any other university or other institute of learning.

Copyright

Acknowledgements

I would like to thank my supervisors Tom Thomson and Valerio Scagnoli, as well as my thesis supervisor at PSI, Laura Heyderman. This project would not have been completed without Valerio's expertise and good humour throughout long (and not always successful) beamtime experiments. I am grateful to have had such a gracious and knowledgeable mentor as Tom, whose cheerful approach often brought the best out of my work. The bulk of data that composes Chapters 5 and 6 were generated at various beamlines, so I further thank the scientists at the I16 beamline, Diamond; MS beamline, SLS; and the BL3, SACLA. Hiroki Ueda deserves special thanks for travelling to Japan to assist with x-FEL experiments. The operation of the ultrafast laser at the Paul Scherrer Instiut could not have been completed without the expertise of Susmita Saha, Sergii Parchenko, and Jingyuan Zhou. The lithography in this project was carried out with the assistance of Anja Weber. Alex Lincoln deserves credit for maintaining high standards within the CMN cleanrooms where samples were prepared. I must also credit Vahid Sazgari for his help with performing electrical measurements which were analysed to present some of the data in Chapter 7.

For the many hours of office discussion within IT109, I must thank Will Griggs, Charley Bull, Phil Thomson, Yuzhe Zhang, Harry Waring, and Cory Emerson. Likewise at the PSI, I also thank Zhentao Liu, Sam Treves, Federico Motti, Aleš Hrabec, Jamie Massey, Aleks Pac, Dario Marty, Max Klein, Dima Ozerov, and Zhouchu Luo for engaging scientific discussion. Though our talks may not always have been purely physics focused, I doubt the project would have been as fruitful without the help of Runze Chen, Yu Li, Adrian Peasey, and Meg Smith in Manchester or Aleksander Kurenkov, Kevin Hofhuis, Gavin Macauley, Andreas Asperos, Rhea Stewart, and Sina Mayer in Villigen.

Unfortunately, such work often finds ways to escape the confinements of the lab. I need to thank all my family and friends for their understanding during all such occasions. My parents, Fearghal and Ann, deserve thanks for their support and encouragement the past 3 years (and then some). Distraction is as important as support at times and for that I know no two better sources thereof than my brother, Tim and my friend, Tim.

Finally, this thesis would not have been completed without the patience and kindness of Leah that has sustained me through the writing process.

a dim lamp was all I had been given
and patience without end
to shine it on the empty shadows

Samuel Beckett, *Molloy*

Research Output

Publications

- W. Griggs, B. Eggert, MO Liedke, M. Butterling, A. Wagner, U. Kentsch, E. Hirschmann, M. Grimes, AJ Caruana, C. Kinnane, H. Wende, R. Bali, and T. Thomson. Depth selective phase coexistence in FeRh thin films. *APL Materials* **8(12)**:121103, (2020)

- M. Grimes, N. Gurung, H. Ueda, D. Porter, B. Pedrini, LJ Heyderman, T. Thomson and V. Scagnoli. X-ray probe of antiferromagnetic ordering in FeRh. *AIP Advances* **12(3)**:035048 , (2022)

- M. Grimes, H. Ueda, D. Ozerov, F. Pressacco, S. Parchenko, A. Apseros, M. Scholz, T. Tadashi, Y. Kubota, K. Yoshikuya, LJ Heyderman, T. Thomson and V. Scagnoli. Determination of sub-ps lattice dynamics in FeRh thin films. *Scientific Reports*, **12**:8584, (2022)

- M. Grimes, V. Sazgari, J. Zhou, S. Parchenko, A. Weber, Y. Seoh, LJ Heyderman, T. Thomson and V. Scagnoli. Static and dynamics of FeRh nanowires for different field orientations [Manuscript in preparation]

Conference Presentations

- Time-resolved MOKE study of FeRh thin films. *Poster* **IOP Magnetism**, Leeds, UK. (2019)

- AF ordering of FeRh thin films at the Diamond Light Source. *Poster* **MaP Graduate Symposium**, Zürich, Switzerland. (2020)

- Non-resonant magnetic x-ray diffraction to monitor the temperature dependence of anti-ferromagnetic order in FeRh. *Poster* **e-European School of Magnetism**, Saarbrücken, Germany. (2020)
- X-ray probe of antiferromagnetic ordering in FeRh. *Virtual Oral* **MMM/Intermag Joint Conference**, New Orleans, USA. (2022)
- Sub-ps investigation of FeRh structural dynamics. *Oral* **IOP Magnetism**, York, UK. (2022)
- Determination of sub-ps lattice dynamics in FeRh thin films. *Oral* **CMD 29**, Manchester, UK. (2022)

Workshops & Meetings

- IOP Magnetism Winter School. **York, UK**. (2018)
- X-PEEM imaging and opportunities at the Diamond Light Source **Didcot, UK**. (2019)
- EMA e-European School of Magnetism **Saarbrücken, Germany**. (2020)
- EPSRC International Network for Spintronics **Leeds, UK**. (2022)

Chapter 1

Introduction

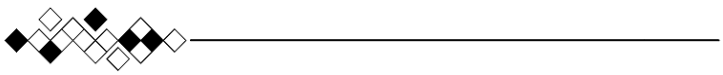

The importance of dynamic material studies is discussed in the context of advanced magnetic materials for applications in data storage and spintronics. A number of the key challenges in creating functional materials and devices are presented. The coupled Meta-Magnetic Phase Transition (MPT) of FeRh offers opportunities to create new materials as the transition is sensitive to a large range of physical stimuli. The research objectives and approaches underlying the work presented in this thesis are outlined.

1.1 Ultrafast Processes in Condensed Matter

Exploiting fundamental research to solve scientific and engineering problems is one of the driving forces behind applied physics. The material world around us can seem at odds with the abstract length- and timescales of fundamental research. Condensed matter physics bridges the gap between well-established laws of microscopic physics and material properties of collected electrons and atoms [1]. From crystallography to metallurgy to magnetism, the theory underpinning technologically important materials around us can be understood by considering the interactions between atoms and electrons. Such interactions can be probed by examining the dynamic response to external stimuli. Further information is found by driving materials into non-equilibrated states where the surplus energy must be dissipated. Phase transitions can even be induced, where dynamic studies demonstrate how the competing phases can be interconverted.

Advances in the generation and detection of ultra-short pulses have pushed the

boundaries of time-resolved techniques forward and it is now possible to probe the ultrafast dynamics in condensed matter on picosecond and femtosecond timescales across the electromagnetic spectrum, ranging from the infrared [2] to x-rays [3]. Ultrafast techniques have broad flexibility, with myriad combinations of excitation and probe sources available. Experimental techniques can be further complemented by theoretical simulations to model high power laser-matter interactions in the pulsed regime, to understand the evolution of non-equilibrium systems. These ultrafast processes can be exploited for applications, from sensing to data storage, and have provided great knowledge of nonequilibrium electronic, optical, structural, and magnetic states as well as phase transitions in matter [4].

The study of dynamics in magnetic materials can be directly applied to information technology. This is most pertinent in magnetic memory storage where a central concern is how fast the two states of a magnetic bit can reliably be transitioned between. This requires a trade-off in balancing the field strength required to switch the states (which incurs additional energy costs) and the stability of magnetic bits to thermal fluctuations. The drive for highly anisotropic magnetic materials [5] to reduce the lateral size of magnetic bits increases the power consumption in writing data. There is a need to bypass the strict field strength requirements which currently dictate the efficiency of magnetic bit switching.

1.1.1 Multifunctional Advanced Materials

Material science offers solutions in the form of multifunctional advanced materials which respond to more than one physical stimulus such as magnetic field [6], temperature [7], or strain [8]. The field of multifunctional materials promises advancement of electric motors, power generators, memory devices, windmills, biomedical devices, energy conversion, and transportation [9]. This advancement is limited by the increased complexity of such materials. In systems with a technologically useful coupled phase transition - with consecutive changes in more than one physical property - optimisation of the material for one physical transformation may require the suppression of another [10]. This project is focused on multi-functional materials that will allow for phase transitions driven by a range of stimuli. This may be expressed as thermal or optical instigation of a Magnetic Phase Transition (MPT), providing for the possibility of low-energy switching in magnetic recording [11].

Ultimately the progression of this field requires an interdisciplinary approach with integration of experimental materials science, computational simulations, practical engineering experience, and cost analysis [12]. A discussion of the ramifications of these concerns on the results presented in this thesis is provided. The underlying physics of the magnetic materials studied in this thesis were explored due to the expectation that the understanding and insights provided will assist in future optimisation of materials for applications.

1.1.2 Multifunctionality of B2-ordered FeRh

The choice of FeRh for this work is due to the coupled nature of its phase transition with electronic [13], magnetic [14], and lattice [15] transformations that occur at accessible temperatures for practical devices [7]. This MPT is directly applicable to the field of magneto-active materials where magnetic fields can be used to change the physical properties of materials [16]. Such field control can be applied from the bulk to nano-patterned objects due to the scalability of magnetic fields [17]. The resulting devices are integrated as composite multilayered structures [11] or achieved in a single-layer by strain nano-patterning [8], ion-implantation [18], or local laser heating [19].

The work reported in this thesis aims to provide further insight into the transient behaviour of a MPT when instigated by ultrafast laser excitation. Excitation drives the system into non-equilibrated states where time-resolved (TR) probes can monitor the relaxation of magnetisation, lattice expansion or contraction, and electronic structure. Such techniques are applied to the unusual MPT of FeRh in a B2-ordered structure from Anti-Ferromagnetic (AF) to FerroMagnetic (FM) (see Chapter 3, Fig. 3.1). This has been of interest to material science since the initial attempts to explain the origin of magnetic order [7]. The MPT is accompanied by an isotropic lattice expansion and reduction in resistivity [20]. This allows the transition to be induced and monitored by a range of stimuli; such as magnetic fields, x-rays, strain, or electric current [21].

1.1.3 Memory Storage Applications using FeRh

The technologically useful MPT of FeRh shows promise as a component in memory storage devices. Two such devices are presented here.

a) **Exchange-spring magnet:** In a bi-layer system with FePt, which usually requires a strong switching field, an exchange-spring magnet can be constructed [22]. The

lower temperature phase of FeRh protects the written state due to the large switching field of AF materials. A laser pulse locally induces the transition. While coupled to the FM phase of FeRh, the system has a reduced switching field (see Fig. 1.1a) allowing for the easy re-alignment of spins with an applied field [23]. This reduces the energy cost of data storage while taking advantage of the higher density of domains associated with AF materials [24].

b) **AF memory:** Another proposed device is an AF Anisotropic Magneto-Resistor (AMR), see Fig. 1.1b [25]. Due to spin-orbit coupling within the AF phase, resistivity depends on the relative orientation between magnetic spins and direction of applied current. This offers a low power method of reading magnetic states. Moreover, in an AF system these bits are protected by the large field ($\approx 10\,\mathrm{T}$) required to reorient the spins [17]. The absence of stray fields allows for a much higher feature density; this has stimulated much interest in the field of AF spintronics [26].

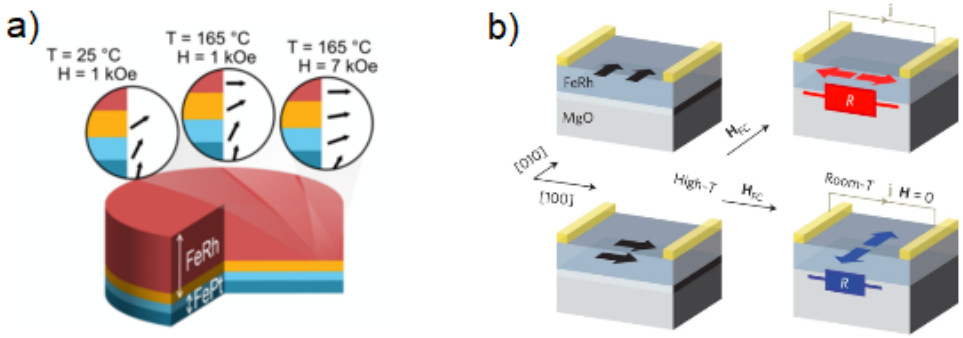

Figure 1.1: a) An illustration of the depth-dependent magnetisation direction in FePt (blue) and FeRh (red) layers as a function of temperature and applied magnetic field. Exchange-spring coupling induces an in-plane moment in the FePt boundary region (turquoise) at elevated temperatures and field strengths. Taken from Griggs et al. [27]. b) Schematic illustration of the AF-FeRh/MgO structure used for memory writing and reading. The soft FM phase (black arrows) allows low field writing along the [001] or [100] direction. The system is field cooled to preserve the Neél vector (red-[100], blue[001]) along a given direction. For reading, current is driven between electrical contacts (yellow bars) along the [100] direction. Taken from Marti et al. [25].

In order to compete with the state-of-the-art areal densities of CMOS technology, feature sizes < 20 nm are required [28]. The effects of lateral confinement (i.e. edge defects) or inherent speed limits could be barriers to the industrial use of FeRh [29]. The lattice and spin transformations through the MPT spread laterally through this

material with the speed of sound (ν = 5.1 km s^{-1}) [30, 31], paving the way toward 25 GHz write speeds on the nanoscale.

1.2 Research Objectives

This project was designed to contribute to the development of the understanding of the temporal characteristics of the FeRh MPT. During the course of this project, the following investigations were carried out to achieve this aim:

(i) Development of a diffraction based probe of the AF order of FeRh using grazing incidence x-rays. An x-ray diffraction probe is useful as it can be extended to TR techniques [32] to monitor the dynamics of the magnetic sub-lattice following laser excitation. This technique allows the spin and orbital components of AF atomic moments to be estimated [33].

(ii) Quantification of the structural dynamics of FeRh by investigation at an x-ray Free Electron Laser (x-FEL) source. The dynamics of the electronic and the spin system are well documented [4, 34]. In contrast, only a few papers detail the evolution of the lattice constant [31]. This is key to understanding whether the volumetric expansion drives the spin evolution via the exchange interaction [35] or vice versa.

(iii) Investigation into the effect of nano-pattering on the dynamics of the MPT. Previous work has focused on static behaviour, demonstrating a shift in Transition Temperature (T_T) and the effects of magnetic interactions on μm scales [29, 36]. We aim to determine if there is a corresponding change in the dynamic transition behaviour.

(iv) Determination of the role of simulations in describing the MPT in FeRh. Specifically, our aim is to explore the transition over a range of timescales using appropriate software and approximations. Such methods can be used to infer information from experiments and provide a deeper insight into the MPT.

1.3 Thesis Outline

The thesis is structured to first present the underlying theory surrounding the structure and magnetism of magnetic materials together with the experimental techniques used.

The results of investigations concerning the FeRh MPT are then reported. Specifically;

Chapter 2 discusses the background theory of x-ray matter interactions and solid-state magnetism. Equilibrium and non-equilibrium magnetisation dynamics are introduced which are important in describing the experimental techniques and analysing the results.

Chapter 3 presents a review of the literature concerning B2-ordered FeRh and the current knowledge on the mechanism and dynamics of the MPT.

Chapter 4 describes methods used to prepare FeRh samples and techniques to investigate the MPT in terms of structural, magnetic, and electronic behaviour. Numerical models are discussed which complemented the experimental approach.

Chapter 5 describes the results of our recently published paper [37] which investigated AF order in FeRh thin films. The optimisation of this measurement is discussed and the temperature dependence of AF order as the sample is heated through the MPT is demonstrated.

Chapter 6 details an experiment performed at SPring-8 Angstrom Compact free electron LAser (SACLA) which probed the lattice dynamics of FeRh thin films [38]. Detailed analysis of structural changes that occur on a ps timescale provide evidence for transient states in the phonon structure following laser excitation.

Chapter 7 describes investigations on patterned FeRh samples. TR-Kerr measurements probing the evolution of ferromagnetism demonstrate the role of shape anisotropy on the MPT. Electrical measurements confirm the field orientation dependence, while finite-element simulations describe the heat dissipation.

Chapter 8 summarises the experimental work undertaken in this thesis and the results obtained, followed by suggestions for future work.

Chapter 2

Theoretical Background

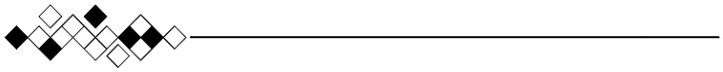

In condensed matter physics the properties of materials are critically dependent on their crystal structures. The formalism of crystallography is introduced in this chapter, including an overview of x-ray interaction with regular atomic arrays. The atomic theory of magnetism is presented with a focus on the micromagnetic energies of FerroMagnetic (FM) and Anti-Ferromagnetic (AF) materials.

2.1 The Crystal Lattice

Due to dependence of magnetic order upon the underlying crystal structure [17], a brief overview of crystallography is presented. Material properties are dependent on the regularity of atomic ordering [39]. As seen in Fig. 2.1, this ordering can be crystalline, polycrystalline, or amorphous - denoting no long-range crystal structure [40]. The basic unit of a crystal structure is the unit cell, the smallest arrangement of atoms in the material that can describe the lattice. All forms of regular crystal structures are captured under the umbrella of Bravais lattices, see Fig. 2.2. The equalities of crystal axis lengths and the relative unit cell angles are used to define to which Bravais lattice a given crystal structure maps. The work described in this thesis is primarily focused on cubic structures; Simple Cubic (SC), Body Centered Cubic (BCC), and Face Centered Cubic (FCC). In such cubic structures the angles (α, β, γ) and lattice constants (a, b, c) are equal using the standard designation [40], see Fig. 2.2;

$$\alpha = \beta = \gamma = \frac{\pi}{2}, \quad a = b = c = a_0. \tag{2.1}$$

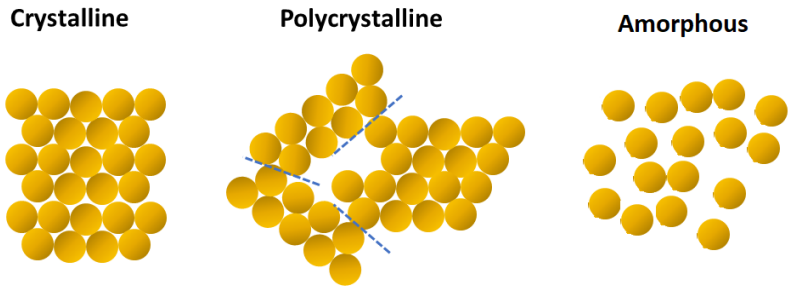

Figure 2.1: Schematic of types of atomic order with grain boundaries indicated by the dotted lines. Amorphous materials have no long-range order.

Lattice vectors are used to denote directions in the crystal structure in terms of the unit cell. The primitive lattice vectors are shown in Fig. 2.2, denoted as $\vec{a}_1$, $\vec{a}_2$, and $\vec{a}_3$. The standard nomenclature of crystallography dictates vectors are written with square brackets, and planes with round brackets [41].

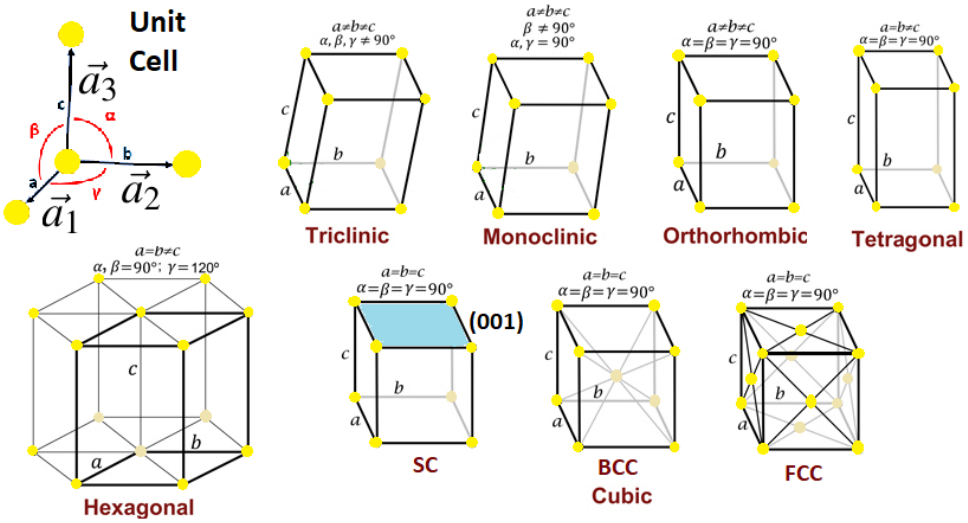

Figure 2.2: Unit cell structures. Shown is the simple structure of each Bravais lattice. Cubic lattices are shown in the bottom row; SC - simple cubic, BCC - body centered cubic, and FCC - face centered cubic. The shaded face (blue) corresponds to the SC (001) lattice plane. Adapted from IQFR-CSIC [42].

When considering long-range ordering across materials, it is instructive to apply Fourier analysis to the crystal structure. In a perfect crystal, the axis vectors $\vec{b}_1$, $\vec{b}_2$, and $\vec{b}_3$ are calculated as [39],

$$\vec{b}_1 = 2\pi \frac{\vec{a}_2 \times \vec{a}_3}{\vec{a}_1 \cdot \vec{a}_2 \times \vec{a}_3}, \quad \vec{b}_2 = 2\pi \frac{\vec{a}_3 \times \vec{a}_1}{\vec{a}_2 \cdot \vec{a}_3 \times \vec{a}_1}, \quad \vec{b}_3 = 2\pi \frac{\vec{a}_1 \times \vec{a}_2}{\vec{a}_3 \cdot \vec{a}_1 \times \vec{a}_2}. \tag{2.2}$$

It can be shown that these vectors form a basis set in reciprocal space and their linear combination describes the entire set of plane vectors in real space [41]. As a consequence, all lattice planes can be defined from an integer sum of axis vectors, $\vec{q} = h\vec{b_1} + k\vec{b_2} + l\vec{b_3}$ [39]. The values hkl are termed the Miller indices of the lattice planes. For (001) shown in Fig. 2.2; $h = 0$, $k = 0$, and $l = 1$. The reciprocal lattice is the set G of all vectors $\vec{q}$, which are wavevectors of the lattice planes with magnitude $2\pi/d$ [41].

2.2 X-ray Interaction with Matter

X-ray based techniques are used as a probe of long-range order in material systems. In order to understand x-ray characterisation techniques, the interaction between atomic centres and photons of x-ray energy is first presented. Diffraction relies upon coherent scattering of x-rays from the lattice planes introduced in Section 2.1. The efficiency of x-ray scattering is governed by the atomic cross-section, from which element-specific and structural information can be extracted [41]. Relative intensities of diffraction from different lattice planes are discussed which can be used to infer the underlying crystal structure. The treatment is extended to interaction with atomic magnetic moments.

2.2.1 Scattering from Single Atoms

The foundation of diffraction theory is based on the scattering of photons from the atomic centre. From the seminal experiments of J. J. Thomson [41, 43], it was shown that scattering is not simply a deflection of photons due to interaction with charged particles. For elastic scattering, the x-ray perturbs the atom from its equilibrium state, in turn emitting a photon at the same wavelength, λ. To estimate the efficiency, Γ of this process, a first-order perturbation of the atom centre is considered. Using the formulation of Griffith [44], Fermi's golden rule describes the x-ray scattering efficiency. The system begins in eigenstate $|a\rangle$ of an unperturbed Hamiltonian H_0. The atom is excited by a perturbation H', the light-matter interaction. For a photon with momentum $|\vec{k}| = 2\pi/\lambda$, the probability of being raised in energy to a state $|b\rangle$ is,

$$\Gamma_{a\to b} = \frac{2\pi}{\hbar} \left|\langle b|H'|a\rangle\right|^2 \rho_b, \quad \text{where } H' = \vec{p} \cdot e^{i\vec{k}\cdot\vec{r}}, \tag{2.3}$$

$\vec{r}$ and $\vec{p}$ are the position and momentum of the atom, and ρ_b is the density of final states. This indicates that the most efficient absorption will occur when the final state,

$|b\rangle$, corresponds to an eigenstate of H_0. This describes the process of x-ray absorption which can be used to create x-ray sources with a very narrow range of wavelengths (e.g. copper Kα; λ = 1.541 Å).

2.2.2 Scattering from a Lattice of Atoms

Having considered the interaction of a photon with a single atom centre, the following section outlines scattering from a lattice of such centres. Assuming the photon energy does not correspond to any interatomic transitions, the cross-section σ_s is defined as the sum over all nuclei where $\vec{k_f} - \vec{k_i} = \vec{K}$ is the momentum transfer for each scattering event;

$$\sigma_s \propto \left| \langle b | \sum e^{i\vec{K}\cdot\vec{r_j}} | a \rangle \right|^2. \tag{2.4}$$

The following derivations are based on the textbooks of Warren [41] and Kittel [39]. In Fig. 2.3, it is illustrated how these scattered photons will interact from a lattice of scattering centres. In a perfectly ordered crystal, the atoms are separated by a fixed distance from their nearest neighbours a_0. Each source of emitted photons is then separated by this distance. The sum total over the set G of reciprocal lattice vectors, $\vec{q}$, in the volume, V, of the scattering events is found from the Fourier series;

$$F \propto \sum_G \int e^{i(\vec{q}-\vec{K})\cdot\vec{r_j}}\, dV, \tag{2.5}$$

the scattering intensity is non-zero where,

$$\vec{q} = \vec{K}. \tag{2.6}$$

As the magnitude of the vectors $\vec{k_f}$ and $\vec{k_i}$ remain unchanged for elastic scattering events, the following diffraction condition holds;

$$2\vec{k_i} \cdot \vec{q} = q^2. \tag{2.7}$$

For photons with wavelength, λ ,at incident angles, θ, and reciprocal lattice vectors of magnitude, $2\pi/d$, the formula can be rewritten to give the well known Bragg's law [45];

$$2(2\pi/\lambda)\sin(\theta) = 2\pi/d \quad \Rightarrow \quad n\lambda = 2d\sin(\theta). \tag{2.8}$$

The spacing, d, is dependant on the chosen lattice plane for a given crystal. From

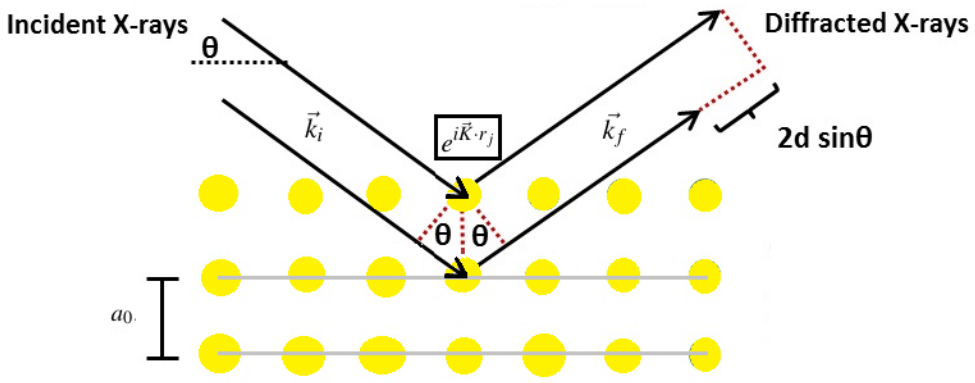

Figure 2.3: The scattering of x-rays from the (001) lattice plane separated by distance, $d = a_0$ will constructively interfere when the phase matching condition is met.

the earlier definition of $\vec{q}$, it can be shown that the lattice spacing along the principal directions of a cubic structure is,

$$d = \frac{a_0}{\sqrt{h^2+k^2+l^2}}. \tag{2.9}$$

This is the case for SC monatomic families of crystals. In order to describe the expected spectra of more complicated structures, the form factor is introduced which describes the scattering intensity, $I \propto |F|^2$. This allows the relative scattering strength of each atom to be considered, resulting in,

$$F_{hkl} = \sum_{j=1}^{N} f_j e^{[-2\pi i\ (hx_j+ky_j+lz_j)]}, \tag{2.10}$$

where f_j refers to the scattering factor of each atom with co-ordinates $(x_j,\ y_j,\ z_j)$. Eq. (2.10) can be used to calculate the relative intensity of each peak. For example in BCC-ordered equiatomic compounds - where A is at lattice position (0, 0 ,0) and B is at position $\left(\frac{1}{2},\ \frac{1}{2},\ \frac{1}{2}\right)$ - the structure factor predicts that the scattering from the lattice planes will occur with intensities as follows;

$$F_{hkl} = \sum_{j=1}^{2} f_j e^{[-2\pi i\ (hx_j+ky_j+lz_j)]} \tag{2.11}$$

$$= f_A + f_B(-1)^{h+k+l}, \tag{2.12}$$

$$|F_{hkl}|^2 = \begin{cases} |f_A+f_B|^2, & h+k+l \text{ (even)}. \\ |f_A-f_B|^2, & h+k+l \text{ (odd)}. \end{cases} \tag{2.13}$$

Further refinements to the description of Bragg peaks are found in the Chapter 4 where thermal [46] and finite size effects [47] are discussed. B2 order is primarily examined in this thesis - a form of BCC structure in equiatomic alloys. Time-resolved experiments are presented in Chapter 6 which examined evolution of Bragg peaks.

2.2.3 Scattering from a Lattice of Magnetic Moments

X-ray scattering processes can be extended to an ordered array of magnetic spins (see Section 2.3.4). In an elastic scattering process, the momentum transfer for emitted light is described using Eq. (2.4). This shift in momentum will also possess a small contribution from interaction with atomic magnetic moments [48], manifested as a change in x-ray polarisation ($\vec{\varepsilon} \rightarrow \vec{\varepsilon}'$). The cross-section of such scattering for photons with angular momentum, ω, is written as [33],

$$\sigma_m \propto \frac{i\hbar\omega}{mc^2} \left| \langle b | \sum_j e^{i\vec{K}\cdot\vec{r}_j} \left[\frac{i\vec{K}\times\vec{p}_j}{\hbar k^2} \cdot \vec{A} + \vec{s}_j \cdot \vec{B} \right] |a\rangle \right|^2, \tag{2.14}$$

where $\vec{K}$ and $\vec{p}$ are defined as before, k is the magnitude of the x-ray wave-vector, and $\vec{s}$ is the spin moment of the electron (see Section 2.3.2). $\vec{A}$ and $\vec{B}$ are defined as [48];

$$\vec{A} = \vec{\varepsilon}' \times \vec{\varepsilon}, \tag{2.15}$$

$$\vec{B} = \vec{\varepsilon}' \times \vec{\varepsilon} + (\vec{k}' \times \vec{\varepsilon}')(\vec{k} \cdot \vec{\varepsilon}) - (\vec{k} \times \vec{\varepsilon}(\vec{k} \cdot \vec{\varepsilon}') - (\vec{k}' \times \vec{\varepsilon}) \times (\vec{k} \times \vec{\varepsilon}), \tag{2.16}$$

where $\vec{k}$ and $\vec{k}'$ are equivalent to $\vec{k}_i$ and $\vec{k}_f$, respectively. This cross-section is greatly reduced in magnitude compared to Eq. (2.4) and is the pure magnetic scattering. These terms can be used to write the magnetisation-dependant part of the cross-section in terms of the orbital, $\vec{L}(\vec{K})$, and spin, $\vec{S}(\vec{K})$, densities as follows [33];

$$\langle M_m \rangle = \tfrac{1}{2}\vec{L}(\vec{K}) \cdot \vec{A}'' + \vec{S}(\vec{K}) \cdot \vec{B}. \tag{2.17}$$

The orbital and spin densities are defined in terms of their expectation values;

$$\vec{L}(\vec{K}) = \langle a | \sum_j e^{i\vec{K}\cdot\vec{r}_j} \frac{i\vec{K}\times\vec{p}_j}{K} |a\rangle, \tag{2.18}$$

$$\vec{S}(\vec{K}) = \langle a | \sum_j e^{i\vec{K}\cdot\vec{r}_j} \vec{s}_j |a\rangle. \tag{2.19}$$

As a consequence of the vector product, the orbital contribution in the direction of momentum transfer $\vec{K}$ is zero. This demonstrates that the orbital and spin components have different contributions to the scattering density. The components may be distinguished by angular analysis [49] by considering how x-rays interact with the magnetic moments (through the magnetic fields and their gradients). For example, the Lorentz force affects only the orbital magnetic moment and not the spin due it being a vector product [33]. This angular dependence is explored in more detail when describing the grazing incidence diffraction experiments in Chapter 5.

2.3 Magnetism Theory

The physics of magnetic materials are outlined, beginning from an atomic model and progressing to the micromagnetic description [17]. Specific topics including antiferromagnetism, band magnetism and magnetisation dynamics are discussed in more detail, as this forms a major part of the theoretical understanding of studies into the FeRh MPT [14] reported in this thesis.

2.3.1 History of Magnetism

Magnetism, as both a scientific topic and a curiosity, has fascinated people since the times of Ancient Greece [50]. Outside of limited uses such as lodestone for compass needles [51], it remained unexploited until a more formal study of physics had developed [52]. Faraday first demonstrated the relationship between the flow of electric current and the generation of magnetic fields [53]. Instead of the traditional north and south pole, it is more apt to describe the magnet as a continuous field acting perpendicular to the velocity of an electronic charge. This ultimately led to the development of Maxwell's equations [54], with which one could mathematically express the relationship between magnetic, $\vec{B}$, and electric, $\vec{E}$, fields. The 4$^{\text{th}}$ Maxwell equation describes magnetic field using a line integral about a portion of material, $d\vec{l}$;

$$\oint \vec{B} \cdot d\vec{l} = \mu_0 I + \mu_0 \varepsilon_0 \frac{d}{dt} \int \vec{E} \cdot d\vec{S}. \tag{2.20}$$

In a wire or a solenoid carrying current, I, depicted in Fig. 2.4a, this law predicts the following field strengths (with time-constant electric field, $\frac{\partial \vec{E}}{\partial t} = 0$);

$$B = \frac{\mu_0 I}{2\pi r} \quad \text{(wire)}, \qquad B = \mu_0 I \, \frac{N}{L} \quad \text{(solenoid)}. \tag{2.21}$$

where r is the distance from the wire, and N/L is the number of solenoid turns per unit length. This can be extended to atomic theory developed by Bohr where the predicted fixed orbits generate field as a consequence of electron motion [55], see Fig. 2.4b. Assuming the fixed orbit of an electron with angular momentum, $\vec{L}$, will create a magnetic moment, $\vec{\mu_L}$, it can be seen how an unpaired electron in an atom could possess a net magnetic moment;

$$\vec{\mu_L} = \frac{e}{2m_e} \cdot \vec{L}. \tag{2.22}$$

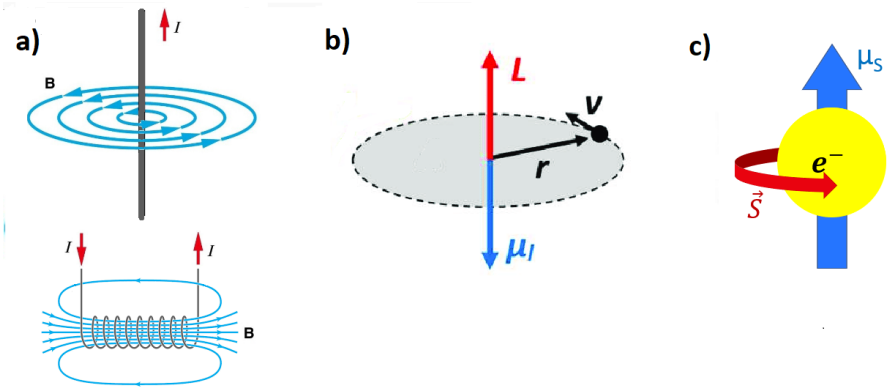

Figure 2.4: a) Magnetic field (B) generated by current (I) carrying wire. b) Field generated by electron in a fixed orbit. c) Field due to intrinsic spin angular momentum of the electron.

With further development of atomic theory and subsequent advances to the understanding of electronic structure in metals, a more coherent picture of magnetism began to emerge. This description was limited as it did not explain the phenomena of permanent magnets and failed to predict the measured moments of naturally occurring magnetic atoms. This orbital theory failed to capture why magnetism was traditionally observed in transition metals. Quantum mechanics is necessary to complete the picture, where phenomena such as spin and exchange interactions can complete the atomic picture. At its most fundamental level, magnetism is a macroscopic realization of a quantum effect [17, 56].

2.3.2 Atomic Model of Magnetism

The early explorations of magnetism describe what is now defined as orbital magnetic moment $\vec{\mu_L}$; which is understood to be the moment generated by unpaired electrons in their fixed orbitals [17]. However, this classical description needed expanding. Further refinements are required upon inclusion of relativistic terms as in the Dirac equation

[57], giving rise to an extra term designated the electron 'spin' $\vec{S}$, see Fig. 2.4c [17]. This spin is not considered equivalent to the classical description of a rotating charge, instead being a fundamental quantum property [44]. The spin angular momentum is found from the spin quantum number, $s = \frac{n}{2}$, where n is the number of unpaired electrons;

$$S = \hbar\sqrt{s(s+1)}. \tag{2.23}$$

A proportionality constant, g_e, accounts for differences between spin and orbital moment generation [17]. Using the Dirac equation, g_e is shown to be ≈ 2 [57], with a full derivation available in quantum field literature [58]. The spin moment, $\vec{\mu}_s$, is [17],

$$\vec{\mu}_s = g_e \cdot \frac{e}{2m_e}\vec{S}. \tag{2.24}$$

Finally, the total atomic moment in zero magnetic field is written as,

$$\vec{\mu_H} = \vec{\mu}_s + \vec{\mu}_L, \tag{2.25}$$

where quantum treatment of the shell electrons further results in quantised orbital momentum, $\vec{L}$, in integer multiples of $\hbar$ [44]. We further consider the spin-orbit coupling, J_{SO}, which links the spin direction to spatial directions of the orbitals [17] due to interaction between the electron and the magnetic field generated by the nucleus;

$$J_{SO} = \gamma_{SO}\vec{L}\cdot\vec{S}, \tag{2.26}$$

where γ_{SO} is the spin-orbit interaction energy which increases strongly with nuclear charge, $\mathbf{Z}$. In free space, these moments are randomly orientated. Under the application of a field, $\vec{H}$, these atomic moments are perturbed. The general Hamiltonian for an electron with momentum, $\vec{p}$, in an applied magnetic field (vector potential, $\vec{B} = \nabla \times \vec{A}$) is written as [17],

$$\mathcal{H} = \underbrace{\frac{\vec{p}}{2m_e} + V(\vec{r})}_{ZF} + \underbrace{\frac{e}{m_e}\vec{A}\cdot\vec{p}}_{PM} + \underbrace{\frac{e^2}{2m_e}\vec{A}^2}_{DM}. \tag{2.27}$$

These three terms refer to the unperturbed Hamiltonian (ZF), the ParaMagnetic response (PM), and the DiaMagnetic response (DM) respectively. From the relative strength of the later two terms, paramagnetism and diamagnetism can be defined (see Fig. 2.5). Summing the response across all atoms, a net magnetisation $\vec{M}$ emerges in

the material. From this the susceptibility, χ, is defined [17];

$$\chi = M/H. \tag{2.28}$$

In the following sections, $\vec{H}$ and H refer to the applied field vector and the applied field strength, respectively. The applied field is related to the magnetic flux density as,

$$\vec{H} = \vec{B}/\mu_0 - \vec{M}. \tag{2.29}$$

2.3.3 Weak Magnetic Interactions

The behaviour of weakly interacting magnetic materials are discussed in this section, with ParaMagnetism (PM) and DiaMagnetism (DM) arising from Eq. (2.27). An overview of the different magnetic interactions can be found in Fig. 2.5.

Paramagnetism

The second term of Eq. (2.27) describes the paramagnetic response. As a consequence of the vector potential, $\vec{A}\cdot\vec{p}$ can be rewritten in terms of the curl to give $\vec{B}\cdot(\vec{r}\times\vec{p})$ [17]. As this curl term is identical to the angular momentum operator $\vec{l}$, the paramagnetic response describes the Zeeman interaction with the orbital moment;

$$E_z = \frac{e}{m_e}\vec{B}\cdot\vec{l}. \tag{2.30}$$

The paramagnetic susceptibility can be found by considering Eq. (2.28) for the average orbital moment, where n is the number density of atoms;

$$\chi_{PM} = \frac{n\langle\vec{\mu_L}\rangle}{H}. \tag{2.31}$$

Paramagnetism is then defined as the weak attraction of materials by an externally applied magnetic field, or in mathematical terms $\chi > 0$ [40]. A schematic is provided in Fig. 2.5.

Diamagnetism

The third term of Eq. (2.27) refers to the diamagnetic response. This is simplified by assuming spherical symmetry which reduces to the semi-classical approach [17]. The diamagnetic response in this case is described by Lenz's law, where the induced

moment acts to oppose the applied field;

$$\chi_{DM} = -\frac{n\,\mu_0 e^2}{6m_e}\langle r^2\rangle\,, \tag{2.32}$$

where $\langle r^2\rangle$ is the mean square radius of the orbiting electron in the Bohr model. This negative susceptibility is present in all atoms subject to a magnetic field. Diamagnetism is then defined as the response present in every material where an applied magnetic field creates a repulsive force, or $\chi < 0$ [40]. A schematic is provided in Fig. 2.5.

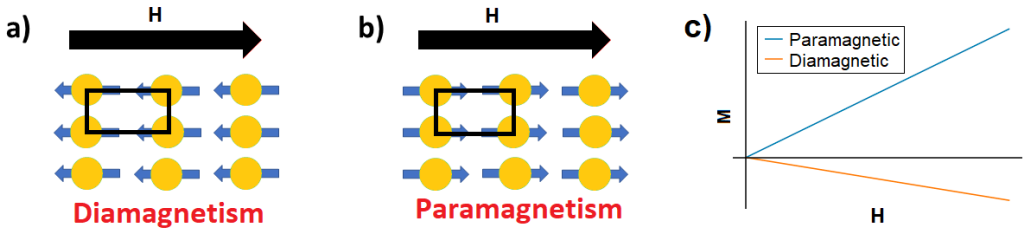

Figure 2.5: **Magnetic interactions:** showing a) diamagnetism in presence of applied field, b) paramagnetism when subject to a magnetic field. c) The relative interactions under applied field from which the susceptibility is derived according to Eq. (2.28). The black rectangle indicates the magnetic sub-lattice which maps to the atomic lattice in such materials.

2.3.4 Magnetic Ordering

For certain magnetic materials, the spin structure remains ordered in the absence of magnetic fields. FerroMagnetism (FM), AntiFerromagnetism (AF), and ferrimagnetism occur as a consequence of short-range atomic interactions establishing magnetic order [17]. The physical origins of these interactions are discussed in Section 2.4. An overview of the different types of magnetic ordering is provided in Fig. 2.6, where the magnetic sub-lattice is illustrated in each case.

Ferromagnetism

Ferromagnetism can be defined as the ability for a magnetic material to maintain a spontaneous magnetic moment in the absence of external field [40]. This implies an energy term that favours parallel alignment of spins on an atomic level so that the magnetic sub-lattice maps exactly to the crystal lattice as in Fig. 2.6a. Examples of

FM materials are the transition metals Fe, Ni, and Co. Properties of FM materials are discussed in more detail in Section 2.4.1.

Antiferromagnetism and Ferrimagnetism

Antiferromagnetism describes magnetic ordering where the magnetic moments of atoms or molecules, usually related to the spins of electrons, align in a regular pattern with neighbouring spins anti-parallel [40]. This results in multiple magnetic sub-lattices of atomic spins with a net magnetic moment of zero as in Fig. 2.6b. This was first observed in transition metal oxides [59]. A detailed discussion of AF materials may be found in Section 2.4.2.

Ferrimagnetism describes the instance where the magnetic sub-lattices possess unequal atomic moments, as illustrated in Fig. 2.6c. This results in a material with anti-parallel spin order with a net magnetic moment, as observed in ferrite, Fe_3O_4 [17].

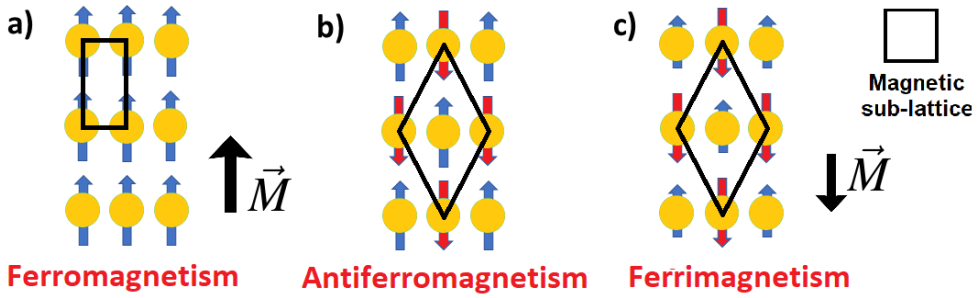

Figure 2.6: **Magnetic order:** a) ferromagnetism under zero applied field, and b) an example of antiferromagnetic order under zero applied field, c) ferrimagnetism where the anti-parallel magnetic sub-lattices have moments of different magnitudes.

2.3.5 Band Magnetism

The atomic theory of Section 2.3.2 is limited to the response of localised electrons under an applied field. Electrons in a material are better described collectively by the electronic band structure [39]. By considering the interaction of correlated electrons with magnetic fields, the origin of atomic moments of non-magnetic elements in alloys can be explained. Furthermore, the interaction between correlated electron spin and magnetic fields can be detailed. The exchange interaction gives rise to spin splitting of electronic band structure in magnetic materials, with regard to the $|\uparrow\rangle$ or $|\downarrow\rangle$

states. The Density Of States (DOS) of these $|\uparrow\rangle$ or $|\downarrow\rangle$ states are found from *ab initio* calculations, see examples provided in Fig. 2.7. Where the Fermi energy, E_f, is coincident with a high DOS of the $|\uparrow\rangle$-band, a ferromagnet with high magnetisation is formed [60]. Results for γ-Fe with different lattice parameters illustrate the sensitivity of Fe moment to atomic spacing in the densely-packed FCC phase [17]. This demonstrates how band structure can influence the magnetic character, giving rise to lower than expected atomic moments.

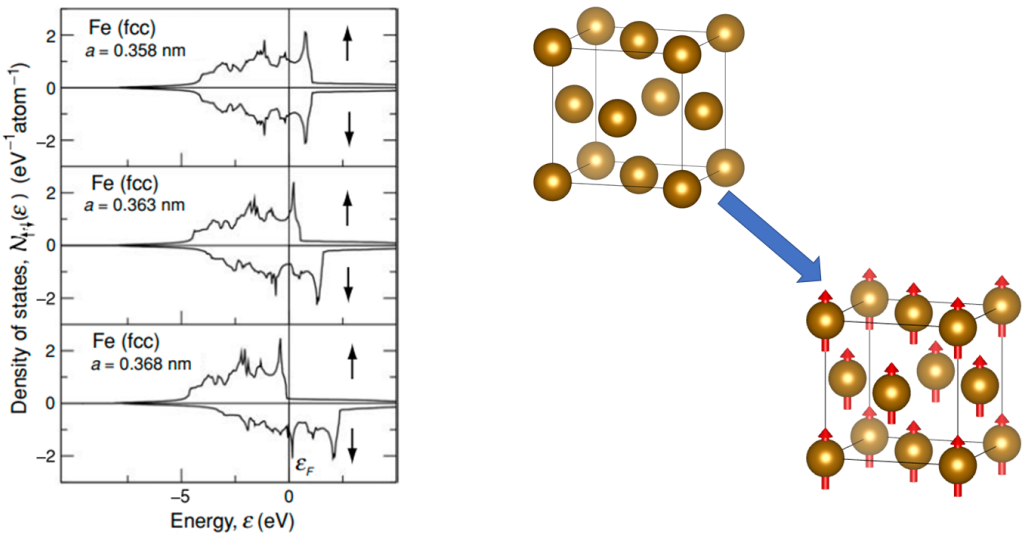

Figure 2.7: Calculated density of states for FCC Fe. The slight increase in the lattice constant results in favourable conditions for FM behaviour based on the band structure. Adapted from Coey (calculations courtesy of Ivan Rungger) [17].

Hybridisation of Non-magnetic Atoms

The Anderson impurity model describes how a magnetic atom interacts with a non-magnetic matrix via hybridisation of the band structure [61]. This can induce a difference (magnetic valence - $\mathcal{Z}_m$) in the DOS for spin systems when there is strong band overlap (such as for 3-d and 4-s orbitals);

$$\mathcal{Z}_m = N^{\uparrow} - N^{\downarrow}. \tag{2.33}$$

The magnetic valence model describes the average moment per atom of d-block elements. Following the derivation of Coey [17], in an alloy composed of such atoms the average moment will be expressed in terms of the magnetic valence, $\mathcal{Z}_m$, using the

number of spin-up d-band electrons, $N_d^{\uparrow}$, of each species;

$$\mathcal{Z}_m = 2N_d^{\uparrow} - \mathcal{Z}, \tag{2.34}$$

where $\mathcal{Z}$ is the number of valence electrons. $N_d^{\uparrow}$ reaches values of 5 for strongly magnetic d-block elements, and is 0 for main block elements. $N_d^{\uparrow}$ can possess non-integer values depending on how electron band are filled when d-band hybridisation occurs [17]. If $N_s^{\uparrow}$ is the number of $|\uparrow\rangle$ electrons in the unpolarised s-p band, the average moment per atom is expressed in terms of the weighted average of $\mathcal{Z}_m$;

$$\langle \vec{m} \rangle = \left(\langle \mathcal{Z}_m \rangle + 2N_s^{\uparrow} \right) \vec{\mu}_B. \tag{2.35}$$

In this way it is possible to estimate the magnetisation of any strong ferromagnetic alloy based on iron, cobalt or nickel, if one can calculate the constituent magnetic valences, $\mathcal{Z}_m$ [17]. Impurities with electrons above the host Fermi level can also introduce virtual bound states where impurity electrons fill 3d orbitals of the magnetic atom, thereby reducing the overall moment. This theory is applied to FeRh in Chapter 3 showing how hybridisation induces a moment at Rh sites [35].

2.4 Micromagnetic Energy

The microscopic energies present in magnetic materials are discussed in this section. The atomic model described previously does not account for long-range magnetic order. Justification is required for why an array of randomly oriented moments would align parallel in the absence of an electric or magnetic field. Any thermal excitation should render the spin orientations randomly distributed resulting in zero stray field above 0 K. It also remained unclear why it only occurred in a select few materials, primarily transition metals. This was first approached by Weiss who demonstrated the behaviour could be explained from the following two assumptions [17, 56].

i) Spontaneous magnetization occurs due to some internal field, H_M.

ii) Magnetic bodies are divided into microscopic randomly-orientated regions of uniform magnetisation, termed domains.

These assumptions are justified by considering the competing magnetic energies in a material. A basic formulation is captured in the micromagnetic energy equation

[62, 63];

$$E_{tot} = E_{ex} + E_d + E_k + E_Z, \tag{2.36}$$

where the respective terms are exchange - E_{ex}, magnetostatic - E_d, magnetocrystalline anisotropy - E_k, and Zeeman energy - E_Z.

Exchange Energy

The advancement of quantum theory by Heisenberg led to a deeper understanding of interactions between electrons of neighbouring atoms, which explains the origin of exchange [56, 64]. As electrons are classified as fermions, Fermi-Dirac statistics apply; namely the Pauli exclusion principle [44]. When applied to two unpaired electrons about neighbouring atoms, this gives rise to an additional quantum term in the classical electrostatic potential; the exchange energy [56].

The exchange between unpaired electronic spins i and j (J_{ij}) exhibits strong short-range interaction with favourable parallel alignment showing great sensitivity to the mean atomic spacing [17]. Considering two identical atoms with non-zero spins, the difference in energy for parallel, E_+, and anti-parallel, E_-, spin alignment is written as,

$$E_{ex} = \frac{1}{2}(E_+ - E_-) = -2\mathcal{J}_{ex}\vec{S}_i \cdot \vec{S}_j, \tag{2.37}$$

where $\mathcal{J}_{ex}$ is the exchange integral [64], and $\vec{S}_i$ is the spin vector of atom i. When $E_{ex} > 0$, FM order is favoured. The collective exchange interaction is related to the Weiss field, H_M, via the number of nearest neighbours in the unit cell, Z, and spin quantum number, S [17];

$$\vec{H}_M = \frac{2Z\mathcal{J}_{ex}S^2}{\vec{\mu_H}}. \tag{2.38}$$

At some temperature T_C, FM order is lost where the thermal vibrational energy (k_BT) exceeds the exchange energy and a FM $\rightarrow$ PM transition occurs. The value of T_C can be estimated as [17],

$$T_C = \frac{2Z\mathcal{J}_{ex}\ S(S+1)}{3k_B}. \tag{2.39}$$

To predict ordering for a given magnetic species, the Bethe-Slater curve (see Fig. 2.8) offers a rough estimation of E_{ex} [17]. This plots E_{ex} across atomic species using the

ratio of atomic radius, r_a, to the 3d electron shell radius, r_{3d}. This demonstrates the preference for FM order above a given ratio, r_a/r_{3d}. These 3d electrons are important factors in the spontaneous magnetisation, exhibiting strong interaction with neighbouring atoms for singly occupied sub-orbitals. As well as explaining the FM behaviour of α-Fe and Co, this curve assists in predicting the magnetic ordering of alloys when the atomic radii is known [17, 56]. For example, in Heusler alloys an increased lattice constant promotes parallel alignment for Mn atomic moments [65].

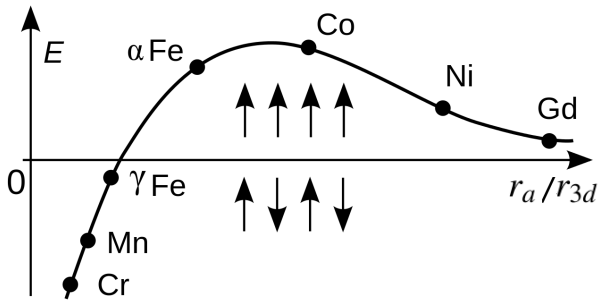

Figure 2.8: The Bethe-Slater Curve presenting how $\mathcal{J}_{ex}$ varies with the ratio of the radius of the atom r_a to the radius of its 3d electron shells r_{3d}. Taken from Coey [17].

The exchange energy further predicts more exotic magnetic orderings [17]. Namely, Neél speculated that negative values would result in anti-parallel spin alignments being favourable [66], which describes the spin order present in AF or ferrimagnetic materials.

Magnetostatic Energy

The magnetostatic energy describes the potential energy of a body in a magnetic field. The free energy can be written by integrating over space as,

$$E_d = \frac{1}{2}\int \mu_0 \vec{H}_d \cdot \vec{M}\, dV, \tag{2.40}$$

where $\vec{H}_d$ represents the demagnetising field, the stray field generated by the magnetization, $\vec{M}$, of a body. Naturally, the system will try to minimise the total self energy. The pole avoidance theory conceptually describes how the curvature of a stray field is minimised, favouring sample magnetisation along a long axis [17] (e.g. y-axis in Fig. 2.9). This is considered mathematically as $\vec{H}_d = N_d\vec{M}$, where N_d is termed the demagnetisation factor.

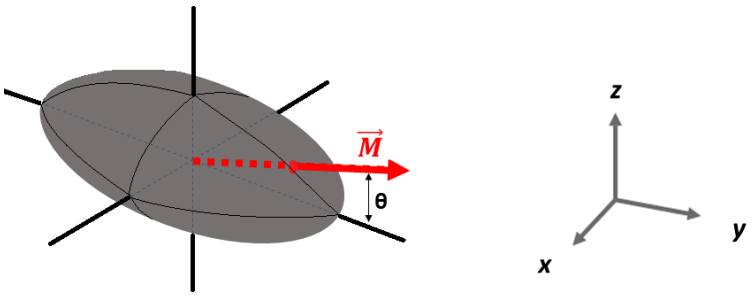

Figure 2.9: Ellipsoid shaped magnetic body with easy axis along the y-direction.

In order to estimate the demagnetisation factors, the relative axis lengths provide a means of deriving the shape anisotropies. In the following discussion, a reference axis system is given in Fig. 2.9. In the most general case of heterogeneous samples consisting of many magnetic bodies the local field, $\vec{H}'$, is fully captured with [67],

$$\vec{H}' = \vec{H} + \mathcal{N} \cdot \langle \vec{M} \rangle + N^P \cdot \left(\frac{\langle \vec{M} \cdot \vec{n}\, \vec{M} \cdot \vec{n} \rangle}{\langle \vec{M} \cdot \vec{n} \rangle} - \langle \vec{M} \rangle \right), \tag{2.41}$$

where $\vec{H}$ is the applied field, $\mathcal{N}$ is the shape anisotropy tensor, $\vec{M}$ is the magnetisation, N^P is the microscopic demagnetisation vector, and $\vec{n}$ is a unit vector in the direction of applied field. Eq. (2.41) is simplified by assuming homogeneity across the sample when fully magnetised. Hence N^P is not considered. Instead the overall effect is captured by $\mathcal{N}$. This tensor is estimated by numerically solving Poisson equations [17]. A diagonal demagnetisation tensor can be found by assuming the sample is an ellipsoid [68]. This simplifies the problem as stray fields from edges and vertices are not considered to give;

$$\mathcal{N} = \begin{pmatrix} N_x & 0 & 0 \\ 0 & N_y & 0 \\ 0 & 0 & N_z \end{pmatrix}. \tag{2.42}$$

A series of tables compiled by Osborn [69] allow for an approximation of the tensor $\mathcal{N}$ for select shapes. Given the scalable nature of magnetic interactions [17], $\mathcal{N}$ is constant for a fixed ratio of ellipsoid axes length. The corresponding internal fields experienced along the principle axes (i) in an ellipsoid are expressed in terms of the

magnetisation, M;

$$H_i = (H_0)_i - N_i M_i, \quad i = x,\ y,\ z. \tag{2.43}$$

By definition, the shape anisotropy, K_{sh}, is the difference between the energy density, $E_{\parallel}$, for magnetization parallel to some easy axis and $E_{\perp}$, along the hard direction. This leads to the well known anisotropy energy for homogenous thin films which favour in-plane magnetisation [17]. By assuming the thin film is approximated as an oblate spheroid with in-plane axis $\gg$ film thickness, the magnetostatic energy is predicted as,

$$K_{sh} = 2\pi M_S^2, \tag{2.44}$$

where M_s is the saturation magnetisation.

Magnetoanisotropy Energy

An important source of anisotropy in many thin films systems is the magnetocrystalline term which describes the energy cost when moments are not aligned to certain crystal axes. The atomic structure imposes fixed directions along which the orbitals can achieve greatest overlap, thereby reducing energy [70]. The spin-orbit interaction of Eq. (2.26) determines the magnitude of coupling between magnetisation and the structure-induced anisotropy. In the simplest case of uniaxial anisotropy, this is defined using a Taylor expansion in spherical polar co-ordinates. An approximation to first order may be written as [56],

$$E_k = K_1 \sin^2\theta + ..., \tag{2.45}$$

for relative angle, θ, between the easy axis and $\vec{M}$, where K_1 is the anisotropy. When $K_1 > 0$, an easy axis is defined along which energy is minimised. For $K_1 < 0$, energy is reduced when the moment aligns in the xy-plane (see Fig. 2.10a), giving rise to the term easy-plane anisotropy. The potential energy surfaces for both instances are illustrated in Fig. 2.10a.

For the cubic structures examined in this thesis, the easy (and hard) axes are defined in terms of α, β, γ - the cosines of the angles M_s makes to the family of $\langle 001 \rangle$ crystal axes. This energy is formulated to second order as [56],

$$E_k = K_1 \left(\alpha^2\beta^2 + \beta^2\gamma^2 + \gamma^2\alpha^2\right) + K_2\alpha^2\beta^2\gamma^2 + ..., \tag{2.46}$$

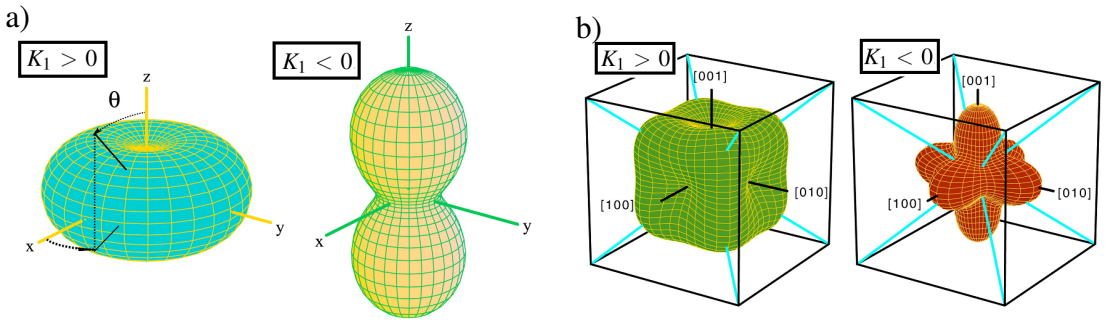

Figure 2.10: a) Potential energy surface for the case of uniaxial anisotropy shown for instances of $K_1 > 0$ (easy axis) and $K_1 < 0$ (easy plane). b) Potential energy surface for the case of cubic anisotropy. Shown for $K_1 > 0$ and $K_1 < 0$. Taken from Herak [71].

where K_1 and K_2 are material dependent quantities with magnitude $\approx 10^4$ J/m^3 [56]. If K_2 can be neglected, then the easy axis for $K_1 > 0$ lies along [001] while for $K_1 < 0$ the easy axis is parallel to [111]. The resulting potential energy surface is illustrated in Fig. 2.10b.

Zeeman Energy

The Zeeman energy captures the interaction between the atomic moments and an external applied field;

$$E_z = -\vec{m} \cdot \vec{B}, \tag{2.47}$$

for each atomic moment, $\vec{m}$, under an applied field, $\vec{B}$. The origin of this energy is directly found from the Hamiltonian describing an atom under applied field, Eq. (2.27).

Magnetisation at Interfaces

The energies introduced in Eq. (2.36) apply to all magnetically ordered materials. As the field of magnetism has progressed with development of physical vapour deposition discussed in Chapter 4, attention has turned to thin films [17]. To this end, the effects of boundary conditions are introduced here.

The demagnetisation field is sufficient to describe the anisotropy of single layer soft FM films in the absence of strong interfacial forces, Eq. (2.44). However, strain at interfaces or grain boundaries incurs an additional energy cost, the magnetoelastic energy E_{ME}. In the case of isotropic strain at a thin film interface, such that $\lambda_{111} = \lambda_{001}$,

the magnetoelastic energy is written as [17, 56],

$$E_{ME} = \frac{3}{2}\sigma_s \lambda_m \sin^2\theta, \tag{2.48}$$

where σ_s refers to the stress, and θ is the angle between σ_s and $\vec{M}_s$. This is expressed in terms of magnetostriction, λ_m, which quantifies the magnetically induced strain in a particular material. Further magnetoelastic energy costs may be incurred in bulk materials due to strain at grain boundaries [72]. Finally, the broken symmetry at each boundary means crystallographic anisotropies do not hold and one must consider the surface anisotropy [73], E_{AS};

$$E_{AS} = \int K_S[1 - \hat{M} \cdot \hat{n}]\, d^2r, \tag{2.49}$$

where K_S is the surface anisotropy energy, $\hat{M}$ is unit vector of magnetisation, and $\hat{n}$ is the surface normal [17].

2.4.1 Domain Theory of Ferromagnetism

Having established the micromagnetic energies that are important in magnetisation processes, bulk magnetic samples can be described. This is first considered in terms of the magnetostatic energy, E_d. If the entire sample was FM with one domain, the stray field would be reduced by halving the material into two separate domains with $\vec{M}$ of each aligned anti-parallel. This can be extrapolated to further reduce the magnetostatic energy by creating ever smaller domains. However, other terms impose a lower limit on the size of these domains. The exchange energy E_{ex} and total anisotropy (K_u) are especially pertinent in domain walls. Non-parallel spin alignment at these boundaries carry a large energy cost, where K_u limits the relative angular shift between neighbouring atomic spins. The transition from one domain to a different anti-parallel domain must be distributed across several atoms resulting in a domain wall shown in Fig. 2.11a. This results in the domain wall energy, proportional to the surface area of the domain walls, which balances the magnetostatic energy. An estimate of the domain wall width, δ_w, and energy, E_w, is predicted from the relative magnitudes of E_{ex} and K_u [17];

$$\delta_w = \sqrt{E_{ex}/K_u}, \qquad E_w = \sqrt{E_{ex} \cdot K_u}. \tag{2.50}$$

Magnetic Hysteresis

The key components of the hysteresis loop in Fig. 2.11b are explained by considering the effect of an applied field, $\vec{H}$. This will change the net magnetisation either by rotating $\vec{M}$ of the domains or moving domain walls. Under strong applied field, these moments will be completely aligned, yielding the maximum magnetic moment. This is defined as saturation magnetisation, M_s, see Fig. 2.11b. This saturation value is the sum total of all FM domain moments.

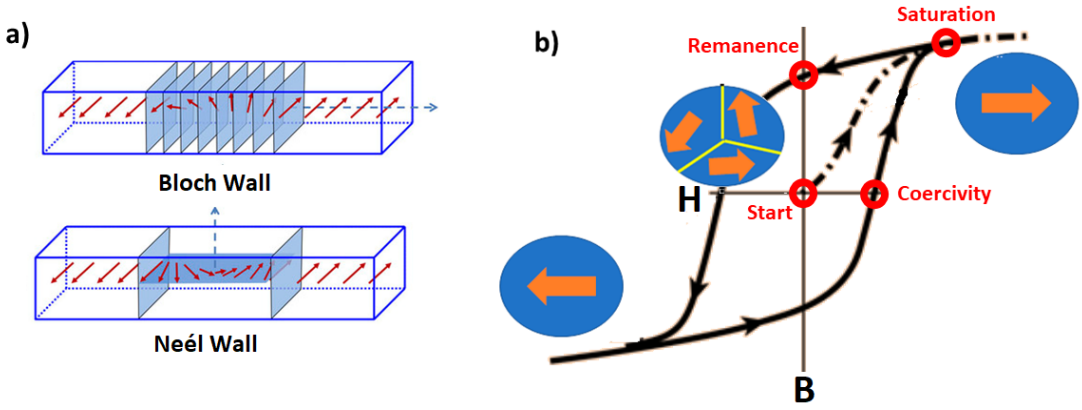

Figure 2.11: a) Examples of Bloch and Neél domain walls with the domain wall width (δ_w) illustrated. Adapted from Bhatia et al.[74]. b) A typical hysteresis curve showing how an applied field aligns randomly orientated domains (start) resulting in net moment at zero field (remanence). The coercivity is seen from the opening of the curve.

Stoner-Wohlfarth Model

The Stoner-Wohlfarth model describes how stabilisation of magnetic moments is provided by internal demagnetisation fields [68]. This results in net moment at zero field, the origin of remanence seen in Fig. 2.11b. Using a simplified model of the sample as a uniformly magnetised ellipse in 2D, the total energy, η, is expressed in terms of a magnetic anisotropy, K_u, and the Zeeman energy, see Section 2.4. The system has one easy axis pointing in plane. The direction of the magnetisation is then stable to external fields when the system is at an energy minimum [68];

$$\frac{\partial^2 \eta}{\partial \psi^2} = \cos(2(\psi - \theta)) + h\cos\psi > 0, \quad \text{where} \quad h = \frac{\mu_0 M_s H}{2K_u}, \tag{2.51}$$

ψ is the angle between the magnetisation $\vec{M}$ and the applied field $\vec{H}$, and θ is the angle between the easy axis and $\vec{H}$.

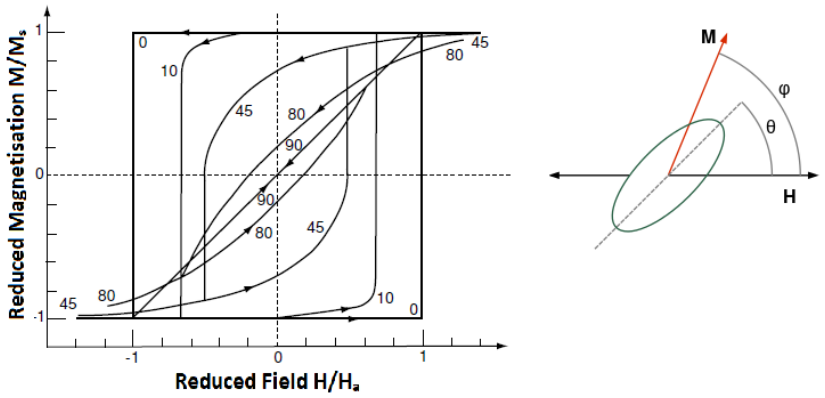

Figure 2.12: Magnetisation curves for the Stoner–Wohlfarth model for various angles θ between the field direction and easy axis. Taken from Coey [17]. H_a is the anisotropy field, where the Zeeman energy exceeds magnetic anisotropy energy. θ and ϕ refer to the angles the easy axis and $\vec{M}$ make to $\vec{H}$ respectively.

The system will then be stable to spontaneous switching below certain values of $\vec{H}$, termed the coercivity. Examining Eq. (2.51) it is seen that this coercivity is strongly dependant on the angle between the easy axis and the applied field [17]. The predicted relationship is shown in Fig. 2.12 where the coercivity is greatest when $\theta = 0°$.

Coercivity of FM Materials

Building on magnetic materials described in Section 2.3.4, 'hard' and 'soft' ferromagnets are defined, whose distinction is important for this project. Hardness is quantified by FM coercivity, Fig. 2.11b. Hardness is defined in a relative sense but as a guide for this thesis, hard magnets have coercive fields of > 400 kA m^{-1} [17]. The Stoner-Wohlfarth model describes the coercivity field in terms of the total anisotropy. With many contributions, no single factor will determine the hardness of a magnet but the most important consideration is the magnetocrystalline anisotropy. Generally an increased E_k, see Eq. (2.46), correlates with increased magnetic hardness [17]. Examples of hard FM materials are NdFeB as shown in Fig. 2.13, where the rare-earth atoms contribute a large magnetocrystalline anisotropy with coercivity up to 2000 kA m^{-1} [75]. In some isotropic FM materials, there is no such easy axis with minimal energy cost for magnetic moments not aligned to the preferred crystallographic directions, such as Fe_3Ni shown in Fig. 2.13b with a coercivity of 0.7 kA m^{-1} [76].

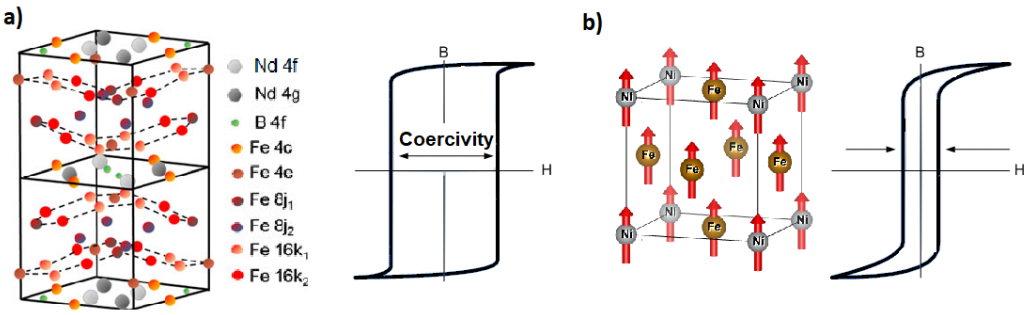

Figure 2.13: a) Example of hard FM material, $Nd_2Fe_{14}B$ with crystal structure imposing an easy axis z, along which the Nd atomic moments align. Adapted from Lewis et al. [75]. b) Fe_3Ni crystal structure in the $L1_2$ (Cu_3Au) ordered phase [77].

2.4.2 Extension to Antiferromagnetic Materials

Similar micromagnetic arguments can be applied to antiferromagnetism which was described in Section 2.3.4. This magnetic ordering relies upon magnetic sub-lattices (M_A and M_B) mapping to a superstructure of the crystal lattice [56], as a consequence of negative exchange interaction ($J_{ab} < 0$), introduced in Section 2.4. The type most applicable to this project is G-type as seen in Chapter 4, Fig. 4.28. This occurs when spins are orientated anti-parallel to each of their nearest neighbours; typically in materials with cubic crystal structures, such as equiatomic alloys adopting CsCl type order [14]. As a consequence, a magnetisation $\vec{M}$ cannot be determined. Instead a concept know as the Neél vector, $\vec{N}$, is defined as pointing along the axis of anti-parallel moments [66], see Fig. 2.14. Similarly, Neél temperature, T_N, is defined as the point where thermal vibrations overcome the exchange energy, so that ordering is no longer favourable.

A molecular field approach describes the field acting on sub-lattice magnetisations $\vec{M}_A$ and $\vec{M}_B$ in terms of the negative Weiss component, n_{ij}, the coupling between moments i and j;

$$\vec{H_A}^{\,i} = n_{AA}\vec{M}_A + n_{AB}\vec{M}_B + \vec{H}, \tag{2.52}$$

$$\vec{H_B}^{\,i} = n_{BA}\vec{M}_A + n_{BB}\vec{M}_B + \vec{H}, \tag{2.53}$$

for an external field, $\vec{H}$. The formation of domains and domain walls can be modelled using the micromagnetic energies, Eq. (2.36). As $|\vec{M}_A| = |\vec{M}_B|$, the net zero demagnetising field simplifies the micromagnetic equation, resulting in domain structures

determined primarily by lattice defect entropies [17]. Hence, AF domains are typically smaller than their FM counterparts ($<$ 100 nm) often mapping to crystal grains [78].

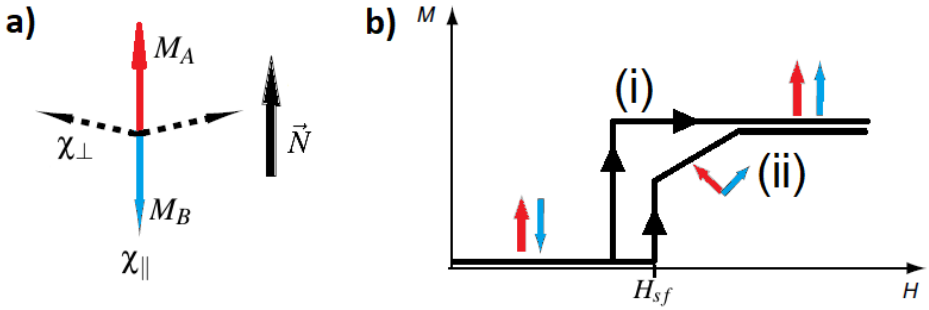

Figure 2.14: a) Magnetisation vectors of an antiferromagnet. The dashed lines show the possible configurations after a spin flop. b) Magnetisation of an antiferromagnet as a function of applied magnetic field, showing: (i) a meta-magnetic transition and (ii) a spin-flop transition. Adapted from Coey [17].

The stability of AF domains to resist external fields is explained by considering the perpendicular ($\chi_\perp$) and parallel susceptibility ($\chi_\parallel$) as shown in Fig. 2.14a.;

$$\chi_\perp = -\frac{1}{n_{AB}}, \tag{2.54}$$

while $\chi_\parallel$ is 0 at 0 K, rising to $\chi_\perp$ at T_N, as described by a Brillouin function. This function describes how the alignment of magnetic moments respond to increasing thermal energy [17]. In Fig. 2.14b, the magnetocrystalline anisotropy, K_1, governs the field at which spin-flop occurs, H_{sf} [17];

$$H_{sf} = \left(\frac{4M_A H_A}{\chi_\perp - \chi_\parallel}\right)^{\frac{1}{2}}, \quad H_A = \frac{K_1}{\mu_0 M_A}. \tag{2.55}$$

For zero temperature, this reduces to $H_{sf} = 2(H_A H_A^i)$, requiring large magnetic fields (up to 10 T) to re-orientate the spins [17]. In Fig. 2.14b, (i) the meta-magnetic transition occurs for materials with relatively low Weiss components, n_{AB}, meaning the coupling between magnetic sub-lattices is relatively weak.

2.5 Magnetisation dynamics

The theory presented in the previous sections describes static magnetism. The main focus of this project is on dynamics and therefore requires an explanation of how magnetic moments react to external factors in the time-dependent regime. This is first described in terms of magnetic moments precessing under application of magnetic fields exhibiting resonance. Non-equilibrium dynamics are then introduced which govern how magnetic moments respond to near-instantaneous physical changes such as heating over fs timescales.

2.5.1 Ferromagnetic Resonance

When a uniform array of magnetic spins is subject to a change in magnetic field, they respond by precessing about the new field direction [62]. Dynamics of magnetic spins are described by extending the Landau-Lifschitz equation to include damping terms in the time-dependant regime [62]. The general form is given as,

$$\frac{d\vec{M}}{dt} = \gamma\left(\vec{M}\times\vec{H}_{eff}\right) - \frac{\alpha}{M_s}\left(\vec{M}\times\frac{d\vec{M}}{dt}\right), \tag{2.56}$$

where γ describes the precession frequency, $\vec{H}_{eff}$ is the effective magnetic field, and α is a damping term. This is known as the LLG equation [62] and describes a magnetic moment precessing about the axis of the vector $\vec{H}_{eff}$ as energy is dissipated. This is the simplest case of time-dependent behaviour. There have been latter extensions to this equation to account for spin-polarised currents [79] and spin-transfer torque [80, 81]. However, these are not relevant to the work of this project.

In the case of thin films with perpendicular anisotropy, Eq. (2.56) predicts precessional motion of the spins with a GHz resonance frequency [17]. This is derived by considering the stray field in a thin film sample when the damping term is negligible. The oscillating components of time-dependent magnetization are defined generally as $m = m_0 e^{i\omega t}$ in the xy-plane;

$$\frac{dm_x}{dt} = \mu_0\gamma\left(-m_x H_z + \vec{M}H_x\right) = -\mu_0\gamma\left[\vec{H}_0 + (N_x - N_z)\vec{M}\right]m_x, \tag{2.57}$$

$$\frac{dm_y}{dt} = \mu_0\gamma\left(-m_y H_z + \vec{M}H_y\right) = -\mu_0\gamma\left[\vec{H}_0 + (N_y - N_z)\vec{M}\right]m_y, \tag{2.58}$$

where $M_z = \vec{M}$ and an external field, $\vec{H}_0$, is applied in the z-direction. The N components are identical to those found in Eq. (2.43). These first order differential equations are solved to give the well known Kittel equation [39, 82] for resonance frequency, ω_0;

$$\omega_0^2 = \gamma^2 \mu_0^2 \left[\vec{H}_0 + (N_x - N_z)\vec{M}\right] \cdot \left[\vec{H}_0 + (N_y - N_z)\vec{M}\right]. \tag{2.59}$$

In order to describe the resonance frequency in a thin film, the demagnetisation factors, $\mathcal{N}$, for an oblate spheroid [68] is used, resulting in a z component of unity. In Eq. (2.56), the $\vec{H}_{eff}$ is considered. When the easy axis is perpendicular to the plane, $\vec{H}_{eff}$ will then be shifted by the anisotropy field of magnitude $2K_1/M_s$. This predicts a resonant frequency of [17];

$$\omega_0 = \gamma \mu_0 \left(H_0 + \frac{2K_1}{M_s} - M_s\right). \tag{2.60}$$

K_1 is taken from Eq. (2.46) for the simplest case of uniaxial anisotropy. These dynamic responses are investigated using the technique of ferromagnetic resonance where a sample is subject to microwave electromagnetic fields and the absorption intensity is recorded [83]. The frequencies of the absorbed microwaves are used to extract information about the saturation magnetisation, while the damping allows for an estimation of anisotropy in magnetic samples using Eq. (2.60) [82].

2.5.2 Non-equilibrium Magnetisation Dynamics

The development of shorter and highly correlated laser pulses has enabled the understanding of magnetism at ever shorter timescales. Where the laser pulse duration was on the order of ps, magnetic interactions that occurred with GHz frequencies could be explored. With the advent of fs laser pulses non-equilibrium states could be probed and stronger nanoscale interactions could be investigated. This was first observed as the demagnetisation of FM Ni, where the magnetic remanence reduced within 2 ps, with subsequent recovery over several ps [84]. From this work, the field of femtomagnetism emerged. It was known previously that the lattice and electronic system of a material interact on a fs timescale due to coupling between electron and phonon states [85, 86]. However, the work of Beaurepaire et al. verified for the first time that the spin systems could interact on sub-ps timescales when excited by fs laser pulses [84]. Beaurepaire et al. reasoned this could be modelled by differences in the transfer of energy to the electronic, phononic, and magnonic systems of the sample. Following

excitation, photon energy is almost instantaneously absorbed by the electron gas [87]. The electron temperature is quickly driven to a non-equilibrium state. Then relaxation occurs via interaction with the phonons and spins from which the relative coupling strengths can be determined, see Fig. 2.15. The pump-probe technique was extended to explore laser-induced modulation of spin-orbit coupling [88] to offer an insight into the exchange interaction in magnetic materials. This was first applied to investigations of exchange bias systems. By weakening exchange bias with strong laser moderation, a coherent rotation of magnetisation was demonstrated [88].

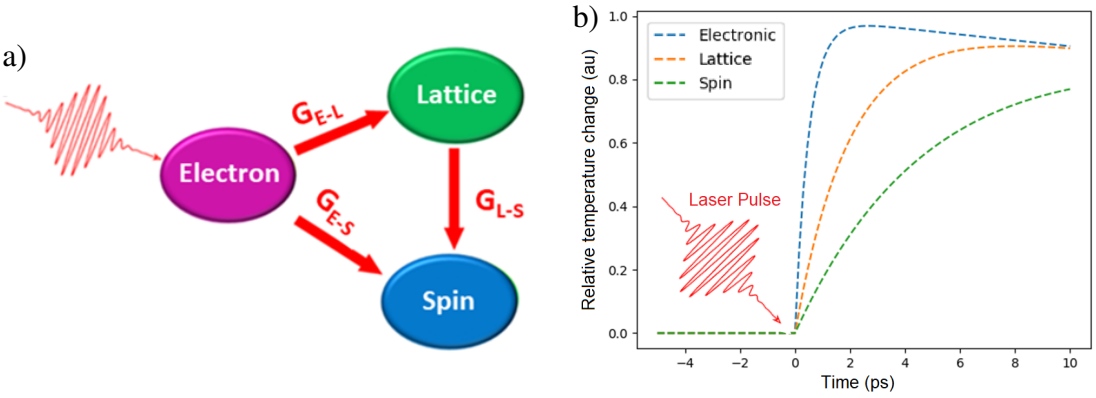

Figure 2.15: a) Laser pulses excite the electron system to a non-equilibrium state which relax by coupling to the lattice and spin systems ($G_{E\text{-}L}$ etc.). b) The normalised temperatures are sketched as a function of time over ps timescales following excitation.

From these pump-probe experiments, phenomenological theory was developed culminating in the three-temperature model. This is modelled by using ordinary differential equations, usually following the generation of a non-equilibrium state by pulsed laser heating [3, 84]. The kinetics of each subsystem can be described in terms of their transient temperatures, $T_i(t)$, following a rapid influx of heat, $Q(t)$;

$$\frac{d[T_{el}]}{dt} = Q(t) - \frac{\gamma_{E\text{-}L}(T_{el} - T_l)}{C_{el}(T)} - \frac{\gamma_{E\text{-}S}(T_{el} - T_s)}{C_{el}(T)}, \tag{2.61}$$

$$\frac{d[T_s]}{dt} = \frac{\gamma_{E\text{-}S}(T_{el} - T_s)}{C_s(T)} + \frac{\gamma_{L\text{-}S}(T_l - T_s)}{C_s(T)}, \tag{2.62}$$

$$\frac{d[T_l]}{dt} = \frac{\gamma_{E\text{-}L}(T_{el} - T_l)}{C_l(T)} - \frac{\gamma_{L\text{-}S}(T_l - T_s)}{C_l(T)}, \tag{2.63}$$

where the subscript refers to the system (el - electronic, l- lattice, s - spin), γ is the coupling between physical systems, and C is the heat capacity. In studies of first-order kinetics, exponential functions are used in order to extract the growth and decay

rate of the temperature-induced changes in each sub-system [89]. For example, the following phenomenological equation is used [4] to track the magnetisation growth process where $G(t)$ is a function that represents the temporal resolution of the probe technique;

$$f(t) = G(t) * \left[A \cdot \left(1 - \exp\left(-\frac{t}{\tau_G}\right)\right) + B \cdot \exp\left(-\frac{t}{\tau_R}\right)\right], \tag{2.64}$$

where τ_G is the growth lifetime of the time-dependent quantity, τ_R is the relaxation lifetime, A and B are constants, and t is the time since laser excitation. The coupling terms from Fig. 2.15a can be inferred by comparing the dynamics of different physical systems following excitation using similar laser pulses. For example, the reflectivity evolution of FeRh can be extracted in tandem with the Kerr signal in Time-Resolved Magneto-Optical Kerr Effect (TR-MOKE) experiments [90]. This allows for a comparison between the electronic and spin systems, providing an estimation of the coupling $G_{E\text{-}S}$.

Chapter Summary

In this chapter, the x-ray matter interaction is described which is foundational to techniques which explore long-range ordering of materials. The magnetic theory discussed here will inform the current understanding of the FeRh MPT outlined in the next chapter. The dynamic studies described throughout this thesis are interpreted using the three-temperature model of femtomagnetism.

Chapter 3

Origin of Physical Transformations in B2-ordered FeRh

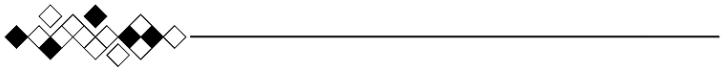

Solid-state literature regarding FeRh is discussed in this chapter, detailing the progression of research from the 1930's to present day. Particular focus is given to the current understanding of the MPT mechanism and the dynamics of the physical transformations in the coupled phase transition.

3.1 Meta-magnetic Transition

FeRh has interested researchers since the preliminary attempts to explain the unusual Magnetic Phase Transition (MPT) of B2-ordered crystals [7]. Fig. 3.1 shows magnetometry performed on a FeRh ingot, with a first-order meta-magnetic transition observed at temperatures about 380 K, which promotes an Fe spin reorientation from anti-parallel to parallel ordering [14]. This involves the transition from G-type AF order to a soft FM phase (coercivity = 20 kA m^{-1}) [91]. Further research revealed the Transition Temperature (T_T) is altered by doping with metallic elements, M, in place of the rhodium site, $Fe_{50}Rh_{50-x}M_x$ [92]. Element specificity was observed, shifting T_T by up to 400 K (Pt doped - 169 K, Ir doped - 585 K) with M_s following the predicted Curie relationship with temperature once the system was in the FM phase. Ellipsometry and x-ray powder diffraction revealed that resistivity and the crystal structure undergo respective transformations at this T_T [13, 15]. As such, it is described as a coupled transition with changes of multiple physical proprieties as T_T is approached.

This early work focused on the bulk properties with research dedicated to the thermodynamics of the phase transition [93]. Calorimetry experiments demonstrated a large change in magnetic entropy [94, 95] which garnered interest due to the potential refrigerant applications [96]. Ball milling of FeRh revealed crystallographic requirements for the MPT [97], with other allotropes not exhibiting such behaviour. It was not until the 1990's when physical vapour deposition techniques had progressed sufficiently that FeRh thin films could be prepared [98]. The coupled transition remained extant in thin film systems and prompted widespread interest in this material as a component in memory storage devices [99]. FeRh could be grown epitaxially on widely available MgO substrates due to lattice matching with the (001) surface [100], leading to extensive research including the first Time-Resolved (TR) studies [88, 90]. This research was motivated by the drive to increase memory areal density [5, 101], where the tunable T_T of FeRh was desirable [92]. Incorporation of a thin FeRh layer with a high anisotropy FePt layer then lead to a thermally switchable exchange spring structure [102] reducing the head write field in recording media.

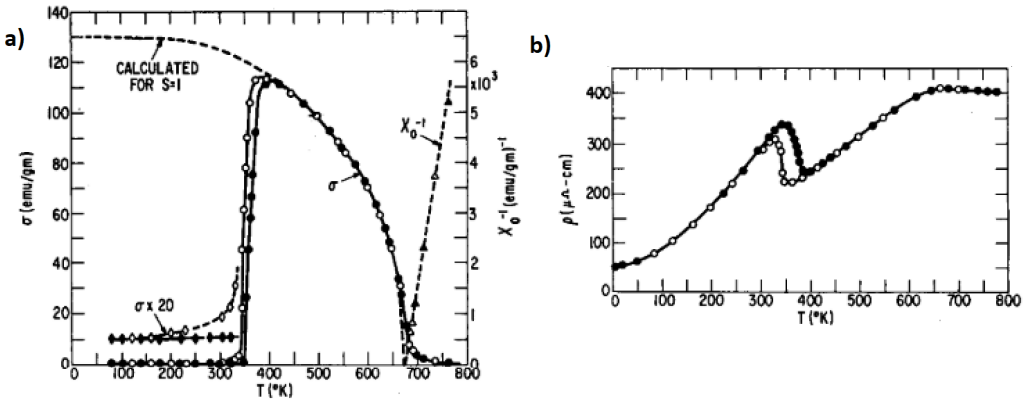

Figure 3.1: a) Magnetisation of an FeRh ingot at 5 kOe and inverse initial susceptibility. A Curie curve is seen to fit the magnetisation curve where T_C = 650 K b) Electrical resistivity for sample heating and cooling. Taken from Kouvel et al. [14].

In tandem with thin film experimental work, increased use of *ab initio* and Density Functional Theory (DFT) simulations led to rapid progress in the understanding of the MPT. It was conclusively shown that the MPT behaviour is only observed with B2 ordered crystals (see Fig. 3.2a) [103], with other common allotropes (FCC structure) exhibiting FM behaviour across all temperatures [97, 104]. The transition occurs via change in the spin alignment on the Fe sites from antiparallel to parallel causing a net moment to appear, as in Fig. 3.2b. Mössbauer spectroscopy has shown that this takes the form of a spin reorientation [105] with the Fe atomic moment relatively unchanged

(3.14 μ_B - AF vs. 3.23 μ_B - FM). This prompted interest into the potential applications for FeRh in AF spintronics [25, 106] where the FM phase provided a pathway to align the Neél vector. Furthermore, insight was provided into the hybridised magnetic moment of non-magnetic Rh atoms in the FM phase [92]. Using DFT simulations it was shown that this moment (1.0 μ_B) is as a direct result of the net field on the Rh atom due to the surrounding Fe cage [107]. Detailed analysis of X-ray Magnetic Circular Dichroism (XMCD) measurements have shown the spin and orbital moments to be m_s = 3.15 μ_B and m_L = 0.072 μ_B for Fe, with m_s = 0.96 μ_B and m_L = 0.057 μ_B for Rh [108]. It was only with the assistance of *ab initio* techniques that these moments were confirmed, further providing estimations for atomic moments in the AF phase [109]. The Rh atom is believed to experience similar hybridisation in the AF phase, but without the field stabilisation of Fe spins no net moment is observed [35].

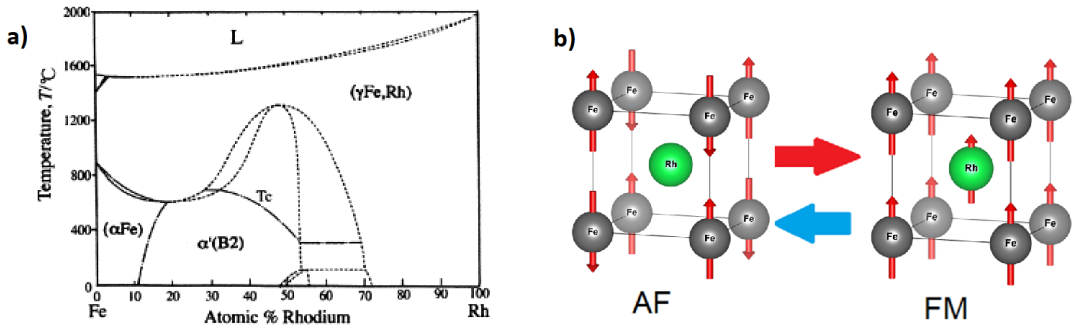

Figure 3.2: a) A phase diagram showing the preferred crystal structure of $Fe_{(1-x)}Rh_x$ as a function of temperature and Rh atomic %, taken from Oshima et al. [110]. b) Change in magnetic order of the FeRh equiatomic alloy from G-type AF to soft FM. Rh atomic moment emerges in FM phase.

Of particular interest is the sensitivity of the transition to a wide variety of factors. This sensitivity is due to the small energy barrier between the AF and the FM states [111]. Numerous theoretical works have examined the relative phase stability and found that they are relativity close in energy [107, 109]. At temperatures close to RT, thermal fluctuations can perturb the system over the phase transition barrier, with T_T found in the range 300-400 K depending on the ratio of Fe to Rh, or by doping with elements such as Pd or Cu [112, 113]. The sensitivity of the transition to external magnetic field offers an insight to the mechanism. As the T_T has a field dependence of 9 K T^{-1}, it can be altered using field strengths available in laboratory settings [114]. Previous *ab initio* simulations, have shown this is due to the slight cant induced on the Fe spins [35, 115]. This cant reduces the energy barrier to the FM state through

a 'feedback' model [94]. The slight tilt induces a small moment on the Rh sites. As discussed previously, the hybridised spin interaction of the Rh atoms is believed to exist in both phases [35]. Usually, the G-type spin order results in a net zero moment. However, with the asymmetry instigated due the spin cant a small Rh moment is predicted. Then in a positive feedback loop, the small Rh moment further cants the Fe spins reducing the energy barrier to the spin-flip (or flop [116]) state. This theory has been described thoroughly but detailed investigations into the Rh electronic structure and the spin vectors of the AF phase are required to confirm the hypothesis [21].

3.2 Coupled Physical Transformations through the MPT

The work reported in this thesis was motivated by broader solid-state research into FeRh which focused on the coupled nature of the transition. As well as the sudden magnetisation emergence discussed above, the resistivity of the material changes due to transformations in the Fermi surface [34] and the phonon bands reorganise as the lattice undergoes an isotropic expansion [21]. By exploring the evolution of these physical properties (see Fig. 3.3), fundamental questions about the MPT can be answered.

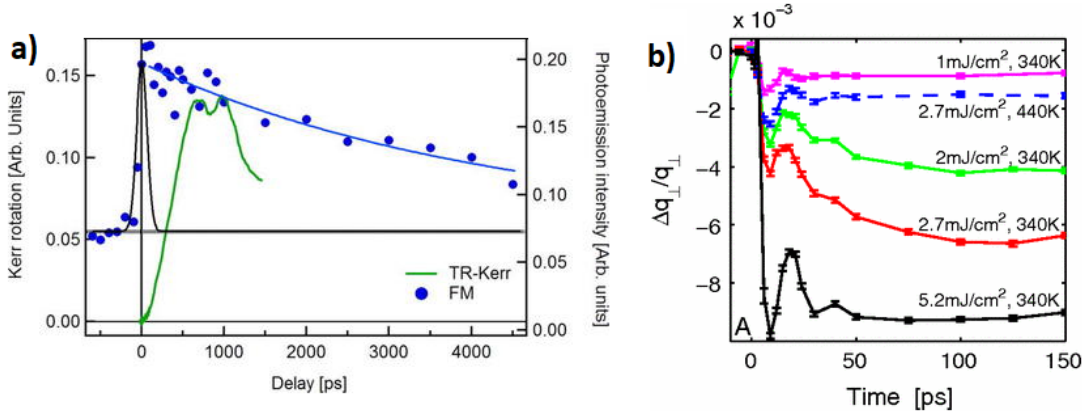

Figure 3.3: a) Evolution of the Fermi edge assumed to be a marker of the FM phase (blue dots) and surface magnetisation (green line) following laser excitation. The changes in electronic structure were detected by x-ray photoemission spectroscopy using a photon energy of 120 eV. It is assumed the electron system is immediately heated by the laser pulse before electron-spin coupling dissipates energy resulting in the emergence of a FM moment (TR-Kerr response). Adapted from photoemission spectra experiments performed by Pressacco et al. [117]. b) Dynamics of the (101) Bragg peak centre shift following laser excitation for a range of fluences. This data is taken directly from Mariager et al. [31].

The simultaneous lattice transition with a volumetric expansion of $\approx 1\%$ occurs as measured by the change in the lattice constant from 2.99 to 3.02 Å [15]. This expansion is isotropic with B2 order being maintained throughout. Additional heating to 680 K on bulk samples demonstrated a region of low thermal expansion assumed to be a second-order FM-PM transition [116]. A more recent experiment by Mariager et al. probed the (001) peak of AF and FM FeRh following local laser heating to estimate the rate of volumetric expansion. It was observed that the peak corresponding to the FM phase emerges within 5 ps with the AF peak disappearing after 30 ps [31] in a first-order transition. In the 10 ps following laser excitation the film exhibits a mixed AF/FM phase. This indicates that the phonon band structure possesses two stable configurations which it fluctuates between; in effect similar to the stability of the parallel and anti-parallel alignment of the Fe spins. This experiment demonstrates the local laser heating induced expansion. It is expected that the bulk volume expands with the speed of sound ($\nu = 5.1$ km s^{-1}) [31] which is similar to the observed dynamic growth of FM domains [30]. Progress in the field of ultrafast structural dynamics [3] has motivated re-examination of FeRh thin films with finer temporal resolution. These are particularly appealing since recent simulations [109, 118, 119] of FeRh phonon bands using DFT have revealed that the lattice dynamics plays a decisive role in the meta-magnetic phase transition, reflected in a significant difference in the expected temperature dependence of lattice vibrations of the FM and AF phases.

Likewise, the MPT is accompanied by a transformation of the electronic valence band. This is manifested as a change of the Fermi surface with a reduction of ≈ 33 % in the bulk resistivity [13]. The magnitude of the resistivity change indicates that the electronic structure of the material is perturbed significantly upon transition, with a DFT calculated example shown in Fig. 3.4. This is expected as the band structure of FeRh evolves to promote a split in energy for the two spin states in the FM state. The lattice expansion will also change the interaction between itinerant electrons. Electronic probes of the MPT are easily realised as a consequence of the increased conductivity in the FM phase, where the potential for electronic control of the MPT has already been confirmed [120]. Previous experiments have further explored this transformation via the optical properties of FeRh thin films [121] and with TR probes of the FeRh photoemission spectra [34, 117]. The electronic band evolution changes the electron-photon interaction of FeRh and by extension the reflectivity spectra. Based on the

Drude model of reflectivity, R, it is approximated to vary at small energies with [122],

$$R \approx 1 - 2\sqrt{\frac{2\varepsilon_0\omega}{\sigma}}, \tag{3.1}$$

where ω is the frequency of observation, and σ is conductivity. One such experiment defined this the spectral reflectivity crossover with changes in reflectance of 5% upon transition observed with 2.0 eV photons [121]. The photoemission spectra is a direct probe of the Fermi surface of the material. The magnitude of the resistivity change ensures that select features are easily identifiable as either FM or AF. Probes of the valence band electronic structure have shown such FM features emerge within 1-2 ps [117]. The spin-polarised Fe band at 150 meV below the Fermi energy was found to be maximally occupied within 0.5 ps [34] with subsequent charge transfer to the hybridised Rh atom. This indicates that the electronic system of FeRh has fully transitioned to the higher temperature state while the lattice and magnetisation still exhibit behaviour associated with the AF phase.

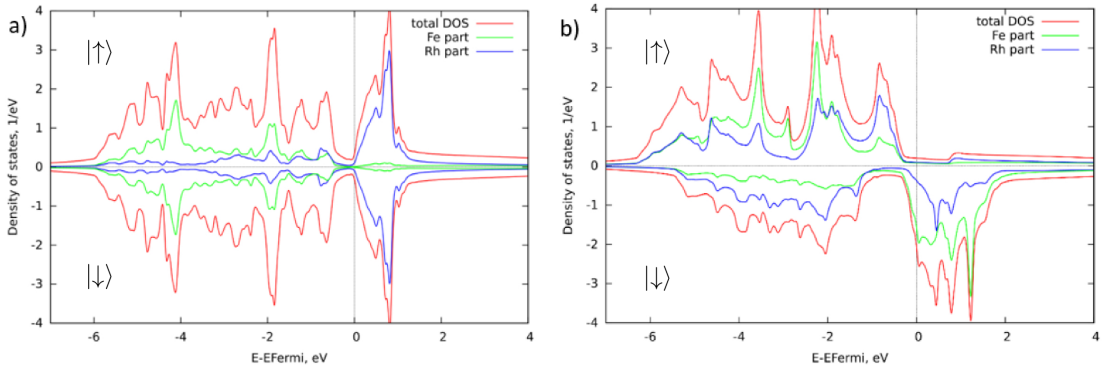

Figure 3.4: Calculated density of states of FeRh in both a) AF and b) FM phase. This is presented for the $|\uparrow\rangle$ and $|\downarrow\rangle$ spin orientations, with Fe and Rh components, and total included. Taken from Bennett et al. (2019) [121].

For comparison, TR Kerr probes of surface magnetisation have shown that the surface moment associated with the FM phase emerges over 100-200 ps following laser excitation [4, 117]. Initially, XMCD measurements indicated that changes of the magnetic structure occur on sub-ps timescales [90, 102]. However, later THz spectroscopy work revealed this was related to a demagnetisation process rather than emergence of FM spin structure, though the magnetic behaviour during the initial 10 ps is still not well understood [123]. This would suggest that the electronic and lattice perturbations drive the spin system to the FM state rather than the expansion being instigated by

exchange interactions [124]. It was further found from PhotoEmission Electron Microscopy (PEEM) experiments that the FM domains do not stabilise until 0.5 ns have elapsed since the laser excitation [30]. These studies demonstrate that the spin system evolves more slowly when compared to other aspects of the coupled transition. Commensurate studies of the dynamics of each system evolution are required to determine conclusively what is the driving mechanism of the MPT [21]. This would then allow the relative coupling strengths to be extracted using the three-temperature model of femtomagnetism [84], see Section 2.5.2.

3.3 Tuning Transition Properties in FeRh

Given the coupled nature of the MPT, FeRh may be considered a multi-functional advanced material. By changing the phonon, electronic, or spin structure, the stability of either phase is perturbed and the transition energy barrier altered [21, 111]. The increase (or decrease) in energy barrier will change T_T as more (or less) thermal vibration is required to excite the material into the FM phase. A perturbation that favours the FM phase such as an increase in the lattice constant [125] or changing the exchange interaction [107, 126] to favour parallel spin alignment should reduce T_T and vice versa. However, intrinsic perturbations such as dopants or the Fe:Rh ratio can alter more than a single physical parameter meaning such control is not a trivial matter [104].

One such parameter that is easily adjusted is the interfacial strain, either through the choice of capping layer [127] or via the substrate [128]. For example, strain due to lattice mismatch can reduce the energy required to overcome the transition barrier as the lattice is in effect already slightly expanded. In the case of epitaxial growth on MgO, this manifests itself as a FM region close to the substrate that is permanently strained [129]. Being purely an interfacial effect, the sample thickness must also be considered [130, 131]. Thicker films are less influenced by the strain and will display properties closer to that of bulk FeRh [109]. The strain is assumed to only influence the lattice constant of the material whilst B2 order is maintained. The MPT is critically dependant on the crystal structure and the degree of disorder in the sample [97, 132]. The FeRh alloy has an energetically favourable γ phase (FCC structure, see Fig. 3.2a) that is FM below T_C [97]. With increasing disorder this phase can be stabilised rather than the B2 structure resulting in permanent FM behaviour. By doping the material both the crystal and electronic structure can be perturbed, possibly promoting the γ-FM phase

[133]. Another way to promote the γ phase is by artificially increasing the disorder by ion irradiation [111, 132, 134]. This provides a depth selective means of changing the material properties. Using SRIM calculations the disorder as a function of depth can be estimated [18] to selectively induce the FM phase. This opens an avenue to using FeRh in bit-patterned media if disorder can be reliably induced laterally by combining ion irradiation and high-resolution lithography [18, 135].

As a consequence of the phase instability, it is expected that the transition should vary across the grains in a thin film sample with local differences in composition, strain, or dopants. This has been confirmed experimentally in Magnetic Force Microscopy (MFM) measurements on thin films and nanowires [136]. It was seen that microscopic grains have individual transition temperatures. These regions extend up to several μm and can have dramatically different transition temperatures than the neighbouring regions (up to 40 K as shown in Fig. 3.5a). This also explains the distribution of T_T for the first-order transition [13, 94]. The sample as a whole is an average of all the regions and rather than a sharp T_T, a sample containing many such regions will have a distribution of T_T. This transition can be modelled using a Gaussian function to define a transition point and a width of transition (ΔT). For example, the first derivative of magnetisation and resistivity with respect to temperature should exhibit Gaussian shapes which can be fitted to extract T_T & ΔT as in Fig. 3.5b.

With a view to applications, it must be considered how the patterning of thin films changes the physical properties - either as a by-product of the lithography process [29] or due to mesoscale magnetic interactions [36]. The edge damage from physical milling processes cause small disordered regions to be formed where the FM phase is stabilised [137]. As discussed above, SRIM simulations assist in predicting the ion-induced structural disorder which can induce a FM phase [132]. This can result from either the formation of γ FeRh, or as a consequence of reduced T_T [29]. This will be an important consideration as patterning dimensions decrease and the disordered regions become more influential on overall behaviour. For example, using a top-down lithography process (such as ion milling at 1000 V [29]) the disorder extends 300 nm from the feature edges. Patterning can also influence transition behaviour for samples that have high shape anisotropy. Chapter 2 discussed how AF and FM materials interact differently with external fields meaning pseudo-1D samples are expected to stabilise the FM phase as a consequence of the internal demagnetisation fields. Work by Uhlíř et al. demonstrated such behaviour in FeRh nano stripes [36]. As well as a shift in

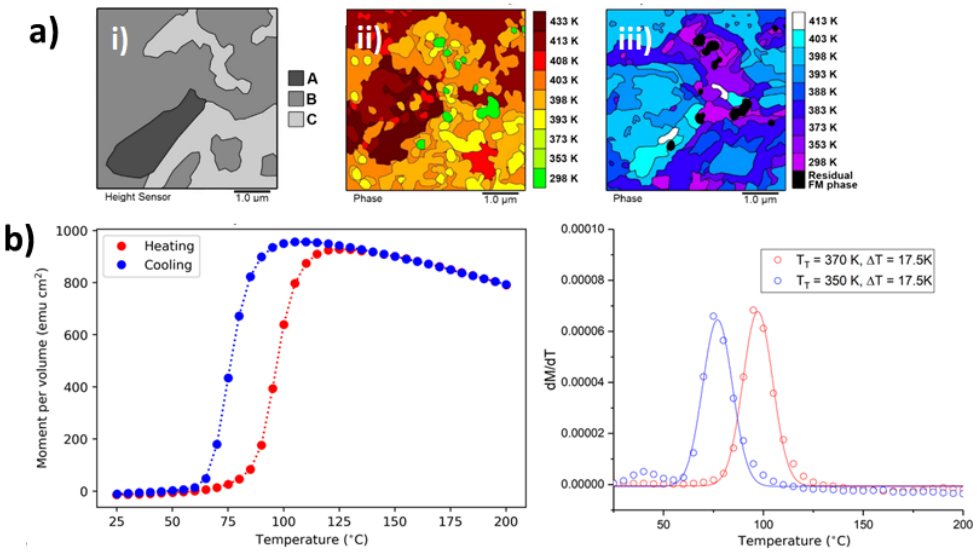

Figure 3.5: a) Series of MFM scans on FeRh thin films by Warren et al. [136]. i) Grain structure as determined by AFM, ii) T_T at which the FM phase emerges, iii) T_T for the reverse transition. b) An example of the extracted T_T & ΔT from fitting Gaussian function to the first derivative of magnetisation vs temperature.

T_T, an asymmetry in the reverse transition (AF $\rightarrow$ FM) was demonstrated where the FM phase existed at lower than expected temperatures. The reverse transition was also observed to occur stepwise rather than the smooth distribution shown in Fig. 3.5b.

Some recent work has attempted the non-destructive patterning of FeRh to achieve reversible manipulation of the material properties. Strain nano-pattering via indentation on thin films has shown changes of T_T can be induced [8]. However, the initial state could only partially be recovered by annealing. Another experiment demonstrated that a laser heated meta-stable state could be induced locally onto thin films [19]. This allows the arbitrary patterning of FM domains with write speeds limited solely by the raster capability of the focused laser. The stability of these domains is due to the undercooling of the FM phase [138], limiting its existence to a $\approx$ 25 K window (ΔT).

3.4 Microscopic Mechanism of the FeRh MPT

Implementing FeRh into devices requires fine control of transition behaviour in order to best exploit the MPT for the intended application. For this reason, the current understanding of the MPT mechanism is presented. The transition from AF $\rightarrow$ FM has

been found to follow a different mechanism than the FM → AF relaxation. This difference is due to the relative size of the domains as predicted from micromagnetic theory and has been demonstrated experimentally, see Fig. 3.6. In general, AF domains are smaller with lengths of 10-100 nm [78] in comparison to FM domains which can be micron size or larger. As a consequence, many AF domains must transition to establish one FM domain. In the work of Baldasseroni et al., it was found through autocorrelation of XMCD [139] and X-ray Magnetic Linear Dichroism (XMLD) [140] signals from PEEM experiments that the FM domains grow by first nucleating then absorbing neighbouring AF domains in thin films. The coherence length of the XMCD signal was assumed to be a reasonable estimate of domain size. Following quasi-static heating, the coherence length increased as the sample was brought through the transition indicating the domain growth mechanism. In contrast to this, the AF coherence length was found to remain at 300 nm through the cooling cycle to the RT phase. The authors explain that the 300 nm figure reported is not representative of a single domain size due to spatial resolution limits. Nevertheless, they conclude that the AF phase emerges solely through a nucleation mechanism [140]. This also explains why the FM moment is seen to take up to 0.5 ns to emerge in pump-probe PEEM measurements [30]. The mechanism of nucleation followed by growth results in a slower emergence of saturation magnetisation. These different mechanisms would suggest a difference in the sites of the nucleation points. Indeed, the AF domains are found to be correlated with defects in the crystal from the XMLD results [140] while the FM domains exhibit no such dependence [139]. Further confirmation is provided by MFM measurements on FeRh wires [136]. Repeated scans of the same sample region across multiple heating-cooling cycles show that the FM domains do not spatially correlate with the grain structure. FM domains were observed to nucleate at different sites between cycles, further indicating that the pinning sites are not restricted to lattice defects.

Although much research been dedicated to the dynamics of the MPT purely in terms of understanding the AF → FM phase changes, some recent work describes how transition dynamics may differ in the mixed phase. Due to the spread of temperatures, ΔT, over which the transition occurs, samples composed of a mixture of AF and FM phases can be stabilised and investigated. For example, spin-wave resonance experiments have been undertaken to demonstrate that first-order dynamics do not hold throughout the transition with exchange coupling at boundaries between the AF and FM domains resulting in second-order transition behaviour [112]. Methods such as nitrogen-vacancy magnetometry [141] or x-ray vector nano-tomography [142]

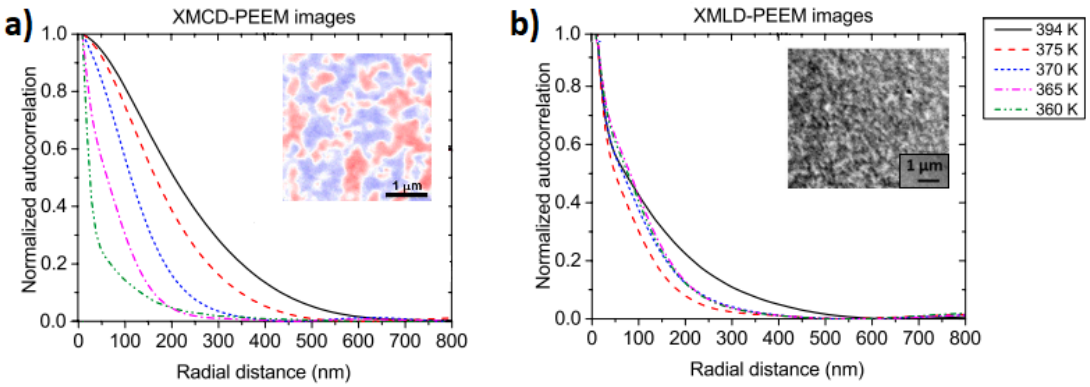

Figure 3.6: Autocorrelation length of PEEM signals as a function of sample heating, shown for a) XMCD and b) XMLD measurements on the Fe K-edge. The a) FM domains (colour inset) are considerably larger than the corresponding b) AF domains (BW inset). Adapted from Baldasseroni et al. [139, 140].

are proposed to bridge this gap of knowledge when applied to the mixed AF/FM phase of FeRh.

3.5 Experimental Outlook

Ultimately, as experimental methods have progressed the understanding of the FeRh MPT, and solid-state physics as a whole, has deepened. The open questions posed in Chapter 1 describe research avenues that remain under-explored. The work outlined in this thesis will show how a detailed experimental approach can assist in furthering the knowledge of this material which has interested researchers for over 80 years [7].

Investigating the spin order in the AF phase remains a challenging prospect due to the weak interaction with external fields. X-ray based probes are more easily realised than previous neutron approaches [91] due to the rapid development of 4th generation synchrotron sources [143]. This may also offer insight into the hybridised Rh moment through resonant techniques [21], or the mixed AF/FM phase [37]. With the increased temporal resolution of x-FEL sources [144], transient states in the electronic [34] and phonon systems [38] cannot be explained by the three-temperature model [84]. The analysis of such work relies upon theoretical phonon band simulations [118, 119], and models explored in the field of structural dynamics [3, 145]. This has important consequences for the physical description of coupling in FeRh where a simultaneous probe

of the lattice and spin systems remains elusive [21]. Building on the phase transition asymmetry observed in previous electrical work [36], TR magnetisation studies of nano-patterned FeRh should be performed. This would inform on the effects that lithography-induced damage and micromagnetic energies have on the AF $\rightarrow$ FM mechanism.

This thesis approached the phase transition from an experimental standpoint, but complementary theoretical work deepens the understanding of physical transformations. Therefore, the FeRh MPT must be implemented in *ab initio* [109], monte-carlo [146], molecular dynamics[115], atomistic [112], and micromagnetic [147] simulation techniques; all of which are challenging to realise due to the inherent phase instability of FeRh.

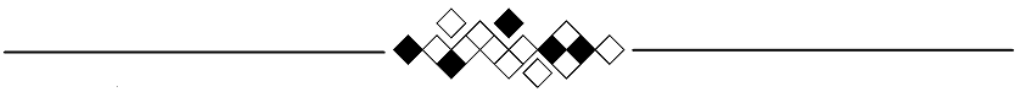

Chapter 4

Experimental and Numerical Methods

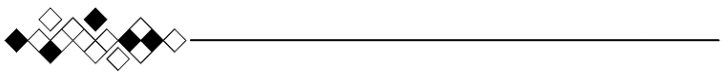

An overview of the experimental techniques used in the course of this project with the relevant background theory. An outline of the simulation techniques is provided. The data analysis is discussed with an explanation of the relevant sources of error and treatments of uncertainty.

4.1 Thin Film Preparation

The sensitive nature of the FeRh MPT outlined in Chapter 3 demands samples of high purity, crystallinity, and consistent physical properties. To achieve this, thin films are prepared by physical vapour deposition. The process is described here as well as factors that hinder production of nm smooth films.

4.1.1 Magnetron Sputtering

Sputtering was the technique chosen for thin film preparation due to the range of materials that can be deposited as well as the control it provides over growth rate and smoothness of deposited films [148]. The technique relies on a physical process of Ar^+ ion bombardment and therefore is not limited by the need to initiate chemical reactions [148]. For films of < 1 μm, it is a fast technique that is readily scaled up for industrial purposes. Sputtered thin films possess consistent density and quality, with strong adhesion [148]. For these reasons, sputtering is often used in material science where the end goal is industrial applications.

This technique is based on emission from high purity target materials when bombarded with plasma. Ar^+ plasma is created by applying a strong current to low pressure gas as in Fig. 4.1. Once ionised, a potential difference accelerates the ions towards the target. This is not a linear relation due to the activation energy, the ionisation energy, and the non-ohmic behaviour of ionic currents. Under rf potential, V_0, the equation of motion for the ions is [149],

$$\frac{d^2x}{dt^2} = \frac{eV_0}{Md} \cdot (\varepsilon + 2\cos(\omega t)), \tag{4.1}$$

where ω is the rf frequency, ε is dimensionless dc bias ($0 < \varepsilon < 1$), M is ion mass, and d is the distance from the cathode to the plasma. Under dc bias, the motion is described by the Lorentz force [149]. Magnets are used to confine electrons ensuring a consistent angular spread of material emission. The emission rate will depend on the adhesion energy, atomic weight, and striking probability of the target species [148]. The rate further varies throughout the sputtering process due to isolated electric charges repelling the ion plasma. Furthermore, the sticking probability of the emitted atom on the substrate, s, is considered in terms of the activation energy, E_{act} [148];

$$s = \sigma f(\Theta) \cdot \exp\left(-\frac{E_{act}}{k_B T}\right), \tag{4.2}$$

where σ is a steric consideration, and $f(\Theta)$ is a coverage dependent function described by the Langmuir model [148].

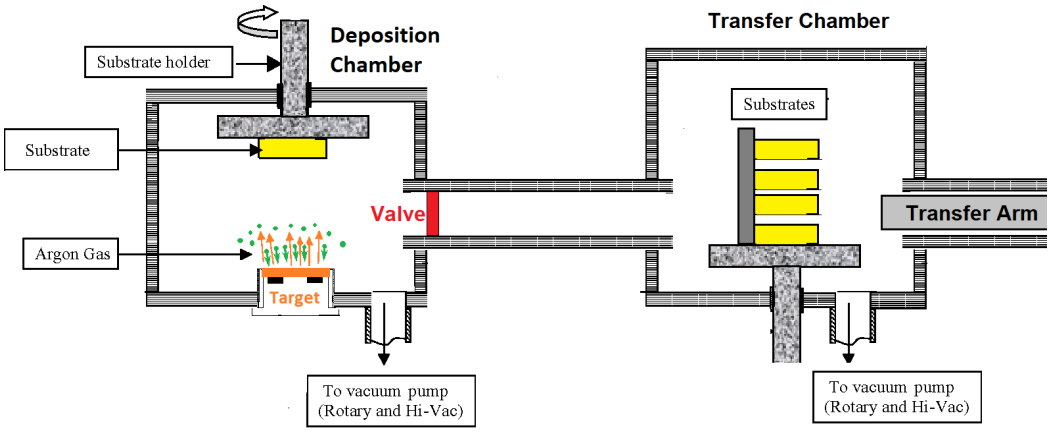

Figure 4.1: Schematic of the AJA sputter system adapted from Mubarak et al. [150]. An illustration of the emission from confocal target (orange) following ion (green) bombardment is provided. The emitted atoms will deposit on the substrate (yellow).

Next we consider how these deposited atoms arrange themselves on the substrate surface. The theory of growth kinetics was initially proposed by Markov in terms of the chemical potential [151], μ, the energy increment associated to the formation of a unit area of deposited film. The chemical potential of layer-by-layer growth $\mu(n)$ is considered as (assuming negligible strain energy);

$$\mu(n) = \frac{1}{n}\left[\mu(1) + (n-1)\mu_\infty\right], \tag{4.3}$$

where μ_∞ is the bulk chemical potential, $\mu(1)$ is the chemical potential of a monolayer on the substrate, and n is the layer number. The derivative $\frac{d\mu}{dn}$ indicates whether the ad-atom cohesive force is stronger than the surface adhesive force. Where the derivative is positive (meaning ad-atom adhesion is stronger) island growth is expected [151]. These energies also depend on the substrate involved and the temperature at which the process is carried out. Increased temperatures increase the mobility of adsorbed atoms, resulting in the atoms finding a lower energy state. $\mu(n)$ will further change as a function of layer thickness. As the number of layers increases, interaction with the substrate weakens and growth will proceed as if upon the bulk material. There are three basic mechanisms described in the field of surface science, illustrated in Fig. 4.2.

a) **Volmer-Weber:** adatom–adatom interactions are stronger than those of the adatom with the surface, leading to the formation of three-dimensional adatom clusters or islands, see Fig. 4.2a.

b) **Stranski-Krastonov:** an intermediary process characterised by both 2D layer and 3D island growth. Transition from the layer-by-layer to island-based growth occurs at a critical layer thickness, see Fig. 4.2b.

c) **Frank-Van Der Merwe:** adatoms attach preferentially to surface sites resulting in atomically smooth, fully formed layers. This layer-by-layer growth is two-dimensional, see Fig. 4.2c.

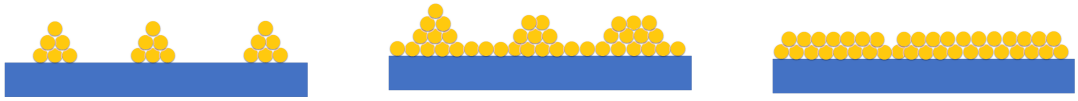

a) Volmer-Weber b) Stranski-Krastonov c) Frank-Van Der Merwe

Figure 4.2: Types of film growth upon nm smooth substrates.

Understanding the growth mechanism can inform the necessary thickness to be deposited. If a film with no gaps is required, e.g. for patterning samples to be used in electrical experiments, the ideal scenario would be Frank-Van Der Merwe. If this can not be achieved by changing the growth conditions, longer deposition times are used so that the islands eventually meld together to form a film. Conversely, island growth might be appropriate for other applications such as studies of grain boundaries. Grain sizes are estimated by considering the wetting angle [152]. The effective surface tension is as a result of the reduced free energy for atoms binding to the same species instead of the substrate species [148]. An approximation for the wetting angle θ_w, the angle between the surface and island edge is,

$$\cos(\theta_w) = \frac{\gamma^{sf} - \gamma^{sd}}{\gamma^{df}}, \tag{4.4}$$

where $\gamma^{sf}, \gamma^{sd}, \gamma^{df}$ are the free energies of the surface-free space, surface-deposited material, and deposited material-free space, respectively.

The AJA-ATC 220 system used in this project is illustrated in Fig. 4.1. This consists of two chambers, the transfer chamber and the deposition chamber. The main deposition chamber consists of a rotating sample arm with 11 targets and target guns. This allows for co-sputtering, depending on the availability of power supplies. Power supplies used are either dc or ac sources. An ac source is necessary when depositing insulating materials, where a plasma cannot be maintained under dc bias. Each gun contains a 2 inch target of material, with purities exceeding 99.9%. For preparation of ultra-thin layers, higher purity sources are used with impurities $< 0.01\%$. Targets are regularly cleaned by pre-sputtering to remove oxides or adsorbed hydrocarbons.

Substrate Cleaning for Uniform Film Growth

One of the most critical aspects to achieving the desired thicknesses and ordering in deposited thin films is smooth and clean substrates. An imperfection on the order of μm can result in a large area where thin film is not deposited, while substrate roughness of 1-2 nm prevent the production of atomically smooth films [148]. These can greatly effect the material properties especially in the very thin film regime (< 10 nm) [153]. Epitaxial growth considerations can further restrict the choice of substrate. Lattice matching can be used to seed the crystal for selective growth of a particular material phase [154]. For these reasons, the substrate chosen for FeRh thin films is MgO [20].

The high durability of the MgO crystal allows for the preparation of substrate surfaces with low roughness [155]. The stability of the (001) face is a further advantage, as this face promotes the growth of B2-ordered FeRh [20]. However, one disadvantage of MgO is the affinity for surface adsorption of organics and water. Therefore, a cleaning procedure was developed in the NEST group based on the literature of Collins et al. [156]. Detergent is necessary to remove the large hydrocarbons [156] as Iso-Propyl Alcohol (IPA) and acetone are not suitable for such purposes [148]. The detergent chosen was Decon-90 due to its availability and easy dissolution in water [157]. The cleaning procedure is carried out in an ultrasonic bath as follows;

- ◇ 1 minute in Decon-90 solution (5% in DI water)
- ◇ 2 x 1 minute in DI water
- ◇ 10 minutes in acetone
- ◇ 10 minutes in IPA

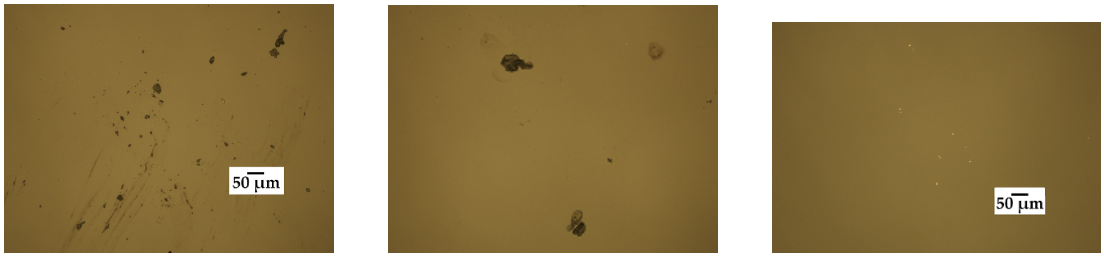

a) 'Dirty' MgO b) Post-detergent c) Full cleaning procedure

Figure 4.3: Optical images of the MgO (001) substrate showing the surface impurities that can effect the subsequent growth of deposited films. The full cleaning procedure is observed to leave the surface optically clean.

As can be seen in Fig. 4.3 the procedure results in the removal of b) organics and c) detergent crystals. It is then necessary to remove persistent adsorbed water and lighter organics. MgO is degassed in vacuum to prevent further adsorption and subsequent reactions that could impair the surface [158]. This step is carried out in the vacuum chamber of the AJA sputtering machine, implemented by heating the substrate to 650 °C at pressures below $5x10^{-8}$ mTorr for a minimum of 2 hours.

Calibration of FeRh Deposition Rate

For the preparation of consistent films of a desired thickness, the deposition parameters of the FeRh must be investigated. This was implemented as a rate test, see Fig.

4.4 where the deposition time, t_d, is varied under fixed sputtering conditions. The recipe was developed by previous members of the group and has been detailed in prior publications [129, 131].

- ◇ MgO substrate baked @ 650 °C for 2 hours
- ◇ Sputter FeRh @ 100 W (dc) for 180 s - shutter closed
- ◇ Sputter FeRh @ 100 W (dc) for t_d s - shutter open
- ◇ Anneal at 750 °C - 2 hours
- ◇ Cool down to RT - minimum 4 hours
- ◇ Sputter Pt @ 100 W for 32 s (prevent surface oxidation)

A series of samples were prepared according to the above process and were characterised in terms of their thickness and magnetic properties. Using GenX, the thickness, roughness, and density of the layers were found from XRR data (see Section 4.5.2). The density used for FeRh was 9.86 g/cm^2, and the roughness was estimated as ≈ 1-2 nm in all instances. The thickness was cross-referenced using VSM magnetometry scans (see Section 4.3.1). The moment per volume has been measured extensively in the literature [14] and is used as a measure of the sample quality.

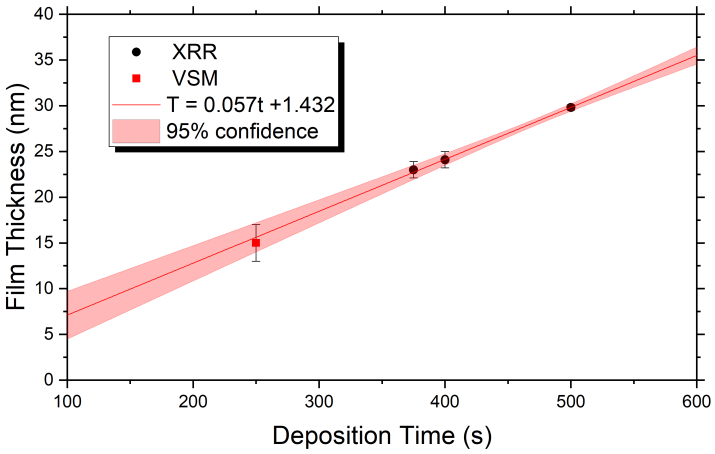

Figure 4.4: Deposition rate of dc-magnetron sputtered FeRh upon MgO (001) substrates using the AJA ATC-2200 at a power of 100 W. Thickness determined either from XRR spectra or VSM (assuming M_s = 1095 A m^{-1}).

From magnetometry performed on the samples, the expected thermal hysteresis was observed [20] with a saturation magnetisation of 1095 A m^{-1}. This compares well

to samples in the literature, approaching the maximum moments that have been observed ($\approx$ 1200 A m^{-1} [159]). The thicknesses in this series of depositions were found to vary between 15-30 nm. Growth is expected to proceed linearly in this range where adatom-adatom interactions describe the deposition process. As such, no reference for the growth rate of ultra-thin films ($<$ 10 nm) is available, where the direct adsorption on the MgO is expected to reduce the rate [151]. This rate test was a reference for all subsequent thin film depositions, where thicknesses ranged from 10-500 nm.

4.2 Nanofabrication Techniques

In order to examine the effect of nanoscale patterning on the dynamic and static properties of the FeRh MPT, lithography is performed on deposited thin films. Electron Beam Lithography (EBL) and ion milling (described in Section 4.2.3) are used for subtractive patterning, while thermal evaporation is used for additive processes.

Patterns are implemented through polymer masks which are spin-coated on samples. EBL is utilised to selectively expose specific regions of the polymer. Exposed regions undergo cross-linking and polymerisation [160] where energy absorbed from the electrons creates radicals, causing a chain growth reaction [161]. In the case of a negative resist, these exposed regions are less soluble in a developing solution. Electron beams offer advantages over photolithography due to the shorter wavelengths, λ, of the electrons yielding a high resolution pattern technique [162];

$$\Delta x \approx \lambda/2, \quad \text{where} \quad \lambda = \frac{h}{\sqrt{2m_e eE^*}}, \tag{4.5}$$

and Δx is diffraction limited resolution at a given electron energy, E^*. However, EBL technology has not yet approached the diffraction limit. Resolution is limited by primary and secondary electron migration. Electrons scatter from collisions with atomic shells of the resist atoms. These collisions further generate secondary electrons which increase the electron absorption cross section. In practice, resolution is usually limited to $\approx$ 30 nm due to secondary electron generation [163]. As the features used in the patterns are well separated, proximity effects in the process are not considered [164].

4.2.1 Top-down Process for Nanowire Fabrication

In order to prepare FeRh nanowires for optical measurements, consistent and smooth features are required. Subtractive lithography on FeRh thin films (see Fig. 4.5) was used for this purpose. EBL allows for patterns with high spatial resolution, while ion milling selectively removes material producing sharp feature edges [148].

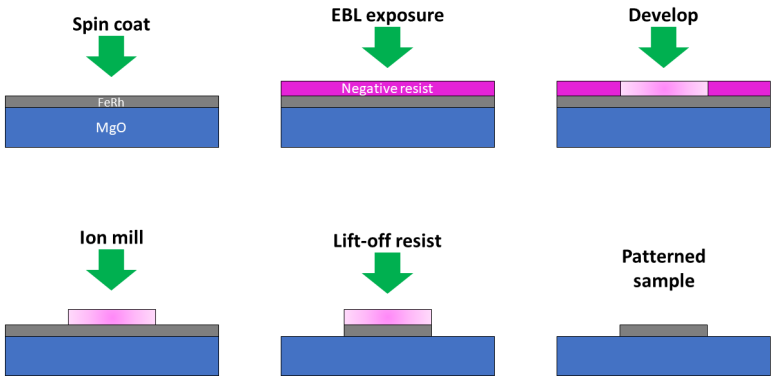

Figure 4.5: Process used in the top-down patterning of FeRh films as described in the wire fabrication steps.

- ◇ Spin coat negative resist (m-N2401) @ 3000 rpm – 1 min. Bake 90 °C - 3 min
- ◇ EBL exposure (Beam size: 220 na; Dose: 500 μC cm^{-2})
- ◇ Development: ma-D 525 (TMAH based) - 50 s
- ◇ Ion mill @ 200 V
- ◇ **Lift-off:** mr-REM 700 (NMP free). Rinse in DMSO, acetone, IPA.

4.2.2 Preparation of 4-point Contacts

To characterise individual FeRh patterned samples, contact pads are deposited for electrical measurement (see Section 4.2.4) in an additive process. Masks are prepared by EBL (see Fig. 4.6), and Au contact pads are deposited using thermal evaporation.

- ◇ Substrate clean: Acetone 2 x 3 min (ultrasonic bath), IPA 2 x 3 min (ultrasonic bath)

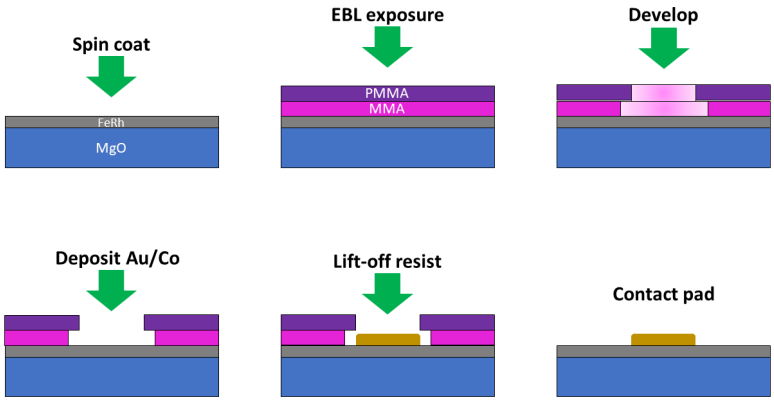

Figure 4.6: Process for depositing contact pads on FeRh patterned samples and films as described in the 4-point contacts steps.

- ◇ Spin coat positive resist (MMA 4%) @ 3000 rpm – 1 min . Soft bake 176 °C - 3 min
- ◇ Spin coat positive resist (PMMA 950K 4%) @ 3000 rpm - 1 min. Soft bake 176 °C - 3 min
- ◇ EBL exposure (Beam size: 220 na; Dose: 500 μC cm^{-2})
- ◇ Development (Hammaker program: 2, ratio 1:3) - 50 s
- ◇ Thermal evaporation: Cr - 5nm, Au - 30nm, Cr - 5nm (rate 1-2 Å/s)
- ◇ **Lift-off:** Acetone 3 x 15 min, rinse with water gun and wipe with RS PRO cloth. Acetone 2 x 3 min (ultrasonic bath), IPA 2 x 3 min (ultrasonic bath)

4.2.3 Ion Milling for Top-down Lithography

The top-down approach for the preparation of nanowires requires removal of surplus material. This is achieved by ion milling - a physical process which is based on the bombardment of a surface with sufficiently accelerated ions to remove surface atoms. In order to pattern the material with the required geometry, removal rates of the surface must be quantified. Therefore, it is necessary to calibrate the mill rate of all materials and deposited resist layers. This ensures that only necessary material is removed. For metallic samples, a simple resistance measurement with an ohmmeter will determine the endpoint of the mill process. Otherwise, milling endpoints are determined by

microscope inspection, Scanning Electron Microscopy (SEM), or profilometry.

Table 4.1: Ion milling conditions used for the removal of FeRh film.

Rotation	Pitch angle	RF power	Beam current	Beam voltage
10 rpm	15°	250 W	50 nA	351 V

Ion Milling Rate Test

An Oxford IonFab 300Plus was used for ion milling in this project under the conditions listed in Table 4.1. Calibration was performed to measure the mill rate of FeRh and photoresist (see Section 4.2.1). A strip of Kapton tape was used as a height reference for FeRh, assuming that any material under the kapton tape would not be milled away. From the comparison of FeRh and photoresist mill rates, it is determined if the resist is sufficiently thick to withstand the entire milling procedure.

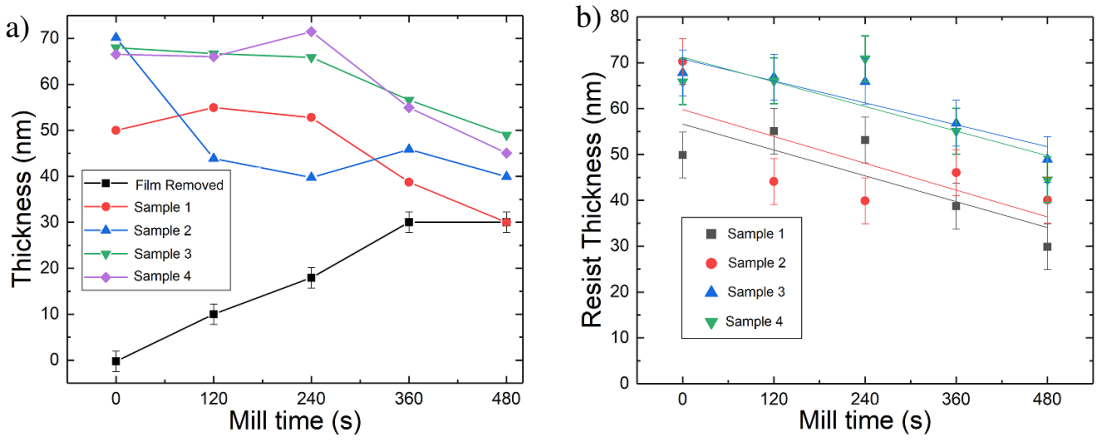

Figure 4.7: Thicknesses extracted from the DEKTAK profilometer following 2 minute intervals of ion milling. a) The height of each array as a function of milling time, with the estimated FeRh thickness. The initial film thickness was 30 nm. b) Extracted estimate of the resist thickness across each array as a function of milling time.

The removal rate is quantified with line scans using a DEKTAK profilometer. Scans are performed across 4 identical features (length 100 μm) and a reference portion of film (thickness - 30 nm). The reported height is a combination of the FeRh film thickness (see Fig. 4.7a) and the resist layer thickness (see Fig. 4.7b). After 6 minutes, film is completely removed where the mill rate of MgO substrate is assumed to be negligible at these voltages. In the case of na-M2401 spin coated at 1000 rpm on the

FeRh||Pt, the rate of milling was 5.0 ± 0.4 nm min^{-1} for FeRh and ≈ 2.6 ± 0.2 nm min^{-1} for the resist layer. For thicknesses of 40 nm - as used throughout this thesis - it is assumed only surplus material will be subject to milling. For thicker films (> 100 nm), it is expected that some of the patterned material would be removed in the process.

4.2.4 Electrical Characterisation

The resistivity of the FeRh B2-ordered phase changes significantly during the MPT [21]. This provides a method of characterising the transition behaviour locally using electrical measurements. The differences in the band structure between the AF and FM phase result in a change of resistivity on the order of 33% [15]. For the characterisation of patterned samples, this offers a method of examining the T_T locally where the sample dimensions are known to a high degree of accuracy. The resistivity (ρ) is found by assuming ohmic behaviour, where the general conductivity σ is simplified under a steady state assumption [54];

$$\sigma(\vec{r},t)\,\frac{\partial^2\Phi}{\partial x^2} = \vec{J} \quad \Rightarrow \quad \rho = \frac{V\cdot A}{I\cdot L}, \tag{4.6}$$

where Φ is the electric potential, J is the current density, and x is the direction parallel to the length, L. V and I are voltage and current, while A is the cross-sectional area. Such measurements can be carried out using a Physical Property Measuement System (PPMS); the field and temperature can be controlled while precise electronic measurements are performed. The small currents used (tens of nA) allow for precise measurements without subjecting the nanostructures to high current densities. Using a 4-point probe as in Fig. 4.8 the resistivity can be monitored over small regions after lithography has been carried out.

This 4-point probe technique is chosen so as to reduce the effect of contact resistance allowing the sheet resistivity, ρ_s, to be determined. The 2D geometry of an infinite film means current sources give rise to a potential that falls off logarithmically with distance [165]. The two outer probes introduce an electric dipole and it can be shown that the potential difference between the two inner probes is [165],

$$\Delta\Phi = V = \frac{I\rho_s}{\pi}\ln 2. \tag{4.7}$$

When a sheet of finite thickness W is considered, the resistivity can be expressed in

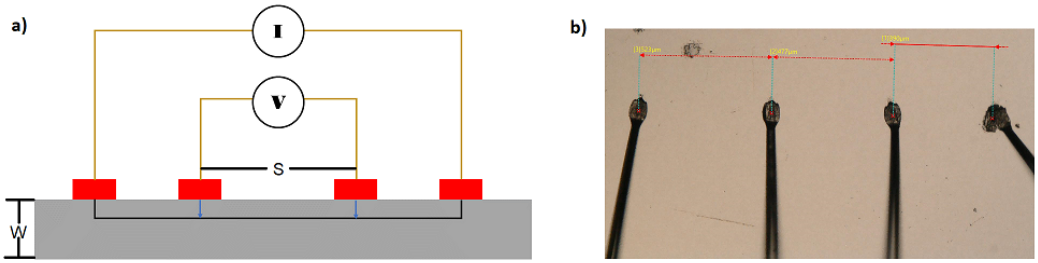

Figure 4.8: a) Sketch of a 4 point probe with contact pads in red. A current is applied and the voltage measured across the region can be converted into a resistance from which the resistivity is calculated. b) An optical image of wire bonding on a thin film surface to produce a 4-point probe.

terms of the sheet resistance. The following relation holds when the contacts are spaced apart by distance s, see Fig. 4.8a;

$$\rho_s = w\frac{V}{I}\frac{\pi}{\ln 2}\cdot F\left(\frac{W}{s}\right). \tag{4.8}$$

The correction factor, F, approaches unity as the thickness reduces; values can be found from the papers of Smits [165] and Uhlir [166].

4.3 Magnetic Characterisation

The magnetic properties of the prepared FeRh samples were quantified in terms of the saturation magnetisation and T_T, at which FM behaviour emerges. Static measurements were complemented by optical-based techniques which investigate the emergence of surface magnetisation as a consequence of local laser heating.

4.3.1 Vibrating Sample Magnetometry

The magnetic properties of a sample are determined when exposed to applied magnetic fields. This can be used to quantify the saturation magnetisation and coercivity, as well as determine sample anisotropies. Due to the thin film samples used throughout the project, the soft FM moment is expected to be inclined in plane. The shape anisotropy in the absence of magnetocrystalline or magnetoelastic anisotropies (see Section 2.4) will impose such an easy axis [17].

A prototypical scan for FM materials is to probe the in-plane moment as an external magnetic field is swept from +2T to -2T. For most FM materials, this allows for the hysteretic behaviour to be observed demonstrating saturation magnetisation, the coercive field and remanence. If sample anisotropy is expected, it is important to examine the behaviour as a function of the applied field angle. Temperature sweeps can be performed if parameters such as the Curie temperature or T_T are of interest.

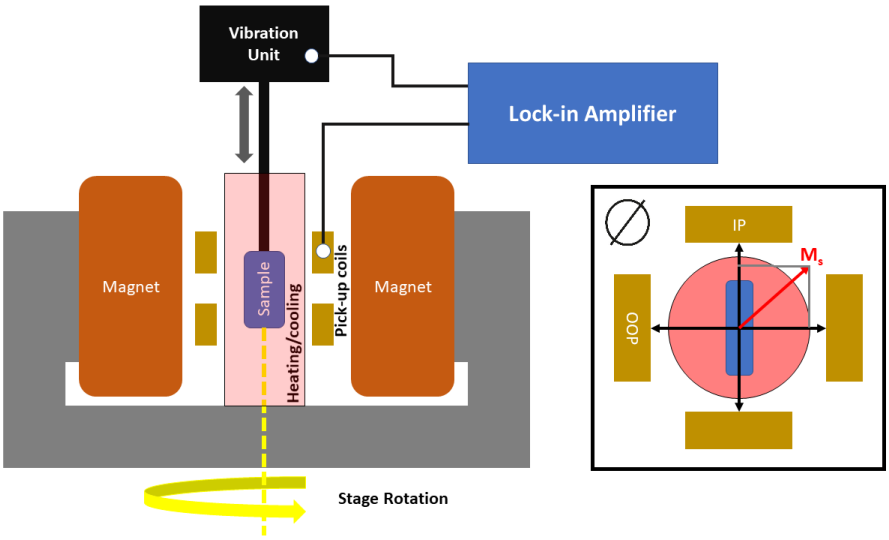

Figure 4.9: Lab-based VSM set-up. The sample is oscillated between the pick-up coils which pass the signal to the lock-in amplifier. The stage can be rotated about its central axis and temperature is controlled with air flow. The orientation of the magnetisation can be determined from the placement of the 4 pick-up coil pairs, see inset.

In this project, such measurements were performed using a lab-based technique, Vibrating Sample Magnetometry (VSM) [167]. A schematic of the essential components of a VSM is shown in Fig. 4.9. In general, the main issue with performing magnetic experiments is distinguishing the sample response from the applied field. The solution is to generate a signal that is ascribed solely to the sample. Hence, the sample vibration in a VSM. The frequency of oscillation is passed to a lock-in amplifier. The moment is extracted from the pick-up coil signal, based on the Maxwell treatment of electromagnetism. A magnetic moment with stray field, $\vec{B}$, vibrating at a fixed frequency will generate an electric field, proportional to the sample moment. The emf, $\vec{E}$, contained within a surface, C is [54],

$$\oint_C \vec{E} \cdot d\vec{l} = -\frac{d}{dt} \iint \vec{B} \cdot d\vec{A}, \tag{4.9}$$

where $\vec{A}$ is the vector area. With consistent pick-up coil position, the change in signal will be linear with respect to the sample moment. The magnetocrystalline, magnetostrictive, and magnetostatic anisotropies can each affect the orientation of the magnetisation vector, $\vec{M}$. In order to estimate the direction of $\vec{M}$, it is important to consider how In-Plane (IP) and Out-Of-Plane (OOP) signals are differentiated. 8 pick-up coils are grouped in 2 sets, with coil pairs being perpendicular to each other within the sample plane, see Fig. 4.9 inset. This quadrupole set-up allows for the extraction of angular dependant signal using the relative responses from the IP and OOP coils. For the determination of sample anisotropies (see Section 2.4), the magnet is rotated about the sample while changes in the angular response of the magnetic moment are detected.

Calibration of System and Background Diamagnetism

In order to fully account for all contributions to the signal, sources of all possible magnetic interactions are considered. The magnetic materials investigated have volumes $\approx 1\text{x}10^{-12}$ m^{-3}, meaning low total moments are expected ($1\text{x}10^{-7}$ A m^2). Sources of diamagnetic and paramagnetic signal are also considered. Paramagnetism results from unpaired electrons in atomic shells which align with applied fields as described in Chapter 2 [17]. The susceptibility to magnetic fields for paramagnetic and diamagnetic materials are found from Eq. (2.31) and (2.32), respectively [17].

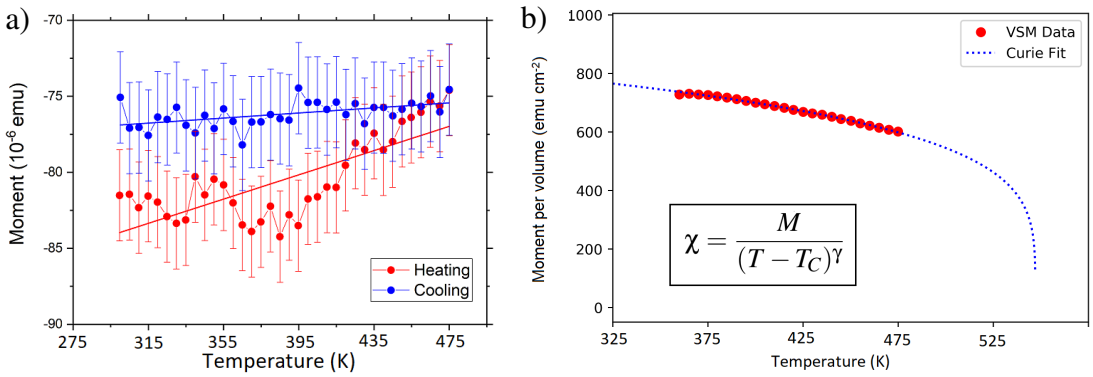

Figure 4.10: a) Moment as a function of temperature of 8 mm disc of MgO substrate at an applied field of 1 kOe. The diamagnetism is seen from the negative response. b) Magnetisation vs. temperature of FeRh sample with guide-to-eye Curie curve. The functional form of the susceptibility is inset where $T_C \approx 550$ K, M = 800 A m^{-1}, and $\gamma = 1$.

In the highly sensitive VSM set-up this diamagnetic response can be detected from the sample holder, substrate, tape etc. It will be the vector sum of all components

exposed to the magnetic field. It is therefore important to measure a reference sample, which is used to account for the diamagnetic background. For samples explored in this project, the majority of experiments are carried out on MgO substrates. Therefore, the system requires calibration using a blank MgO substrate for the diamagnetic reference. In all cases, samples are ground into 8 mm discs where the grinding medium consists of silicon carbide particles suspended in glycerine. The diamagnetic response of an 8 mm MgO disc and sample measuring rod is shown in Fig. 4.10a. The signal is weakly negative showing a slight reduction in magnitude as temperature is increased.

Temperature scans demonstrate how magnetism evolves when perturbed by anharmonic thermal vibrations, which informs on exchange interactions based on the Curie theory of ferromagnetism [17]. When performing scans to determine the T_T as in Fig. 4.11, this reduction in moment should be considered. By fitting with the Curie curve, the temperature dependant behaviour can be estimated even when T_C is beyond the range of the VSM set-up as seen in Fig. 4.10b. This demonstrates how saturation moment varies as a function of temperature which is useful in comparing the magnetic moment of samples with different T_T.

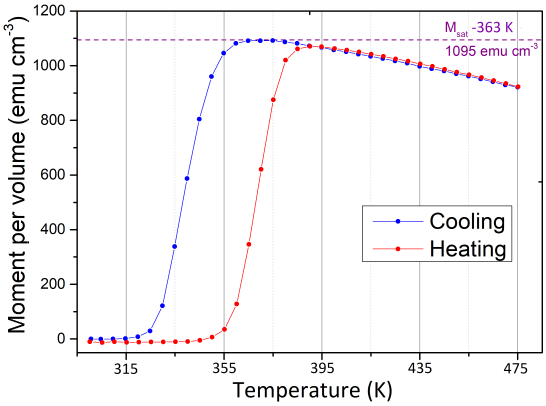

Figure 4.11: Typical magnetometry scan of 30 nm FeRh thin film vs temperature that demonstrates the sudden increase in magnetisation upon transition and the under-cooling that is expected for the first-order MPT.

4.4 Optical Probe of Magnetisation - Kerr Effect

The Magneto-Optical Kerr Effect (MOKE) offers a method of probing magnetisation within the skin depth of materials ($\approx$ 20 nm) by examining the changes in polarised light following reflection [168]. This was used to perform time-resolved experiments where temporal resolution depends on pulse length and stability of the laser system.

4.4.1 Interaction Between Surface Magnetisation and Polarised Light

MOKE experiments rely on the anisotropic permittivity of magnetic materials, which can effect both the intensity and polarisation of reflected light. The dielectric tensor ε describes interaction of light with an arbitrary magnetisation $\vec{m} = m_x + m_y + m_z$ [169, 170];

$$\varepsilon_k = \varepsilon_{xx} \cdot \begin{pmatrix} 1 & -iQm_z & iQm_y \\ iQm_z & 1 & -iQm_x \\ -iQm_y & iQm_x & 1 \end{pmatrix}. \tag{4.10}$$

The magneto-optical constant, Q, is defined in terms of the dielectric permittivity tensor, ε, of the magnetic material [171],

$$Q = i\frac{\varepsilon_{xy}}{\varepsilon_{xx}}. \tag{4.11}$$

We are interested in the real component of the Kerr signal which manifests itself as a rotation of the polarisation angle. Likewise, the imaginary components would describe the change in ellipticity. The equation are simplified in the case of Polar, $m_z = 1, m_y = m_x = 0$, and Longitudinal, $m_y = 1, m_z = m_x = 0$, setups. The angular dependence of the Kerr signal, Θ_K, is described by the formulas of You et al. [170];

$$\begin{aligned} (\Theta_K^p)^{pol} &= \frac{\cos\theta_0}{\cos(\theta_0+\theta_1)} \cdot \frac{in_0n_1Q}{(n_1^2-n_0^2)}, \quad (\Theta_K^p)^{long} = \frac{\cos\theta_0\tan\theta_1}{\cos(\theta_0+\theta_1)} \cdot \frac{in_0n_1Q}{(n_1^2-n_0^2)}, \\ (\Theta_K^s)^{pol} &= \frac{\cos\theta_0}{\cos(\theta_0-\theta_1)} \cdot \frac{in_0n_1Q}{(n_1^2-n_0^2)}, \quad (\Theta_K^s)^{long} = \frac{\cos\theta_0\tan\theta_1}{\cos(\theta_0-\theta_1)} \cdot \frac{in_0n_1Q}{(n_1^2-n_0^2)}, \end{aligned} \tag{4.12}$$

where θ_0 is the angle of incidence, θ_1 is the refracted angle found from Snell's Law, p and s refer to the polarisation axis of the light - parallel, or *senkrecht* (perpendicular)

to the plane of incidence. n is the refractive index (with subscripts: 0-vacuum/air, 1-magnetic material).

Quantifying the Polarisation Shift

In order to monitor the changes in photon polarisation following interaction with the magnetic sample, the initial polarisation must be well known. For dynamic measurements discussed below, the reference signal is the emisison from the unpumped sample. This unpumped case has a polarisation angle 45° to reference angle of the photodetector shown in Fig. 4.12). A polarising crystal within this detector evenly splits the light into vertically and horizontally polarised light. This ensures that A and B signals are equal in magnitude. For the longitudinal case examined in this project, the sum signal, A+B, describes the reflectivity, while the difference, A-B, describes the shift in polarisation, assumed to be proportional to surface magnetisation.

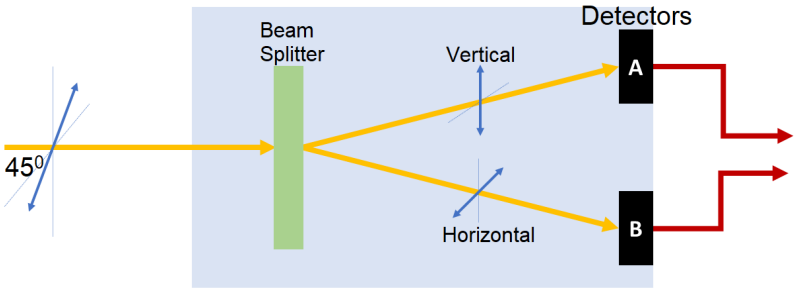

Figure 4.12: Light that is polarised at 45° and enters the photodetector is split evenly between vertically and horizontally polarised light. When suitably calibrated, a rotation in the polarisation axis results in a measurable difference in the signals A-B.

Extracting Magnetic Information from Reflected Light

In order to fully extract the magnetic behaviour from the signal, it is necessary to account for dynamic evolution of the sample reflectivity. Heating of the electron gas [87] causes increased reflectivity. One solution is to compare the signal both with and without an external magnetic field. This will further illustrate any artefacts arising from non-perfect alignment of the polarisation axis, see Fig. 4.12. Further improvements can be realised in soft FM samples where field is applied in two opposing directions. This should promote opposite changes in the Kerr signal. It is expected that the dynamic reflectivity evolution is consistent for both field applications.

Electromagnets offer fine control over the magnetic field. The system in Fig. 4.13 was fully calibrated by converting the applied current to a magnetic field value. The field is inhomogeneous in the plane of the magnet. Therefore the calibrated field refers to that found at the approximate centre of the quadrupole. With the quadrupole layout of the electromagnet used, flux densities of up to 110 mT can be applied in a variety of directions, i.e. positive and negative. The arbitrary phase offset of the lock-in amplifier (see Section 4.4.2) is corrected for by using r, the magnitude of measured signal. Separate sum, $A+B$, and difference, $A-B$, signals are recorded at the lock-in amplifier for parallel, +, and anti-parallel, -, magnetic field orientations. Then the magnetisation M within the probed volume is found with,

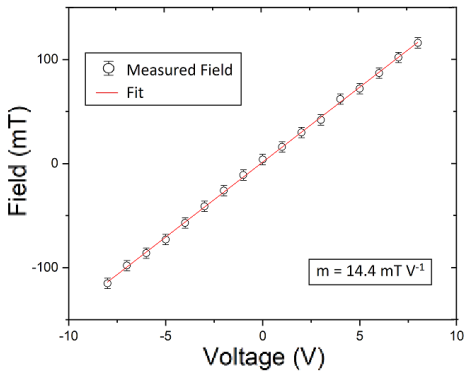

Figure 4.13: Magnet calibration showing the dependence of field strength on applied coil voltage.

$$M \propto \frac{r_{A-B}^{(+)} - r_{A-B}^{(-)}}{r_{A+B}^{(+)} + r_{A+B}^{(-)}}. \tag{4.13}$$

4.4.2 Ultrafast Laser Set-up

Pump-probe MOKE is achieved by using a beam splitter to generate two pulses highly correlated in time from the same laser source. Following Second-Harmonic Generation (SHG) of one beam, these pulses are differentiated by their power and wavelength. For highly intense beams, two photons can interact within a material to generate a third photon with twice the frequency (and energy) of the exciting light. As this is a Non-Linear Optics (NLO) effect, shorter (50 fs) and therefore more intense pulses generate significantly more SHG photons than longer pulses (300 fs). On passing through a medium of length, z, SHG intensity, $I_{2\omega}$, varies as [40],

$$I_{2\omega}(z) \propto I_{\omega}^{2}\, z^{2}\, \frac{\sin^{2}(\delta)}{\delta^{2}}, \qquad \delta = \frac{(2\vec{k}_{\omega} - \vec{k}_{2\omega}) \cdot \vec{z}}{2}, \tag{4.14}$$

where ω is the original frequency of light, and δ is the dimensionless phase mismatch. δ is maximised when $\vec{k}_{\omega}$ is aligned to the required crystallographic axis [122]. The

proportionality depends on the second-order susceptibility tensor, $\chi^{(2)}$, which is appreciable when laser light drives the electron system far from the harmonic approximation. In the experimental set-up in Fig. 4.14, the SHG is used to generate the pump beam (515 nm), while infrared light (1030 nm) is the laser probe beam. Changes in the polarisation of the probe beam are attributed to the longitudinal Kerr effect as described above. Magnetisation dynamics are extracted by changing the arrival time between the two pulses using the delay stage to change the path length of the probe beam.

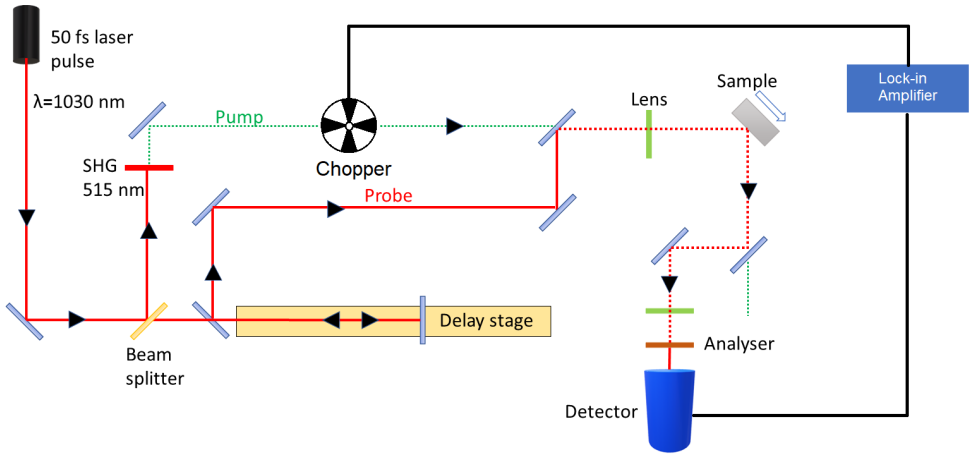

Figure 4.14: Laser pulses are emitted from source with a 200 kHz repetition rate. Pump and probe beams are coherently generated with a beam splitter and recombined after a time delay between pulses is introduced. The pump beam is filtered out before the detector. An analyser allows for the 45° polarisation axis to be achieved.

The beam is modulated by a chopper in the pump beam path. This supplies a frequency to the lock-in amplifier to monitor the fine changes between the pumped and un-pumped probe pulses. Standard operation frequency was 1 kHz. The probe beam is isolated from the pump beam following the sample excitation. This is achieved using a series of mirrors and bandpass filters that are selectively tuned to certain wavelengths. Those used were Thorlabs products, such as 'FBH520-40 - Premium Bandpass Filter' which possesses 90% transmission at 520 nm, and blocking above 556 nm (for perpendicular incidence). These are based on thin film interference where alternate layers of optical coatings selectively reinforce certain wavelengths of light [172].

The spatial overlap of the pump and probe beams on the sample surface is examined in the first instance using a remote digital camera with high magnification, and adjusting mirrors in the beam path. Further optimisation is achieved by manually adjusting the optical components (lenses & mirrors) to maximise the $r_{(A+B)}$ signal of a

reference Si(001) sample. This method is subjective, however the appreciable difference in beam sizes (100 μm - pump, 30 μm - probe) discount the need for perfect beam overlap.

Estimation of Experimental Temporal Resolution

Interpreting the results of such experiments requires fine knowledge of the temporal resolution. This is estimated by probing the reflectivity of a reference Si(001) sample as the delay stage is swept for a fixed laser fluence, see Fig. 4.15a. The reflectivity of the Si(001) sample will almost instantaneously increase due to lattice heating [173] and generation of an electron-hole plasma at the surface [174], resulting in observable changes with a lifetime 32 ± 5 fs [175]. By fitting the change in intensity (dR/dT) with a Gaussian function, time zero position, x_0, of the delay stage is established further providing an estimate of the temporal resolution. The delay stage position in mm, x, is converted to time in ps by considering $c = 0.29979$ mm ps^{-1},

$$t = \frac{2}{c} \cdot (x - x_0). \tag{4.15}$$

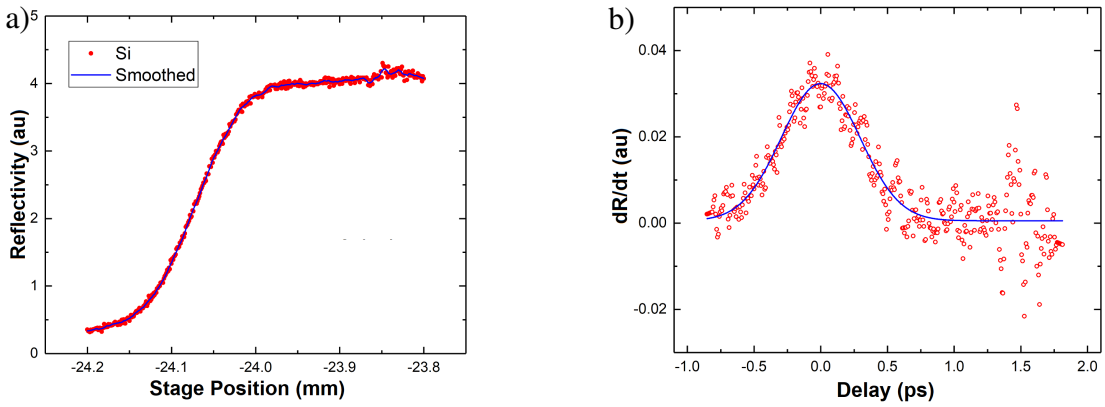

Figure 4.15: a) Time zero and temporal resolution where the laser had a pulse length of 300 fs are estimated from delay scan of Si(001) reflectivity following laser excitation with 0.12 μJ pulse energy.b) Resolution is estimated as 0.35 ps from the width of the fitted Gaussian function (blue).

As the changes in reflectivity occur over timescales much faster than the resolution of the set-up, it is assumed that the Gaussian width is a measure of the temporal resolution; resulting from the overlap of the pump and probe pulses and instrumental broadening. The delay stage piezomotor can reliably move in 0.001 mm increments, ≈ 7 fs. Therefore, scans with time steps smaller than the temporal resolution can be

performed and the data is smoothed using an available Savitsky-Golay filter in OriginPro 9.1 to improve the measured signal [176]. The data presented in Fig. 4.15 predicts a temporal resolution of 0.35 ps.

Pump Laser Fluence

The evolution of physical changes is related to the magnitude of local heating, quantified by the laser fluence. Fluence describes the energy per unit area of each pulse, and is therefore proportional to the absorbed energy. Due to the short pulse duration (50/300 fs) it is assumed that this energy is absorbed instantaneously [87], in comparison to the time scale of the experiments (ps to ns). The beamwidth is crucial in determining the fluence of a laser pulse. Beamwidth is measured by a knife edge method, where a sharp edge is defined on the sample and the beam is slowly moved across the edge (x). The change in signal (I) is expected to form an error function as a result of the Gaussian beam profile, as seen in Fig. 4.16. A sharp edge with a roughness much smaller than the beam width is required to ensure this method is accurate, such as those prepared by nano-lithography. Beamwidth is then estimated from fitting the differentiated signal, dI/dx with a Gaussian function. It is necessary to measure the beam width in two directions as it is not perfectly circular following repeated reflections from the series of mirrors (Fig. 4.14) in the set-up prior to sample excitation.

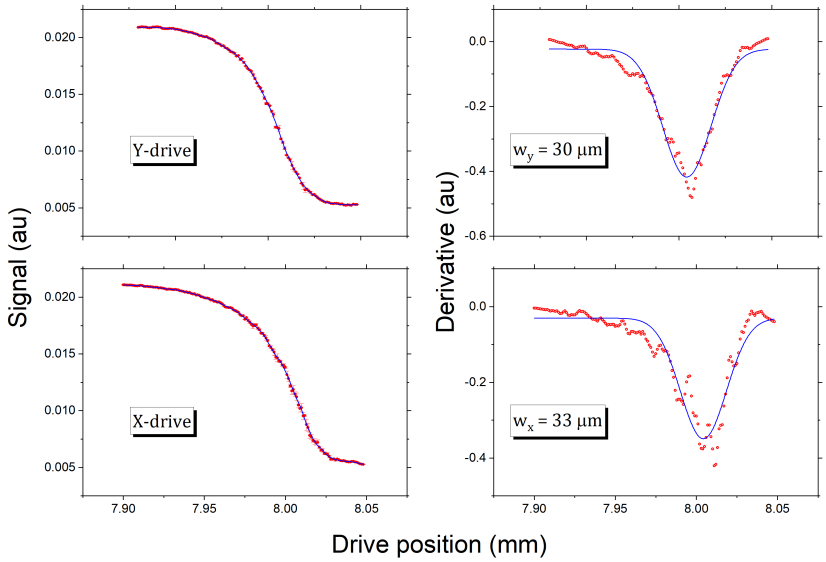

Figure 4.16: Knife-edge scans taken at 0.12 μJ pulse energy. The derivative is used to fit a Gaussian function from which the beamwidth is assumed to be σ of the Gaussian function. The averaged data is shown as a blue line which used a Savitsky-Golay smoothing method with a window of 15 points.

In order to control the laser pulse power, it is necessary to use a graduated absorber in the path of the pump beam. A piezoelectric motor allows for precise positioning of the absorber. It has been found that the laser power does not always return the maximum measured value at a given absorber position and it is therefore recommended that the power is calibrated for each run of experiments in order to ensure that the correct values of laser power are used in any later calculations.

The width as a function of fluence is measured, as the absorber (see Fig. 4.17a) may present NLO behaviour, where the absorbance depends on beam intensity. This would narrow (or broaden) as seen in Fig. 4.17b. For the fluences of interest, it is constant at $\approx 35\ \mu$m in both the x and y directions. The beam width further depends on the incidence angle, which increases the width in x. Considering the above discussion, it is then possible to calculate the fluence, F, of each pulse as,

$$F = \frac{1}{\sin\theta_0} \cdot \left(\frac{W}{f\ \sigma_x\ \sigma_y} \right), \tag{4.16}$$

where W is the power, the rep-rate, f = 200 kHz, while σ_x and σ_y are the measured beamwidths, and θ_0 refers to incidence angle of the laser in the set-up geometry.

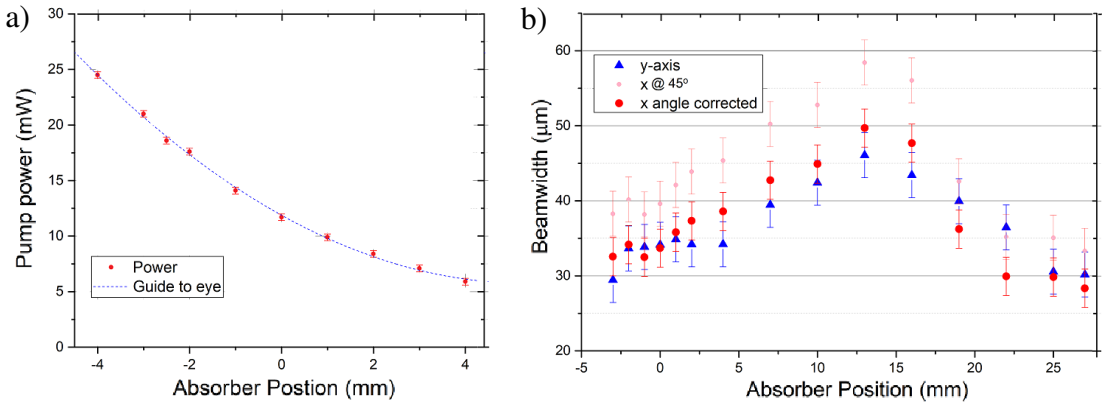

Figure 4.17: Calibration of components of the pump-probe laser set-up. a) The variation in laser power depending on position of the graduated absorber. b) Measured beamwidth of the laser pule as the position of the graduated absorber is swept.

4.5 Simulation Techniques

Simulations of the physical systems are used in tandem with experiments to estimate material properties, offering insight to processes that are beyond the capabilities of current experimental probes. In this project, simulations complemented dynamic studies of magnetic and lattice systems.

4.5.1 VAMPIRE Atomistic Software

In order to determine the coupling between the lattice and electronic systems of FeRh, the atomistic software VAMPIRE was used [177]. This acts as a bridge between the *ab initio* and micromagnetic simulations. It allows for the inclusion of interatomic interactions. The properties can be extracted from *ab initio* simulations and included as a fixed spin at each atomic site. This allows for the modelling of true atomic scale variations of the magnetization which are not captured in micromagnetic simulations. Based on the nearest neighbour and next-neighbour interactions, the evolution of the lattice temperature (see Appendix A, Fig. A.1) can be accurately modelled on a sub-ps timescale. The parameters of the FeRh material were taken from a series of theory papers [108, 109, 178]. A series of simulations were performed for increasing laser fluences to determine if the lattice and electronic system are coupled within 5 ps. Even in the case of the highest laser fluence (> 10 mJ cm^{-2}), the coupling occurs within 5 ps. This is an important consideration in the COMSOL model which will only predict reasonable lattice and electron temperatures when the systems are in thermal equilibrium. Specifics about the VAMPIRE simulation of the FeRh system can be found in Appendix A.

4.5.2 COMSOL - Finite Element Software

Simulations of sample heating were implemented using the finite element software, COMSOL® [179]. It operates by solving the required ODE using a numerical method for a chosen cell size. The differential equations are solved iteratively between the cells until a steady state solution can be found, with the multiphysics packages allowing many physical properties to be included in the analysis. It further allows for time evolution of physical properties.

The iterative solver is based on a conjugate gradient (cg) method [180], with a

defined tolerance to end the iteration. This is initially set as 10^{-3} by default but can be changed for more or less precise results. The tolerance should not be set lower than the relative uncertainty of the material parameters, as a general rule. From the set of ODE defining the system, $\mathbf{A}$, where $\mathbf{b}$ is known, an approximation of $\mathbf{x}$ is sought such that,

$$\mathbf{A} \cdot \mathbf{x} = \mathbf{b}. \tag{4.17}$$

The iteration follows the cg-method [181] with the aim to reduce the k-th residual, $\mathbf{r}_k = \mathbf{b} - \mathbf{A} \cdot \mathbf{x}_k$, to within a specified tolerance. $\mathbf{A}$ is an $n \times n$ matrix that is real, symmetric, and positive-definite. An initial $\mathbf{x}_1$ is chosen and iteration occurs with the knowledge that $\mathbf{x}$ is also a minimizer to the quadratic function, $f(\mathbf{x})$;

$$\nabla^2 f(\mathbf{x}) = \mathbf{A}, \quad \nabla f(\mathbf{x}) = \mathbf{A} \cdot \mathbf{x} - \mathbf{b}. \tag{4.18}$$

The convergence relies upon a conjugacy constraint, $\mathbf{p}_k$, which is calculated by defining the $k+1$ step to be orthogonalised to the k^{th} and all previous steps;

$$\mathbf{p}_k = \mathbf{r}_k - \sum_{i<k} \frac{\mathbf{p}_i^T \cdot \mathbf{A} \cdot \mathbf{r}_k}{\mathbf{p}_i^T \cdot \mathbf{A} \cdot \mathbf{p}_i} \cdot \mathbf{p}_i, \tag{4.19}$$

where T indicates the transverse matrix. Then the next optimal step uses the constraint, $\mathbf{p}_k$, as,

$$\mathbf{x}_{k+1} = \mathbf{x}_{k+1} + \alpha_k \mathbf{p}_k, \quad \text{where} \quad \alpha_k = \frac{\mathbf{p}_k^T \cdot \mathbf{r}_k}{\mathbf{p}_k^T \cdot \mathbf{A} \cdot \mathbf{p}_k}. \tag{4.20}$$

In order to determine the effect of laser heating on the FeRh thin films, a model was devised that used a sudden pulse of energy (less than 1ps) to excite the sample. It is assumed in these models that the electron-phonon coupling is fast enough that the two systems are fully equilibrated. For the relatively long timescales of heat dissipation (several ns), this is a reasonable approximation.

Cell Size of the Simulated System

The material under investigation in a COMSOL model is broken up into a 3D grid termed a mesh. The size of the meshed elements plays a crucial role in the runtime of the simulation with smaller fragments required for more accurate modelling. The shape of the elements can also be changed, depending on the geometry of the objects and the physics under investigation. They are usually based on tetrahedrons or swept

polygons. Swept polygons were used for thin film simulations, analogous to grains of sputter deposited material. The larger elements in the simulation could be modelled with coarser meshes to optimise computation time. A smaller region surrounding the interfacial portion of the substrate has a finer mesh to better capture the thermal properties as seen in Fig. 4.18.

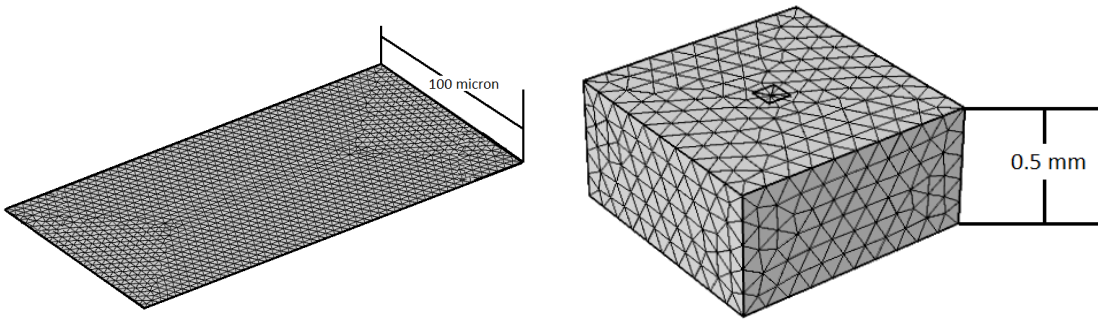

a) 100 x 200 x 0.04 μm b) 1 x 1 x 0.5 mm

Figure 4.18: Mesh generated for a) portion of an FeRh thin film, and b) MgO substrate to simulate the thermal properties. Dimensions are provided.

Physical Transformations through the FeRh MPT

To model the material accurately, it is important to consider the electronic, lattice, and magnetic properties of the films in the simulation. These are included as parameters in the COMSOL model and are necessary due to the coupled nature of the FeRh MPT, with changes in the electronic, phononic, and spin systems [21]. The values of the parameters were obtained from experimental reports in the literature [15, 93, 94, 182]. In order to model the transition, the properties of the material vary with temperature. As discussed in Chapter 3, this is defined using T_T and ΔT to describe the distribution of microscopic transitions [136]. This is expressed in the heat capacity [93, 183], the resistivity [15], and density [31] of the material which vary with a Gaussian form. An error function was required to model the behaviour of the density, resulting from the lattice expansion of the material seen in Fig. 4.19. The heat capacity and thermal conductivity are seen in Fig. 4.20.

The other parameter that had to be included for accurate simulations of the heat dissipation was the heat conductivity, k_{IF}, between the FeRh film and the MgO substrate. This is sample dependent and is discussed further in Chapter 7.

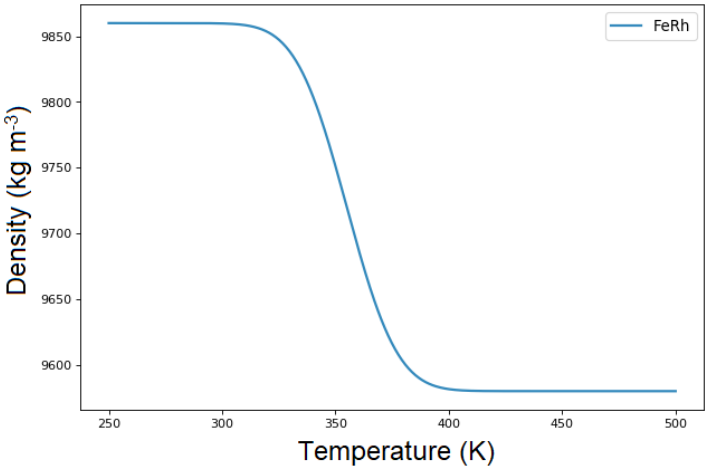

Figure 4.19: Evolution of the density of the FeRh film as it undergoes a lattice expansion of $\approx 1\%$ [31]. This figure describes a sample where the MPT occurs with T_T of 355 K and ΔT of 25 K.

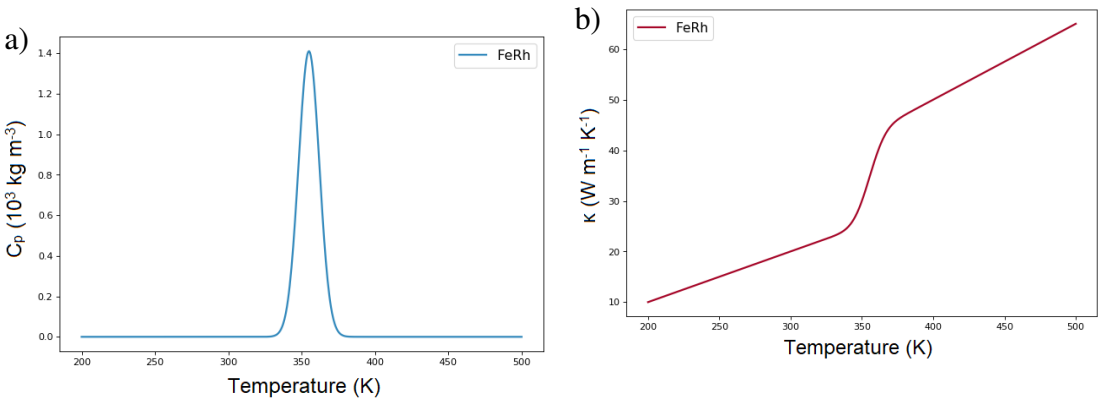

Figure 4.20: a) Additional heat capacity due to the latent heat of transition of the film [183] used in the COMSOL model. This is included as a Gaussian peak about the transition point [93]. b) The thermal conductivity of the two phases from *ab initio* literature [109] where the behaviour in the mixed phase is assumed to be a numerical average of the AF and FM values [136].

4.6 Static x-ray Measurements

Since first discovered by Röntgen [184], x-rays have offered a probe into internal structures not accessible by visible light. Coherent x-ray beams can be generated in house using a laboratory based instrument, or at large scale facilitates such as synchrotrons. The relative efficiency of the x-ray scattering determines the brilliance required. For reflectivity and Bragg peaks, the Rigaku SMARTLAB diffractometer at the Henry Royce Institute suffices. To examine weaker events such as non-resonant magnetic scattering, high photon fluxes are required. A guide to modern x-rays sources can be found in Table 4.2 & Fig. 4.27 [32, 143, 185, 186, 187].

Table 4.2: Comparison of x-ray sources in terms of brilliance and x-ray energy.

Source	Brilliance (ph/s)	Spectral Range (keV)	ΔE/E (%)
Laboratory	10^9	8.048 (Cu K-α)	0.01
Synchrotron	10^{23}	6-250 (ESRF)	0.1
x-FEL	10^{31}	2.2 - 36 (SPring-8)	0.01

4.6.1 X-ray Diffraction

In Chapter 2, the interaction of x-rays with matter was introduced. This is mainly used to determine the crystal structure using the Bragg peak reflections. Such measurements were carried out with the Rigaku SMARTLAB system of the Henry Royce Institute [188]. A schematic of the instrument is provided in Fig. 4.21a. X-rays are generated using a Cu K-α source to produce a highly collimated beam with a wavelength of 1.541 Å. The resolution is improved by monochromators and Soller slits which act to limit the spectral and spatial width of the beam, respectively. Monochromators limit reflection to a single wavelength of light, providing beams with narrow bandwidths. Soller slits improve beam convergence, producing parallel x-ray beams. It is possible to examine these peaks under vacuum and at a range of temperatures from 50-1100 K using an Anton-Parr DHS-1100 heated stage, see Fig. 4.21b. The dome consists of either graphite or Poly-Ether Ether Ketone (PEEK) to maintain a stable experimental environment. Detection of the x-rays is achieved using a 1D strip detector [188].

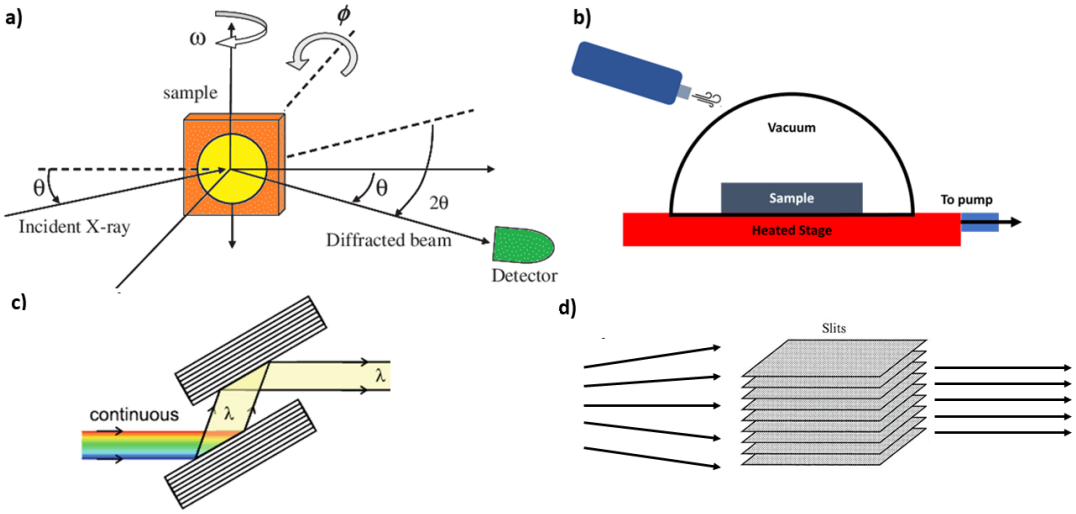

Figure 4.21: a) Schematic of the Rigaku diffractometer geometry showing the angles about which the sample and the detector could be rotated. Adapted from Wang et. al. [189]. b) Heated stage that can be inserted in the diffractometer consisting of graphite or PEEK dome cooled by an air jet which allows for sample heating sample *in vacuo*. c) 2-bounce monochromator, adapted from Cramer [190]. d) Soller slits which are used to improve beam collimation.

Factors Affecting Bragg Peak Intensity

As well as determining the lattice spacing, Bragg peaks provide further information about the crystal structure. This can be used to interpret how ordered the films are, assuming any variations in scattering intensity are due to crystal disorder. The predicted peak intensities from the crystal structure have been discussed in Chapter 2. If the relative peak intensities are exactly the ratios estimated from Eq. (2.13), then the crystal is perfectly ordered, corresponding exactly to CsCl structure. The intensity of a given peak is governed by the relative scattering strengths from the atomic centre of the species involved. This is characterised by the well known $\mathbf{Z}^4$ dependence [191]. Knowing the expected efficiency and relative intensities of each peak is important for examining structural perturbations and measuring the degree of ordering in the examined sample. The order parameter of FeRh is found by using the integrated intensities of the FeRh (001) and (002) peaks in Eq. (4.21) [20]. 1.07 is found from theoretical intensities of the (001) and (002) peaks in a perfect B2-ordered structure [191];

$$S = \sqrt{\frac{I_{001}}{I_{002}}} \cdot \frac{1}{1.07}. \tag{4.21}$$

The order parameter, S, varies between 0 (disorder) and 1 (perfect B2 order). This theory can be fully captured in diffraction and crystallographic software which allows for the predication of x-ray spectra. A predicted spectra for FeRh in both the AF and FM phase (different lattice constants) is seen in Fig. 4.22a, generated using the VESTA-3 software [192]. It can be seen that the intensities do not exactly follow the rules outlined in Section 2.2. The (001) and (002) peaks have different intensities due to the Lorentz-polarisation factor and relative scattering strengths from the Fe and Rh varying as a function of incidence angle [193]. However, the VESTA generated XRD spectra assume very sharp peaks with no instrumental broadening and zero background.

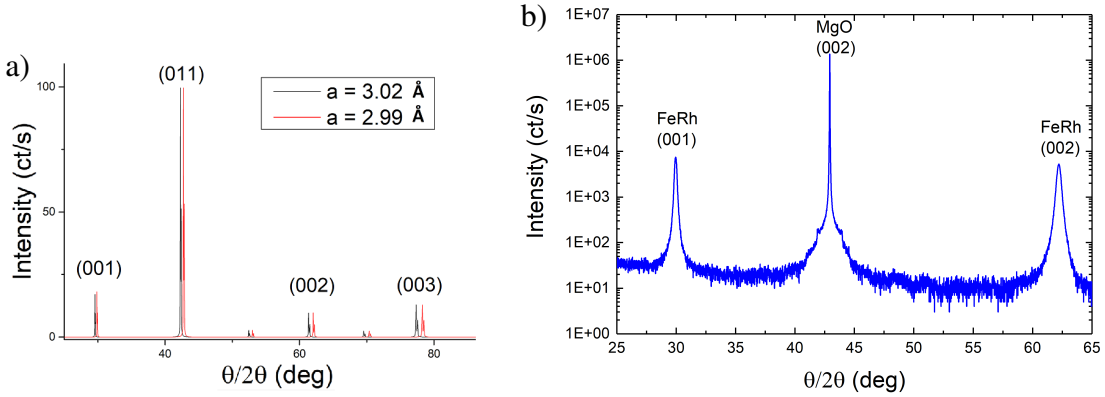

Figure 4.22: a) Predicted $Fe_{50}Rh_{50}$ XRD based on the CsCl structure with lattice parameters of the AF and FM phases. b) Typical XRD spectrum of FeRh showing the (001) and (002) peaks of the CsCl lattice. The FeRh (011) peak is obscured by the strong substrate peak - MgO (200).

The intensity further depends on the sample temperature. Thermal vibrations about the atomic centre can be captured by defining each pair of nearest neighbours as individual Einstein oscillators [194]. Increasing temperature increases the mean oscillator displacement reducing the efficiency of constructive interference that gives rise to the measured XRD peaks. Assuming the vibrations can be approximated by harmonic well, the motion is described by the Debye-Waller interpretation [195, 196]. This approximation is valid above the Debye temperature, a material dependent property [197]. According to this theory, the ratio of coherent to total scattering is defined as the Debye-Waller Factor (DWF). The intensity of a given peak is expected to change with temperature as,

$$I(T) \propto F^2 \left(e^{-\left\langle \vec{q} \cdot \vec{u}_n^2 \right\rangle} \right), \tag{4.22}$$

where u is the mean atomic displacement, F is the form factor from Section 2.2.2, and

$\vec{q}$ is the scattering vector of the peak investigated.

Factors Affecting Bragg Peak Width

Peak broadening (as distinct from peak overlap, see Fig. 4.23a) will occur when there exists any distribution of the variables from Eq. (2.8). There are many factors that must be considered, whether that be the energy broadening of the x-ray source, a distribution in the angles of the collimated beam, spread of lattice constants, or grains causing multiple scatterings [198].

The assumption of a perfect crystal is fundamentally flawed. Even in ideal growth conditions, thermodynamics forbids the production of perfect crystals when grown above 0 K [39]. Further sources of imperfection are atomic rearrangement following sputtering and annealing, and strain gradients at interfaces due to the imperfect lattice matching [131]. In the case of strain gradients, the distribution of lattice constants due to the strained layers will cause a distribution of diffraction peaks. This would be expected to produce asymmetric peaks; where the strain is gradually relieved through the film thickness (see Fig. 4.23b) [38].

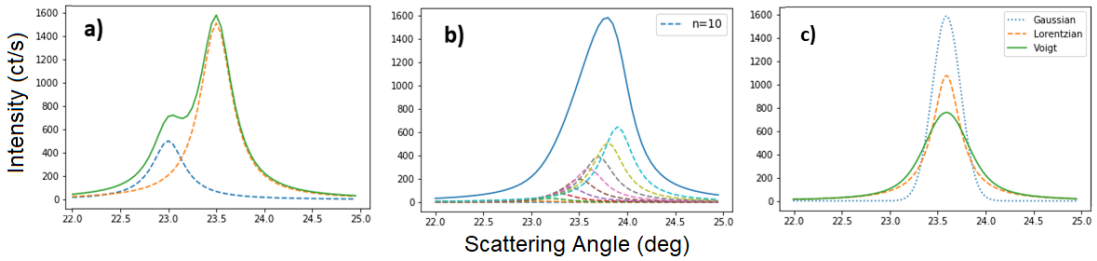

Figure 4.23: a) Overlapping Bragg peaks. b) Tailed peak as a result of a strain profile that is relieved through the film thickness. c) Comparison of Gaussian, Lorentzian, and Voigt functions.

However, the most prevalent peak broadening is as a consequence of the grain structure of deposited films. The derivation of Bragg peaks assumes that scattering occurs from an infinite array of lattice planes but more rigorous analysis demands the coherence length be considered. Diffuse scattering will be proportional to the density of point defects, substrate defects, etc. Entropic considerations impose there be a certain number of Schottky defects per unit volume [40], about which grains will form [148]. If the average crystallite is composed of N lattice planes then the structure factor

as a function of the scattering vector, $\vec{q}$, is [47],

$$s(q) = \frac{1}{N}\frac{\sin^2(Nqa_0/2)}{\sin^2(qa_0/2)}, \tag{4.23}$$

where a_0 is the lattice constant. The formula is simplified from the small angle approximation ($\sin\theta = \theta$) and solving the resultant linear equation gives the well-known Scherrer formula [47];

$$\tau = \frac{K\lambda}{\beta\cos(\theta)}, \tag{4.24}$$

where $\tau = Na_0$ is the mean crystallite size, and β is the measured peak Full-Width Half Maximum (FWHM). K is a parameter that describes crystal structure and crystallite isotropy. The DWF discussed above also introduces a broadening that is Lorentzian in nature. This is why $\bar{\tau}$ is instead used, defined as the minimum mean size. β is found from a given Bragg peak will always underestimate the crystallite size due to other forms of broadening. The scattering angle θ is considered in the analysis as higher scattering angles will have broader widths. This is due to the reduced lattice spacing associated with higher order peaks [45]. Small displacements about the central point increase diffuse scattering for shorter lattice plane separations.

Accounting for Instrumental Error

Instrumentation will introduce a systematic broadening in the Bragg peaks. Systematic error arises from measurement procedure and can result from the precision of the instrument used or errors in alignment. Some of the most common types of systematic uncertainty are the resolution of the beam and background noise. Given the x-rays generated are highly collimated with a known wavelength of 1.541 Å, the greatest source of resolution error is the diffractometer optics. This is most heavily affected by the choice of slits. The Soller slits can reduce the beam divergence following scattering to within 1°. The spectral narrowing of a 2-bounce monochromators results in an angular spread of 0.01° [188], at a cost of lower beam intensity. This can decrease the signal to noise ratio as the sources of background are unchanged but the peak intensity will be diminished. To account for different types of broadenings, Voigt functions are fit to the Bragg peaks, a combination of Gaussian and Lorentzian peaks (see Fig. 4.23c).

The background noise comes from a variety of sources but is dominated by the mounting plate. As the x-rays will also interact and scatter from this material, it is

important to estimate the expected spectrum. The most common method to reduce the noise is through the use of a 'no-noise' plate. This mounts to a high quality Si slab cut along the (510) lattice plane, which is beyond the diffraction limit of Cu K-α photons. This eliminates sample mount background from 20-120°. In the case of heated XRD, the dome used to cover the sample can be a source of background, in which case it is necessary to have a spectrum of the dome material, either graphite or PEEK obtained prior to any measurements. Errors also arise due to the alignment procedure such as the sample not being perfectly flat. A bowed sample for instance, would result in broader peaks as the incident normal is not consistent across the sample. This is why the optical and sample alignment are critical in reducing systematic error. In the case of the Rigaku SMARTLAB diffractometer used in this project, the system has a pre-installed alignment procedure. Any systematic errors that do persist will therefore be carried through in any measurement and can be subtracted if known.

Mosaicity and In-plane Ordering

The above analysis refers to the $\theta/2\theta$ scans which probe the $\vec{k}_z$ vector. These scans do not measure in-plane order. Methods to quantify the mosaicity and plane dislocations rely on fixing the diffractometer θ and 2θ axes (see Fig. 4.21) at a given scattering angle and scanning about a chosen sample axis. In this project reference is made to two such scans.

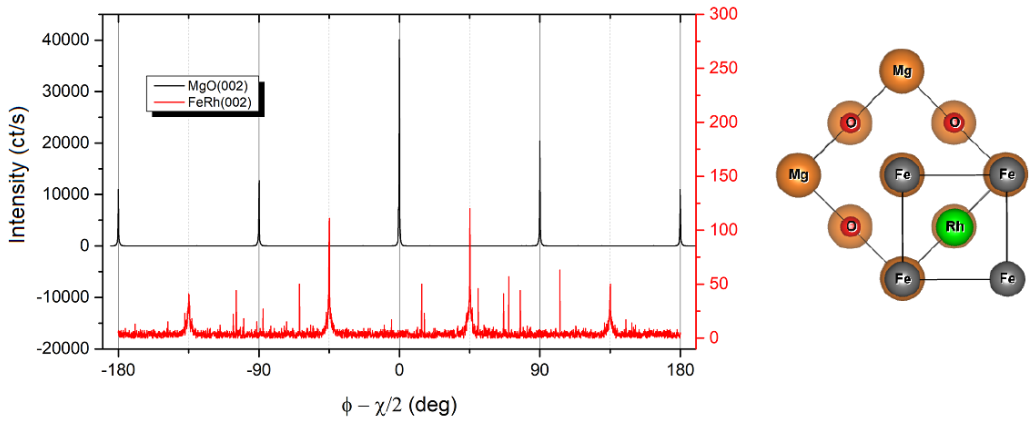

Figure 4.24: An in-plane XRD carried out on a 10 nm sample of FeRh deposited on MgO. Angles quoted refer to those illustrated in Fig. 4.21. The MgO (200) peak was used to map the in-plane order of the substrate. The (200) peak of FeRh was chosen to determine the in-plane order of the deposited film. The second panel shows the expected relative orientations of the crystal structures.

i) **Rocking Curves** tilt the sample about angle, ω, (see Fi.g 4.21a) about a given Bragg peak to determine the parallelism of lattice planes. The width of the intensity about ω is used as a measure of in-plane variation of crystallite alignment.

ii) **In-plane XRD** uses a grazing incidence geometry. The sample is rotated about its surface normal, ϕ, while the diffractometer is fixed at a chosen Bragg peak. If in-plane order exists, such as in Fig. 4.24, this is an indication that epitaxial growth has occurred along a lattice vector of the substrate.

4.6.2 X-ray Reflectivity

X-Ray Reflectivity (XRR) is used as a probe of the thickness, roughness, and densities of thin films [199]. This relies on the constructive interference of reflected and refracted light from thin film samples (1-100 nm). Fig. 4.25 illustrates how the measured beam is composed of the combination of these scattered sources. The classical interpretation of reflectivity is based on the complex refractive index, $\tilde{n}$ [122];

$$\tilde{n} = n_1 + in_2 = 1 - \delta + i\beta. \tag{4.25}$$

Dispersion and absorption are defined for a given wavelength, λ, as [122],

$$\delta = \frac{r_0\lambda^2}{2\pi}\left(Z + f'\right)\cdot n_{atom}, \quad \beta = \frac{r_0\lambda^2}{2\pi}(f'')\cdot n_{atom}, \tag{4.26}$$

where f' and f'' are correction factors referred to as anomalous scattering, r_0 is the Bohr radius, and $Z \cdot n_{atom} = \rho$ is the electron number density per unit volume of the material [122]. The Fresnel equations can be used to predict the relative efficiencies of reflection, r, and refraction, $1 - r$, at an interface for s and p polarised light (see Section 4.4.1);

$$r_s = \frac{n_1\cos\theta_i - n_2\cos\theta_t}{n_1\cos\theta_i + n_2\cos\theta_t}, \qquad r_p = \frac{n_2\cos\theta_i - n_1\cos\theta_t}{n_2\cos\theta_i + n_1\cos\theta_t}, \tag{4.27}$$

where θ_i is the angle of incidence, and θ_t is the angle of refraction at an interface. From this formalism, it can be seen that there is some angle below which no absorption occurs resulting in Total External Reflection (TER). This is referred to as the critical angle [122],

$$\theta_C = \sqrt{\frac{r_0\lambda^2\rho}{\pi}}. \tag{4.28}$$

Ideally this appears as a sharp edge in the XRR spectrum. In reality this is not the case. This is due to a number of factors, the most important being surface roughness and beam profiles of finite sharpness. The Gaussian profile of x-ray beam results in a spread of incidence angles on the sample surface, magnified in the grazing incidence geometry of reflectivity experiments. As this spread is consistent across reflectivity experiments with the same instrumentation, it can be modelled in reflectivity analysis software [200]. This allows for the surface roughness to be extracted, as the specular reflection from the surface will also affect the shape and intensity observed at the critical angle.

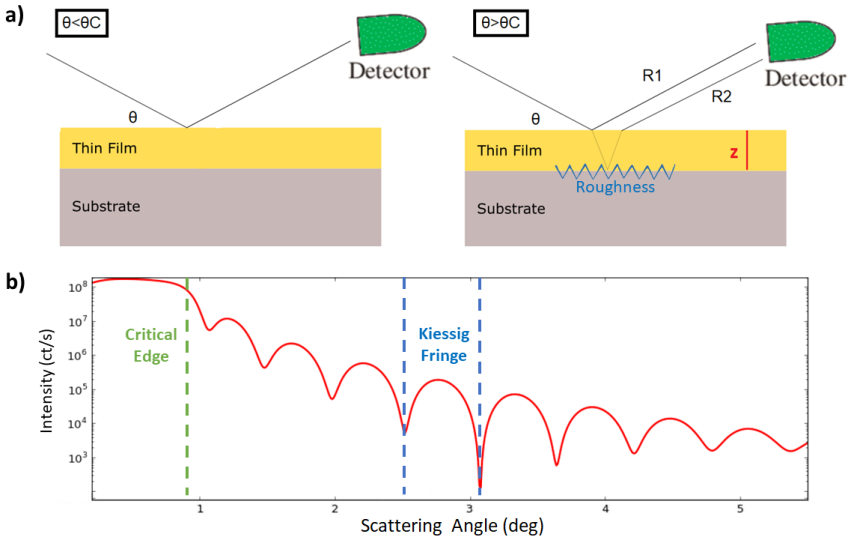

Figure 4.25: a) Reflectivity from a thin film showing instances below and greater than the critical angle, θ_C. b) Spectrum from a 15 nm film with 0.5 nm roughness demonstrating θ_C and the Kiessig fringes. Roughness is expected at each interface.

The reflectivity spectrum is not limited to this critical edge, as would be the case for an infinite single-layer material. There exist further interactions between layers, which appear as Kiessig fringes described as the interference between the wavefronts from the reflected, R1, and refracted, R2, beams shown in Fig. 4.25 [201];

$$\theta_m^2 - \theta_C^2 = m^2 \frac{\lambda^2}{4d^2}, \tag{4.29}$$

where m is the order of the fringe, and d is the increased path length (refracted through the layer). From the width of fringe, $\Delta\theta$, the thickness of the layer, z, is [201],

$$z = \frac{\lambda}{2\Delta\theta}. \tag{4.30}$$

This is the case for a single layer. For multilayers and more complicated structures, it is necessary to consider how the densities of each layer and interference between each refracted beam can effect the spectrum. This analysis is well suited to being calculated by computational methods [200]. The multilayer structure can be modelled as a series of layers and the spectrum plotted from the initial parameter guesses, which is then compared to the actual spectrum [202].

The roughness of each layer needs consideration, as each interface is a potential source of specular and diffuse reflection. The intensity of the fringes will decay rapidly in the case of high roughness. This can be explained by considering the roughness as an uncertainty in the thickness of the layers. The islands and gaps of the layer mean that the density of the layer is distributed through the boundary instead of being a sharp interface between two densities. As the fringes depend on the constructive and destructive interference an uncertainty in thickness, and by extension the path difference, will result in some distribution about the angle, θ_m. At higher order angles, the x-rays will pass through the refraction medium a greater number of times and this uncertainty in path length will compound. If the path length difference for the first fringe could be expressed as $d = d' \pm \Lambda$, where Λ is the roughness, then later fringes are expected to vary as, $d_m = d'_m \pm (m^{1/2} \cdot \Lambda)$. This results in reduced fringe contrast as θ is swept due to the increasing uncertainty.

GenX - Reflectivity Fitting Software

GenX is a simulation software designed to assist in building layer models from reference reflectively data [200]. Based on the principles described by Schlomka et. al. where the reflectivity profiles of many layers can be summed together [202], the software must first estimate the thickness resolution in order to compute the number of layers it will consider [203]. The resolution will be based on the diffractometer and the optics used. It is important to have consistent optics to minimise the uncertainty in these parameters. This can be beneficial, especially when modelling upwards of 15-20 parameters as is the case with multilayered structures. The optics resolution is therefore assumed to be fixed between experiments. Due to the fact that fringes are broader with thinner films, the resolution is also dependent on the thickness of layers. Thinner layers will require very high resolutions. Parameters carried to the next iteration are calculated using a genetic algorithm [204], to prevent it falling into local minima.

One can estimate densities from the crystal structure and input the initial conditions

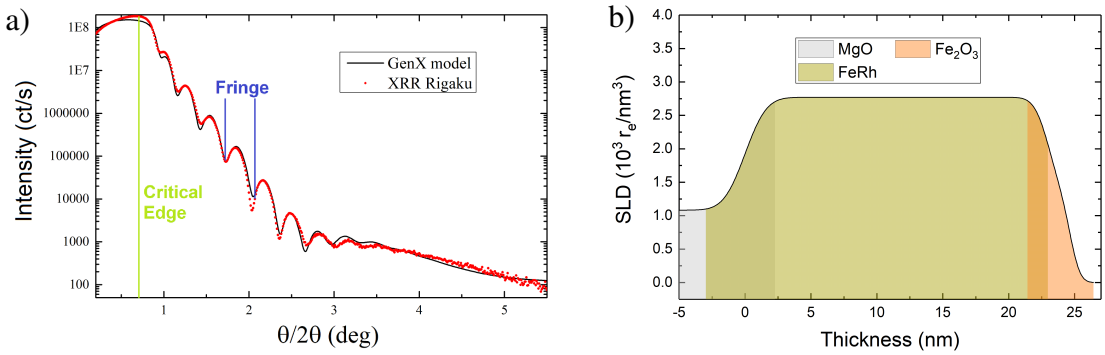

Figure 4.26: a) XRR carried out on a sample of 25 nm FeRh. The key features are critical edge, fringe width and height. Fitting with GenX (with reasonable assumptions) allows for the estimation of layer thicknesses, densities and roughnesses. b) The software generated SLD from the fitted model is shown with overlapping shaded regions depicting interfacial mixing.

and bounds based on the predicted thicknesses. With regard to substrate and inter-layer roughnesses, the interfaces are assumed to have Gaussian shaped boundaries [205] to describe the interdiffusion process between the layers. This is not a truly physical picture, but is instead chosen as the reflectometry scans average over many grains. Factors in the roughness, be they island growth or lattice dislocations, will be homogeneous with regards to the thickness. This can be seen in the example Scattering Length Density (SLD) profile, Fig. 4.26. The Gaussian profile of the roughness generates an error function between the two regions that describes how the density changes. For example if the two layers had densities, ρ_1 and ρ_2, with an interfacial roughness, Λ, then the profile with regards to the thickness, x, would be realised as,

$$\rho(x) = \rho_1 + [\rho_1 - \rho_2] \cdot \left[\mathrm{erf}\left(\frac{x - x_1}{\Lambda\sqrt{2}} \right) \right], \tag{4.31}$$

where x_1 is the position of the interface. The above procedure is implemented for both surface-air and material interfaces. In these cases, the density changes smoothly from one value to the other and an error function is a suitable description of the system. However, if there is strain at the interface between layers, it may not be accurate. There are also cases where the rough interface of one layer promotes island-like growth of subsequent layers, resulting in an interface where the density drops rapidly before returning to the value of the next layer. In this case, the GenX model will not be able to find a suitable minimisation of the parameters. Therefore, an understanding of the physics and possible growth mechanisms is beneficial in interpreting the values

obtained from the analysis. Generally, deviations from the non-ideal case are first approximated by introducing another layer of the same material [132]. This could take the form of a layer with increased density due to some strained layers. Cases of very rough interfaces could be modelled as a layer of very low density material. It is important to use the same material to account for the scattering factors of the atoms. The absorption relies upon both the number density and the constituent atoms in the crystal due to the $\mathbf{Z}^4$ dependence of x-ray scattering.

Treatment of Uncertainty in Numerical Models

For simulations that are numerical in nature, there will inherently be uncertainty arising from the modelled system being an approximation of the real system. Further uncertainty arises from the fitting procedure. As a model explores parameter space, it must take finite steps in the direction of some parameter. The curvature about the minimum must then be calculated to find a reasonable step size to determine the minimum point [206]. The curvature, k, about one parameter, m, with respect to m is,

$$k = \frac{m''}{(1+m'^2)^2}, \tag{4.32}$$

where m' refers to the derivative with respect to the parameter space. These first and second derivatives are also approximations that depend on the step size used in the fitting algorithm. Finally, a covariance matrix is built to determine how the curvature changes with small perturbations of each parameter [207]. An example of a covariance matrix for 3 parameters is shown;

$$C = \begin{pmatrix} \delta_{11} & \delta_{12} & \delta_{13} \\ \delta_{21} & \delta_{22} & \delta_{23} \\ \delta_{31} & \delta_{32} & \delta_{33} \end{pmatrix}, \tag{4.33}$$

where co-dependence, δ_{ij}, describes how parameter i varies as j is changed in small increments. For a simple case where the non-diagonal terms are zero, which is assumed in the Gaussian treatment of error propagation for independent variables [208], the error in each parameter is then the diagonal term squared, $\sigma_1 = \delta_{11}^2$. Where such a matrix cannot be defined analytically, the variable value, i, is changed until the chosen Figure Of Merit (FOM) changes by 5% to estimate the uncertainty. This algorithm

will only allow for the diagonal terms of the covariance matrix to be estimated. This is a concern, as for certain parameters such as the thicknesses of two layers, the values will be dependent on each other. If these values are to be quoted as the errors in the fit, the co-dependence of the parameters should be referred to. A standard FOM used in goodness-of-fit testing is the reduced-χ^2, defined as χ^2 per degree of freedom, ν [208];

$$\chi^2_\nu = \frac{1}{\nu}\sum_i \frac{(O_i - C_i)^2}{\sigma_i^2}, \tag{4.34}$$

where O_i is the observed value, C_i is the predicted value, σ_i is the variance, across the complete dataset. A value $\gg 1$ indicates the model is not describing the data.

If χ^2_ν is used as FOM in a GenX fit, the fitting is heavily weighted toward higher counts as a consequence of Poisson counting statistics ($\sigma \propto 1/\text{counts}$). A provision is available termed the log error, which further weighs the points by the log of count rate. This is important in fitting the fringes, as they are often still discernible even when the count rate has dropped to < 10 ct/s, in the case of very smooth interfaces. The log method includes more fringes, allowing a broader scope of parameter space to be explored. The number of simulated layers should also be considered when interpreting the FOM. Adding another layer often introduces three new parameters; the thickness, density, and roughness of the given layer. This provides more scope in the parameter space to find a minimum but increases the risk of over-parametrisation. As a rule of thumb, new layers can be added until there is no significant improvement in the software calculated FOM [132].

The simplest model that possesses a FOM close to the optimum (e.g. $\chi^2_\nu = 1$) is then assumed to represent the best estimate of the data unless there is supporting data for a more complicated model. It is important to realise that a model with better χ^2_ν does not necessarily mean a better fit. The uncertainty in the calculated χ^2_ν can be as large as 10-20% for non-linear models [209] and it is unlikely that one would be able to find much better models once the χ^2_ν has dropped below 1.3 for a fit. It is worth remembering that 'a' fit of the data does not mean 'the' fit of the data [208].

4.7 Synchrotron Based Techniques

In order to determine magnetic and structural properties with greater precision, brilliant and stable sources of photons with tunable energies are required. Synchrotrons are one such source. These facilities first emerged from cyclotron particle accelerators where the emitted light was a by-product of the high-energy physics experiments [210]. This eventually progressed into stand-alone facilities where the emission of tunable light depending on the particle acceleration was the main focus [211]. The development of high-brilliance x-ray sources has steadily progressed through the decades and research is currently carried out on 3rd and 4th generation synchrotrons, with the development of new injection facilities, beam focusing, and undulating magnets [212].

4.7.1 Operating Procedure of 3rd Generation Synchrotron

In the following sections, the important components of large-scale synchrotrons will be discussed. Fig. 4.27 shows the general layout of a 3rd generation facility and the current energy ranges and brilliances of publicly accessible synchrotrons worldwide. As part of this project, beamtimes were carried out at Diamond Light Source, SLS and SACLA (see Fig. 4.27b).

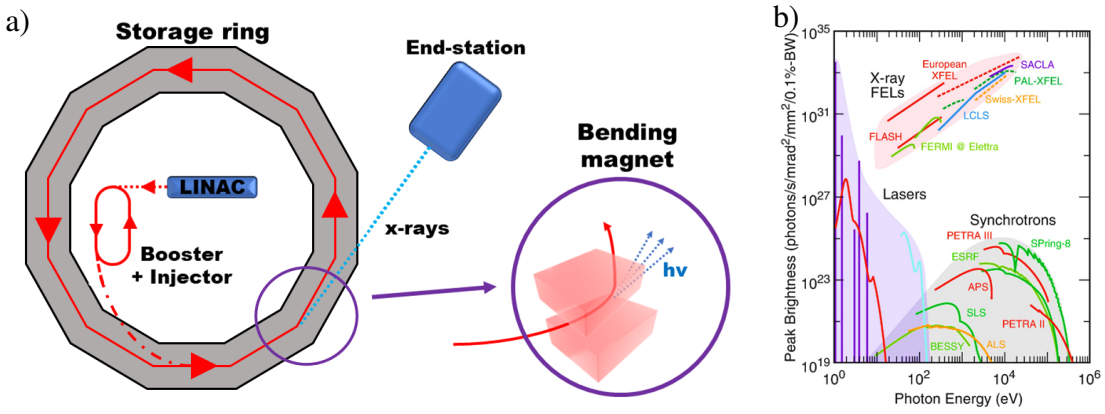

Figure 4.27: a) Simplified sketch of a large-scale synchrotron showing particle injection and acceleration, as well as radiation emission from the bending magnets. b) Comparison of peak brightness as a function of photon energy between conventional lasers and higher harmonic generation sources, synchrotron sources, and X-ray free electron lasers, taken from Boutet and Yabashi [143].

Beam Injection

In order to separate the particle emitter from the closed ring of the synchrotron a beam injector is required, commonly implemented as a LINear ACcelerator (LINAC). Thermionic emission from a metallic source produces the electron bunches. Earthed anodes provide the initial acceleration, before using RF cavities in the LINAC to approach near relativistic speeds (100 MeV in the case of Diamond Light Source) [213]. Next a booster ring as seen in Fig. 4.27a is used to accelerate the electron bunch to GeV energies [214]. The voltage and number of particle bunches introduced into the synchrotron are optimised to maximise the charge with respect to the initial accelerating voltage [215].

Beam Focusing and Storage Ring

The particle bunches are contained in the storage ring. In order to maximise the light produced for the beamline end-stations, photons are emitted at fixed locations. Between these points the particles follow an arced path, while at the required points bending magnets and undulators adjust the angular momentum to produce the required light. This results in the rounded polygon shape that has proliferated in 3rd generation facilities [216]. To prevent losses after beam deflection from bending, it is required to refocus the electrons within in narrow region through the use of magnetic lenses. The use of alternating gradient focusing was found to enable strong focusing where strength increases with greater alternating component of the gradient [217]. Strong focusing prevents losses in the bunch energy and number.

Tuning Photon Emission with Undulator Magnets

The emission of photons occurs when the charged particles are accelerated with the application of magnetic field. In the simplest case of a bending magnet (see encircled area in Fig. 4.27a) with field strength, B, and path length, γ, Bremsstrahlung with angular frequency, ω_c, occurs as [217],

$$\hbar\omega_c = \frac{3e\hbar B\,\gamma^2}{2m_e}. \tag{4.35}$$

More complex bending procedures exist which increase total shift in particle momentum over a given path length. The current standard is a series of dipolar magnets that can undulate or 'wiggle' the particle bunch. This was shown to produce very intense

photons with a narrow bandwidth about ω_c [218];

$$\hbar\omega_c \propto \left[\lambda_u\left(1+\frac{K^2}{2}+\gamma^2\theta^2\right)\right]^{-1}, \quad \text{where } K=\frac{eB_0\lambda_u}{2\pi m_e c}. \tag{4.36}$$

The spacing between the magnets, λ_u, and the field strength, B_0, allow for the fine tuning of the x-ray energies, depending on angle between the wave normal and the undulator axis, θ. Due to the near-relativistic speed of electrons in a synchrotron, the point source assumption of a tangent point for wigglers and bending magnets does not hold. A phase correction factor may be found in nuclear physics literature [219], outside the scope of this project.

Beamline End-stations

Monochromators at end stations are used to further refine x-ray energies, providing both resonant and non-resonant signals. Resonant x-ray energies examine electron bands, where electronic or hyperfine structures of atoms can be extracted. The availability of highly polarised x-rays allow for high resolution coherent scattering. Beamline end-stations provide for advanced characterisation techniques. Multi-axis diffractometers manipulate both sample and detector geometries to achieve experimental set-ups not available in standard lab-based equipment [220]. This allows for a wide range of geometries including in-plane, grazing incidence, and horizontal scattering set-ups that require high brilliances for meaningful count rates. The available detectors (such as the Pilatus series [221]) advance experimental capabilities, with pixel selection and selective bandwidth functions to optimise observed signals.

4.7.2 Non-resonant Magnetic Diffraction

As discussed in Section 2.2, coherently scattered x-rays from a sample will possess contributions from both the charge and magnetic cross-section. If these are co-incident in k-space, as is the case in FM materials, the signal at each Bragg peak is dominated by the charge contribution, given that the relative intensity is a factor 10^6 greater than that of the magnetic scattering [49, 222]. Polarisation analysis can show the magnitude of the magnetic scattering due to the transfer of angular momentum but the signal to noise ratio is so low as to make such a task experimentally challenging. When the magnetic ordering occurs as a superstructure of the crystal lattice, magnetic Bragg peaks are found to occur at forbidden points of reciprocal space for the charge peaks.

For G-type AF materials (see Fig. 4.28) these occur within the $(\frac{1}{2}\ \frac{1}{2}\ \frac{1}{2})$ family of planes. In this instance the AF sub-lattice maps to the crystal lattice with atoms aligned anti-parallel. When the atomic spins that align parallel to each other are considered, the lattice constant is twice that of the original which in effect allows for the observation of magnetic order between lattice planes having half integer values of (hkl). Based on the high brilliance of synchrotron sources, this weak phenomena (in comparison to charge-based x-ray diffraction) can be observed provided the background noise is reduced to a sufficient level and the sub-lattice ordering has high coherence length. In order to maximise the signal, it may be necessary to work with thicker films (up to 500 nm) or single crystals.

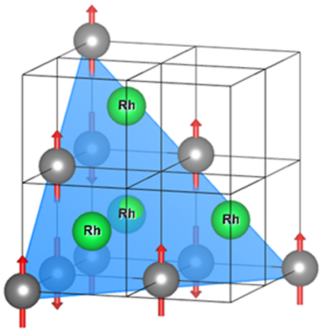

Figure 4.28: G-type AF order of FeRh illustrating the lattice plane along which the spins align parallel.

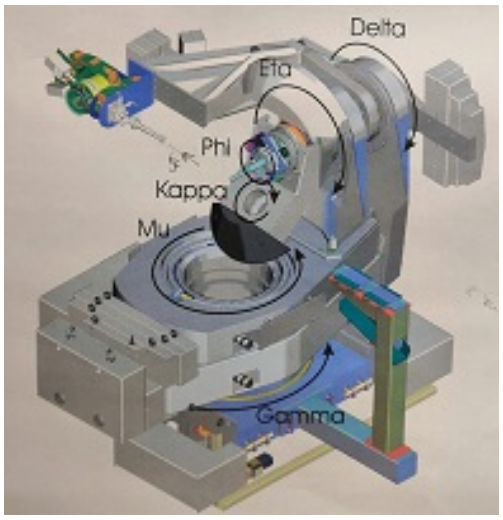

Figure 4.29: Diamond I16 - 6-axis kappa diffractometer. Sample stage housed on Phi axis. Detector swept using Delta motor.

Next, specific instrumentation at the Diamond Light Source is briefly discussed as the results reported in Chapter 5 were obtained from beamline I16. This facility is optimised to combine high x-ray flux and high resolution in diffraction experiments, with a wide and continuously tunable energy range [223]. The instrumental set up can be seen in Fig. 4.29 consisting of a '4S+2D' diffractometer [224] (4 sample & 2 diffraction axes). The many degrees of freedom of this diffractometer allow for a wide range of scattering experiments. Specific to the work of this project, the facilities allow for rocking curves of the magnetic Bragg peaks to be measured with precise determination of the peak width and scattering intensity.

To ensure that the peaks being measured correspond to the assumed magnetic sublattice, it is necessary to perform polarisation analysis. This was discussed in Section 2.2 in order to distinguish between charge and magnetic Bragg peaks. In experimental laboratory settings, further sources of incoherent scattering should be considered. The main concern is the increased scattering from the air, as this could mask slight changes in polarisation the x-rays have experienced due to the magnetic structure. As it is not feasible to place the entire system *in vacuo*; a Be dome (see Fig. 4.30a) is instead used to prevent air scattering in the vicinity of the sample. Be is chosen as it does not interact strongly for the photon energy used to cause further scattering [225]. The use of a vacuum environment provides confidence in the assumption that any changes in polarisation are due to the angular momentum exchange from magnetic spins. The change in polarisation is determined using a graphite analyser crystal.

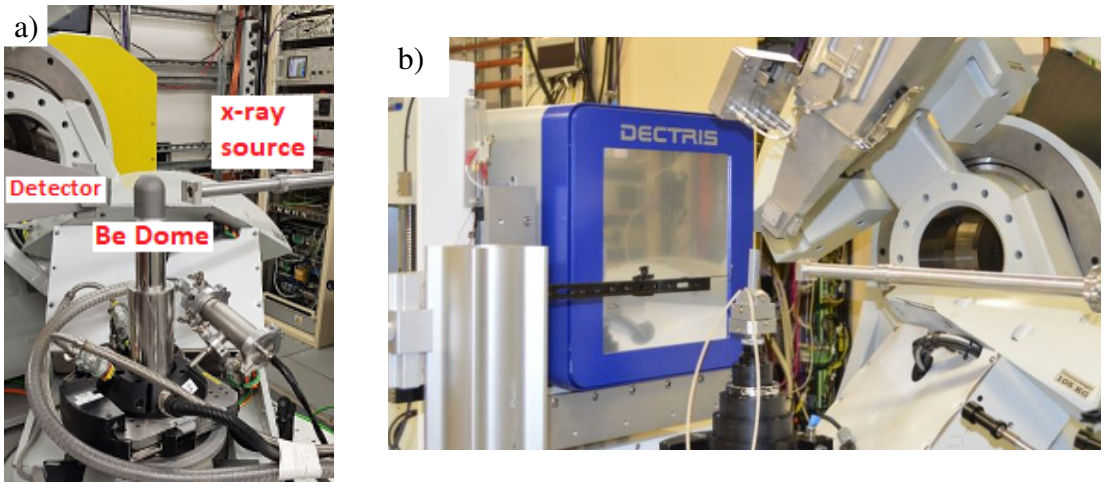

Figure 4.30: Instrumentation used in the beamtime at the I16 experimental hutch. a) Be dome which reduces incoherent scattering from air. The detector and x-ray source are shown. b) The 2D detector is shown (blue DECTRIS). Both images are taken from the Diamond Light source website [223].

The detector at the I16 beam-line is a Pilatus 2D detector (see Fig. 4.30b). The angular resolution of such set-ups far exceeds that available for laboratory detectors due to smaller pixels and increased arm lengths [226]. This allows for imaging of the peaks in a small window of reciprocal space when scanning the angular range with high sensitivity. Another advantage of using a 2D detector is the ability to define a region of interest (ROI) within the small window of reciprocal space. Provided the width of the rocking curves are known, the pixels of interest can be used to separate

the peak signal from the background. Furthermore, the statistics can be improved by recording the entire 2D image of the signal. Through the use of a background ROI for subtraction [227], it is possible to improve the certainty in peak signal within the measured ROI. Further refinements can be found by setting an energy threshold for the incoming photons, requiring an energy calibration of the pixels [228]. This reduces the effect of incoherent scatterings such as sample fluorescence.

The diffractometers and detectors of the MS beamline, SLS; and BL3, SACLA do not exactly match the specifications of I16 but are sufficiently similar to not warrant individual discussion. The MS beamline has a '3S+2D' axis diffractometer and uses a Dectris Pilatus 300K detector [221]. BL3 possesses a multi-axis diffractometer and receives x-rays using a DAPHNIS platform with a Multi-Port Charge-Coupled Device (MPCCD) [229, 230].

4.8 X-ray Free-electron Laser Techniques

x-ray Free Electron Laser (x-FEL) represents the fourth generation of synchrotron radiation with typically linear geometries. The essential components of an x-FEL are shown in Fig. 4.31. A number of these components are similar to those already described for the 3rd generation synchrotrons. The basis of laser generation relies on the production of a beat wave that synchronises with the electron pulse emitted from the LINAC. This is achieved by tuning the wiggler parameters and radiation frequencies. The electron energy transitions occur in a continuum meaning lasing is not contingent on discrete energy levels. The thermal energy generated is carried away at near-light speed as the electrons act as the lasing medium [231], allowing for high brilliance. This creates a laser that is continuously tunable, with high peak power, and can be adjusted to achieve a range of pulse shapes. A number of varieties exist; namely the Self-Amplified Spontaneous Emission (SASE), a Master Oscillator Power Amplifier (MOPA), or Harmonic Generation (HG) schemes [231]. The methods of choice for established x-FEL sources are SASE which amplifies shot noise on the electron beam in a single pass, and HG which uses a seed laser at a sub-harmonic of the desired output frequency [232, 233].

For example, the most recent facility to come online, the Swiss x-FEL operates on the SASE principle where regions of pulse that develop coherence are due to relative

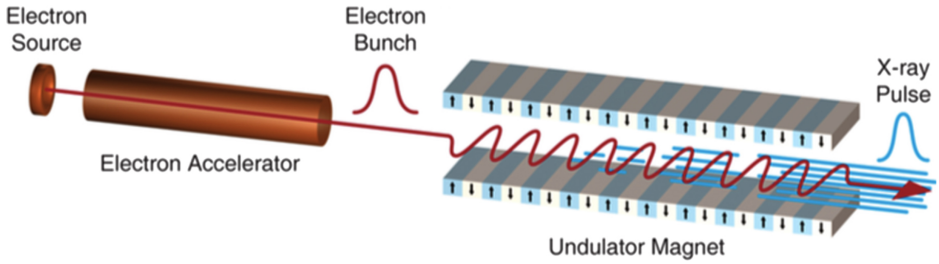

Figure 4.31: FEL schematic, showing an electron beam propagating through an undulator and the emitted radiation. Taken from Pellegrini [32].

slippage between electrons and emitted radiation over one gain length of the undulator (see Fig. 4.32). This slippage is as a consequence of the finite charge and duration of the electron pulse, yielding a range of wavelengths of radiation. A short period undulator is then used to lower the beam energy requirement for target wavelengths [233]. The coherence of SASE can be improved by seeding the x-FEL with a conventional source with high temporal coherence which is maintained throughout the amplification process [233]. It is achieved by spectrally altering the radiation at an early stage of amplification, a technique called 'self-seeding'. This is because the altered light is used as the seed laser in the second pass through an undulator providing a narrow spectral line with large spectral brightness [234]. Using such techniques, peak brightnesses of 10^{33} ph s^{-1} [143] can be achieved with high temporal coherence ($\approx$ 20 fs) [185].

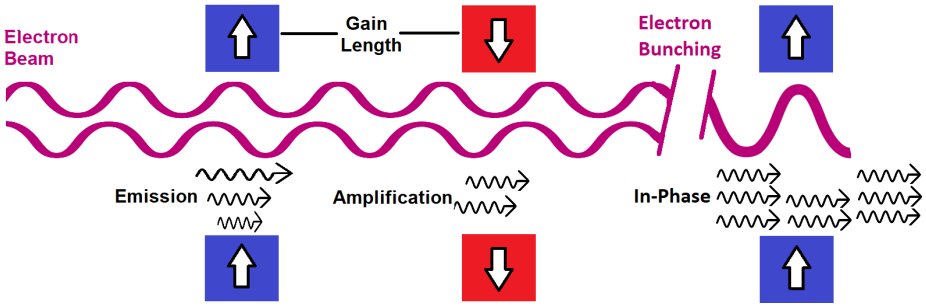

Figure 4.32: A simplified illustration of the SASE process. Acceleration by the magnet pair produces a photons with wide spectral range. The desired wavelength of emission is selectively enhanced by changing the gain length. By tuning the gain length and field strength, a coherent x-ray source with high brilliance is produced.

4.8.1 Improving Temporal Resolution using Jitter Correction

The time resolution of an x-FEL source is theoretically limited by the pulse length of the x-rays. However, in pump-probe experiments there is the further requirement that

the pump and probe events have to be temporally correlated. In the case of excitation by an external optical laser such as those used by the FLASH or SACLA, these are correlated by electronic triggers [235]. Small variations (0.3 mm over 750 m path length) in the electron bunch emission can vary the arrival time by ps amounts. In such cases, jitter correction is required to achieve the theoretical maximum resolution. For instance, this improved the temporal resolution of experiments carried out at the SACLA facility, presented in Chapter 6.

A detailed description of the equipment and procedure for jitter correction at the FLASH facilities is provided in a work by Savelyev et. al. [236]. The most important component is the Beam Arrival Monitor (BAM) which is placed before the undulator and records the shot-to-shot variation in the timings of the relativistic electron bunches. In the case of SACLA, example data to demonstrate the jitter correction is provided for the analysis of data acquired at the facilities [144]. The SASE bunching changes the arrival time of the x-ray pulses and means the TR experiments as monitored by the delay stage of the system do not achieve sub-ps resolution. Fig. 4.33a shows the examples of the Bi(111) peak excited by an 800 nm laser of BL3 of SPring-8 [229]. It is expected that oscillations with a period of 300 fs would be observed.

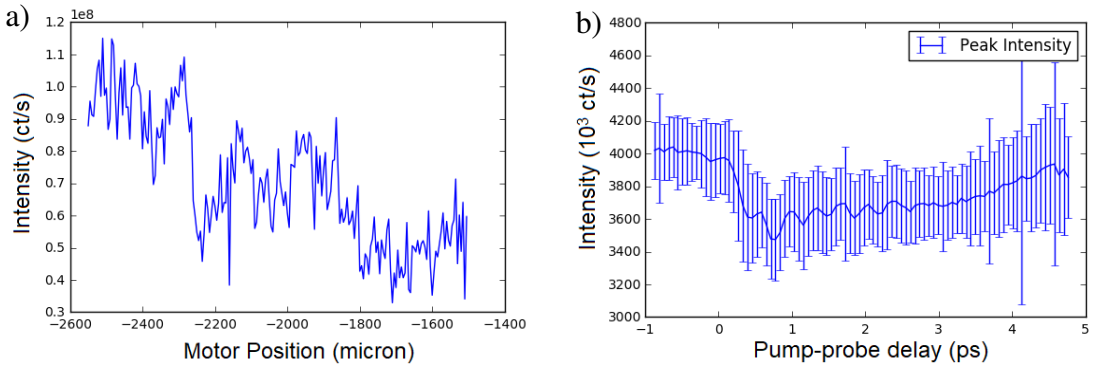

Figure 4.33: a) Intensity of the Bi(111) peak as a function of pump-probe delay following laser excitation. b) The jitter correction procedure shows the improvement in temporal resolution that can be achieved.

The poor temporal resolution means the only discernible dynamics are the drop in intensity of the peak following laser excitation. Further work is required to produce the data reproduced in Fig. 4.33b. The arrival-time jitter and drifts in the relative timing between the pump-probe laser and the x-FEL are corrected for using information recorded by the BAM. Note that the BAM does not measure directly the arrival-time

jitter between the pump-probe laser and the x-FEL pulses, which is the actual quantity of interest, but rather the arrival-time jitter of the electron bunch with respect to the master laser oscillator, which is closely related when the feedback and synchronization systems are functioning [236]. The analysis software TimingMonitor available at the SACLA HPC facility is used to correct the shift in delay [144]. The leading edge of BAM data is fit with an error function to estimate bunch width, σ_B, and actual time zero, t_0, similar to that performed in Section 4.4.2;

$$f(t) = \frac{a}{2}\left(\mathrm{erf}\left(\frac{t-t_0}{\sqrt{2}\sigma_B}\right)+1\right)+bt+c, \quad \begin{cases} b = b_-, & t < t_0. \\ b = b_+, & t > t_0. \end{cases} \tag{4.37}$$

The terms a, b, and c account for drift in electrical signal of the BAM.

The data of all the shots taken is then binned according to their corrected pump-probe delays. By plotting the difference between the jitter and delay scan positions, as in Fig. 4.34, it is seen how the SASE can introduce a variance of 0.2 ps into the delay between probe and pulse beam. Some of the points are up to 2 ps away from their actual positions. The data is binned by the corrected delay and from this the intensity and variance of each delay data-point is estimated.

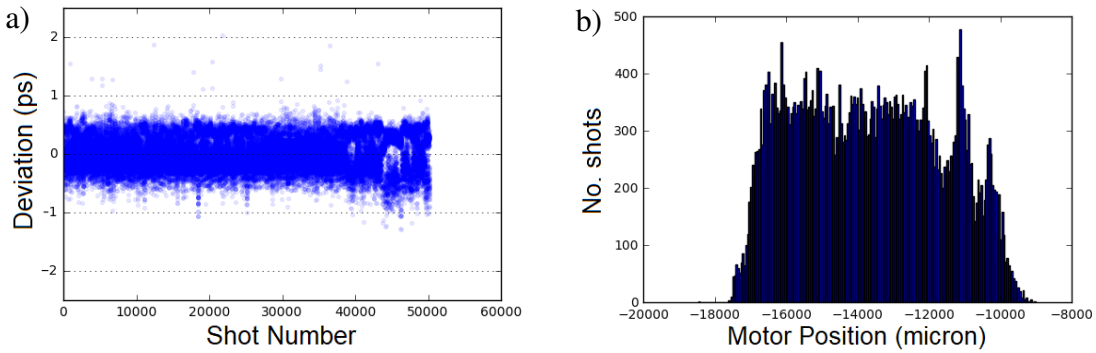

Figure 4.34: a) Jitter correction data showing the spread of actual delays as recorded by the BAM and b) binning of the data following the TimingMonitor analysis provided by the High Performance Computing (HPC) of SACLA.

Following this data treatment, the oscillations of the Bi(111) peak following excitation are clearly seen in Fig. 4.33b. The jitter correction allows for the improvement of the time resolution that beam bunching and shot-to-shot variations have previously restricted to ps resolution. The corrected temporal resolution can now be approximated as the correlation between the laser pulse length, $\sigma_L^2 = 35$ fs, and the x-ray bunch length,

$\sigma_B^2 = 20$ fs [185], to yield $\sigma_T^2 = (\sigma_B^2 + \sigma_L^2)$ approaching 40 fs. As a cautionary note, this method overestimates the uncertainty as seen by the large error-bars in 4.33b. This is due to the standard deviation across a bin being used. More robust estimates can found by pooling the data from each bin and comparing the calculated pool estimates to formulate a standard error for each data point. Improvements to the operation frequency (60 Hz $\rightarrow$ 1 MHz [32]) are expected to reduce the uncertainty in normalised intensity considerably.

Chapter Summary

An overview of the methods used in this thesis have been described detailing sample preparation, bulk magnetometry, time-resolved optical probes, and x-ray based techniques. These are used to examine the magnetic and crystal structure of FeRh thin films and patterned samples both in the static and dynamic regimes. These techniques were used to produce the results in the following chapters. Simulations are also described which assisted in interpretation of the experimental data.

Chapter 5

Non-resonant x-ray Magnetic Scattering for Observation of AF Order

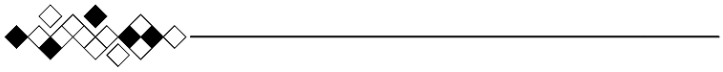

This chapter details experiments carried out at synchrotron x-ray sources to investigate the long-range magnetic ordering of FeRh in the Anti-Ferromagnetic (AF) phase. The temperature dependence of the magnetic scattering was investigated as well as the minimum mean coherence length of the AF ordering. The data and findings of this chapter have recently been published in AIP advances [37].

Since first described by Neél [66], the primary barrier to investigating AF materials is the negligible field interaction due to the compensated spin ordering. However, the magnetic sub-lattice offers a technique to explore AF order in FeRh thin films using non-resonant magnetic x-ray scattering. In particular, x-rays at energies below the Fe K-edge can be used for the observation of magnetic Bragg peaks. Due to the low efficiency of the magnetic scattering, a grazing incidence geometry was used to optimise the diffraction intensity from thin film samples. Based on Scherrer analysis we estimate a minimum coherence length of 40 nm, which is similar to the thin film grain size. The temperature dependence of AF order is inversely correlated to the emergence of FM moment, as expected from the known MPT behaviour [14]. This work reveals that AF order can be probed through the MPT, with significant scattering at temperatures where FM domains are expected to form. This technique can be used to explore the evolution of the magnetic sub-lattice while offering insight into the AF/FM mixed phase.

5.1 Sample Characterisation

The sample investigated was a dc-magnetron sputter deposited 500 nm FeRh film grown on a MgO (001) substrate, capped with 3 nm Pt. The sample was characterised using VSM & XRD as discussed in Chapter 4. This further provides a reference for the transition temperature, T_T and the width of the transition ΔT, which are important for comparisons to previous reports on FeRh in the literature.

5.1.1 Magnetic Properties of the FeRh Thin Film

The temperature dependence of the magnetic properties of the sample was measured by VSM, shown in Fig. 5.1. An in-plane field of 1000 Oe was applied, with in-plane moment recorded in increments of 5 K for both heating and cooling cycles. A reference background was used to account for the diamagnetic response of the MgO substrate. Sample volume is estimated from a uniform thickness of 500 nm across a disc of diameter 8 mm. By fitting the dM/dT data with a Gaussian function, T_T and ΔT of the transition are estimated. The derivative is found using the data analysis software, Origin 9.1 which estimates the slope using piecewise averaging with a window size of 3 (10 K). This treatment allows for the estimation of the transition point in the heating cycle as T_T = 355 K and ΔT = 25 K, which compares to similar FeRh samples in the literature [20]. Saturation magnetisation reduces with temperature, with maximum observed moment in the FM phase measured as M_s = 920 kA m^{-1} (@ 410 K).

5.1.2 X-ray Diffraction

The crystal structure of the deposited film is determined by performing a $\theta/2\theta$ scan on the sample in the range 2θ = 20° - 70°. The MgO(002), FeRh(001), and FeRh(002) peaks are identified in Fig. 5.2. The heated XRD scans were carried out using an Anton-Paar DHS1100 heating stage fitted with a carbon dome to maintain low pressures ($\approx 2\text{x}10^{-3}$) to prevent sample oxidation. The presence of both FeRh peaks in this angular range confirms that B2 order for FeRh is maintained across this temperature range [20]. Additional unmarked peaks in the XRD spectrum are due to scattering from the carbon dome. The film is found to align in-plane 45° to the cubic MgO substrate ($a = 4.21$ Å), see Fig. 4.24. This fulfils the lattice matching condition with a mismatch of $< 2\%$ [237] for planes FeRh[001](011)||MgO[001](001). The lattice expansion of the FeRh through the MPT was measured to be 0.75% when heated from 303 K to 473

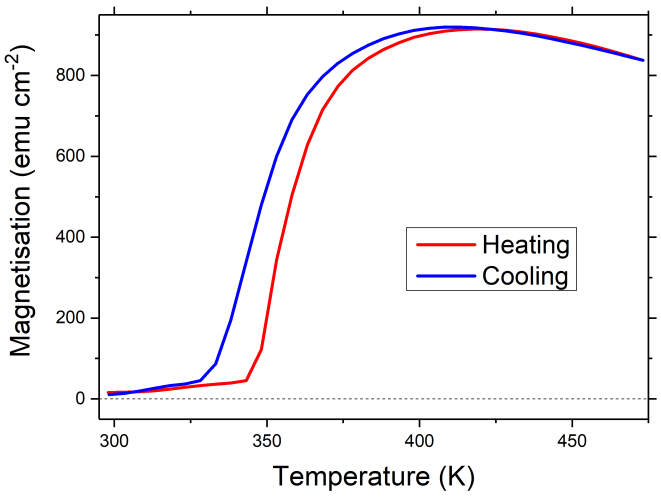

Figure 5.1: Magnetic moment as a function of temperature for nominally 500 nm thick FeRh samples as measured by VSM. The film is entirely AF below temperatures of 323 K, and entirely FM above 400 K. The highest saturation moment is seen at ≈ 410 K, with T_T estimated as 355 K.

K, with the expansion in the MgO lattice ≈ 0.01%. A factor of 70 difference (see Table 5.1) implies that interfacial strain is not driving the expansion.

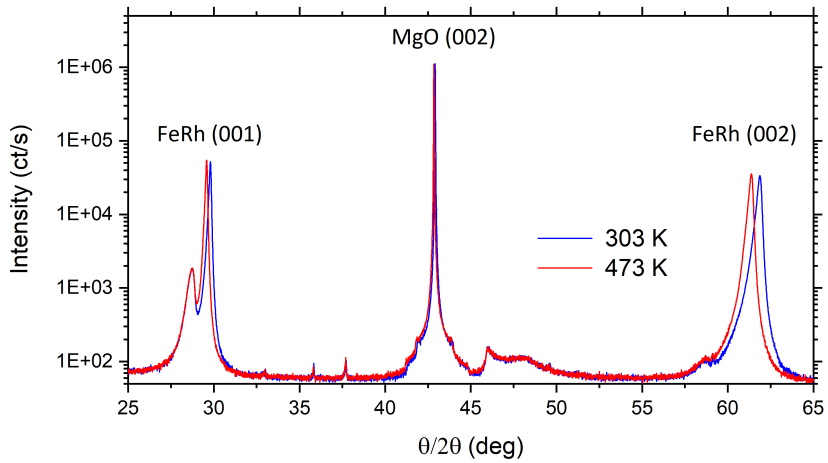

Figure 5.2: XRD spectrum of the sample with peaks labelled. Lattice expansion with sample heating is seen from the reduction in scattering angle. Comparable intensities of the (001) and (002) peaks predict an order parameter, S = 0.9 ± 0.1.

5.1.3 Reciprocal Space Map

A reciprocal space map provides a measure of rocking curves about the peaks for a range of 2θ. This provides useful background information for the analysis of the

Table 5.1: Identified sample and substrate XRD peaks. The lattice expansion has been calculated using the Bragg diffraction condition.

	2θ @ 303 K	2θ @ 473 K	Expansion (%)
FeRh (001)	29.80°	29.57°	0.8
FeRh (002)	61.88°	61.38°	0.7
MgO (002)	42.925°	42.919°	0.01

magnetic peaks described later, providing a reference for the FWHM of the peaks as measured at the synchrotron. The symmetric shape of the rocking curve and the similar shape across different 2θ show the consistency of the (hkl) values in Fig. 5.3. The maximum (002) peak FWHM is seen to be perpendicular to the 2θ scan, indicating the isotropic lattice vectors (see Section 2.1) are well aligned to the XRD scattering vectors, k_i.

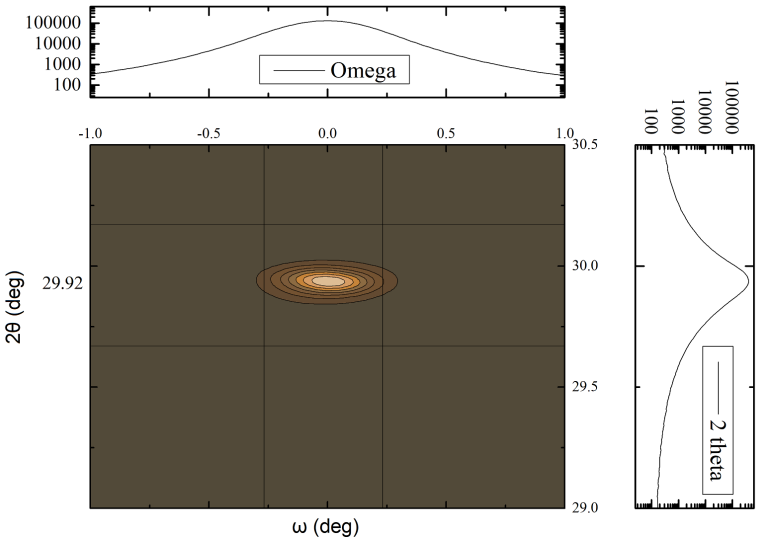

Figure 5.3: The reciprocal space map of the FeRh (001) as measured using XRD. The σ of 0.4° is found by fitting the peak with a Gaussian function in Origin Pro 9.1.

This alignment shows that the expected crystal growth has occurred with epitaxial deposition of FeRh on MgO. The FWHM of 0.4° compares well to those previously found in the literature [238]. We expect a slight improvement in the FWHM at large-scale facilities due to the highly optimised beam optics and collimated beam. This reduces sources of instrumental broadening.

5.2 Magnetic Scattering Volume

This section details the expected x-ray scattering efficiencies from the magnetic sub-lattice which informs the optimisation process for this non-resonant technique. The change in polarisation of scattered x-rays is further discussed. This offers an estimate of the spin and orbital contributions to the atomic moments of which the magnetic sub-lattice is composed.

5.2.1 Ratio of Charge to Magnetic Scattering

From the treatment of the magnetic scattering cross-section in the seminal work of Blume and Gibbs [33], it is possible to estimate the scattering efficiency from the magnetic sub-lattice using the resulting cross-section, see Section 2.2. Referring back to Eq. (2.4) & (2.14), it is shown that the respective x-ray cross-sections from a lattice of charge centres, I_c, and from a lattice of spins, I_m, for momentum transfer, $\vec{K}$, are,

$$I_c \propto \langle b| \sum_j e^{i\vec{K}\cdot\vec{r}_j} |a\rangle \,, \tag{5.1}$$

$$I_m \propto \frac{i\hbar\omega}{mc^2} \langle b| \sum_j e^{i\vec{K}\cdot\vec{r}_j} \left[\frac{i\vec{K}\times\vec{p}_j}{\hbar k^2} \cdot \vec{A} + \vec{s}_j \cdot \vec{B} \right] |a\rangle \,, \tag{5.2}$$

over electrons with position, $\vec{r}_j$, momentum, $\vec{p}_j$, and spin moment, $\vec{s}_j$. The expected relative efficiency has been previously explored by Brükel et al. [222] in a resonant x-ray scattering experiment on GdS. Based on the non-resonant x-ray energies used in Section 5.3, we expect a relative efficiency of,

$$\frac{\langle f_m \rangle}{\langle f_c \rangle} \approx \frac{\lambda_C}{d} \cdot \frac{N_m \cdot f_m}{N \cdot f} \cdot \langle \vec{S} \rangle \,, \tag{5.3}$$

where f refers to the form factor, and N refers to the number of electrons. The subscript denotes charge, c, or magnetic, m, scattering. $\langle \vec{S} \rangle$ is the expectation value of the spin quantum number. In general, this will result in a maximum ratio of efficiencies of 10^{-6} [49]. As shown later in Section 5.3.3 (see Fig. 5.7), this is close to the measured ratio of 10^{-6} - 10^{-7} [239]. As a minor x-ray event, significant count rates can only be obtained with strongly coherent x-ray sources with high brilliance, limiting such experiments to large-scale facilities [143].

5.2.2 Orbital and Spin Moment

Based on the full derivation from the original theory paper of Blume and Gibbs [33] as described in Section 2.2.3, the scattering efficiency is dependant on the interaction with both the atomic orbitals and the electron centre. Therefore, it is possible to determine the ratio, $|\vec{L}|:|\vec{S}|$, of atomic moments in the magnetic sub-lattice. Following the derivation of Blume [48], $g(k)$ describes the ratio of momentum for the orbital and spin components of the moment for a fixed x-ray wavelength. The scattered intensity of parallel, $I_{\parallel}$, and perpendicularly, $I_{\perp}$, polarised light is shown to vary with the incidence angle, θ, as,

$$I_{\parallel} = (1+P)(1+g^2)^2\sin^2\theta + (1-P)(1+2g\sin\theta)^2, \tag{5.4}$$

$$I_{\perp} = (1+P) + (1-P)(1+g^2)^2\sin^2\theta, \tag{5.5}$$

where P is the linear component of the Poincaré-Stokes vector [33] (± 1 - linearly polarised, 0 - unpolarised). This yields a change in polarisation, P_1, defined as,

$$P_1 = \frac{I_{\perp} - I_{\parallel}}{I_{\perp} + I_{\parallel}}. \tag{5.6}$$

However, over the range of angles measured, little contrast in the polarisation changes is predicted, meaning estimation of the $|\vec{L}|$ & $|\vec{S}|$values is not feasible. For the low $|\vec{L}|$ in the FeRh alloy, we expect little variation in the polarisation. The contrast is maximised when the ratio, $|\vec{L}|:|\vec{S}|$, is approximately one. Values in the literature for Fe moment in FeRh obtained from *ab initio* determinations are regarded as 3.15 μ_B for the spin moment of Fe and 0.072 μ_B for the orbital moment [108], close to the measured ratio of $\frac{m_L}{m_S} = 0.054$ found from XMCD experiments [108]. This is a 20% increase of the value found in elemental Fe, being 0.044 [240].

Fig. 5.4a shows that the expected moments for Fe in the FeRh alloy do not allow for a good estimation of the orbital moment using non-resonant scattering. The predicted polarisation shift for $g(k) = 0.05$ has an angular dependence similar to that for a ratio of $\frac{m_L}{m_S} = 0$. Over the angular range of the synchrotron experiments, it can be seen that a 400% increase in the orbital moment will result in a polarisation change of $\approx 0.02\%$. It is nearly indistinguishable from similar curves for a wide range of values of $\vec{L}$. We further show in Fig. 5.4b the effect of having comparable spin and orbital moments. It is not feasible to operate this experimental technique at higher scattering angles. In Section 5.3.3, we demonstrate why grazing incidence is the preferred experimental

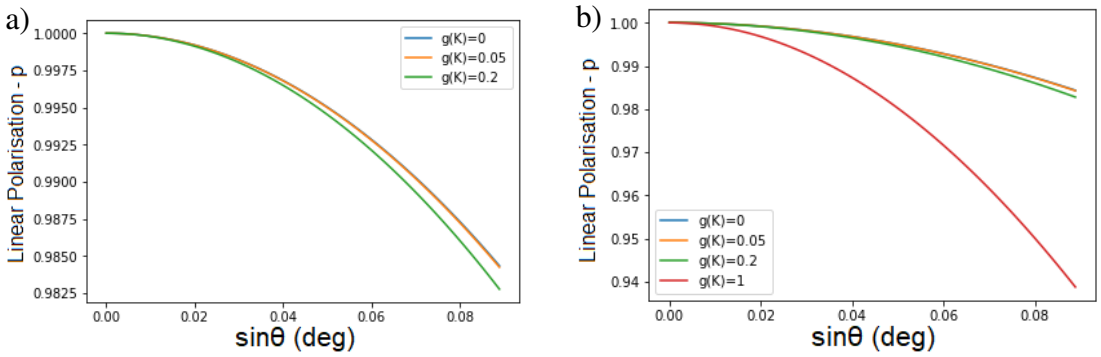

Figure 5.4: a) Polarisation as a function of incident angle, θ about grazing incidence. b) This was performed for a variety of ratios, g(k). This demonstrates the difficulty in precise orbital moment extraction for AF materials using grazing incidence scattering geometries.

geometry as a consequence of the resulting increase in probe volume.

5.3 Non-resonant Scattering from AF Bragg Peaks

X-ray scattering experiments were performed on 5 x 5 mm^2 films at the I16 beamline of Diamond Light Source, and the MS beamline [221] of the Swiss Light Source using x-ray energies of 4.998 keV and 6.408 keV. These energies are below that of the Fe shell electrons (K-edge = 7.112 keV [241]). During the I16 measurements, temperature was controlled with the available 6K-800K ARS GM cooler.

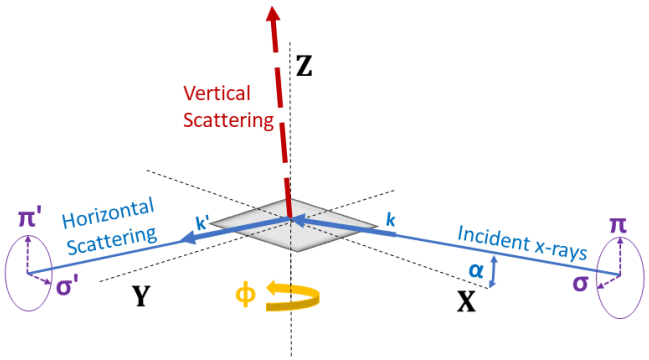

Figure 5.5: Schematic of synchrotron experiments using the sample reference axes. The angle α refers to the incidence angle of the x-rays, and the sample was rotated about ϕ to produce the rocking curves in the measurements. The rotation of polarisation in the σ-π' channel was of interest.

5.3.1 Sample Orientation

In order to observe the required XRD peaks from the sample, it is necessary to construct a matrix which defines the sample placement in the diffractometer co-ordinate system [242]. This can be extended to account for deviations from an isotropic lattice as a consequence of strain or imperfect epitaxial growth. A minimum of two rocking curves for non-collinear Bragg peaks are recorded, where the exact peak centres inform on the relative orientation of the sample reciprocal axes to the Cartesian coordinate system of the diffractometer [242]. Using the Miller indices, the column vector in the reciprocal space lattice system is,

$$\mathbf{h} = \begin{pmatrix} h \\ k \\ l \end{pmatrix}. \tag{5.7}$$

Following the derivation of Busing et al., **U** is the orthogonal matrix which relates the ϕ-axis system to the crystal Cartesian system and **B** transforms the reciprocal lattice vectors to the crystal Cartesian system so that,

$$\mathbf{h} \xrightarrow{\mathbf{B}} \mathbf{h}_c \xrightarrow{\mathbf{U}} \mathbf{h}_\phi. \tag{5.8}$$

The orientation matrix is then defined as the product, **UB**, such that for every vector of indices, $\mathbf{h}_i$, will transform as [224, 242],

$$\mathbf{h}_{i\phi} = \mathbf{UB} \cdot \mathbf{h}_i, \tag{5.9}$$

where the vector, $\mathbf{h}_{i\phi}$, describes the scattering when the sample is mounted on the diffractometer with every diffractometer circle set to zero [224]. In general, this is extended to other diffractometer axes by further multiplying by the corresponding orthonormal matrices [224]. This is required to achieve the specified grazing angles, α (see Fig. 5.5), in the following experiments.

5.3.2 Energy Dependence

During the synchrotron experiment, we focused on measuring the magnetic Bragg peaks in a $Fe_{50}Rh_{50}$ film originating from the long-range AF order. In order to establish the efficiency of x-ray magnetic scattering, the 'charge' peaks - those corresponding to the nuclear x-ray scattering - were used as a reference. The noise was reduced by defining a Region Of Interest (ROI) for each peak on the Pilatus 3-100K 2D detector

and normalising against a background ROI. To confirm that the signal of the $(\frac{1}{2}\ \frac{1}{2}\ \frac{1}{2})$ peaks were indeed of magnetic origin, a pyrolithic graphite polarisation crystal was initially used (with the x-ray energy tuned to 5.22 keV). Due to the required exchange of angular momentum [33], it is expected that significant intensity is measured in the rotated polarisation channel in Fig. 5.5. The channel used was the σ-π', referring to the shift in x-rays polarized parallel to the surface. At low angles, this will exhibit a 90° shift in the polarisation axis due to the relative spin and orbital moments [49]. As shown in Fig. 5.4b, the degree of polarisation is expected to be unity, with signal seen when the analyser allows x-rays to pass through the π' axis. The low orbital moment of FeRh means this polarisation change should be similar across all incidence angles, see Section 5.2.2. In this experimental configuration (see Fig. 5.5), with an incident angle $\alpha = 2°$, we obtained count rates of the order of 40 ct/s for the $(\frac{3}{2}\ \frac{1}{2}\ \frac{1}{2})$ reflection in the vertical scattering configuration. We lowered the energy of the x-rays to 4.998 keV to establish more favourable conditions for measuring AF peaks. At this energy the $(\frac{3}{2}\ \frac{1}{2}\ \frac{1}{2})$ magnetic peak occurs for a horizontal scattering angle of 90°, where nuclear Bragg peaks are suppressed. It is therefore possible to measure without a polarisation analyser, as only the magnetic signal is present at this scattering angle and horizontal geometry. Indeed, we found a count rate of 2500 ct/s for the $(\frac{3}{2}\ \frac{1}{2}\ \frac{1}{2})$ magnetic peak ($\alpha = 2°$). In order to confirm these efficiencies, a higher x-ray energy (6.408 keV) was used to check the $(\frac{5}{2}\ \frac{1}{2}\ \frac{1}{2})$ Bragg peak. In this case we obtained a count rate of 1000 ct/s ($\alpha = 5°$), again using the horizontal scattering geometry. The efficiency of magnetic scattering can be estimated by comparing the intensity of the magnetic and charge peaks. The ratio of these intensities is estimated to be $I_c/I_m = 1{\times}10^{-7}$ when comparing similar incidence angles and correcting for the attenuation of the x-rays. This is close to the expected value presented in Section 5.2.1 [222]. Finally, we attempted to observe resonant enhancement of the magnetic scattering in the vicinity of the Fe K-edge. However, above these energies (@ 7.6 keV [243, 244]), the signal is dominated by the background due to Fe fluorescence.

Fluorescence Background

Rocking curves measurements were taken at energies above the Fe K-edge to determine the merit of resonant x-ray scattering. Theoretically this should result in an increase of the magnetic cross-section due to the increased x-ray absorption as a consequence of the energy matching condition. Above the K-edge, the photons excite core

electrons of the Fe atoms to a higher energy level. The short lifetime of this excited state results in re-emission of photons (at a reduced energy) as electrons return to their ground state. The Fe K-edge occurs at an energy of ≈ 7.1 keV [243]. The scan in Fig. 5.6a shows the result of a ϕ-scan taken using x-rays of energy 7.6 keV [221]. This clearly shows the increased background noise from the use of x-rays of this energy when compared to rocking curves at a lower x-ray energy of 6.4 keV (see slight peak in Fig. 5.6b). For minor x-ray events, a slight increase in noise (200 cps) masks the signal. The increased x-ray scattering does not assist in resolving the spin structure of the materials. As we are only interested in the magnetic sub-lattice and their weak interaction with the incident x-rays, reduction in noise is preferable to increased signal. The scan was repeated using a threshold energy of 7.4 keV to minimise this contribution [220], but was not found to fully compensate the noise. We therefore only operate in the non-resonant regime to maximise the count rate of coherently scattered x-rays.

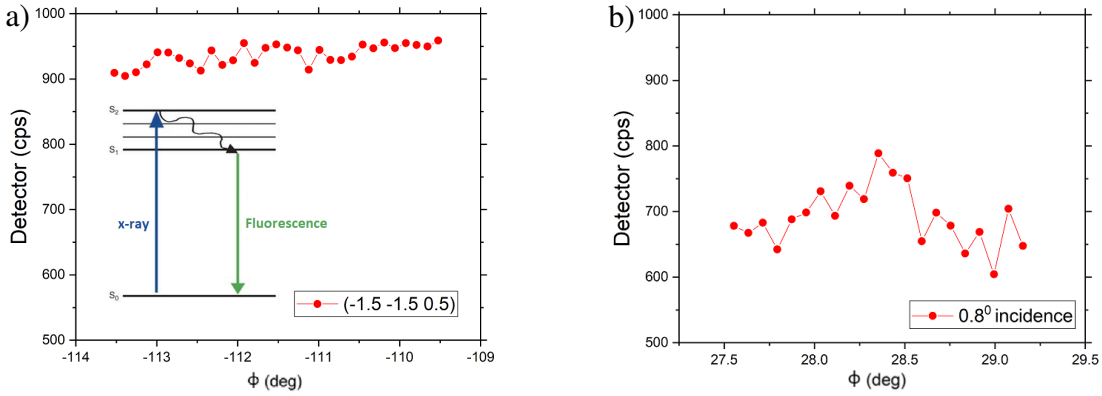

Figure 5.6: a) Rocking curve data taken at 7.602 keV with a diffractometer position corresponding to (-$\frac{3}{2}$ -$\frac{3}{2}$ $\frac{1}{2}$) peak of FeRh, for α = 2°. Inset shows Jablonski diagram for fluorescent processes. b) Rocking curve at 6.408 keV with α = 0.8°The emergence of a slight peak demonstrates that a reduction in the background noise of ≈ 200 cps is required to be experimentally feasible.

5.3.3 Incidence Angle Dependence

Non-resonant magnetic scattering can be further optimised by considering the experimental geometry, specifically the incidence angle which will yield the strongest signal. The incidence angle dependence was measured at an x-ray energy of 6.408 keV with horizontal scattering, see Fig. 5.5. Similar scans were performed on a charge Bragg peak for comparison, FeRh (201). The angular dependence of the incident x-rays is

shown in Fig. 5.7, and in both cases exhibits a steep drop off in signal for incident angles below 1°. In the case of magnetic scattering, no discernible peak is present for angles less than 0.5°. As the same drop-off is also observed in the charge peak signal, we believe this results from less efficient x-ray scattering. Overall, there are less photons available for coherent scattering due to the experimental geometry. The angular dependence can be partially explained by considering the effect of grazing incidence geometry on the spot size of the x-ray beam. The maximum signal is expected when the scattering volume is comprised of the entire film. The beam profile cross-section was found to have a FWHM of 80 μm. When this beam is incident at near grazing angles, the larger footprint results in an increased volume of the thin film sample being illumined. For a perfectly flat film, we estimate the footprint to be several mm when angles of less than 1° are employed. Therefore, below these angles x-ray beam beyond the edges of the film will not be scattered. Small mislineations will greatly reduce the signal.

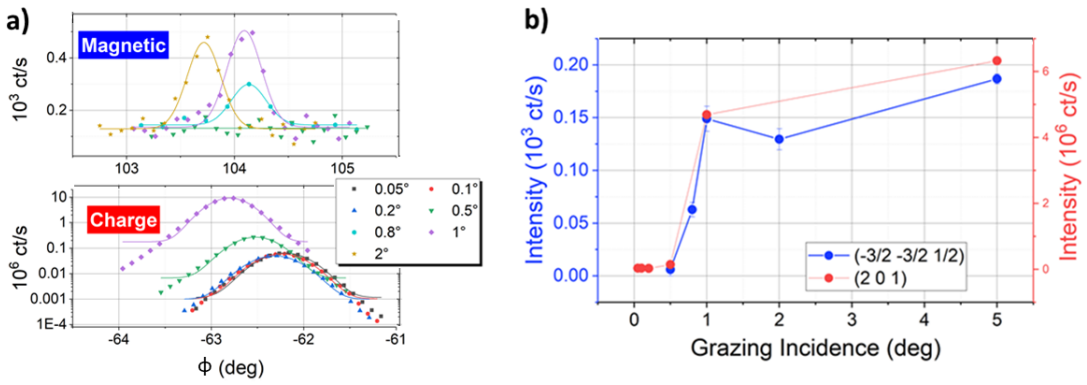

Figure 5.7: a) Rocking curves of the magnetic peaks for increasing incidence angle, and similar scans for the charge peaks (on a log scale) as measured at 6.408 keV. Intensity and FWHM of the peaks was found to vary as the incident angle of the x-rays was changed. b) peak intensity as a function of incidence angle is presented.

This effect is compounded by Total External Reflection (TER) at low incidence angles for x-rays, see Section 4.6.2. This can be explained by the x-ray-metal interaction where a refractive index of slightly less than 1 is observed [122]. Therefore, the x-rays can reflect from the sample surface (the refractive index of air is taken as unity). The following equation can be applied where 1 - δ is the real refractive index at x-ray energies,

$$\cos\theta_c = n_2 = 1 - \delta. \tag{5.10}$$

Using the Taylor expansion of the cosine function and approximating for low angles,

we estimate the critical angle in degrees as,

$$\theta_c \approx 81\sqrt{\delta}. \tag{5.11}$$

The literature is sparse when calculating or measuring the optical properties of FeRh at such energies but we can estimate a range of values by comparing the experiments of Kim et. al. [245] to the calculation based on the nuclear tables for Fe and Rh atoms [246]. Kim et al. found $\delta = 6.86\text{x}10^{-6}$ for x-rays @ 16.22 keV, while from the tables we estimate a value of $4.5\text{x}10^{-5}$ @ 6.408 keV. The trend for smaller delta at higher x-ray energies is consistent across metallic samples [122, 246]. This yields an estimated critical angle, $\theta_c = 0.54°$. This value correlates with the drop off in intensity seen in Fig. 5.7. We expect TER to be the greatest contribution to the intensity of these peaks, especially as a horizontal experimental geometry was employed.

The results of the grazing incidence scans taken at I16, Diamond are presented in Fig. 5.8a. From these scans, the results presented in Fig 5.8b were derived. These scans were taken at 4.992 keV, showing a similar angular dependence. Each point was taken from the integrated intensity of the FeRh $(\frac{3}{2}\ \frac{1}{2}\ \frac{1}{2})$ peak on the 2D detector of I-16 as the axis, μ, was swept (being equivalent to ϕ in Fig. 5.5). The rocking curves were fitted with Gaussian functions to extract the intensity (ct/s) and FWHM (°) at each angle of incidence.

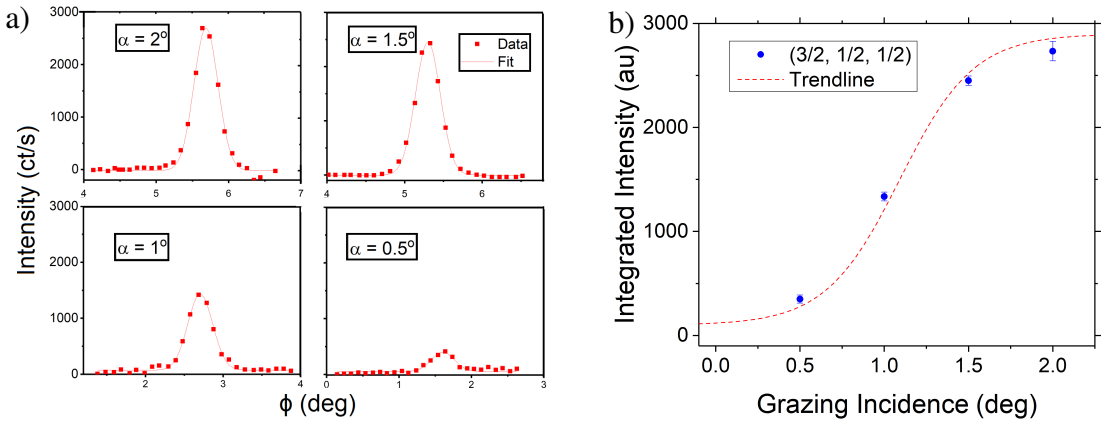

Figure 5.8: a) Rocking curves of the $(\frac{3}{2}\ \frac{1}{2}\ \frac{1}{2})$ peaks of FeRh as measured at I16, Diamond Light Source (E = 4.998 keV) about μ (equivalent to ϕ in Fig. 5.5). b) α refers to the incidence angle of the x-rays with respect to the sample surface.

TER is again evident and in comparison to the data presented earlier, shows a

larger θ_c at this x-ray energy. This is expected for metallic samples, indicating a larger δ. Based on the tables of Henke et. al. [246], FeRh possesses a value of $\delta = 7.1\text{x}10^{-5}$, predicting $\theta_c = 0.63°$. Such behaviour is further validation of the grazing incidence requirement for the observation of these peaks, and important for future work exploring the AF order of FeRh using x-ray based techniques.

5.4 Temperature Dependence of AF Order

In order to confirm that the signal from the $(\frac{1}{2}\ \frac{1}{2}\ \frac{1}{2})$ family of peaks of FeRh has no contribution from the charge centres, we measured the peak intensity as a function of temperature through the MPT. The results are presented in Fig. 5.9, where the intensity of the AF peaks were found from fitting the rocking curves with Voigt functions. The integrated intensities of these peaks were used as a measure of the AF order in the system, once the background was subtracted. The intensity was found to steadily decrease for increasing temperature as expected due to increasing non-coherent phonon scattering in the sample [39]. This is assumed to be equivalent to the Debye-Waller Factor (DWF) for charge Bragg peaks. Near T_{VSM} (where the MPT occurs according to the VSM data) the intensity drops significantly in the interval 360-390 K (Fig. 5.9a). Based on the measured XRD data of the (001) and (002) peaks of the FeRh we expect no significant change in the form factor. The charge Bragg peaks measured at 303 K and 493 K show no change in the integrated intensity. Therefore, the drop in intensity is indicative of reduced order in the measured lattice planes. These measurements demonstrate that the observed $(\frac{3}{2}\ \frac{1}{2}\ \frac{1}{2})$ peak is due to magnetic scattering from the AF lattice.

As the AF-FM transition occurs over a range of temperatures, the AF order does not evolve as a single first-order phase transition where the properties would be expected to change over a narrow temperature interval. Instead, previous experiments into the microscopic structure of FeRh have shown that the sub-micron regions have an independent transition temperature [136], each with a first-order transition. By fitting the change in intensity vs temperature with a Gaussian function in Fig. 5.9b, we can compare the transition as monitored by VSM (T_{VSM} = 356 K) to the change in AF order ($T_{x\text{-}ray}$ = 377 K). From the signal, it appears that the FM moment begins to emerge before the AF order is completely lost. The mixed phase of the material still exhibits long-range anti-parallel ordering of the Fe spins. It is quite likely the sample

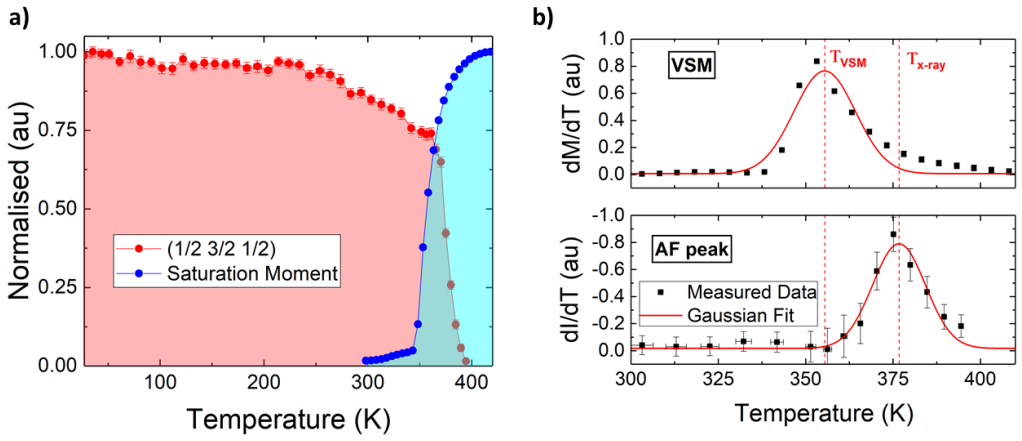

Figure 5.9: a) Inverse correlation between the intensity of the FeRh ($\frac{1}{2}$ $\frac{3}{2}$ $\frac{1}{2}$) magnetic peak as measured at 4.992 keV, and the saturation moment of the FeRh film, measured using VSM. b) Comparison of Gaussian fits to the transition behaviour for the VSM (T_{VSM} = 356 K) and the diffractometer data ($T_{x\text{-}ray}$ = 377 K) showing a shift in the temperature envelope over which changes occur.

temperature at the beamline was lower than measured. The quoted temperature refers to that at the base of a coil-heated sample stage, whereas the VSM system operates with a constant stream of heated air. By allowing the sample to thermalise for 30 minutes at the beamline we attempted to mitigate the differences in set-up. Considering uncertainties due to thermometer calibration ($\pm$ 5 K), the difference in the two transition temperatures remains significant (>20 K).

This is in agreement with previous work where the nucleation and growth of FM domains through the MPT was investigated [139, 247]. FM domains have been seen to first nucleate and then grow by absorbing neighbouring AF domains. If we assume that the AF domains are much smaller than the FM domains [17], it is possible to still have coherence within the AF domains while a significant portion of the material has transitioned to the FM state. Therefore, we suggest that this is further evidence for the previously reported dynamics of the MPT [140]. It will also be useful to have such long-range order in the mixed phase when measuring the lattice dynamics of the MPT [112]. Using a similar probe of AF ordering, it would be possible to examine with fine detail how quickly the film transitions with regard to the Fe spin re-orientation.

The information extracted from fitting of these magnetic Bragg peaks further allows the 2θ position to determined as a function of temperature. Re-alignment is required after every heating step so it is not possible to calculate exactly the sub-lattice

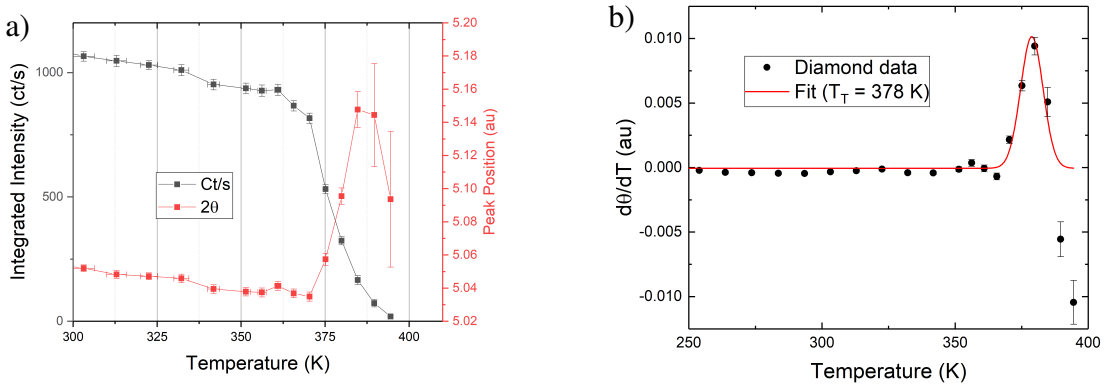

Figure 5.10: a) The shift in 2θ of the AF peak as a function of temperature. This is compared to the reduction in intensity. Error-bars are found using a Voigt fitting function. b) The first derivative provides an estimation of the temperature at which greatest peak shift occurs.

constant, as seen from the slight drift across the measurement. Peak position is determined using the centre of mass of the fitted Voigt functions. Plotting this position against temperature in Fig. 5.10a, we observe slight drift until close to the transition point. A sudden change in peak position (see Fig. 5.10b) is found to correlate strongly with the reduction in peak intensity (see Fig. 5.9b). This shows how the peak can be used as a probe of both lattice (peak position) and spins (intensity of magnetic Bragg peaks). The peak position is not reliable above 385 K due to the loss in peak integrated intensity. It is generally assumed that the AF domains transition individually [140] and expand to form μm sized domains. The simultaneous change in the magnetic sublattice volume and the AF ordering is further confirmation of the mechanism described in the work of Baldasseroni et al. [140].

5.4.1 Scherrer Analysis of Magnetic Bragg Peaks

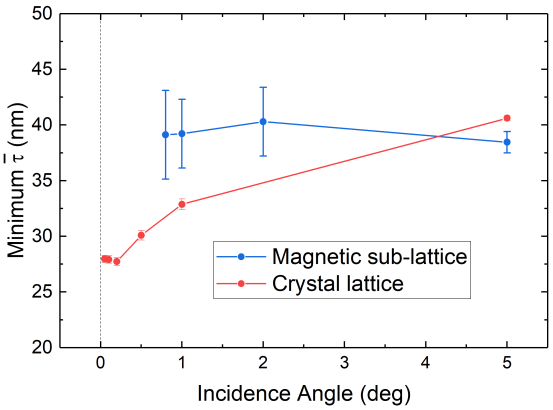

Figure 5.11: Extracted coherence length for the AF order and crystal structure. This was found by applying Scherrer analysis to the charge and magnetic peaks of Fig. 5.7.

In Chapter 4, the origins of Bragg peak width were discussed. Given the finite number of lattice planes in the average crystallite of a thin film, the infinite system assumed for the Bragg derivation does not hold [47]. This results in peaks with measurable width. Broadening further resulting from instrumental sources is more difficult to quantify; emerging from the beam width, internal optics and angular offsets in the alignment procedure. Such broadening should be reduced in a beamline when compared to an in-house diffractometer [221] due to the high precision optics used. The spectral width further broadens the peak as x-rays of different energies will scatter with different angles [45]. If we can extract the broadening solely due to the crystal structure, we can apply the Scherrer equation, see Eq. (4.24). In magnetic diffraction studies, we consider lattice planes with half-integer h, k, l values. The factor K from Eq. (4.24) is assumed to be 0.94 for thin films, λ is the wavelength at 6.408 keV, β is the broadening due to the finite coherence length, and θ is the scattering angle [47]. Extracting θ from the experimental set-up conditions, we can estimate a lower bound for the crystallite size by letting the FWHM be β. As a consequence of the instrumental and spectral broadening, the average crystallite size is larger than the quoted values. For the (201) peak at an incidence angle of 5°, this predicts a minimum coherence length of 40 nm.

The magnetic and charge peaks of Fig. 5.7a were found to possess respective FWHM of 0.38° and 0.39°. This is used to estimate the coherence length of the AF ordering and crystal structure. The resulting coherence lengths from the MS beamline data are seen in Fig. 5.11. Using the same energy and employing the same experimental set-up, it is assumed that any differences in the FWHM are not due to either spectral or instrumental broadening [221]. We do not observe an increase in the FWHM for the half-integer peaks, implying that the ordering of Fe spins in the AF phase are of a

similar long-range order to the crystalline coherence length. Across the measured incident angles, AF coherence length is consistent, with increasing certainty at higher angles. Using a weighted average of values obtained from a Scherrer analysis of these fits predicts a minimum mean coherence length of 40 $\pm$ 3 nm. It compares well to the estimated crystallite coherence length, determined using the same method. This would suggest an AF domain structure smaller or close to the crystallite size of sputtered FeRh films, indicating that such domains are limited by crystallographic defects [17, 24]. This has been previously seen in AF metal oxide thin film samples, with domain sizes of less than 50 nm observed in NiO and $LaFeO_3$ [24, 78].

Similar analysis can be applied to monitor the coherence length of the AF ordering while being heated through the MPT, as recorded at the Diamond Light Source. Comparable rocking curves of the charge peaks were not recorded for comparison in this instance. Due to differences in the experiential set-up between the Diamond and Swiss Light Sources, FWHM is presented a qualitative measure of grain size. By plotting the normalised inverse of the extracted FWHM as a function of temperature in Fig. 5.12a, we observe a consistent domain size up to 350 K. An apparent decrease is observed close to the transition point. The fit error increases significantly near the transition point due to the decrease in signal and the resulting reduction in fit confidence.

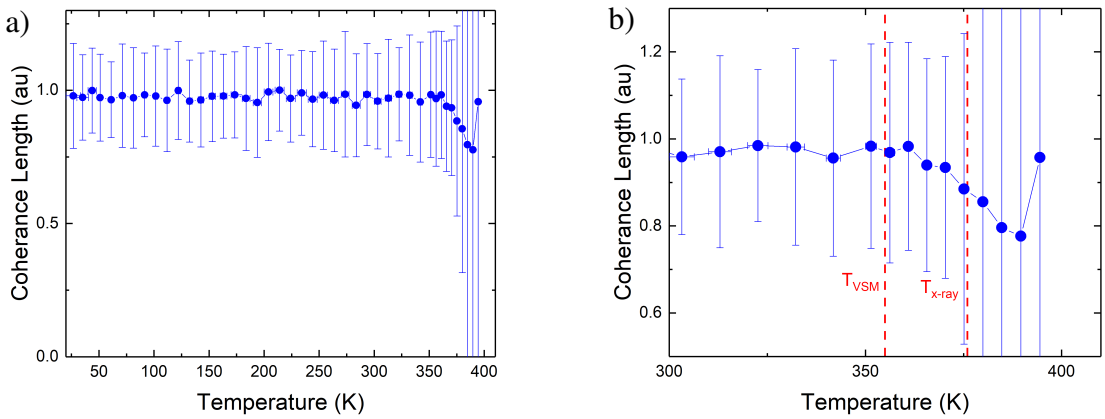

Figure 5.12: a) The normalised coherence length extracted from the AF peaks. b) The temperature dependence is demonstrated showing no change until $T_{x\text{-}ray}$ is approached.

The normalised coherence length is presented in more detail close to the transition point in Fig. 5.12. It is seen that the domain size remains constant across all temperatures up to the transition point where a small decrease is observed. Assuming that the domains are on average $\bar{\tau}$ = 40 nm, this would result in a drop of coherence length

to $\bar{\tau} \approx 32$ nm. Upon closer examination, the coherence length does not reduce significantly until after T_{VSM} has been passed. This is consistent with the assumption that FM domains nucleate and grow within an AF matrix. The domain size of the AF phase does not change as the FM domains nucleate. The drop is observed around $T_{x\text{-}ray}$ where the fit uncertainty increases significantly. This is further evidence for our assumption that a non-resonant x-ray probe can be used to monitor the coherence length of anti-parallel Fe spins through the mixed phase of FeRh.

Conclusions

In conclusion, the work described in this chapter has demonstrated that the long-range ordering of the Fe spins in the AF phase can be quantified using non-resonant x-ray techniques. Due to the weak scattering efficiency of this method - as expected from the magnetic cross section - the signal optimisation is discussed, involving tuning of both the x-ray energy and experimental geometry. Grazing incidence geometries above the critical angle maximise the count rates of coherently scattered x-rays for a given photon energy. The experiments are performed below the Fe K-edge to reduce fluorescence, thereby reducing incoherent background noise. The temperature dependence of these magnetic peaks is verified experimentally, demonstrating that AF ordering persists in the mixed phase of FeRh. This result is in agreement with previous descriptions of the AF $\rightarrow$ FM domain growth mechanism. It may allow for the monitoring of AF coherence length through the FeRh MPT. This work has already verified that the AF domains are limited in size by crystallographic defects, yielding an estimate of minimum 40 nm. Non-resonant magnetic diffraction is easily extended to the dynamic regime, where pump-probe methods involving x-rays are well established [3]. This could be used to examine long-range AF order [248] in FeRh as the MPT proceeds, where volumetric expansion has been previously demonstrated to occur within 10-30 ps [31]. This would permit simultaneous probing of both the spin and lattice structures to directly track the relative rates of transformation.

Chapter 6

Time-resolved x-ray Diffraction as a Probe of Electron-Phonon Coupling

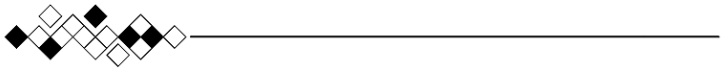

Understanding the ultrafast lattice dynamics of FeRh motivated this project which was enabled by the advent of x-FEL sources. In this chapter, the results of experiments undertaken at the Japanese x-FEL, SACLA are described. A manuscript summarising our conclusions has recently been published in Scientific Reports [38].

Understanding the ultrafast structural transformations of the FeRh MPT is a key element in developing a complete explanation of the mechanism driving the evolution from an AF to FM state. Using an x-FEL source, evolution of the intensity and 2θ position of (-101) diffraction peaks are determined with sub-ps temporal resolution following excitation with a 35 fs laser pulse. The response to laser fluences > 5 mJ cm^{-2} indicates the existence of a transient lattice state distinct from the high temperature FM phase. By extracting the lattice temperature and comparing it with values obtained in a quasi-static diffraction measurement, we estimate the electron-phonon coupling in FeRh thin films as a function of laser excitation fluence. A model is presented which demonstrates that the transient state is the α'(FCC) phase [21], associated with ParaMagnetism (PM). Quantifying the lattice dynamics of FeRh will help bridge the understanding between the ultrafast reconstruction of electronic structure (sub-ps) and the slower emergence of magnetisation (100's ps) [21]. The non-trivial dynamics observed indicate that the coupling between the electron and phonon system is dependent on the fluence of the exciting laser pulse.

6.1 Sample Preparation and Characterisation

The samples used for the experiment at the x-FEL were identical to those described in Chapter 5; nominally 500 nm thick $Fe_{50}Rh_{50}$ films on MgO (001) substrates grown using a magnetron sputtering process outlined in previous work [30, 131]. The B2 order was confirmed from the observation of both FeRh (001) and (002) peaks [20] as measured by XRD using the Rigaku SMARTLAB diffractometer of the Henry Royce Institute. VSM confirmed that the MPT occurs at 355 K with ΔT = 25 K, with maximum saturation magnetization M_s of 920 kA m^{-1}. The sample was prepared for synchrotron experiments by cutting it into a 5 × 5 mm^2 square using a diamond saw. A PMMA layer was deposited prior to cutting to prevent film damage and flaking before subsequent removal using acetone and IPA. The sample dimensions were chosen to be compatible with the mounting stage of the goniometer used in the x-FEL facility.

6.2 Lab-based Heated XRD

In order to extract quantitative information from TR-XRD experiments, it is essential to have complementary information from quasi-static measurements. It is well known that laser excitation provides a local source of heat. Previous pump-probe experiments on FeRh have shown that laser fluences on the order of 3-5 mJ cm^{-2} instigate the transition to the FM phase [117]. With higher pump fluences, it is possible that the high-temperature α'(FCC) phase can be accessed. We therefore determined the lattice properties of FeRh significantly beyond the AF/FM transition with (static) diffraction measurements taken as a function of temperature up to 1023 K, which corresponds to the annealing temperature used following magnetron sputtering deposition. The results gathered on the FeRh (002) diffraction peak are shown in Fig. 6.1.

The shift in the (002) peak of FeRh is observed when the sample is heated above T_T. This shift is seen to persist up to high temperatures with a slight contraction when the sample is brought above 700 K. This is unusual and warranted further investigation. Non-trivial lattice expansion of FeRh has previously been reported [116], described as low thermal expansion close to the Curie temperature. In contrast, the MgO peak undergoes a shift in direct proportion to temperature, indicating linear thermal expansion.

To quantify the lattice expansion, the peak shape must be considered. As the peaks

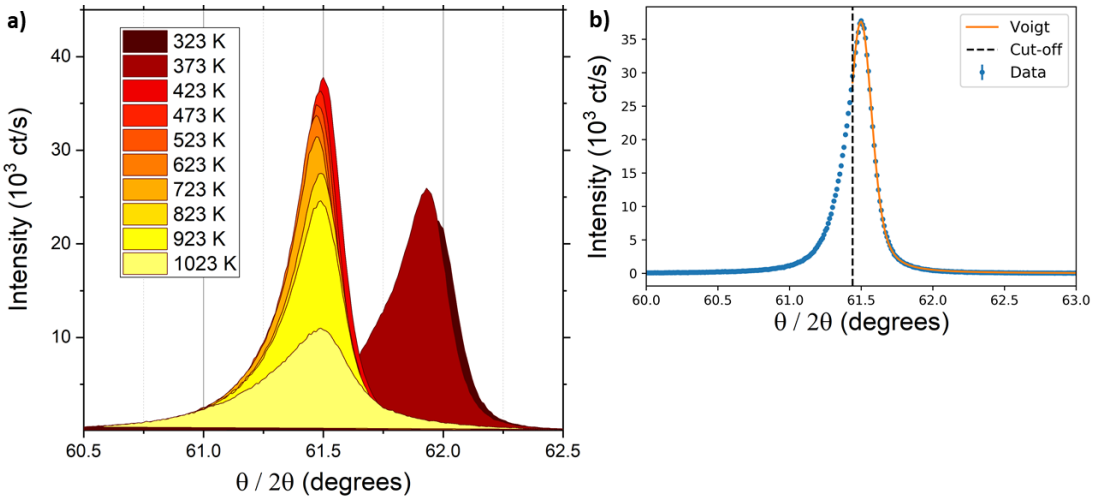

Figure 6.1: a) Quasi-static measurement of (002) FeRh peak as a function of temperature determined using an Anton Paar DHS 1100 heated stage on a Rigaku SMARTLAB XRD diffractometer. The sample was maintained under vacuum with a PEEK dome and allowed to thermalise at each temperature for 30 minutes before the scan was performed. b) Fitting applied to data of the FeRh (002) peak at 423 K. The fit is applied to the data from 61.8° and above. The threshold was found from applying a filter of 80% of the max value in the array.

do not show simple Voigt or Lorentzian shapes, an alternative model had to be devised. Based on the work of Barton et. al. [131], an inhomogeneous strain profile across the film would explain such a peak shape. This work found a shift in the (002) peaks of FeRh as the strain is relieved. This has also been observed in FeRh grown on different substrates where the strain evolves throughout the MPT [249]. From the data presented in Fig. 6.1, it appears that the tail has a Voigt shape but the leading edge is composed of a series of strained contributions. This corresponds with the assumption that film is strained near the interface. Then, a large portion of the film is unstrained yielding the peak tail. In order to consistently treat the data, we only applied fitting to the high angle peak tail using the portion with values 80% of the maximum and above, see Fig. 6.1b. The truncated data was fit with a Voigt function in order to extract the position, width and intensity. From this, the lattice constant of FeRh at each temperature could be calculated using the Bragg equation, Eq. (2.8). Finally, the relative expansion was found from comparison to the thermal expansion of the MgO substrate. This was found using the isothermal (002) peak of MgO to account for any contributions due to inconsistent sample alignment, or substrate induced expansion. Fig. 6.2a was plotted by applying the following relation to estimate the corrected

volumetric expansion, $\Delta V(T)$;

$$\Delta V(T) = \left[\frac{V_{FeRh}(T) - V_{FeRh}(RT)}{V_{FeRh}(RT)} \Big/ \frac{V_{MgO}(T) - V_{MgO}(RT)}{V_{MgO}(RT)} \right], \tag{6.1}$$

where $V_i(T)$ describes the volume of the respective species i, extracted from the Bragg diffraction treatment, Eq. (2.8). Fig. 6.2a shows the expected volumetric expansion upon transition (> 355 K), followed by a slow increase up to ≈ 700 K, at which point a contraction is observed with further heating. This demonstrates the unusual lattice behaviour of FeRh at highly elevated temperatures. In Section 6.3, we compare this behaviour to transient XRD data at high laser fluences, where a reduction in the lattice constant is expected for transient temperatures exceeding 700 K.

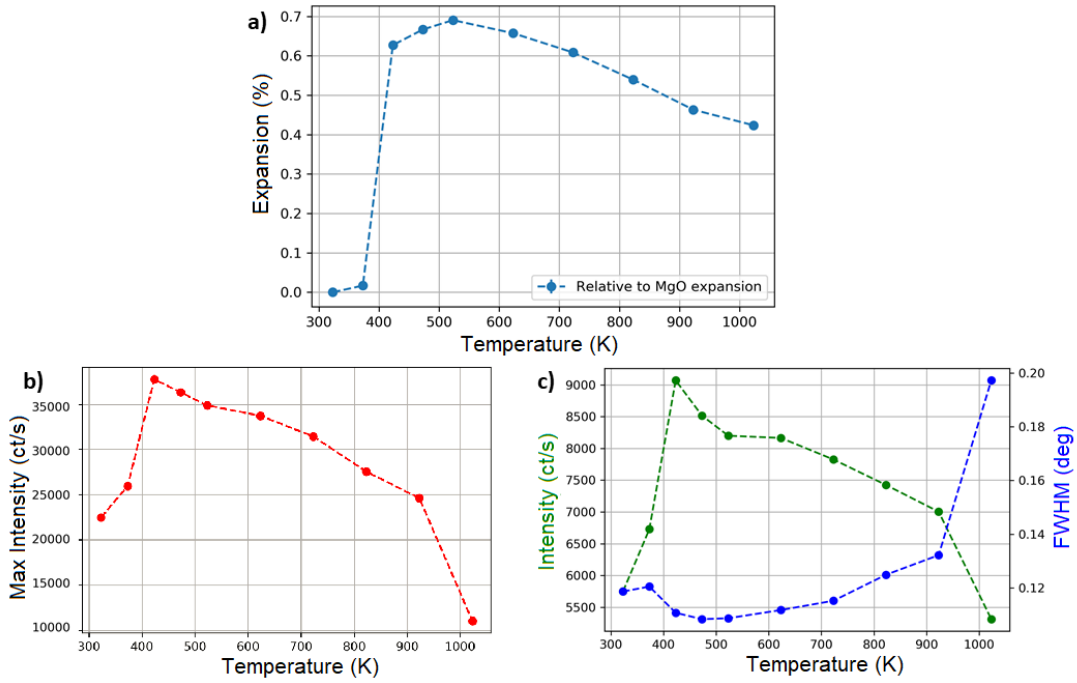

Figure 6.2: Comparison of FeRh (002) peak properties as a function of temperature. a) Expansion of the FeRh film relative to the measured shift in the MgO lattice constant according to Eq. (6.1). b) Maximum recorded count of the peaks. c) From Voigt fitting analysis, the integrated intensity and FWHM are plotted. There is a large jump in FWHM at 1023 K.

The other parameters of the Voigt fit further verify the strain profile model. The reduction in the FWHM as a function of temperature (see Fig. 6.2c) appears to correlate with an increase in the intensity, suggestive of a narrowing of the inhomogeneous strain. This is further confirmation of the strain gradient model based on the work of

Barton et al. [131]. The peak shift upon transition relives the strain across the sample resulting in the narrower diffraction peak.

In order to relate these results to the TR-XRD results of Section 6.3, the DWF is used as a probe of the lattice temperature [250]. The form factor, F, is expected to remain unchanged through the MPT as it expands isotropically with a change of lattice constant of 1% [15]. As discussed in Section 4.6.1, displacement about the atomic centre will reduce the efficiency of coherent scattering. The Debye-Waller interpretation [195, 196] predicts that changes in the lattice temperature, T_L, will result in changes to the XRD peak intensity (with reciprocal lattice vector, $\vec{q}$) according to Eq. (4.22) where atomic displacement, $\vec{u}_n$, is described using [145],

$$\left\langle \vec{u}^2 \right\rangle = \frac{9\ \hbar^2 T_L}{M k_B \Theta_D^2}, \tag{6.2}$$

where M is the mass of one unit cell, and Θ_D is the Debye temperature of FeRh. The FM peak intensity reaches its maximum at a temperature where the film is fully transitioned (423 K). The reduction in intensity after this point is attributed to the DWF. The FWHM increase in this region demonstrates that the ratio of non-coherent scattering from the (002) peak has increased. Both the maximum of the peak and the integrated intensity show a general downward trend as the sample is heated. The FWHM is by contrast relatively constant except at very high temperatures (above 800 K) when it increases sharply. This corresponds to the regime where sample annealing occurs.

6.3 Time-resolved XRD at the SACLA x-FEL

Following the seminal time-resolved x-ray diffraction experiment of Mariager et al. [31] and recent theoretical predictions [119] of a significant difference in the expected temperature dependence of lattice vibrations of the FM and AF phases, we performed a x-FEL based time-resolved experiment to determine the FeRh AF and lattice dynamics on a sub-ps time scale.

TR-XRD measurements were carried out on BL3 of the SPring-8 Angstrom Compact free electron LAser (SACLA) [185, 235] in Japan with the experimental geometry illustrated in Fig. 6.3a. The sample temperature was raised using a pulsed laser excitation with wavelength 800 nm and pulse duration of 35 fs. A cryoblower was used to

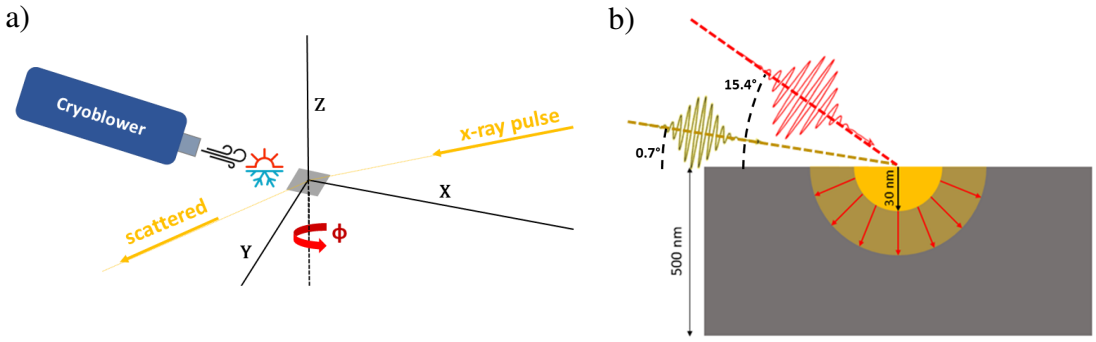

Figure 6.3: a) Schematic of grazing incidence pump-probe experiment showing the angle ϕ about which the sample was rotated to generate the rocking curves. A cryoblower maintained ambient temperature throughout the experiment. b) Sketch of the pump-probe angles used in the SACLA experiment where the penetration depth of the laser (red) was $\approx$ 30 nm while, the grazing incident x-rays (gold) are expected to have a penetration depth of $\approx$ 100 nm

stabilise the temperature and ensure the sample does not slowly heat over the period of the experiment. The laser spot was elliptical with minor and major axes of the beam cross-section 480 & 500 μm, respectively. The angle of incidence used for the pump laser was 15.4°, also corresponding to the angle between the incoming x-rays and the laser as shown in Fig. 6.3b. The crystal orientation was found by scanning rocking curves of the (001) and (111) peaks of the FeRh. The corresponding orientation matrix was used to calculate the relevant goniometer angles for the (-101) Bragg peak under grazing incidence conditions. The scattered x-rays were received on a 2D detector which was fixed in position while the angle about surface normal, ϕ, was swept to examine the rocking curves. The 2D detector was a multi-port charge coupled device (MPCCD) having 512 $\times$ 1024 pixels [251]. The temporal resolution can approach $<$ 50 fs using the trigger capability of the Beam Arrival Monitor (BAM) to correct for shot-to-shot variance resulting from the SASE procedure [144, 229, 236], see Section 4.8.1.

Both magnetic and charge Bragg peaks were investigated but due to time and sample constraints, TR-XRD was only performed on the charge peaks. To maximize the flux on the sample, the beamline was operated in 'pink beam' mode [229] (without monochromator), to deliver photons with energies close to 6.408 keV. The chosen energy was below the Fe K-edge to minimize the background signal resulting from the

excitation of Fe fluorescence. The grazing incidence of 0.7° was chosen based on previous work carried out at the Swiss Light Source using x-rays of similar energies [37]. This incidence angle increases the scattering volume of the sample. At shallower angles the length of the beam footprint approaches that of the sample (5 mm), yielding no further increases in the scattering volume. Furthermore below 0.7°, TER of the x-ray beam is expected, with θ_c estimated to be 0.5 - 0.6° from the real portion of the refractive index ($\tilde{n}$ = 1 – 4.85x10^{-5}) of FeRh at x-ray energies [245, 246]. In this set-up, heating propagates from the surface down in contrast to the entire sample being uniformly heated was the case in lab-based measurements, see Section 6.2. For a given wavelength, λ, the penetration depth, δ_p, is estimated as [122],

$$\delta_p @\ 6.408\ \text{keV} = \frac{\lambda}{2\pi \cdot \text{Im}(\tilde{n})} \cdot \sin\theta, \quad \tilde{n}(\lambda) = 1 - \delta + i\beta. \tag{6.3}$$

For imaginary refractive component, β = 3.684x10^{-6} [246], this results in probe beam penetration depth of 100 nm at an incidence angle, θ = 0.7°. The penetration depth of the laser was estimated to be 30 nm based on the angle of incidence (see Fig. 6.3b) and refractive index at UV-Vis wavelengths [121]. The sample thickness (500 nm) meant that the MgO interface is not considered in the analysis. The strained portion of the film [252] should not contribute to the measured x-FEL pump-probe signals. As such, we assume the film is allowed to expand uniformly and isotropically in the pumped volume.

The observed charge Bragg peaks are shown in Fig. 6.4, with examples of both the 'pumped' and 'unpumped' images, referring to the presence or absence of laser illumination. The intensity of pumped (-101) peaks were normalised using an equivalent unpumped peak, to correct for drift in the laser power across the experiment runtime. The x-FEL pulse rate was 60 Hz while the laser pulse rate was 30 Hz, allowing interleaved measurements of excited and non-excited states with the datapoint at each delay being averaged over 300 pump cycles.

The experiment focused on the time evolution of the (-101) Bragg peak of FeRh following excitation from the optical laser. The normalised intensity refers to the change in the integrated peak intensity within the ROI shown in Fig. 6.4. The peak position was found by a Centre Of Mass (COM) fit to the intensity of the peak. From this it was possible to monitor the lattice expansion of the sample within the laser pumped region. Fig. 6.5a shows data over the entire 200 ps range, while Fig. 6.5b concentrates

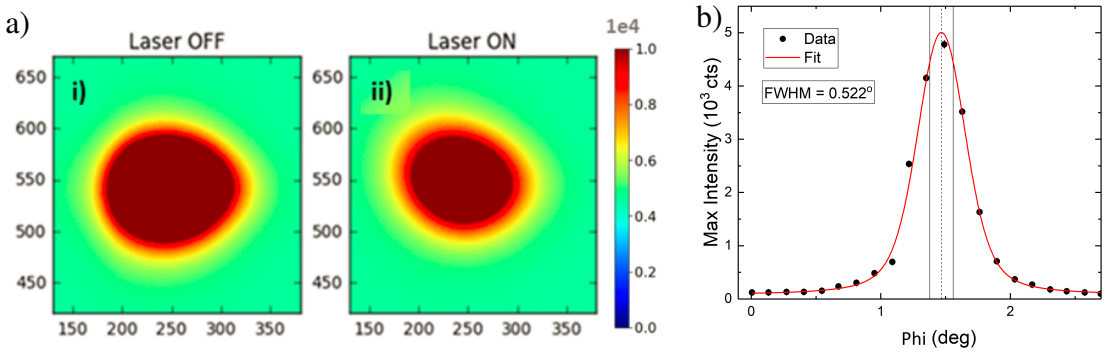

Figure 6.4: (-101) peak of FeRh as a) imaged by the 2d photodetector of SPRING-8 beamline. The x-ray energy was 6.408 keV, and the delay time between the pump and probe was 10 ps. The laser fluence for the' Laser ON' figure was 9.1 mJ cm^{-2}. The reduced intensity and peak shift is clearly observed by comparing the dark-red regions - corresponding to high scattering intensity. b) Rocking curve of the (-101) peak about the angle ϕ, showing the range of intensities expected for the measured shift in 2θ from the fitted Voigt function.

on the initial 15 ps. The observed shift in the position of the signal is due to the lattice expansion, whereas the change in the peak intensity can be used to infer the lattice temperature via the DWF [3, 145]. At a pump fluence of 2.9 mJ cm^{-2} the intensity and peak shift show similar dynamics, with a maximum change observed within 10 ps followed by a gradual relaxation over 100's of ps. Such behaviour is similar to that previously reported by Mariager et. al. [31] In this case, the FM phase is found to emerge with a growth lifetime, τ_G, of 6 $\pm$ 1 ps as calculated by modelling the data with a growth-decay model adapted from Radu et. al. [4] for t $>$ 0, as,

$$\Delta I(t) = A\left(1 - e^{\frac{-t}{\tau_G}}\right) + B\left(e^{\frac{-t}{\tau_R}}\right), \tag{6.4}$$

where $\Delta I(t)$ is the change in the scattering intensity, A and B are fitting constants, t is the delay between the pump and probe pulses, and τ_G and τ_R refers to growth and the relaxation lifetimes of the transient FM phase.

On short time scales (t $<$30 ps), the intensity for all fluences decays with a characteristic time constant, $\tau_G \approx$ 6-12 ps, comparable to previous reports in the literature [31, 238]. Over longer timescales, the change in intensity reaches an asymptotic value for low fluences, while for higher fluences we observe a continuous intensity decrease with a time scales in the range 80-120 ps. This indicates the existence of a different sample heating regime, which we associate with heat dissipation occurring from the laser excitation centre to the unexcited sample volume probed by the x-rays (given that

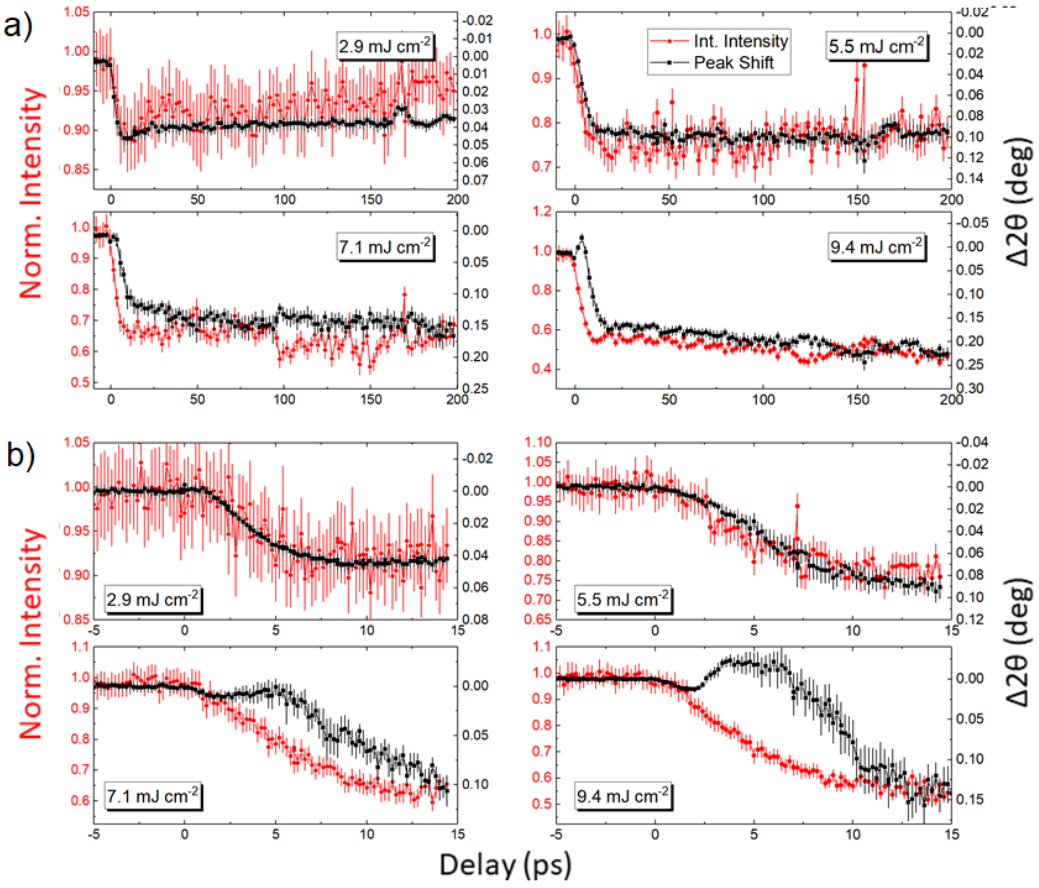

Figure 6.5: a) Peak intensity and 2θ shift as a function of probe delay for the FeRh (-101) XRD peak. This was found by fitting the cross-sectional intensities of the peaks shown in Fig. 6.4 with Gaussian functions as a function of laser delay. Peak intensity and 2θ show similar dynamics, initially decaying within 10-30 ps and recovering over 100's of ps. b) The same quantities are presented with a focus on the initial excitation (up to 15 ps probe delay). For fluences above 5.5 mJ cm^{-2} the peak shift shows different dynamics to that of the intensity, with increasing divergence for increasing fluence.

they interact with a larger sample volume than is excited by the laser pulse). The longer scans demonstrate the FM phase possesses a lifetime of between 100-200 ps.

In contrast, the short time interval data of Fig. 6.5b show the peak shift does not evolve consecutively with the transient intensity at high laser fluence. In order to explain such behaviour, the transient temperature and FWHM are explored in the following sections to inform on processes that occur over sub-ps timescales.

6.3.1 Transient Lattice Temperature

The transient lattice temperatures during x-FEL experiments can be inferred from the measured peak intensities of Fig. 6.2, by estimating the Debye temperature of the material [145]. This calculation is based on a simplified form of the Einstein-correlated model, where the atoms are assumed to act under a harmonic potential [197]. This is a valid assumption for the acoustic phonon modes, or for temperatures above Θ_D [3]. Based on specific heat measurements on FeRh [183] and *ab initio* calculations [109], this is valid above 300 K. The DWF presented in Eq. (4.22) & (6.2) can be rearranged to provide the following estimate of the lattice temperature as a function of the scattering intensity;

$$T_L = T_0 - \chi_D \cdot \ln\left(\frac{I}{I_0}\right), \quad \text{where} \quad \chi_D = \frac{M k_B \Theta_D^2}{3\,\hbar^2 \vec{q}^2}. \tag{6.5}$$

We apply this treatment to the heated XRD peaks to estimate the pre-factor, χ_D, of Eq. (6.5), yielding a value of 0.69 $\pm$ 0.08 10^3 K as demonstrated in Fig. 6.6a. This treatment assumed T_0 = 423 K, as the most intense peak measured using the laboratory based diffractometer occurred at this temperature. The linear DWF model predicts Θ_D = 230 $\pm$ 60 K, which is lower than that found in specific heat measurements. This is due to the Debye model of x-ray intensity only considering acoustic phonons in monatomic systems [197], so called Θ_M. By accounting for the crystal structure and chemical species of FeRh, we predict an adjusted Θ_D = 330 $\pm$ 80 K, which agrees with *ab initio* predictions for the FM phase of 300 K [109].

Using the extracted value of χ_D, the lattice temperature as a function of probe delay can be estimated. As we consider a different $\vec{q}$ in Section 6.2, the pre-factor is changed to account for the different lattice spacing in the dynamic experiments. The resulting plots of lattice temperature vs pump-probe delay are presented in Fig. 6.6b showing how the lattice is expected to achieve temperatures of up to 700 K within 10

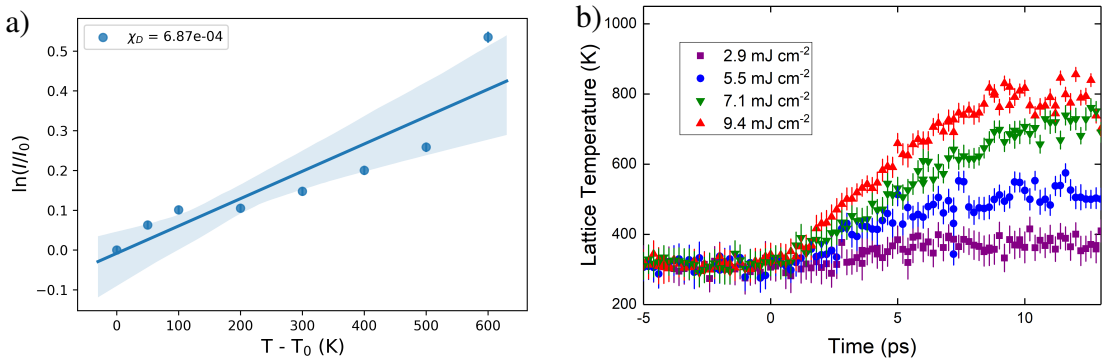

Figure 6.6: a) Extraction of the DWF where peak intensity vs temperature is used to estimate the coherent x-ray scattering. The 95% confidence bands are shown by the shaded region. Error bars (not visible) refer to the uncertainty in the Voigt fitting of the integrated intensity. b) Lattice temperature as a function of pump-probe delay based on the intensity of transient XRD peaks.

ps following laser excitation.

6.3.2 Temperature Dependence of Lattice Dynamics

We performed further scans at different ambient temperatures to demonstrate that the observed behaviour is due to ultrafast sample heating. By reducing the temperature, a given fluence is expected to excite a lesser portion of the sample to the high temperature FM phase. From delay scans taken at 280 K and 260 K shown in Fig. 6.7a, we observe a smaller change in intensity and a reduced shift in the (-101) peak of FeRh. This indicates that a lesser degree of phase transition is instigated in the samples for a fixed laser fluence. This is as expected and verifies that the simple heating model used in Section 6.3.3 to describe the FeRh lattice is valid. At 260 K, we observe almost no transition behaviour. The energy provided at this fluence is not enough to excite the sample to the point of transition. Such a result is useful knowledge when estimating the energy absorbed by the electron system following laser excitation. This assists in the construction of ODE describing the three-temperature model, see Section 6.4. Scans were performed at higher temperatures shown in Fig. 6.7b, where a percentage of the film is already in the FM state. This exhibits slower dynamics than observed at RT. In contrast to the reduced ambient temperature scans, these results correspond to higher fluence scans. The fitted dynamics at 300 K showed that the higher fluence scans result in slower growth dynamics as was also observed for scans taken at the higher ambient temperature.

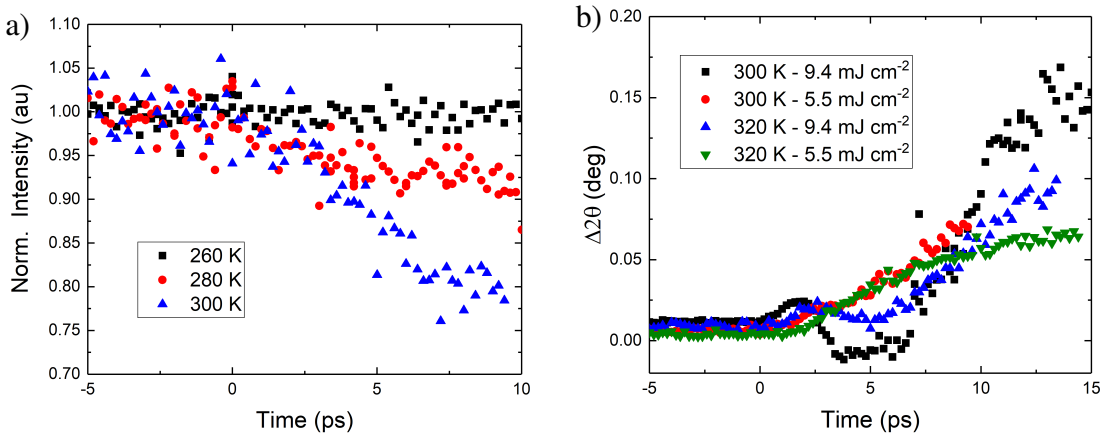

Figure 6.7: a) Intensity as a function of probe delay observed in the (-101) FeRh peak when subject to fluences of 2.9 mJ cm^{-2}. Sample temperature was controlled with a liquid nitrogen cryoblower. b) Peak shift observed in the (-101) FeRh peak when excited across a range of laser fluences and ambient temperatures.

The results of these temperature scans corroborate our assumption that the local heating is in direct proportion to laser fluence. By reducing the temperature, greater fluence is required to instigate the MPT. This is further evidence that the peak shift can be used as a measure of the phase transition progression. The lattice expansion is therefore directly proportional to the relative change in the AF:FM phase ratio [31].

6.3.3 FWHM as a Probe of 1st Order Dynamics

From the results of Section 6.3.2, it is assumed the peak shift is a measure of the FM phase proportion in FeRh. This assumption requires the transition to be first order, having previously been demonstrated by Mariager et al. [31]. However in this experiment, we are unable to resolve the individual peaks associated with the AF (and FM) phases where a_0 = 2.99 (3.02) Å. The reason for this is that the pink beam of the FEL x-rays has sizeable spectral width (Δ E = 40 eV $\approx$ 0.2°), the increased broadening of the peak is such that the two phases are not well separated. There is significant overlap between the shift in 2θ = 0.4° for the lattice expansion, and a FWHM of 0.45° when the convolution of the sample, beam, and instrumental broadening are considered. We construct a model to explain the FWHM dynamics seen in Fig.6.8a following laser excitation to confirm that the transition is indeed first order. The percentage of each phase as a function of temperature was estimated from the VSM data. Lattice temperature following excitation was assumed to follow a simple asymptomatic curve. We could

then observe how the FWHM of the (-101) peak evolves by fitting a Gaussian to the sum total of the overlapping AF and FM peaks. By comparing the shape of the FWHM curves from the simulation to experimental results, we demonstrate that the first order assumption is indeed valid, and the above model of the peak shift can be used.

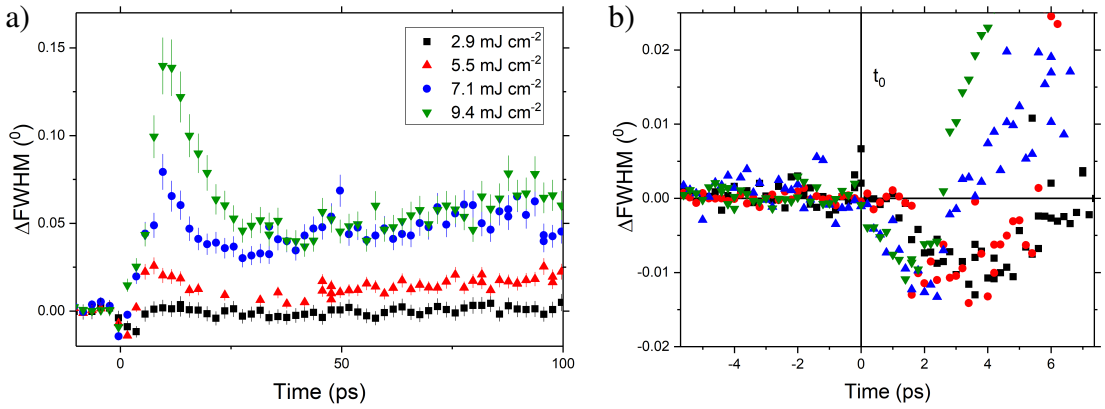

Figure 6.8: a) FWHM of (-101) peak as a function of probe delay for investigated laser fluences. The initial peak points to the greatest mixing of the two phases due to the associated shift in 2θ upon expansion. A longer trend is seen in higher fluences which we ascribe to thermal diffusion in the sample. b) Irrespective of laser fluence, an drop in FWHM is observed over the initial 2-5 ps.

The model relies on providing a COM shift and estimating FWHM using the known parameters of the FeRh MPT following ultrafast lattice heating. Based on the magnetometry results (see Fig. 5.1), we determined the ratio of each phase at a given temperature. The proportion of the FM phase vs temperature follows an error function profile with centre, T_T, and width, ΔT. This profile is based on previous experiments in the literature which have shown that the transition is first order with a linear distribution of transition temperatures [106, 136]. The difference in T_T can be seen on a microscopic scale due to local compositional or strain gradients [136] which average out to a Gaussian distribution across macroscopic thin film samples.

Having found the normal distribution of transition temperatures, we then assume the ratio of peak intensity referring to each phase are in direct proportion to the ratio of the phases. Peaks were modelled as Voigt functions with FWHM taken from the XRD data. Using the x-ray energy of the pink beam available at SACLA (6.408 keV), the diffraction angles are calculated. These angles were converted to pixels based on the sample to detector distance (0.75 m) and the area of the photodetector pixels (200 x 200 μm^2). This shows a spread of photon counts across the pixels as seen in Fig. 6.4. Fitting the AF/FM peak overlap with peak finder software as demonstrated in Fig.

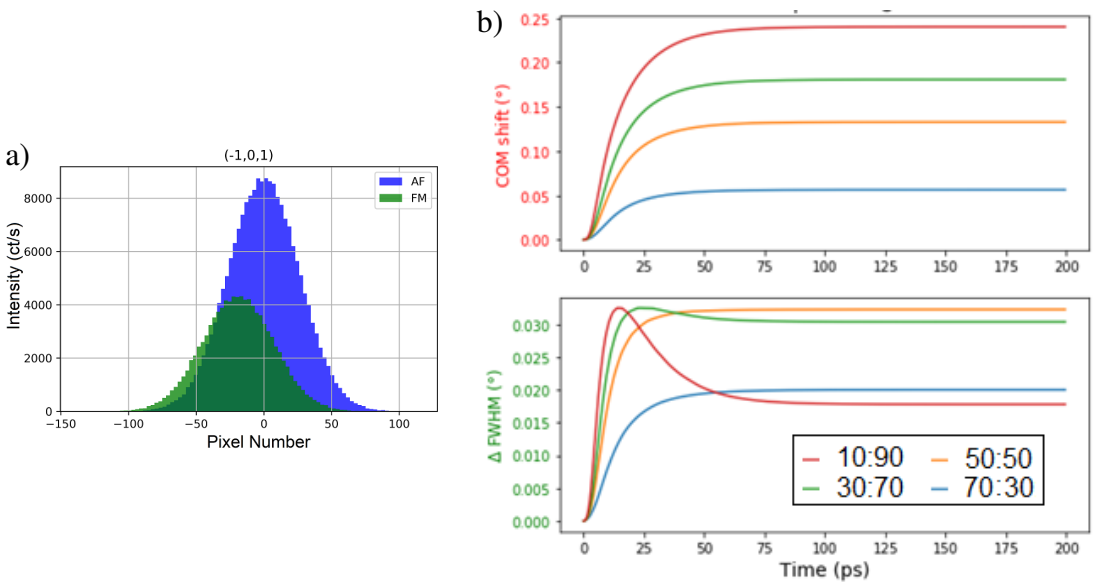

Figure 6.9: a) Simulation of the predicted detector counts from the (-101) peak for the AF and FM phases. Extracted COM and FWHM of the (-101) peak as a function of time for FeRh undergoing first-order dynamics. The peak in the FWHM appears when the sample is sufficiently heated through the transition so that the FM phase becomes dominant. Legend indicates the equilibration AF:FM ratio.

6.9a, we extract COM and FWHM exactly as performed in the experimental data analysis. Using a simple asymptotic heating model with τ_G = 10 ps, we were then able to replicate the long time traces seen in the lattice dynamics. This was plotted for different equilibrium temperatures to show how the fluence can change the FWHM curve shape. This simulation confirms our assumption that the observed transition was first order and the peak shift can be attributed to lattice heating of FeRh. In Fig. 6.9b, the expected FWHM dynamics are shown for different final ratios of the AF:FM phases from 30:70 in stepwise increments to 10:90. This shows how the FWHM is expected to change across a range of different laser fluences until the heating is sufficient to fully induce the FM phase. It is seen how the COM shift is larger for greater laser heating as expected.

In a second order transition, the expansion occurs in a continuum about T_T. This would result in a second peak that shifts in 2θ while intensity increases, whereas the first peak reduces in intensity at a fixed scattering angle. This is modelled by assuming the ratio between the two peaks (AF and FM) changes as function of temperature, with the resulting FWHM shown in Fig.6.10. This is achieved by shifting the FM peak

position as a function of temperature, only reaching the final position once the film has fully transitioned. Such a model exhibit similar peak shift dynamics to that seen in Fig. 6.9b, while the FWHM has a manifestly different shape. The maximum FWHM is not easily resolved and the change in FWHM as a function of time is reduced. Therefore, these simulation results confirm that the lattice follows a first-order transition during isotropic expansion.

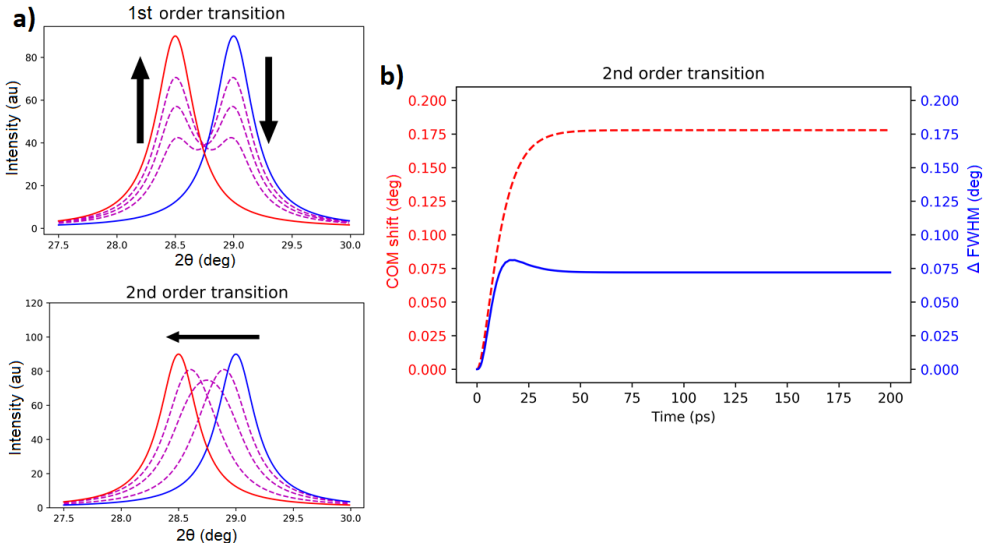

Figure 6.10: a) First and second order transition schemes with reduced FWHM for clarity. b) Simulation of the expected change in the FWHM of the (-101) peak of FeRh if the transition followed second order dynamics. A reduced peak in the dynamics of the FWHM is observed with a smaller equilibrium FWHM.

However, this model does not capture non-monotonic behaviour of the FWHM that occurs in the first few ps (Fig. 6.8b). In particular, there is a reduction in the FWHM immediately following laser excitation that recovers within 5 ps. For this short-lived period, the sample has a narrower diffraction peak than in the unexcited state. Assuming the transient FWHM behaviour can be attributed purely to the changes of sample structure, this indicates the system becomes more ordered on a sub-ps timescale following laser excitation, which is counterintuitive. In order to understand this observation, the static XRD results shown in Fig. 6.2 offer an explanation. The (002) peak narrows in the temperature range 350-450 K. This is consistent with the release of inhomogeneous strain across the film in the mixed AF/FM phase, where substrate induced strain acts to expand the lattice [131].

6.3.4 Transient State in FeRh Lattice Transition

Further instances of non-monotonic behaviour are the complex peak shift dynamics shown in Fig. 6.5b. The data from the initial 5-10 ps indicates that a lattice contraction is competing with isotropic expansion of the FeRh film. To explain this behaviour, we include another growth-decay term in our model with faster dynamics and opposite sign. This assumes there are two channels through which the electron-lattice coupling occurs with independent growth lifetimes; the usual channel which acts to expand the lattice and a transient mode which acts in opposition. A fit to the peak shift is presented in Fig. 6.11. This transient state is characterised by adding another term to Eq. (6.4) of magnitude, C, with independent τ_G* and τ_R* as follows,

$$\Delta 2\theta(t) = A\left(1 - e^{\frac{-t}{\tau_G}}\right) + B\left(e^{\frac{-t}{\tau_R}}\right) - C\left(1 - e^{\frac{-t}{\tau_{G*}}} + e^{\frac{-t}{\tau_{R*}}}\right). \tag{6.6}$$

This function was fitted to the peak shift. This state disappears within 10-15 ps, which indicates a short relaxation lifetime and by extension, strong coupling. Using Eq. (6.6), the observed peak shift as a function of delay time could be described (see Fig. 6.11). The second panel shows a plot of the estimated contribution of this transient state to the peak shift and demonstrates how this term strongly depends on the laser fluence. This deviation increases in both intensity, C, and lifetime, τ_{R*}, for increasing fluence, indicating an excited state that is more dominant with greater laser heating. The short lifetime of this state does not indicate that this could be a strain wave, as propagation through a 500 nm film would result in a mode with frequency $\approx$ 200 ps, based on the speed of sound in FeRh [31, 95] (ν = 5.1 km s^{-1}). This analysis demonstrates that a transient lattice state with a lifetime, $\tau_{R*} \approx 6$ ps is competing with the expected FeRh isotropic expansion following laser excitation.

Having established the presence of such a transient lattice state, we measured the change in intensity and peak shift of the (-101) peak as a function of laser fluence at a fixed delay of 4 ps (see Fig. 6.12), in order to determine the laser fluence required to excite this state. Contrary to the expectation that there should be an asymptotic peak shift since the full AF $\rightarrow$ FM transition is induced by increased laser heating, we instead observe a change in behaviour for fluences greater than 5 mJ cm^{-2}. Above this fluence, the peak shift starts to decrease rather than reaching an asymptotic value. The extracted intensity of the observed peaks suggests that the sample is significantly heated, which is likely to be beyond the AF $\rightarrow$ FM transition temperature, and approaches the α' (FCC) phase [116, 253].

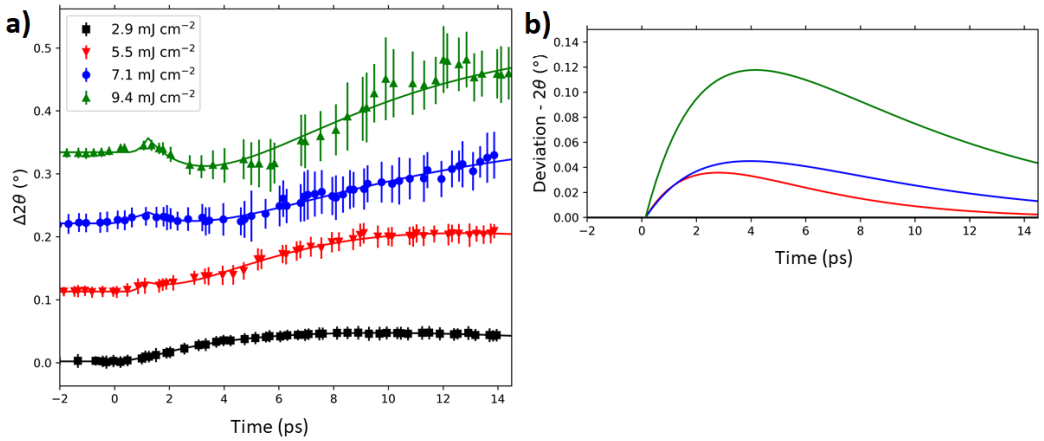

Figure 6.11: a) The shift of the (-101) FeRh peak as a function of probe delay. Data is offset vertically for clarity. Error bars represent the standard deviation of the intensity of the individual measurements when binned according to a jitter correction procedure. Eq. (6.6) was fitted to the data shown by the full lines. b) The transient term that acts to contract the lattice is plotted using the parameters obtained from fitting the data. This shows that higher laser fluences result in a stronger and longer-lived transient state with $\tau_G^* \approx 3$ ps and $\tau_R^* \approx 6$ ps.

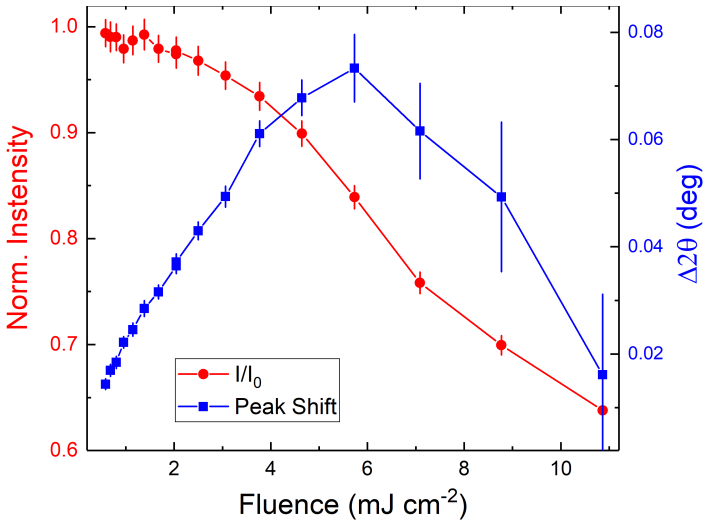

Figure 6.12: Peak shift and change in intensity of (-101) FeRh Bragg peak as a function of laser fluence, at a fixed time delay of 4 ps. The increasing pump fluence causes a steady decrease in intensity. The reduction in peak shift > 5 mJ cm^{-2} is assumed to be due to the induced transient state.

The competing expansion-contraction model described here will also be instructive in the future investigation of AF order of FeRh. The comparison between lattice dynamics and evolution of AF order following local heating can be used to examine the exact mechanism of the MPT. Further modulation of the phonon bands at high laser fluence to an 'overheated' state must be considered. The spin canting model offers one possible explanation which speculates how the ordering of the spins may evolve [21, 254]. The ultrafast timescales over which this is predicted to occur will require careful consideration of the laser fluence and dynamics of the charge Bragg peaks when interpreting the data.

6.4 Energy-Dependant Phonon Coupling

The non-monotonic behaviour shown in Fig. 6.11 provides motivation for construction of a more accurate model to describe the structural dynamics. The three-temperature model [84] presented in Chapter 2 is suitable only to describe the dynamics of the Bragg peak intensities, providing an estimate of the overall coupling strength, $G_{E\text{-}L}$, between the electron and phonon systems [255, 256].

Above a laser fluence of 5 mJ cm^{-2}, dynamics diverge from those predicted using a collective coupling model. This divergence may be captured by including a transient phonon state in the three-temperature model in the form of an intermediate lattice coupling. This additional term is described in the review article of Johnson et al. [3] as a 4th temperature which provides a competing pathway for relaxation to the equilibrium state [145, 257]. The transient lattice state with faster growth dynamics (τ_G*) is assumed to be related to a 'hot phonon' channel [256] that is heated more efficiently than the lattice as a whole. By adapting the three-temperature model, we can infer the lifetime of such a hot phonon state as a function of fluence. This assumption requires the availability of optical phonon modes which couple more strongly to electrons than anharmonic acoustic phonons [3, 255]. It is assumed such modes are readily excited by the electronic system due to the e-field produced from the out-of-phase vibrations. A recent TR-photoemission study proposed changes in the electronic structure occur via charge transfer from Fe to Rh [34], implying the electronic structure is highly correlated with lattice vibrations of Fe-Rh modes. This would indicate strong coupling between the electronic system and such optical phonons. Examples of optical phonon branches along the [110] direction of FeRh have been explored in detailed *ab initio*

and spin-polarised calculations using DFT [118, 119] which assist in constructing the model. Modelling the relaxation dynamics of the film according to the hot phonon model of Mansart et al. [145] allows a theoretical estimate of the lattice temperature to be obtained, which is compared to the transient temperatures presented in Fig. 6.6a.

6.4.1 Simple Electron-phonon Coupling

To model this behaviour, an ODE solver described by phenomenological theory [84] is applied to the FeRh system. To simplify, phonon-spin coupling in not considered over such timescales [3]; we focus solely on the electron-phonon coupling. Previous MOKE experiments have shown that the spin re-orientation occurs on a timescale of hundreds of ps [117], and is therefore a minor contributor over the timescales of interest. The kinetics of electron-phonon coupling following rapid electron heating, $Q(t)$, are described by [85],

$$\frac{d[T_{el}]}{dt} = Q(t) - \frac{\gamma(T_{el} - T_l)}{C_{el}(T)}, \tag{6.7}$$

$$\frac{d[T_l]}{dt} = \frac{\gamma(T_{el} - T_l)}{C_l(T)}, \tag{6.8}$$

where γ describes the electron-phonon coupling, C is the heat capacity, and the subscripts 'el' and 'l' refer to the electronic and lattice systems respectively. These equations were numerically solved by the ODE solver provided by the Python library, SciPy with 0.1 fs timesteps [258]. The value for γ is estimated from the inverse of the growth lifetime, τ_G, and the thermal properties of FeRh [183], set as 3.20x10^{17} J m^{-3} s^{-1}. The laser-induced sample heating is directly attributed to non-reflected photons. Using previously determined refractive index and experimentally obtained reflectivity data [121, 259], the skin depth, δ_p, and reflectance of 800 nm photons are calculate to determine the excited volume. These values were estimated as δ_p = 31 nm, and R = 0.7. The fluence then allows the energy introduced per unit volume to be calculated. As heating occurs almost instantaneously, the RT heat capacity is used to model the coupling; this yields a constant τ_G throughout the transition as was assumed in the fitting of experimental data, Eq. (6.4). The resulting evolution of the electron and lattice temperatures are shown in Fig. 6.13, which conforms to lattice dynamics observed in the lowest fluence case, see Fig. 6.5b.

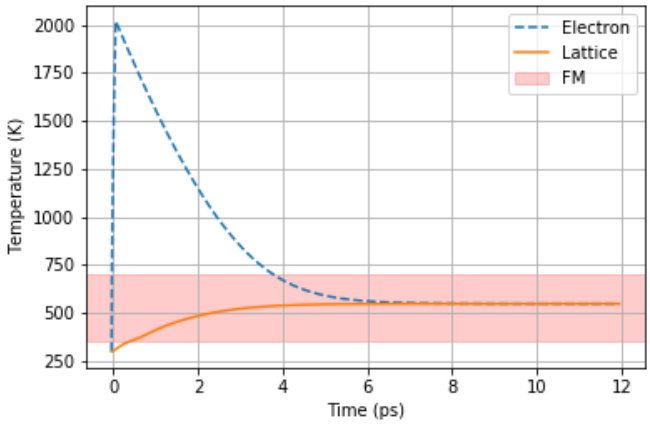

Figure 6.13: Results of the solved ODE for the simple electron-phonon coupling model. The electron system is immediately heated before energy is transferred to the lattice system over ps timescales.

6.4.2 Inclusion of the Hot Phonon Transient State

In order to model the highly excited system we adapted the equations to include the transient state by allowing the electronic system to relax via two channels [257]. This allows for growth lifetime of the excited state, τ_G*, to be included in the analysis. The system is described with the following ODE [145],

$$2 \cdot \frac{d[T_{el}]}{dt} = \frac{2(1-R)}{\delta_p} \cdot \frac{I(t)}{C_{el}(T)} - \frac{\gamma^*(T_{el} - T_{l*})}{C_{el}(T)}, \tag{6.9}$$

$$\alpha \cdot \frac{d[T_{l*}]}{dt} = \frac{\gamma^*(T_{el} - T_{l*})}{C_{l*}(T)} - \frac{\gamma^1(T_{l*} - T_l)}{C_{l*}(T)}, \tag{6.10}$$

$$(1-\alpha) \cdot \frac{d[T_l]}{dt} = \frac{\gamma^1(T_{l*} - T_l)}{C_{l*}(T)}, \tag{6.11}$$

where '*' refers to the transient lattice state. α refers to the relative occupation of the hot phonon bands in terms of the entire phonon system. The coupling between excited and equilibrium states is governed by γ^1. These can be estimated from the lifetime as above but due to the two-step mechanism, the following relation is used [89];

$$\gamma^T = \frac{\gamma^1 \gamma^*}{\gamma^1 + \gamma^*}. \tag{6.12}$$

This results in the effective coupling constant, γ^T, the total electron-phonon energy transfer term, described by τ_G in Eq. (6.6). We assume the excited state coupling is stronger than general electron-phonon coupling [255]. Using previously published

data from calorimetric measurements on FeRh, we can estimate the heat capacity of the electron and phonon systems of FeRh [35, 93, 183], shown in Fig. 6.14a. The latent heat of the transition is captured as a Gaussian function about 355 K, with a value of 2.2 kJ kg^{-1} [183, 260]. The non-equilibrium coupling between the electron and phonon systems has been exhaustively explored for metals but shows little variation over the temperature range [261], meaning a fixed value can be used.

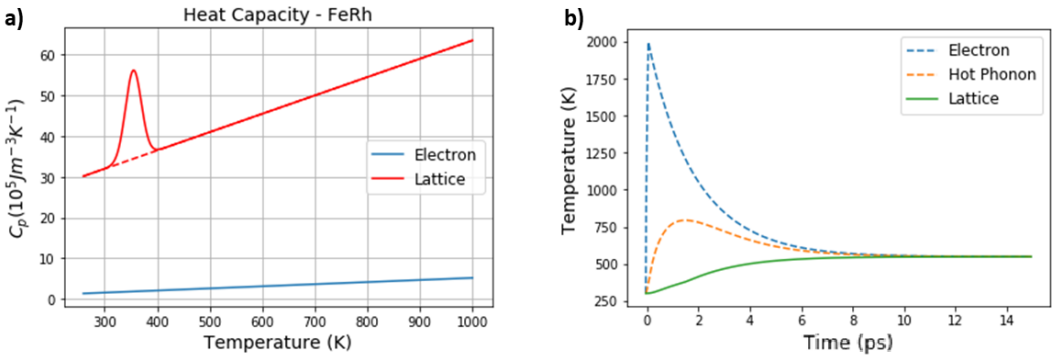

Figure 6.14: a) Heat capacity of the FeRh electronic and lattice systems found using thermodynamic data from the literature [93, 183, 260]. The latent heat of the transition is captured as a Gaussian peak in C_L about T_T. The electronic heat capacity is linear across this temperature range. b) The temperature of each subsystem as a function of time is presented following 7 mJ cm^{-2} laser excitation. The equilibrated state is reached within 10 ps.

Next the behaviour of the systems is solved using the above equations. This allows for estimation of the transient state dynamics in comparison to the overall lattice as shown in Fig. 6.14b. The effect of changing the ratio of highly coupled phonon modes is shown in Fig. 6.15. This demonstrates how the behaviour reverts to the simple case of electron-phonon coupling as $\alpha \rightarrow 1$.

The model presented in Fig. 6.16 incorporated a 15% fraction of efficiently coupled phonon modes, based on the Vibrational Density Of States (VDOS) found from nuclear resonant inelastic x-ray scattering [118] along these phonon branches in the AF phase. Coupling parameters were estimated from the inverse of the growth lifetimes derived from data shown in Fig. 6.11 as before. The thermal properties of FeRh were found from calorimetric data in the literature [93, 183, 260]. Fluence is changed by increasing the intensity of the electron heating. It was assumed that the FM phase occurs between 355 and 700 K based on VSM measurements, while the α'(FCC) phase associated with PM exists above 700 K based on a stoichiometric ratio of $Fe_{50}Rh_{50}$ [104] and the

quasi-static XRD measurements shown in Fig. 6.2.

To model the experimental results of Section 6.3, the following parameters were used; laser fluences correspond to those used for the dynamics measurement of Section 6.3 (2.9, 5.5, 7.1, 9.4 mJ cm^{-2}) and γ^* = 6.0x10^{17} J m^{-3} s^{-1}. We observe in Fig. 6.16, how the hot phonon phase can access the α'(FCC) phonon bands on short timescales using this treatment of optical and acoustic phonons. The dotted lines describe the hot phonons, which act to contract the lattice while decoupled from the acoustic phonons (if the α'(FCC) phase can be accessed); the full lines describe the overall system as it undergoes expansion (AF → FM transition). This α'(FCC) phase correlates with the transient lattice state described above, with a lifetime of less than 10 ps across all laser fluences. This model slightly underestimates the lattice heating at high fluence. It provides estimates of the maximum temperature reached being 425, 537, 600 and 683 K for the discussed fluences. This compares to calculations of the lattice temperature (@ delay = 10 ps) from the TR-XRD data being 384, 520, 683, and 785 K (± 25 K). The deviation over longer timescales is due to heat dissipation processes that occur after the initial excitation. For the highest fluences, the sample continues heating over 100's of ps which corresponds to heat transfer in metals over micron lengthscales [262].

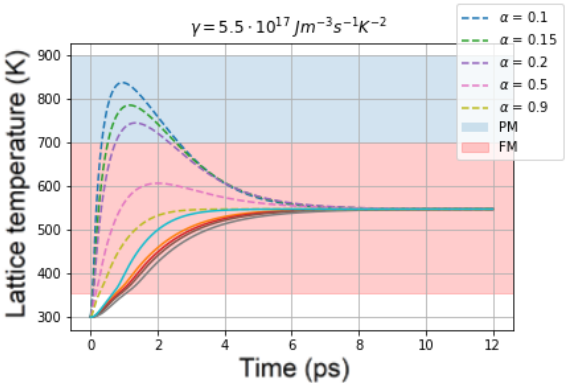

Figure 6.15: The effect of varying the parameters of the hot phonon channel (dashed lines) is shown. As α tends to one, the normal electron-phonon coupling is regained for a fixed coupling strength. The solid line describes simple electron-phonon coupling.

This is further explored by changing the ambient temperature. An example is provided in Fig. 6.17, where the experimental parameters of Fig. 6.7b and 6.7a were implemented in the hot phonon model. It can be seen that lattice dynamics are slower at higher temperatures and fluences as we have previously observed when fitting the transient intensity of the peaks. This can be understood by considering that the the system remains in a non-equilibrated state for longer periods. The transient lattice state is predicted to last for 10-15 ps at at 320 K under high laser fluences. In contrast, the peak shift is diminished for temperatures below RT due to a reduced portion of film entering

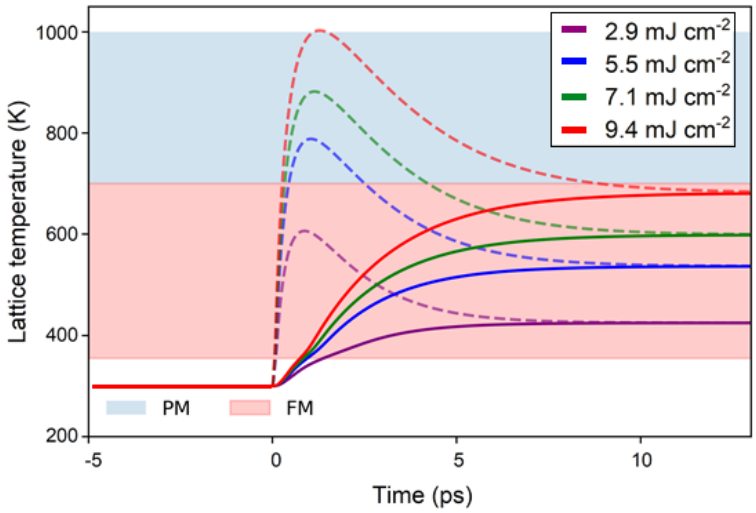

Figure 6.16: Simulated evolution of the lattice temperature using the hot phonon model for the fluences explored in the x-FEL experiments. The dotted line refers to the transient lattice state - presumed to be optical modes- and the full line refers to the average lattice temperature of the entire system.

the FM phase. The model predicts that we should observe a stronger shift in the peaks at 260 K. However, this could be due to poor sample alignment or ice build-up (-13°C) on the surface increasing diffuse scattering. This would reduce the energy absorbed by the sample and explain the lower than expected equilibrium temperature.

In general, this model predicts slightly faster changes of peak intensity and higher equilibrium temperatures than are observed in the experiments, both of which are more pronounced at lower fluences and ambient temperatures. At very high fluences ($>$ 5 mJ cm^{-2}), the model predicts reduced equilibration temperatures. Based entirely on the theoretical properties of FeRh [109] (which is found to posses a range of transition temperatures and widths [92]) and phenomenological models [145], this is a good first approximation. The model appears to be underestimating the latent heat for the AF $\rightarrow$ FM transition. This would explain why the model more closely predicts the behaviour when the full MPT transition is expected to occur ($\approx$ 5 mJ cm^{-2}). This could be improved with more accurate measurements of the heat capacity at high temperatures (above 600 K), and a better understanding of the nature of the transient lattice state (more accurate estimations of α and γ^*).

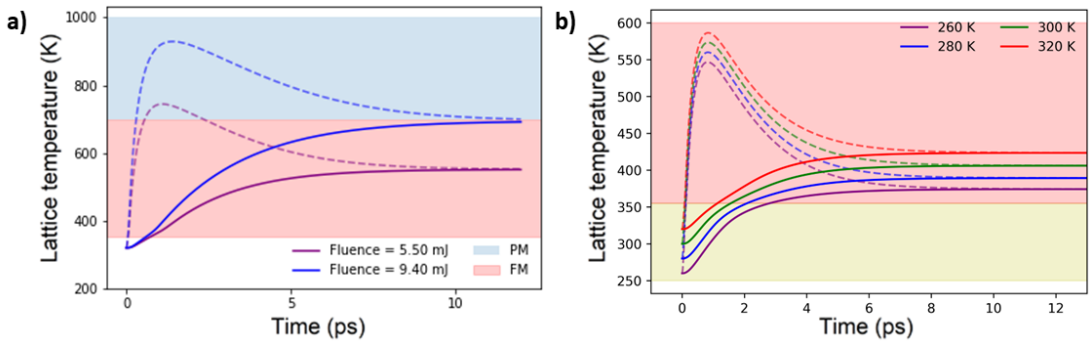

Figure 6.17: The hot phonon model is applied to the FeRh system using different ambient temperatures. The plot of the lattice temperatures as a function of delay is presented for; a) excitation using the fluences from 6.7b with T = 320 K, and b) the effect of changing the temperature from 260 K up to 320 K when the sample is excited by a laser fluence of 2.9 mJ cm^{-2}. The yellow region is the AF phase. Dashed lines again refer to the hot phonon temperatures.

6.5 Sample Damage Due to x-FEL Beam

The magnetic peaks (as shown in the preceding chapter) could not be observed as a result of reduced photon fluxes during this beamtime (estimated as a factor of 100 reduction from the image of the direct beam). In addition to the reduced brilliance, the unattenuated x-ray beam is observed to cause sample destruction. When the sample is examined in a Scanning Electron Microscope (SEM) [263] following unattenuated x-FEL exposure, significant surface damage is observed. SEM images of FeRh sample following the SACLA beamtime are presented in Fig. 6.18, imaged using a Zeiss Supra VP55 high resolution field emission SEM system of the Paul Scherrer Institut. This suggests that the combination of laser and x-ray pulses ablated 500 nm of FeRh over the course of several hours. This is an important consideration for thin film samples in all future x-FEL experiments.

The long streaks seen in Fig. 6.18 indicate the x-FEL source is responsible, with a shallower angle of approach compared to the optical laser. In contrast, the pump beam had a much larger footprint of 500 x 500 μm. The severe damage is most easily seen in the marked 101 μm region - as a result of checking sample position when the damage was first observed to occur. The plurality of damaged areas seen in Fig 6.18a are due to initial explorations of the sample damage threshold. The data presented in the previous sections was performed on another portion of the film which was subject to an x-ray

flux significantly lower than the damage threshold.

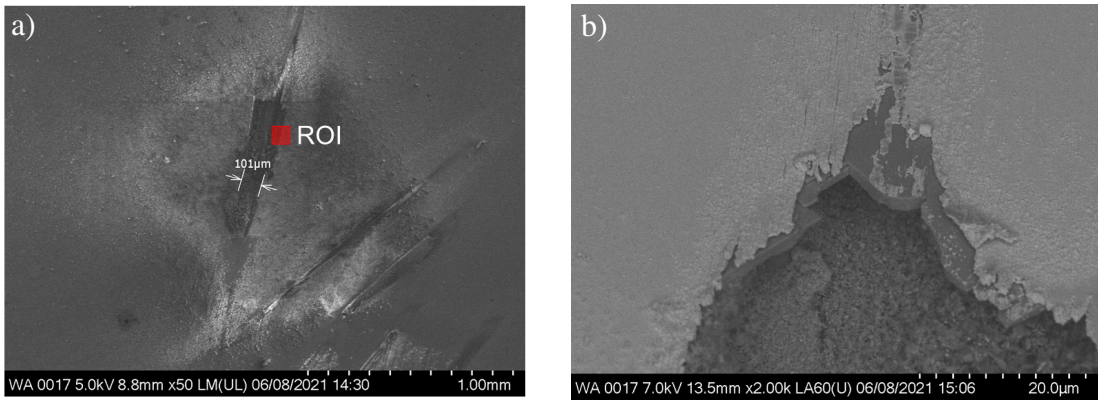

Figure 6.18: a) SEM image of the sample following x-FEL measurements. The dark region was exposed to the unattenuated x-ray beam. b) We observe that the film was completely ablated and some of the MgO substrate was also seen to be removed. The light grey region contained Fe and Rh traces which were not seen in the dark grey areas.

In Fig. 6.18, the marked ROI was investigated with an element sensitive probe of the SEM, Energy-Dispersive x-ray Spectroscopy (EDS). The EDS images in Fig. 6.19 demonstrate how film is stripped away exposing the MgO substrate. These images are found by filtering scattered electrons by energy and comparing to known elemental edges [263]. For the substrate, these are the K-α edges of Mg and O. The L edge of Fe, and M edge of Rh were used to probe the deposited film. There were trace amounts of Al, C and Pt in the EDS signal, but these are not shown here as they constituted less than 1% percent of the total signal. These traces are assumed to arise from adsorbed hydrocarbons and the Pt cap on the film. The left-hand region of Fig. 6.19a was exposed to x-FEL radiation whereas as the right-hand region lay outside the most intense portions of the x-FEL beam. The Fe and Rh contributions in the exposed portion are significantly smaller, where Mg and O dominate. It is definitively seen how beam exposure causes sample ablation. We propose that by attenuating the beam and especially using a monochromator for the 'pink beam' in future x-FEL experiments, the observed damage may not be as severe.

The reduced count rates due to the x-FEL beam damage are compounded by the overall weaker than expected intensities of the Bragg peaks. Rocking curves of these peaks show the total number of scattered photons per shot was 10^6 at these angles. Considering the magnetic scattering efficiency of FeRh based on the photon-spin interaction, this would result in less than 10^{-1} photons [222, 239]. Factoring in the

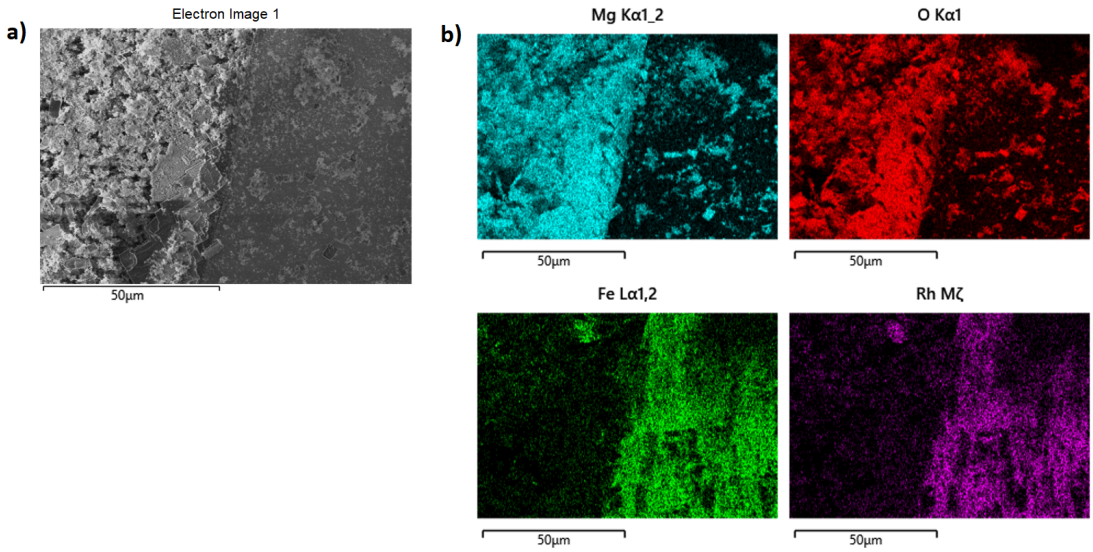

Figure 6.19: a) SEM image of the scanned region (marked ROI, Fig. 6.18). b) EDS data showing the Mg, O, Fe, and Rh signals from the same region of damaged FeRh film. It is seen how the MgO and FeRh are localised in different areas of the image. The laser ablation completely removes the thin film and shows the bare substrate.

attenuation of the x-FEL beam, we could expect less than 100 photons per shot scattered at such angles. In cases such as this, a detector that can measure single photons is required. Photons absorbed by the MPCCD detector have long drift path and contain split patterns over several pixels, making single photon counting more difficult [251]. The threshold required for each pixel is quite close to the background noise. As the x-FEL operates in a shot mode as opposed to a continuous beam [185, 235], the runtime of scans must be increased significantly. This is especially applicable for x-FEL investigations of minor x-ray events, such as x-ray nonlinear optic studies or x-ray photon-correlation spectroscopy. Increased repetition rates (up to 1 MHz [143]) at other x-FEL sources may also prove useful.

Conclusions

The sub-ps capabilities of the SACLA x-FEL have allowed for the investigation into ultrafast behaviour of the FeRh lattice following laser excitation. The lattice dynamics of the FeRh volumetric expansion are shown to be non-trivial across all fluences of laser excitation. Indeed, the system shows non-trivial dynamics at high fluences which heat the sample significantly beyond the AF-FM transition temperature. This was compared to the quasi-static behaviour of the Bragg peaks measured using conventional heated XRD. The intensity and 2θ position of these peaks could be used to describe the lattice temperature and expansion as a function of pump-probe delay with a temporal resolution not previously reported. This resulted in a perturbation to the expected dynamics at high laser fluence where the lattice contracts before finally expanding as initially predicted. While the exact mechanism of this state cannot be commented on, it is demonstrated that a four-temperature model based on previous investigations on structural dynamics using a transient lattice state maps the observed behaviour. Such a model suggests that the system relaxes through a subset of the optical phonon bands which are highly coupled to the electronic system. These results provide important evidence for inclusion of the PM phase in analysing the laser-induced MPT of FeRh, and the model developed provides an understanding of the longer dynamics of the electron-spin and lattice-spin coupling in this material.

Chapter 7

Optical Investigation of Magnetisation Dynamics in FeRh Nanostructures

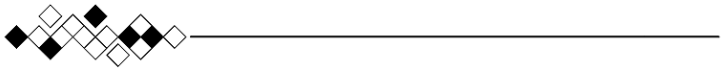

This chapter describes time-resolved optical experiments on FeRh thin films and nano-patterned wire arrays. A delay between the appearance of initial Kerr response and 'FM signal' was observed in all FeRh systems. The field orientation dependence of the Kerr response was investigated with strongest FM signal observed when field is applied along the wires, suggesting that shape anisotropy affects the FM phase stability.

7.1 Motivation

Physical properties at the nanoscale are expected to be different, where emerging dynamic studies can shine new light on feature-edge effects and short-range interactions [28, 264]. Recent experiments have demonstrated that static properties of patterned FeRh samples exhibit different phase transition behaviour to that of thin films, with changes of T_T [29] and asymmetry reported when AF→FM is compared to FM→AF [36] which may pose challenges to the industrial use of FeRh. To this end, magnetisation dynamics across a range of thin films and patterned arrays were studied. The magnetic transitions examined in the following sections are slower than their lattice counterparts described in Chapter 6. Therefore, Finite-Element Modelling (FEM) is sufficient to describe the physical transformations of the system; being applied to the heat dissipation following laser excitation. Micromagnetic interactions are examined by probing the phase transition of nano-patterned arrays in the static regime.

7.1.1 FeRh Thin Films and Nanowire Arrays

FeRh thin films (nominally 30 nm) were deposited using dc-magnetron sputtering as described in Chapter 4 and were characterised using the standard techniques of XRD, VSM and XRR [20]. The films were determined to be 29.4 ($\pm$ 0.6) nm thick, possessing the required B2 ordering, and exhibited the expected magnetic transition upon heating [14] (see Fig. 7.1). The measured T_T = 353 K was found to have a transition width of 25 K. The Pt capping layer was of thickness 1.1 ($\pm$0.5) nm.

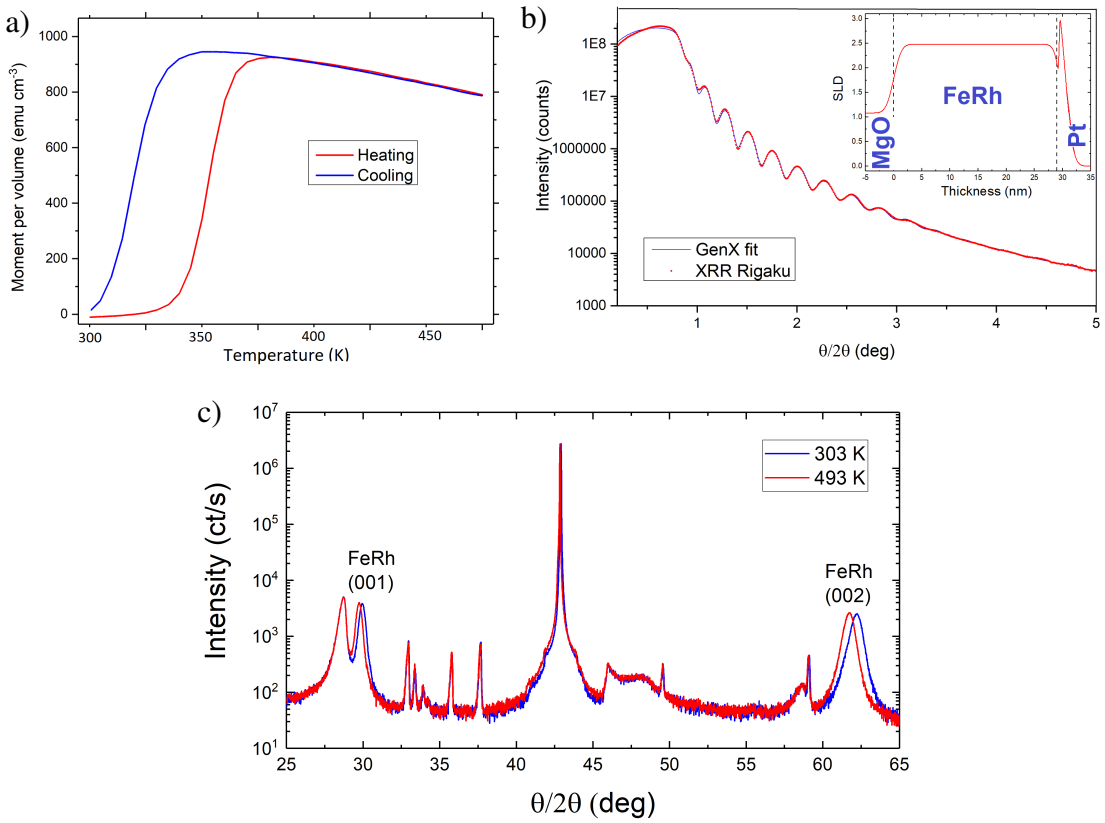

Figure 7.1: a) Transition behaviour of FeRh sample was confirmed by VSM to yield T_T = 353 K. b) The thickness was 30 nm as determined from XRR, with inset SLD. c) The (001) and (002) XRD peaks of FeRh confirm the B2 is achieved. The lattice expansion upon transition is confirmed by the shift to lower scattering angles.

Nanowires were patterned from the deposited films using the top-down lithography techniques described in Chapter 4 to produce the chip pattern illustrated in Fig. 7.2a. An example of the resulting nano-structures as imaged by an optical microscope is shown in Fig. 7.2b. A wire array of widths 2.5 μm was then inspected using atomic force microscopy. Line scans across the wire width in Fig. 7.2c show that consistent patterning has been achieved with sharp features. The full set of patterned wire arrays

are available in Table 7.1, where the thickness is assumed to be that of the film (30 nm). In order to ensure an equivalent pumped surface area across samples during optical experiments, the number of wires in each array was scaled inversely to width. The widest wires (2.5 μm) were in an array of 10, while the 0.5 μm wires were in an array of 50. This ensures equivalent surface area across the arrays in order to maximise the reflectivity and extracted Kerr signal. Wires were spaced equally far apart to minimise dipole interactions and were of length 150 μm.

Table 7.1: Full list of the nanowire samples, differentiated by width. The techniques that were used to investigate each wire array are indicated in the table.

Array	Width (μm)	No. wires	MOKE	COMSOL	4-point probe
i)	2.5	10	✓	✓	-
ii)	1.0	25	✓	✓	✓
iii)	0.8	32	✓	-	-
iv)	0.5	50	✓	✓	✓
v)	0.3	84	✓	-	-

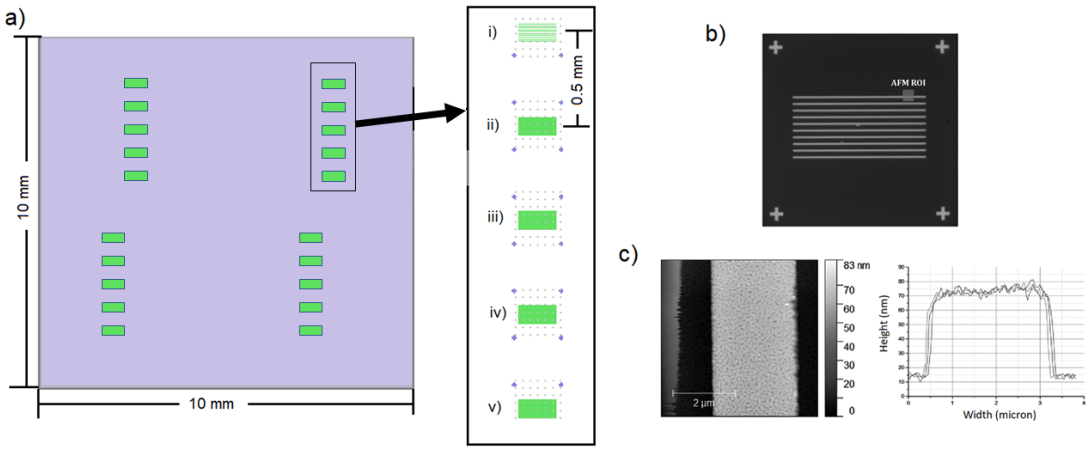

Figure 7.2: a) Illustration of a patterned FeRh sample with inset showing the explored wire arrays on the chip surface, i-v) ranging from 10 x 2.5 μm wires down to 80 x 0.3 μm wires. b) Optical image of array, i composed of 2.5 μm wide wires. c) AFM of the surface and line traces are provided for the marked ROI. This demonstrates the consistency of lithography procedure across the sample.

Table 7.1 further describes the set of experiments to which each wire array was subject. The wires were first investigated using TR-MOKE to quantify the rate of

surface magnetisation evolution. Next, simulations were carried out on a subset of the nanowires arrays. The dimensions chosen for these simulations span the range of sizes which showed the greatest divergence in dynamic behaviour. Finally, select arrays were characterised using electrical measurements. The wire arrays that were characterised matched most closely the dimensions of individual wires investigated by Uhlíř et al. [36] using similar electrical experiments. FeRh thin films were investigated using all techniques described in this chapter.

7.2 Resonant Enhancement of Kerr Signal

The lithography process inevitably reduces sample reflectivity as a consequence of less material being available, meaning enhancement of Kerr response is desirable. This has been approached previously by considering the interaction between polarised light and surface magnetisation [265, 266]. The optical properties of solids are a well-understood topic offering a wealth of methods to change dielectric properties at interfaces [122]. This is important in the field of magneto-optic recording as a means of increasing optical responses from ever smaller features. By changing interfacial properties through deposited dielectric layers [267, 268], Kerr signal can be increased by adapting the refractive index. This is investigated with regard to metallic films probed by visible and near-IR light.

7.2.1 Dielectric Layer - Non-resonant

To test the effect of changing the refractive index at the magnetic interface, a permalloy sample with a spin-coated PMMA layer was prepared. PMMA-495 (2%) was spun on the surface at 1000 rpm for 60 s. The variation in thickness across the sample is expected to suppress interference effects. The Kerr signal, Θ_k, at a dielectric||magnetic interface can be shown to vary as [169],

$$\Theta_k \propto \frac{1}{n_0^2 - n_1^2}, \tag{7.1}$$

where n_0 is the refractive index at the interface (air or dielectric layer), and n_1 is the sample refractive index. The refractive index of PMMA is 1.49 times that of air [269] predicting an increase in signal off 1.25 given the optical properties of NiFe @ 660 nm ($\tilde{n}$ = 2.6824 + 4.0857i [270]). This was seen to increase the Kerr signal (see Fig.

7.3a) with no change in bulk magnetic properties. This was confirmed with the SQUID where bulk magnetisation was unchanged, see Fig. 7.3b.

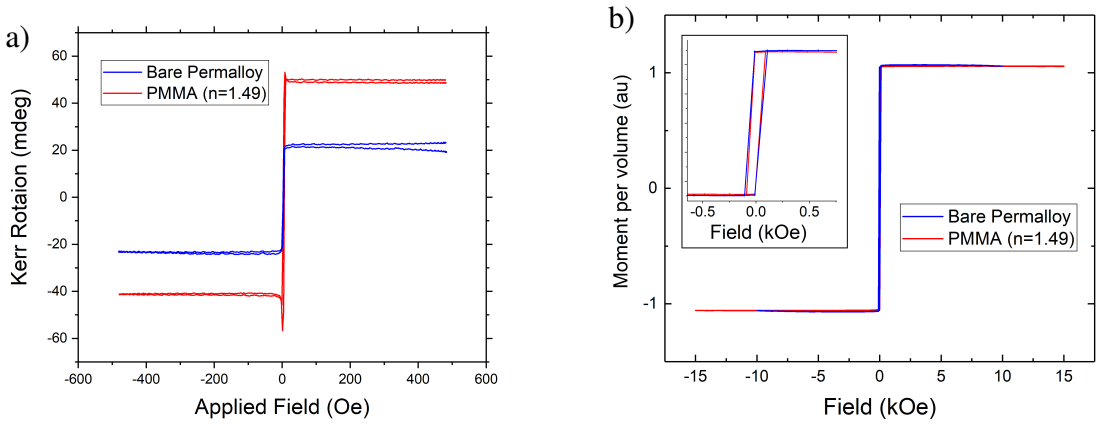

Figure 7.3: a) Comparison of the Kerr rotation with and without a PMMA layer as measured with a NanoMOKE system at 660 nm. b) Saturation magnetisation of permalloy sample with and without PMMA layer.

7.2.2 Effect of Dielectric Layer - Resonant Enhancement

Further enhancement of the Kerr signal is achieved when the dielectric layer acts as a resonant cavity [268, 271], shown in Fig.7.4. As a periodic effect, this occurs at multiple thicknesses of the dielectric layers. The first resonant peak is chosen so as to minimise signal losses arising from absorption within the dielectric layer.

The following theory is an extension of the work by Riahi et. al.[271], where the dielectric is chosen to be SiO_2. Transmission and reflection of light at each interface is described using the Fresnel equations (see Section 4.6.2) [122]. Total reflectance, R, will be the sum of reflections from the dielectric layer;

$$R = r_{01} + t_{01} r_{12} t_{10} e^{itz} + ..., \tag{7.2}$$

where r refers to the reflection at each interface and t is the transmission. The subscript refers to the index of the reflections i.e. 0 - free space, 1 - air||dielectric interface, etc. Summing to infinity, the reflection as a function of thickness, z, is formulated. This is

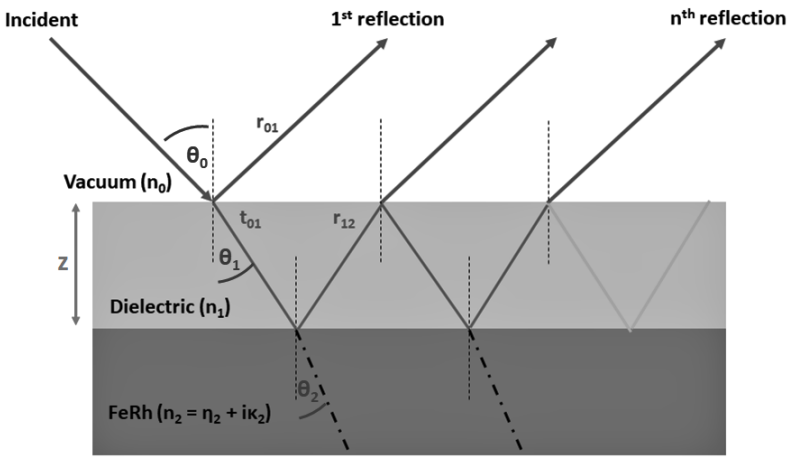

Figure 7.4: Ray diagram of the reflections and refractions within a dielectric cavity of thickness z upon FeRh, adapted from Riahi et al. [271]. The incidence (θ_0) and refraction angles (θ_1, θ_2) of the beam are shown within the respective layers.

converted to the real and imaginary components as follows [271];

$$R(z) = \frac{r_{01} + r_{12} \cdot e^{itz}}{1 + r_{01} r_{12} \cdot e^{itz}}, \tag{7.3}$$

$$\Theta_p(z) = -\frac{iQ(r_{01}^2 - 1)(1 + r_{12})t_{21} \cdot e^{itz}}{4(r_{01} + r_{21} \cdot e^{itz})(1 + r_{01} r_{12} \cdot e^{itz})}, \tag{7.4}$$

where $r_{01} = \frac{1}{4} \cdot (1 - n_1)/(1 + n_1)$, and $r_{12} = \frac{1}{4} \cdot (n_1 - n_2)/(n_1 + n_2)$ are the coefficients of reflection at the air$||$$SiO_2$ interface and at the $SiO_2||$FeRh interface respectively. Q is the magneto-optical constant from Section 4.4.1. In the paper of Riahi et al., the real components are synonymous with the rotation of Kerr signal, and the imaginary with ellipticity. This allows for the expected enhancement of the signal as a function of dielectric thickness to be calculated. The first resonant peaks of the real and imaginary components are shown in Fig. 7.5a & 7.5b.

The above theory describes enhancement of the polar Kerr signal. For soft FM thin films, in-plane moment is investigated via longitudinal Kerr signal as described in Section 4.4.1. For application to the FeRh samples, the derivation is therefore adjusted to consider the longitudinal geometry. Based on the paper of You et. al. [170] and the Snell law of reflection, s-polarised light has the following dependence on the angle, θ_1,

$$f(\theta_0) = \frac{\cos\theta_1 \cdot (m_z - m_y \cdot \tan\theta_1)}{\cos(\theta_1 - \theta_2)}, \quad \text{where } \theta_1 = \sin^{-1}\left(\frac{n_0}{n_1}\sin\theta_0\right). \tag{7.5}$$

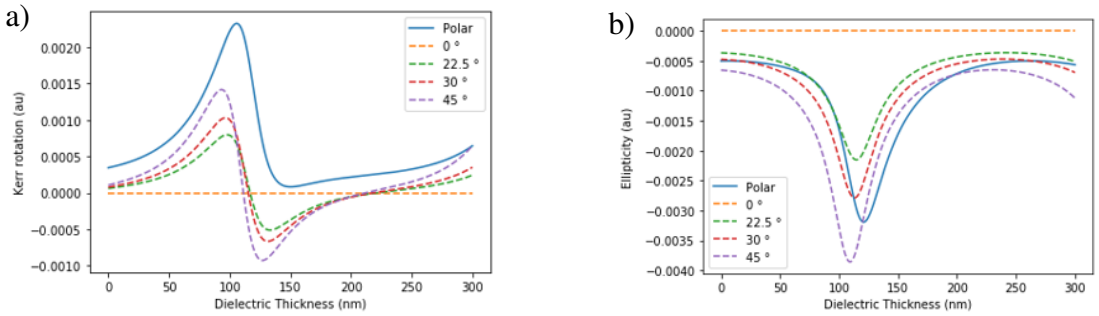

Figure 7.5: Calculated a) rotation and b) ellipticity components of the longitudinal Kerr signal as a function of dielectric thickness. The refractive indices used correspond to SiN_x on FeRh probed by 1030 nm light. The full line refers to the polar signal as described by the theory of Riahi et al. [271].

The path length, z_l, is changed to consider refraction through the dielectric layer;

$$z_l = \frac{z}{\cos\theta_1}. \tag{7.6}$$

By assuming the first reflection has no magnetic character, being the air$||SiO_2$ interface, angular dependence is not considered in the infinite sum and the longitudinal enhancement, Θ_l, is written in terms of Eq. (7.4) & (7.5);

$$\Theta_l(z,\theta_0) = f(\theta_0)\cdot\Theta_p\left(\frac{z}{\cos\theta_1}\right). \tag{7.7}$$

Using Eq. (7.7), it is possible to plot the effect of dielectric thickness on the Kerr signal for a range of angles shown in Fig. 7.5a and 7.5b. The angular dependence of the optimal thickness is understood conceptually by considering the increased path length of the refracted beam.

The resonant cavity model was considered in the case of FeRh to predict a dielectric thickness that will maximise Kerr signal. The optical properties of FeRh and SiO_2 [259, 272] were input to Eq. (7.7), resulting in the thickness dependence seen in Fig. 7.6. Given an angle $\approx 45°$, 90-95 nm of SiO_x will maximise Kerr signal at a wavelength of 660 nm (NanoMOKE laser). Care is taken to not exceed the optimal value of z when depositing films, due to the steep reduction in enhancement with increasing thickness.

Expanding on the results of Section 7.2.1, the resonant effect was investigated by depositing SiO_2 dielectric layers on magnetic samples. This was applied to the material

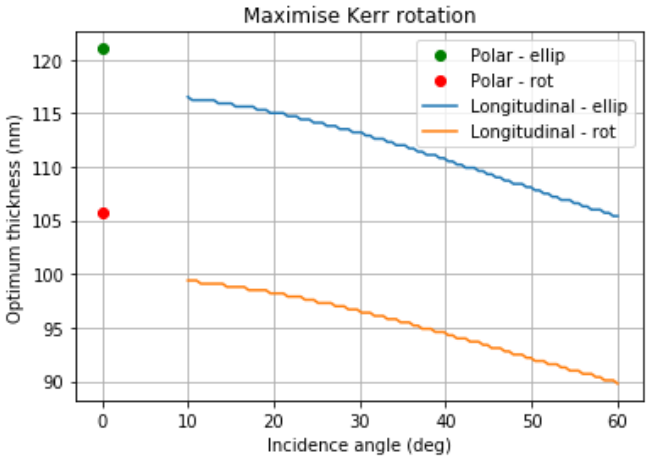

Figure 7.6: Optimal thickness to enhance Kerr rotation as a function of incidence angle @ 660 nm. Enhancement of the Kerr rotation is of interest for the pump-probe laser.

of interest throughout this thesis, FeRh. A sample that is FM at RT enables MOKE measurement to be performed under ambient conditions. Accordingly, a lightly Cu-doped FeRh thin film was employed [92, 96]. As a control, an identical SiO_2 layer was deposited on permalloy. Eq. (7.7) predicts an increase in Kerr signal for permalloy with no resonant enhancement. In Fig. 7.7a and 7.7b, Kerr rotation as a function of applied field is presented. It is seen that the dielectric layer increases the Kerr signal in both instances. However, the relative increase is much larger for FeRh. The Kerr signal increased by 280% for FeRh, significantly more than the 50% improvement observed with permalloy. This improvement is attributed to the dielectric layer acting as a resonant cavity as predicted by the above theory.

Finally, we consider how nanoscale patterning can increase the proportion of diffuse reflection. There is a significant increase in incoherent scattering reducing the total Kerr signal. Hence, a patterned permalloy sample was investigated. The pattern used was identical to that described in Table 7.1. The results are presented in Fig. 7.8 and show an increase in Kerr signal when a dielectric layer is deposited. However, it is seen that the enhancement is reduced. This is due to the imperfect edges and redeposition of material around the wires reducing interface quality. It is also seen that the coercivity of permalloy has increased. This is expected due to defects from the physical milling process acting as pinning sites, preventing FM domains from switching [76]. An increased magnetic field strength is required for realignment of the domains. The increased noise evident in Fig. 7.8a (red line) illustrates one drawback of the dielectric layer. The deposited film will decrease overall reflectivity due to absorption

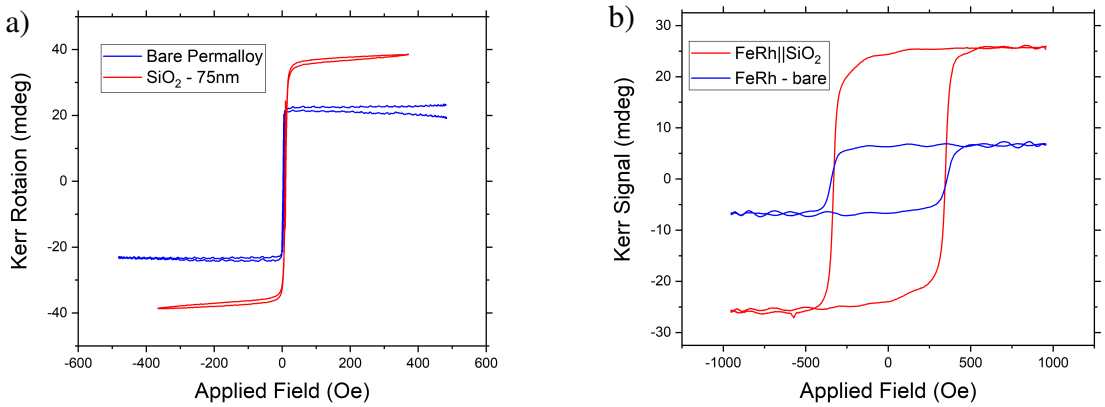

Figure 7.7: Comparison of the Kerr rotation for a) permalloy and b) FeRh with and without the SiO_2 layer. Measured with the NanoMOKE system @ 660 nm. Significant enhancement of the FeRh Kerr signal is attributed to the resonant cavity effect.

and photon diffusion at the surface. If the resonant enhancement of the signal can not be achieved, the signal-to-noise ratio will be no better than that observed for uncoated samples. The choice of dielectric and the method of deposition are therefore key to implementing such enhancement layers.

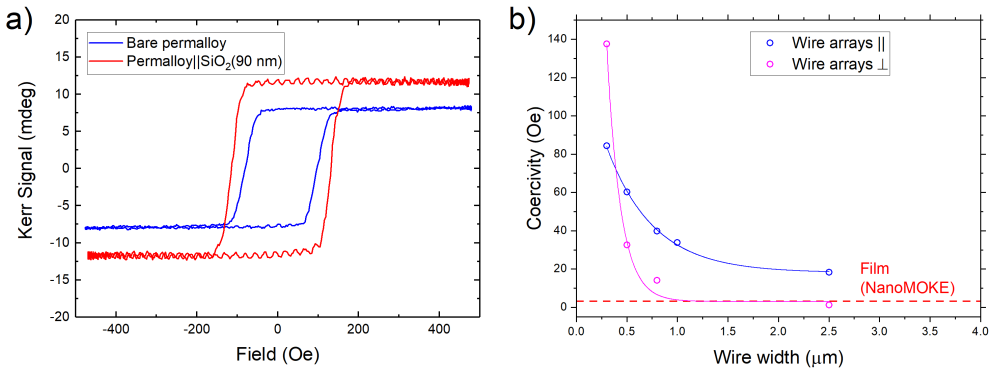

Figure 7.8: a) Comparison of the Kerr rotation for permalloy array of 300 nm wires with and without a dielectric cavity. The increased coercivity (100 Oe) is presumed to be due to pattern-induced domain pinning [76]. b) Observed change in coercivity as extracted from NanoMOKE scans for fields applied $\perp$ or $\parallel$ to the wires.

This investigation provides a foundation for improving weak signals in TR-MOKE experiments. Using the optical properties of FeRh at a probe wavelength 1030 nm [259], the required thickness of dielectric in order to maximise the measured Kerr signal is estimated. To investigate the in-plane moment, the longitudinal Kerr set-up is used where $\theta_i = 45°$. A UNIVEX 450 (Leybold vacuum) thermal evaporation system

was used to deposit SiO_2 films with thicknesses of 110 nm on FeRh samples.

7.3 Time Resolved MOKE Study of FeRh Nanostructures

This section describes experiments which monitor how lateral confinement affects the dynamics of the laser-induced FeRh MPT. The results are compared to identical experiments on FeRh thin films.

7.3.1 Initial TR-MOKE Results

Initial calibration comparing with previous results in the literature [102] focused on the fluence required to induce the transition under saturating fields ($\approx$ 2-300 mT) achieved with a rare-earth based permanent magnet. The reflectivity and Kerr signals were extracted as discussed in Chapter 4 where $\theta_0 = 45°$ (see Fig. 7.4). Reflectivity changes are attributed to the rise in electron temperature on short timescales [122], while the longitudinal Kerr signal is proportional to the surface magnetisation [168].

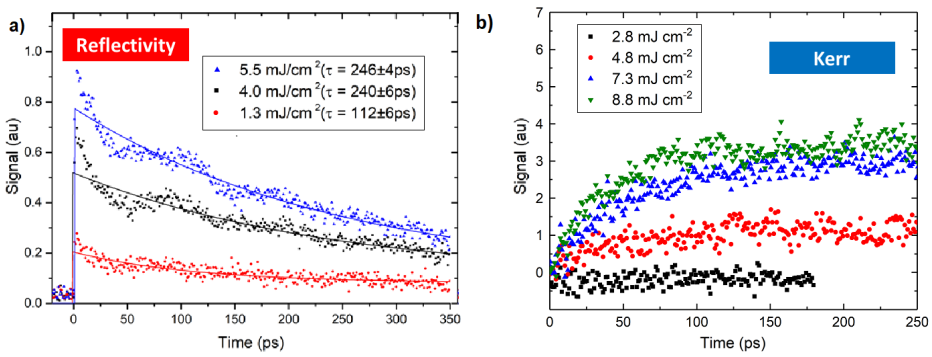

Figure 7.9: a) Reflectivity change and b) Kerr signal vs pump-probe delay for 30 nm FeRh film. A range of fluences were used to excite the sample. Fluences below 2 mJ cm^{-2} induce a response in reflectivity with no observed Kerr signal.

This was performed on thin film samples across a range of fluences and in all instances demonstrated a rapid reflectivity change ($<$ 3 ps) with a slower emergence of Kerr signal (100 ps). This is seen in Fig. 7.9a where the reflectivity increase is observed for all fluences; greater fluences correlate with longer relaxation lifetimes as has already been observed in the TR-XRD data of Chapter 6. This is presumed to be

due to the system being driven further from equilibrium with increasing laser excitation power. However, a measurable Kerr signal is only observed above some fluence threshold. A fluence of < 2 mJ cm^{-2} does not heat the system to 353 K at which the FM phase is stable. The surface magnetisation dynamics of FeRh are described in a number of studies [4, 102, 273], being consistent with the results in this work.

Furthermore, resonant enhancement of Kerr signal in the pump-probe experiments could be achieved. The data in Fig. 7.10 shows the Kerr response. A threefold increase in signal is seen, comparing similar fluences both with and without a deposited SiO_2 layer. However, it was observed that signal degrades over time. As a consequence, scans are either performed with short runtimes, or the laser spot is frequently moved about the sample surface. Microscope inspection confirmed light ablation and/or discolouration of the pumped dielectric surface at fluences which instigate the FeRh MPT.

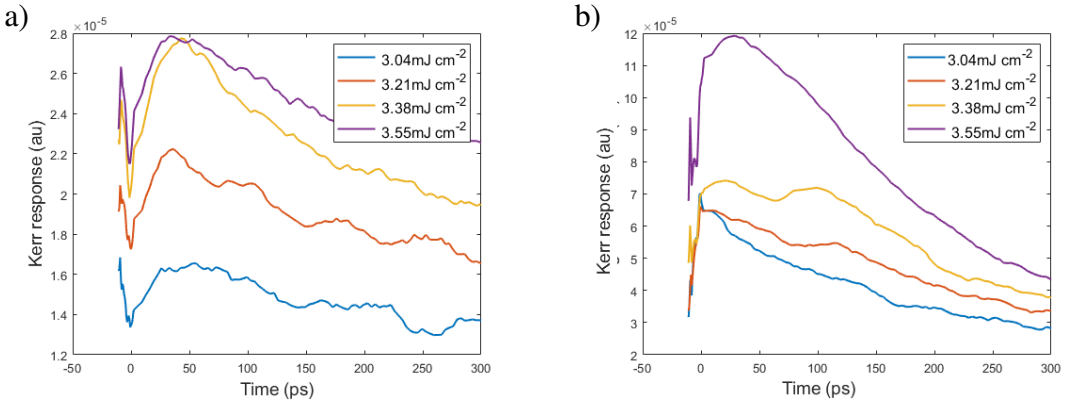

Figure 7.10: a) Transient longitudinal Kerr signal response from a 30 nm FeRh thin film for a range of laser excitation fluences. b) Transient longitudinal Kerr signal from an MgO||FeRh(30 nm)||SiO_2(110 nm). A significant enhancement of the signal is seen with the resonant layer.

7.3.2 Extracting Ferromagnetic Signal from FeRh Thin Films

In order to determine the transient magnetic properties of the FeRh thin films following laser excitation, field sweeps were performed from -110 mT to +110 mT at fixed probe delays as seen in Fig. 7.11. This determines the switching properties of the material following laser excitation [168, 169]. The Kerr response is maximised when the FM domains of the sample are fully saturated along one direction. By sweeping from high positive to high negative applied field, the signal is averaged and the dipolar Kerr

response extracted. Instead of a simple dipolar Kerr signal (difference in Kerr rotation for parallel and anti-parallel applied field), field dependent behaviour is observed.

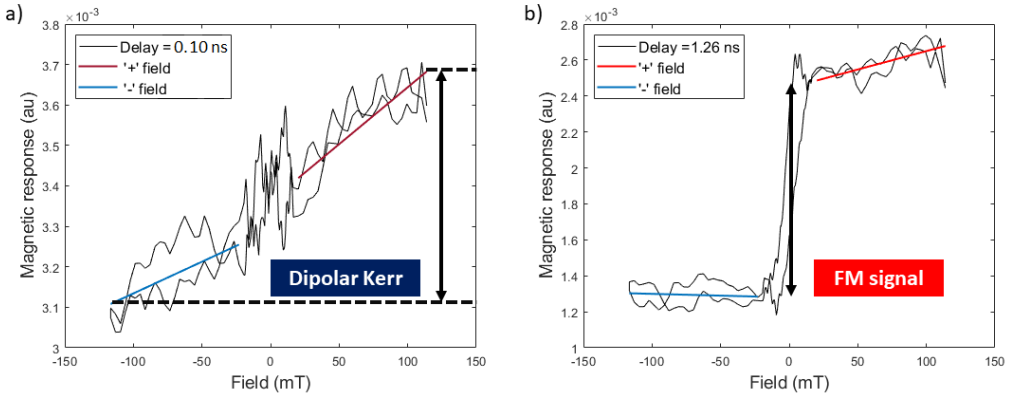

Figure 7.11: The transient longitudinal Kerr response as a function of applied field shown for selected pump-probe delays wherein PM and FM type behaviour could be observed (for fluence = 4.0 mJ cm^{-2}). a) The dipolar Kerr signal begins to appear. No saturation observed after 100 ps. b) The saturation magnetisation is observed with a probe delay of 1.2 ns.

Fig. 7.11a shows the magnetic response during the first 100 ps following excitation of 4.0 mJ cm^{-2}, demonstrating a linear relationship with applied field. There is no evidence of saturation in the signal. In order to extract the dipolar Kerr response, the signals under parallel and anti-parallel fields were fit with straight lines. From this, the dipolar Kerr response (Θ_k[+0.1T] - Θ_k[-0.1T]) can be extracted as a function of delay time. However, at longer probe delays, the field sweeps show a different response. The signal has an opening as seen in Fig. 7.11b suggesting saturation of the magnetic response. In order to extract this saturation, the signal under parallel and anti-parallel fields are fit with straight lines. The dipolar Kerr response was extracted as before, from the end points of the fitted lines. The saturated Kerr response of the sample - akin to a FM hysteresis curve - is estimated as the difference in y-intercept of these two lines. This is defined as the FM signal.

Care must be taken in interpreting these results [274]. The field sweeps are similar to hysteresis loops in VSM measurements where the field is swept from high positive to high negative values. However, in this case distinction must be made between initial coercivity and final coercivity [275]. Initial coercivity refers to that measured by a hysteresis loop with no laser excitation [274], while final coercivity describes the

response observed for negative pump-probe delays while under continuous laser excitation [275]. The final coercivity as defined by Li et al. [275] is zero for FeRh due to the AF state at the ambient temperature. As this AF phase exhibits no field hysteresis [17], the average response of the FM state at a given time delay and field strength is probed. This is sufficient to extract the transient magnetisation. The spontaneous magnetisation around zero field in the NanoMOKE results in Fig. 7.7b is not present in Fig. 7.11b for this reason; such information is only available from probes of the initial coercivity [275].

By applying this analysis for delay times up to 2.5 ns, the dipolar Kerr response is compared to the FM signal in order to quantify the respective dynamics following local laser heating (see Fig. 7.12b). Fitting of the data in Fig. 7.12b was carried out by adapting the expression presented in Eq. (2.64) of Radu et al. [4] with adjusted time zero, t_0, as,

$$\theta_k(t) = \begin{cases} c_0, & t < t_0, \\ G(t) * \left[A \cdot \left(1 - \exp\left(-\frac{(t-t_0)}{\tau_G} \right) \right) + B \cdot \exp\left(-\frac{(t-t_0)}{\tau_R} \right) \right], & t \geq t_0, \end{cases} \tag{7.8}$$

where c_0 is an arbitrary offset, $\theta_k(t)$ is the transient Kerr response, while $G(t)$, A, B, τ_R, & τ_G are defined as in Chapter 4.

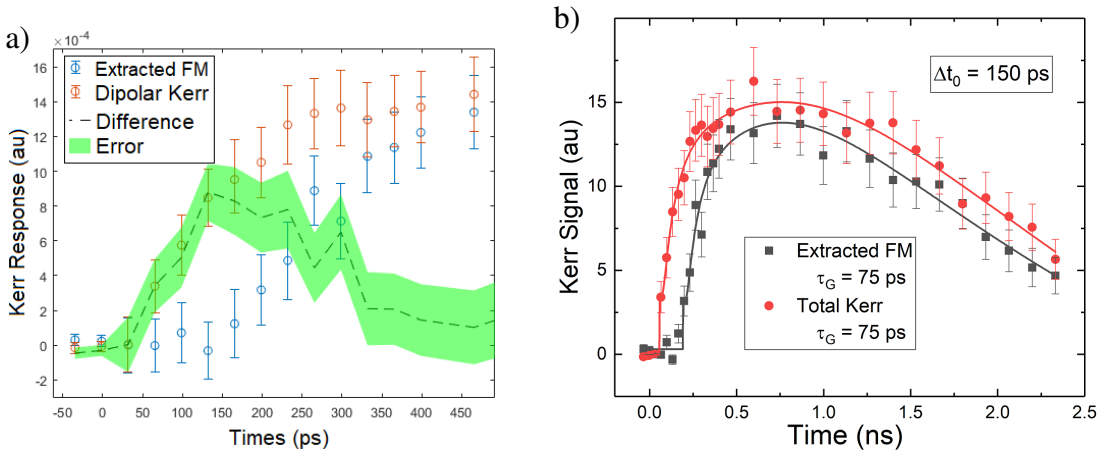

Figure 7.12: a) The Kerr signal vs extracted magnetisation over short timescales. A difference between the two signals is observed in the initial 400-500 ps. b) The time delay is evident from the fitting of the data. Using a growth and decay model, a delay time of 150 ps for the FM signal to emerge is found.

The dipolar Kerr signal increases rapidly after excitation showing maximum response within 200 ps. In contrast, the FM signal is slower to emerge, appearing 150 ps after excitation (see Fig. 7.12a). The maximum value is observed after 500 ps. This suggests that different dynamics are being observed depending on how the Kerr signal is extracted. The traditional dichroism predicts that sample magnetisation quickly grows with a growth lifetime, τ_G = 75 ps. In contrast the FM signal has a delay, t_0, of 150 ps with a similar τ_G. This can be related to previous XMCD studies in the literature [139]. Such experiments have shown that the initial formation of isolated FM domains occurs very quickly but the saturation that defines a FM material only emerges once the domains are capable of interacting on a μm scale [30]. The work of Baldasseroni et al. [139] suggests that the dynamics of FM domains in FeRh is instigated by domain nucleation and followed by domain growth. The dipolar Kerr response could be an indication of the domains nucleating following laser heating. Subsequently, the FM signal would then track the growth of the FM domains where they are now large and dense enough to interact. The decay lifetimes correspond with PhotoEmission Electron Microscopy (PEEM) work of Unal et al. [30] tracking the spatial extent of FM domains as a function of probe delay where relaxation occurred over several ns, suggestive of dissipative thermal processes. The FM signal dynamics observed in Fig. 7.12b indicate that this analysis is tracking the behaviour of fully grown FM domains in FeRh following laser excitation.

7.3.3 Field Orientation Dependence in FeRh Nanowires

Having established the dynamics of FM-like behaviour in thin films, the same analysis is applied to a series of wire arrays to examine the asymmetries in the functional form of the transition that have been reported in static probes of the AF $\rightarrow$ FM phase transition [29, 36]. Due to enhanced stability of the FM phase, it is expected that the dynamics in patterned samples should differ to those presented in the Section 7.3.2. The wire array dimensions were chosen so that the laser spot does not extend beyond the patterned features at low angles of incidence. Beamwidth was measured as < 40 μm (see Chapter 4). using the SMARACT piezoelectric motors of the sample stage, arrays could be moved in 10 μm steps reliably. This allowed the laser spot to be centered on the arrays, thereby maintaining consistency across the measurements. Field sweeps up to 110 mT are performed at each delay point where the laser fluence is maintained at 4.0 mJ cm^{-2} throughout.

The scans were repeated for two field configurations, illustrated in Fig. 7.13. The

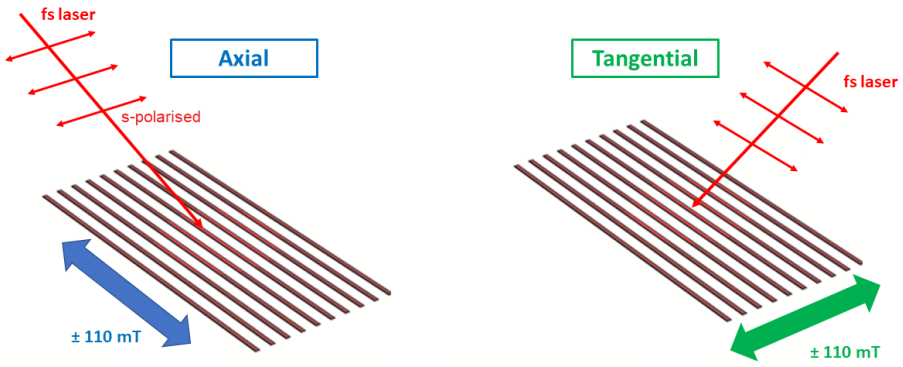

Figure 7.13: Experimental geometry for the longitudinal MOKE experiment. Arrows indicate the two magnetic field directions; blue - axial, green - tangential.

first configuration involves the field being applied along the wire length (axial field). The in-plane moment of the sample was of interest with the longitudinal Kerr response monitored. The second configuration involved field being applied across the wires (tangential field). An identical in-plane longitudinal signal was monitored. In the tangential field experiment, the magnetic moment along the wire width is extracted from the longitudinal Kerr response. In the case of 2.5 μm wires as shown in Fig. 7.14, it is evident that the responses are different for the two configurations. Under an axial field, the sample exhibits an FM signal that saturates within 400-500 ps and does not decay over the delay range investigated. In contrast, the tangential field shows a small FM signal that appears within 500 ps but relaxes back to zero within the timeframe of the scan ($<$ 2.5 ns). The axial field appears to stabilise the FM signal. In the tangential configuration, the system briefly shows field hysteresis but quickly relaxes. The Kerr response is also observed to relax more quickly indicating the excited magnetic state possesses a shorter lifetime under application of tangential field. The field strengths applied should be sufficient to saturate the magnetic moment both along and across the wires when the sample shape anisotropy is considered.

The results from further set of arrays are shown in Fig. 7.15 & 7.16. The FM behaviour is consistent across the entire range of wires under an axial magnetic field. Maximum signal emerges within 0.5 ns and possesses much longer lifetimes than seen in FeRh thin film 7.12b. However, the tangential field response is noticeably different. The dipolar Kerr signal is present in all cases but exhibits faster relaxation to ambient behaviour than seen for an axial field. The scans suggest that the FM phase is established briefly in the widest wires with the moment disappearing for narrower wire arrays. The difference between FM and dipolar Kerr signal diverges as the wires

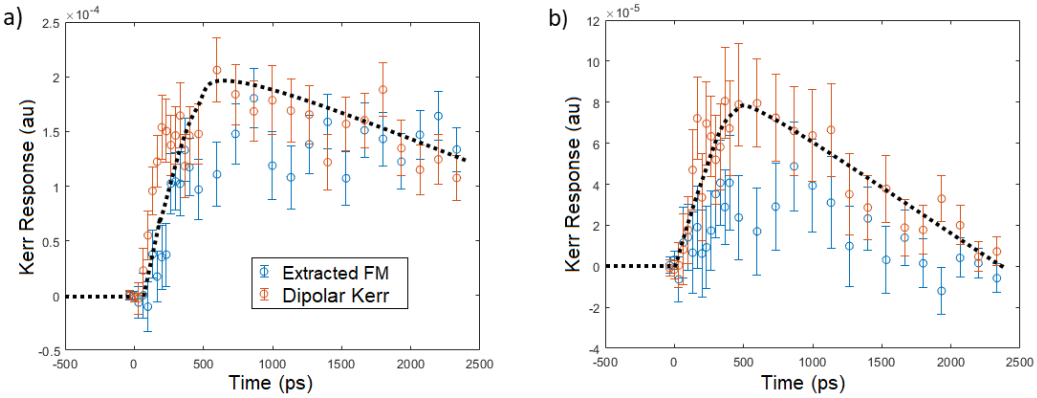

Figure 7.14: Transient magnetism for 2.5 μm wide wires extracted using the process described in Section 7.3.2 under a) axial and b) tangential fields. The fields were swept at each delay point from -0.1T to +0.1T. Dotted lines are a guide to eye showing the increased lifetime of the magnetic behaviour for the axial field.

reduce in width, more similar to the magnetic field dependence shown in 7.11. The 0.5 μm wire array exhibits almost no FM response in the field sweeps in the tangential configuration as expected from the severe shape anisotropy.

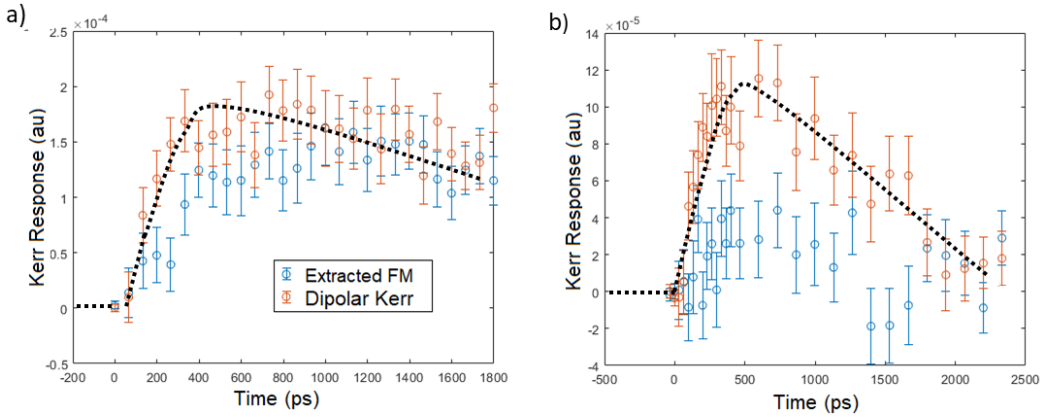

Figure 7.15: Extracted transient magnetism for 1.0 μm wide wires under a) axial and b) tangential fields. Dotted lines are functionally identical to those used in Fig. 7.14.

In order to compare magnetisation dynamics of wires to that of the thin film, the axial signals were fitted with Eq. (7.8). The time delay for the FM signal to emerge was observed for the FeRh nanowires. Δt_0 and τ_G for each set of wires are available in Table 7.2 demonstrating that the FM order begins to emerge $\approx$ 120 ps following laser excitation. Growth rates are consistent within error across the wire arrays. τ_G is found to be in the range 90-200 ps, in agreement with previous growth rates observed for FeRh films [102, 117]. The extracted τ_R is subject to significant uncertainty as the

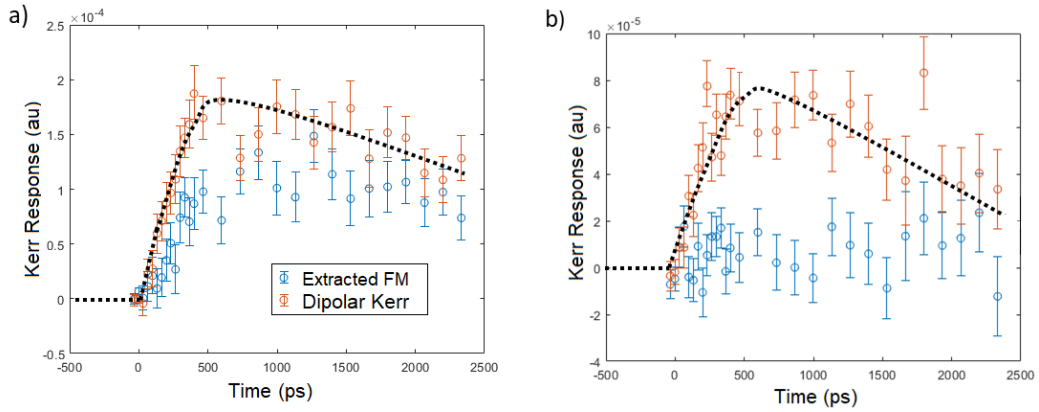

Figure 7.16: Extracted transient magnetism for 0.5 μm wide wires under a) axial and b) tangential fields. Dotted lines are functionally identical to those used in Fig. 7.14

signal does not decay significantly over the measured timescales. This would agree with the conclusions of Uhlíř et al. [36] where asymmetry in the FeRh MPT was observed. The FM phase was frustrated and the FM $\rightarrow$ AF transition occurred in a step-like fashion instead of the normally smooth temperature range [136]. Though the MOKE axial investigations of the FeRh nanowires provide further evidence for field-induced FM stability, step-like or avalanche behaviour in the back transition is not observed.

Table 7.2: Fit results to measured FM signal in FeRh nanowires - axial field. The weighted average of these results are included in the bottom row.

Width (μm)	Δt_0 (ns)	Growth rate - τ_G (ns)	Lifetime - τ_R (ns)
0.3	0.19±0.22	0.11±0.07	4±6
0.5	0.10±0.05	0.22±0.09	5±4
0.8	0.13±0.05	0.09±0.07	3±1
1.0	0.13±0.05	0.18±0.03	7±5
2.5	0.13±0.01	0.12±0.07	4±1
Average ($\bar{x}$)	0.12±0.002	0.15±0.001	3.9±0.9

7.3.4 Persistent FM Behaviour - Possible Explanations

The magnetisation dynamics of FeRh wires are observed to be different when compared to the response of FeRh thin films. The differences were observed across all

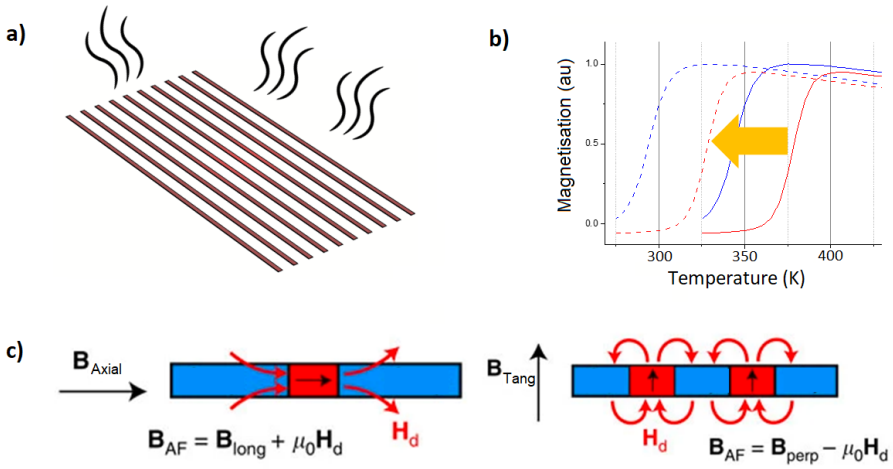

Figure 7.17: Schematics for possible causes of persistent FM behaviour in FeRh nanowires. a) Poor thermal diffusion, b) change in T_T, c) field-stabilised FM phase in the mixed AF/FM phase (red/blue) under fields applied along and across the wire lengths - adapted from Uhlíř et al. [36].

wire arrays suggesting structural disorder at feature edges may be the cause [29]. To understand the underlying physics, the following arguments are explored to describe the origin of the longer-lived FM signal in nanowire arrays (see schematic in Fig. 7.17);

a) **Reduced Heat Dissipation:** If the thermal heat dissipation is poor within nanowire arrays, it could be that the sample temperature does not reach ambient RT between laser pulses and it remains above T_T over longer timescales. The thin film and patterned systems are simulated using FEM to investigate thermal diffusion. This is performed for a range of patterned sample and thin films composed of FeRh on MgO substrates. Results from the heat dissipation simulations are discussed in Section 7.4.

b) **Change in T_T:** Nano-lithography of FeRh has been previously shown to induce structural disorder locally, especially at the feature edges. Work by Temple et al. [29] has shown that T_T is reduced following high-energy (1000 V) ion milling processes. This arises as a consequence of reduced B2-order promoting FM behaviour [132] in 100-300 nm edge regions of the patterned samples. The increase in structural disorder was mitigated by using reduced voltages during the ion milling process (350 V). In Section 7.5, electrical measurements are presented which measure the T_T across each wire array.

c) **Enhanced Stability of the FM Phase:** Neither of these explanations describes the

observed behaviour under tangential applied fields. If these explanations can be discounted, it is likely that the enhanced stability of the FM phase is the cause of persistent signal in the axial field [36]. This is tested by performing electrical measurements on the wires and investigating how the FM phase persists as both field and temperature are swept. Increased stability of FM vs AF phase would be verification of the hypothesis suggested by Uhlíř et al. [36] where the demagnetisation field of FM domains increases the internal field strength. This is further explored in Section 7.5. An estimation of the demagnetising factors for the investigated samples is provided.

7.4 Finite Element Modelling of Heat Dissipation

In order to understand the role of heat dissipation in the dynamics of the FeRh MPT in thin films and nanostructures, heat transfer within FeRh systems grown upon MgO substrates was modelled with the FEM software, COMSOL® [179]. This allows for an prediction of differences in heat dissipation across a range of patterned samples. Slow relaxation to ambient temperatures could explain the longer-lived FM state observed in wire arrays.

7.4.1 Time-dependent Solver

The timescales in a pump-probe process vary from fs (initial laser excitation) to ns (heat dissipation on μm scale) which causes the problem to be multi-scale in time. Such a range demands that resolution of the simulated time steps be carefully considered, especially due to the steep gradient of the heat flux introduced during laser excitation. This was achieved by using logarithmic time steps which are extensively used to model such heat transfer problems [276]. During excitation, the time step is fine enough to capture this highly non-equilibrated behaviour. Next, when the material cools down excessively long computational times are mitigated by using coarser steps, as the ratio of cooling time over pulse duration is estimated from the MOKE data as 1:100. The time solver ranged from 1 fs up to 10 ns, across 7 orders of magnitude (10^{-15} - 10^{-8}).

7.4.2 Input Parameters

The initial conditions of the system and parameters of the heating pulse are described in this section. The laser and material parameters can be found in Table 7.3. The

Table 7.3: Parameters used in the FEM simulation for a laser fluence of 5.5 mJ cm^{-2}.

Laser & Optics		FeRh material parameters (@ 300 K)	
Power (mW)	50	C_P (J K^{-1} kg^{-1})	347
Pulse (fs)	50/300	ρ_{AF} (kg m^{-3})	9860
σ_x (μm)	35	ρ_{FM} (kg m^{-3})	9580
σ_y (μm)	35 (@ $\theta_0 = 0°$)	Young's Modulus (Pa)	$1x10^9$
Emissivity	0.8	κ (W m^{-1} K^{-1})	50

system temperature is initialised at 300 K, and the transition properties of the material were set at T_T = 353 K and Δ T = 25 K, based on the sample characterisation shown in Fig. 7.1. Laser excitation was included as a heat gradient at the surface [276] with duration equal to that of the laser pulse (50 or 300 fs) with a Gaussian profile across the 'pumped' area. This could be achieved by perturbing the system with a heat pulse, $Q(x,y,t)$, of the form;

$$Q(x,y,t) = A(t) \cdot \exp\left(-\left(\frac{(x-x_0)^2}{2\sigma_x^2} + \frac{(y-y_0)^2}{2\sigma_y^2}\right)\right), \tag{7.9}$$

where σ_x and σ_y are the respective beamwidths in x and y directions, and $A(t)$ is a step profile proportional in intensity to the emissivity-corrected laser fluence with a time interval equal to the laser pulse duration. Material parameters could be found from *ab initio* simulations and calorimetric studies of FeRh [96, 109, 121, 183, 277]. Further details are provided in Chapter 4. The heat transfer coefficient (k_{IF}) between the MgO and FeRh interface is not included and is varied in order to find a reasonable approximation. It is expected to be on the order of 10^9 W m^{-2} K^{-1}, based on the heat transfer coefficient within the two materials and a sub-nm roughness. The value was estimated by observing the dynamics in a 2D rotationally symmetric system (see Fig. 7.18) following laser excitation [278, 279]. To this end we compared the simulated temperature change in the FeRh film to the relaxation rate of the reflectivity signal from TR-MOKE experiments (see Section 7.3). Reasonable agreement with experimental dynamics is found when $k_{IF} = 5\times10^8$ W m^{-2} K^{-1}.

The density, $\rho(T)$, of the FeRh material was allowed to change as the system was heated through the phase transition. An error function was utilised to model transformations in physical properties across the width of transition, ΔT, changing from ρ_{AF}

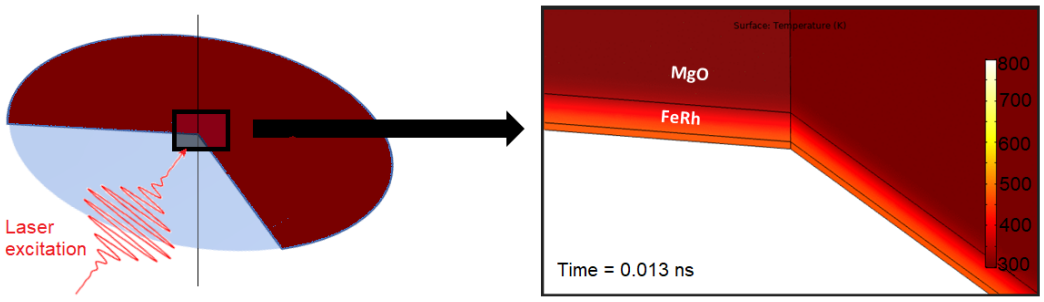

Figure 7.18: Snapshot from the 2D centro-symmetric simulation used to determine the interfacial heat transfer between FeRh and MgO. An internal cross-section is presented corresponding to 13 ps after 3 mJ cm^{-2} laser excitation from the bottom surface. Temperature scale (K) provided.

to ρ_{FM} above 355 K;

$$\rho(T) = \rho_{AF} + (\rho_{AF} - \rho_{FM}) \cdot \left(\mathrm{erf}\left[\frac{T - T_T}{\Delta T} \right] - 1 \right). \tag{7.10}$$

Then the average density of the probed volume (based on the probe beamwidth) was used as a measure of the transition that has occurred. For TR-MOKE experiments on FeRh, the system has to be sufficiently heated in order to measure surface magnetisation (353 K). The density is used to quantify the ratio of FM phase which could be compared to the Kerr signal in the pump-probe experiments.

7.4.3 Simulation of Local Laser Heating

When comparing probes of the lattice and electron temperature presented throughout this thesis (in the forms of TR-XRD and reflectivity respectively) it is seen that the electron heating occurs faster than that of the lattice [87]. FEM simulations do not account for the equilibration process caused by electron-phonon coupling [85]. Instead, it probes the average temperature of the system when total heat capacity, $C_P = C_{EL} + C_L + C_S$, is considered. Therefore, it should demonstrate the equilibrium behaviour of the system. Understanding this, thermal behaviour of the FeRh films and wires following laser heating is monitored on a ns timescale to understand the heat dissipation.

Simulation of FeRh Film Heat Dissipation

The simulations were first performed for an FeRh thin film, of thickness 30 nm, to compare to TR-MOKE results presented in Section 7.3. The simulated response to laser excitation is shown in Fig. 7.19a, where the magnitude of density changes are proportional to the laser fluence. It is seen that heating is almost complete across the probed region (30 x 30 μm^2) within 10 ps for the range of fluences used, comparable to lattice transformations presented in this thesis [31]. The simulation results shown in Fig. 7.19b were modelled over 10 ns to demonstrate that the sample is expected to return to ambient temperatures over such timescales. For the laser repetition rate of 200 kHz, the downtime between laser excitation is 5 μs. Therefore, gradual heating across the runtime of experiments is considered to be negligible. The equilibrium temperature is assumed to be ambient room temperature ($\approx$ 300 K).

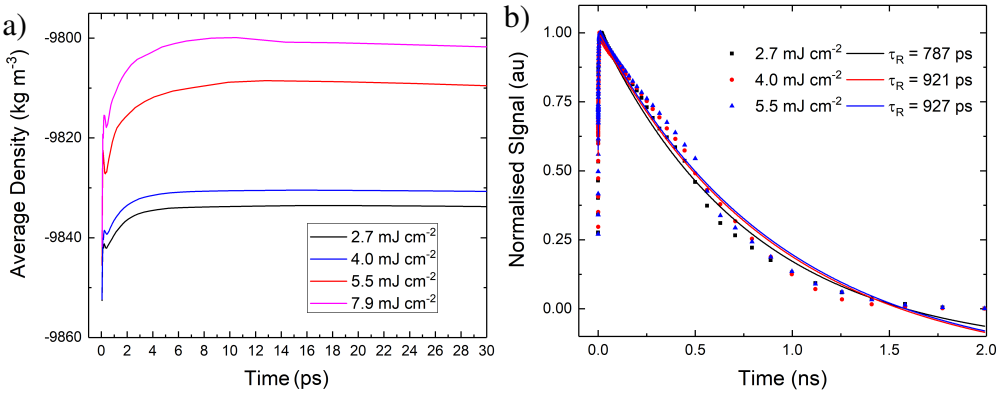

Figure 7.19: Transient density of a 100 x 150 μm^2 region about the laser pulse of the FeRh film subject to a series of laser fluences. Presented for timescales over a) ten's of ps which demonstrate the rapid expansion, and b) several ns showing the relaxation to RT density. Fitting results using Eq. (2.64) are inset.

For comparison to the experimental results, the fluence dependence of the thin film relaxation is presented in Fig. 7.19b. There is a gradual increase of excited state lifetime with increasing laser fluence. This is further evidence that the simulations are providing a reasonable estimation of the heat transfer within the sample. As has been seen in both TR-MOKE data and TR-XRD experiments [4, 31], increase in laser fluence results in slower dynamics as the system is driven further into the non-equilibrium regime [84].

Fitting using Eq. (2.64) over a timescale of 2 ns as in Fig. 7.19b, it is seen that

the signal is longer lived than for reflectivity data in Fig. 7.9. As discussed in Chapter 4, the dynamic reflectivity signal is a measure of the change in electron temperature as a function of time [173]. Signal in the FEM simulation is due to the density change, reducing when the system reaches temperatures below T_T. Therefore on these timescales, it will persist longer than the reflectivity signal. Over longer timescales, reduced (and more accurate) estimates of τ_R are found.

Simulation of FeRh Nanowire Heat Dissipation

Wires were accounted for by replacing the thin film of FeRh on top of the MgO substrate with cuboids of the required dimensions. The heating was included at the surface face of each wire, again using Eq. (7.9). Heat transmission to the MgO substrate only occurred at the bottom face using the same value of interfacial thermal conductivity - k_{IF}. The gaps between wires meant direct laser heating of the MgO surface was considered. This was implemented using Eq. (7.9), but with a lower effective fluence to reflect the reduced absorbed power. Based on the spacing of the wires, 75% of the light will reach the MgO. In order to accurately simulate the heat transfer on sub-μm scales, it is necessary to reduce the cell size. This allows for a heat gradient to exist within the narrow confinements of the wire width (100's of nm).

This simulation was carried out for 2.5, 1.0 and 0.5 μm wide wire arrays. The signal presented in Fig. 7.20 is found by normalising the measured density changes to the peak value. This allows for the comparison between dynamics of thermal dissipation in each system. A change in behaviour for the wires vs for the film is seen where laser pulse beamwidth and fluence are constant. The FM phase (based on the average temperature and by extension the density) is predicted to relax more quickly in wire arrays. This model suggests that the reduced heat energy in wires is quickly dissipated by the MgO bulk despite the laser-induced substrate heating.

Simulation of FeRh Patch Heat Dissipation

Finally, differences in relaxation lifetimes arising from cell sizes in the FEM software were investigated. This was achieved by including a 'patch' of FeRh of similar dimensions to the wire array, containing no gaps through which the MgO substrate would experience laser heating. The increased computation time associated with smaller cell sizes was mitigated by modelling a structure of 150 x 100 μm. The cell size was consistent between the patch and the wire arrays, both constructed from swept polygons.

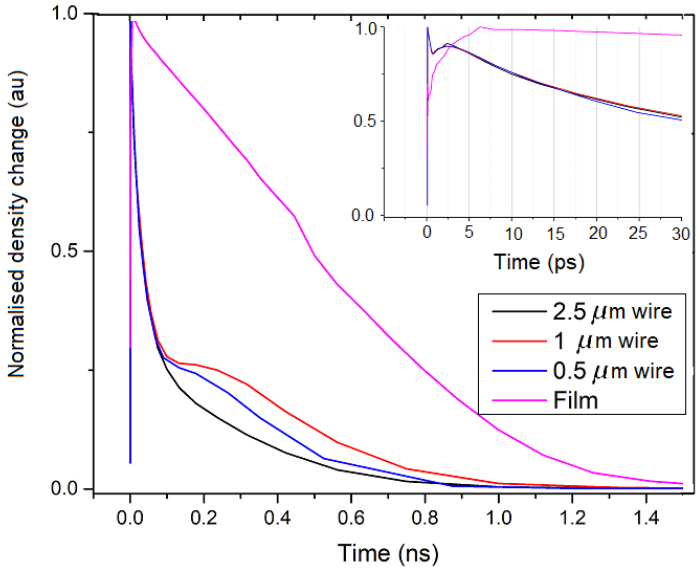

Figure 7.20: Normalised transient change in simulated FeRh density following laser excitation. Shown for thin films and a range of wire widths. Changes over shorter timescales are presented in the inset.

This also accounted for the longer range heat dissipation (both lateral and through the film thickness) that exists in the film but not in the wires. Such heat dissipation would not be considered in our experiment as a small probed volume is monitored.

The full timespan of the simulations are further shown in Fig. 7.21, demonstrating that equilibrium temperatures (RT=300K) are reached within 3 ns in all instances. The simulated density dynamics predict that the 0.45 wires undergo faster relaxation than the film. The film and patch are nearly identical in behaviour, indicating that the difference in dynamics of the simulations is not due to differences in cell size or lateral heat transfer processes. The relaxation timescales of the simulated system are comparable in those extracted from reflectivity data of FeRh films following laser excitation, see Fig. 7.21a & 7.21b.

It is seen in Fig. 7.21that patch dynamics follow film dynamics more closely than that of the wires. This suggests that the change in dynamics is as a consequence of the overall reduced heat absorbed by the nanowire samples. Based on the near-identical results between this patch of FeRh and a thin film, the heat transfer module does not differentiate between lateral heat flow and that through the depth. This further implies that the cell size, and more importantly the boundaries of cells, do not change dynamics of the simulation for cell sizes used. This is further evidence that the difference in

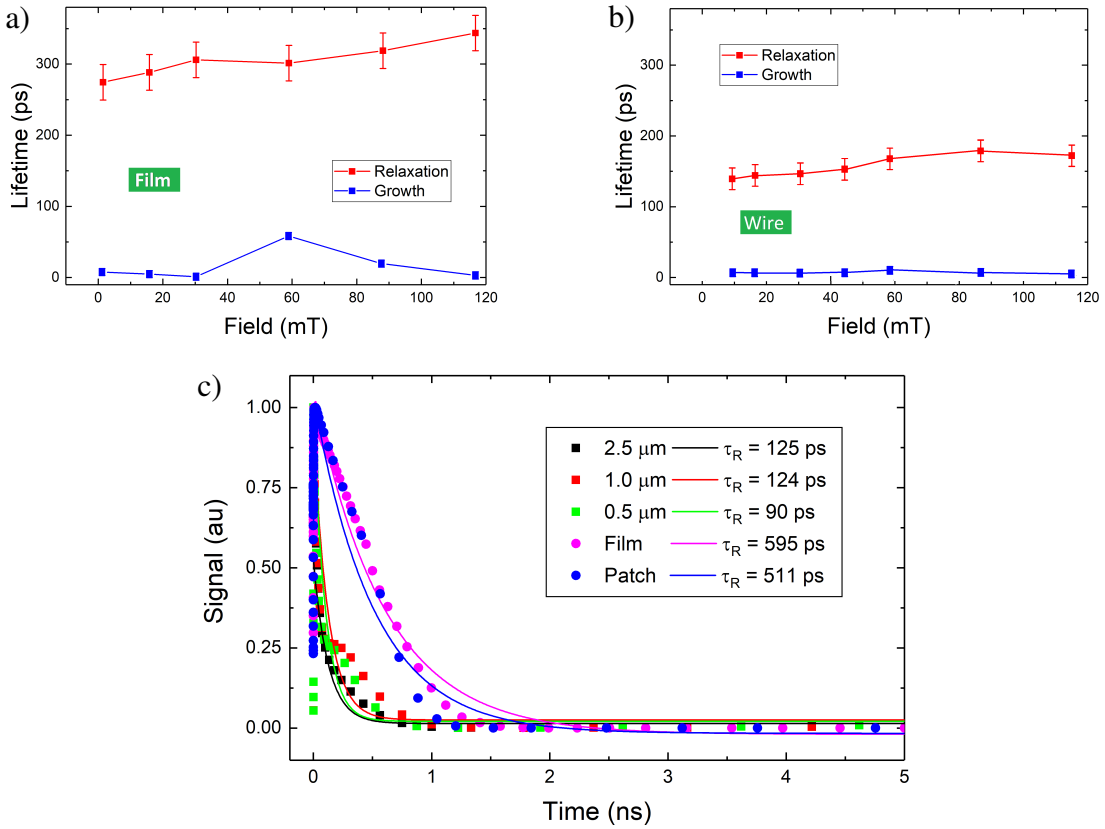

Figure 7.21: Reflectivity dynamics of a) thin film, and b) 0.5 μm wires following laser excitation for different field strengths. These were found from a series of delay scans performed on thin films and wire arrays for a range applied field strengths. Extracted by fitting with growth-decay exponential function. c) Dynamics extracted from FEM simulations are collated with fitted decay lifetimes included.

the simulated wire dynamics observed is not due to differences in the model set-up.

From this analysis, we must discount the hypothesis that a difference in transient FM behaviour of nanowires is due to a reduced ability to transfer heat laterally, in comparison to thin metallic films. Indeed, these simulations predict that the heat dissipates more efficiently in the wires than in the film and FM lifetimes would be shorter if average temperatures were the only criteria for the transition dynamics. Simulation of an FeRh patch shows that the effect is not simply due to the small area of the material being excited, with different relaxation dynamics only observed for μm features. The lower overall energy in nanowires is easily dissipated to an equivalent MgO substrate volume. However, it should be stated that Eq. (7.9) does not consider the depth dependence of the laser spot. It is expected that there is significant heating to the skin depth

($\approx$ 30 nm for the pump beam wavelength - 515 nm [39, 259]). This would also heat the MgO substrate slightly which may explain the slower than expected dynamics. A more sophisticated model of the initial heating step may more accurately predict the rate of heat transfer seen in the experimental results. Currently, the model overestimates relaxation lifetimes for the thin film simulations. Further refinements may be found by considering Casimir classical size effects [280] at grain boundaries and feature edges.

7.5 Resistivity as a Probe of T_T in Nanowires

The nanowires were characterised using a deposited 4-point probe with the assistance of Vahid Sazgari. The lithography procedure for the electrical contacts has been outlined in Chapter 4. An optical image of the resulting contact pads is provided in Fig. 7.22.

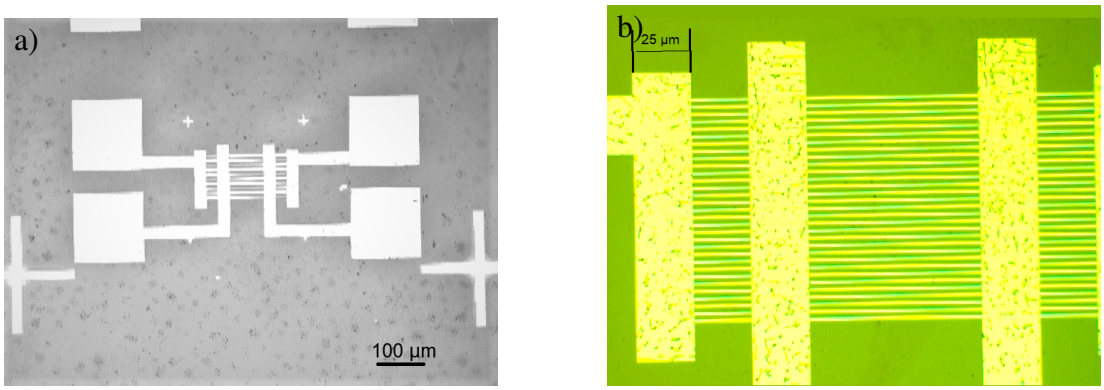

Figure 7.22: Optical images of the wire contact pads used to perform the 4-point probe resistivity measurements. a) 10x zoom - 2.5 μm wires. b) 50x zoom - 0.5 μm wires.

In order to characterise the FeRh transition and determine if there was a reduction in T_T for the wire arrays due to structural disorder arising from the milling process [29], the resistivity of individual arrays were measured. This probes the FeRh electronic band curvature as it transforms from AF to FM magnetic ordering [15, 121] reducing the resistivity by 33% [21]. Similar to treatment of magnetometry data, T_T is defined as the inflection point of the R vs T curve. The resistivity of wire arrays were measured under Zero Field (ZF) and applied fields of 1 T, both axial In-Plane (IP) and Out-Of-Plane (OOP). For each scan, the sample was heated in a cycle 300 $\rightarrow$ 400 $\rightarrow$ 300 K, with constant field maintained throughout.

Resistivity of the 1 μm wire array through the MPT is shown in Fig. 7.23, where an OOP field causes a noticeable shift in T_T. This is a drop of $\approx$ 3 K when compared

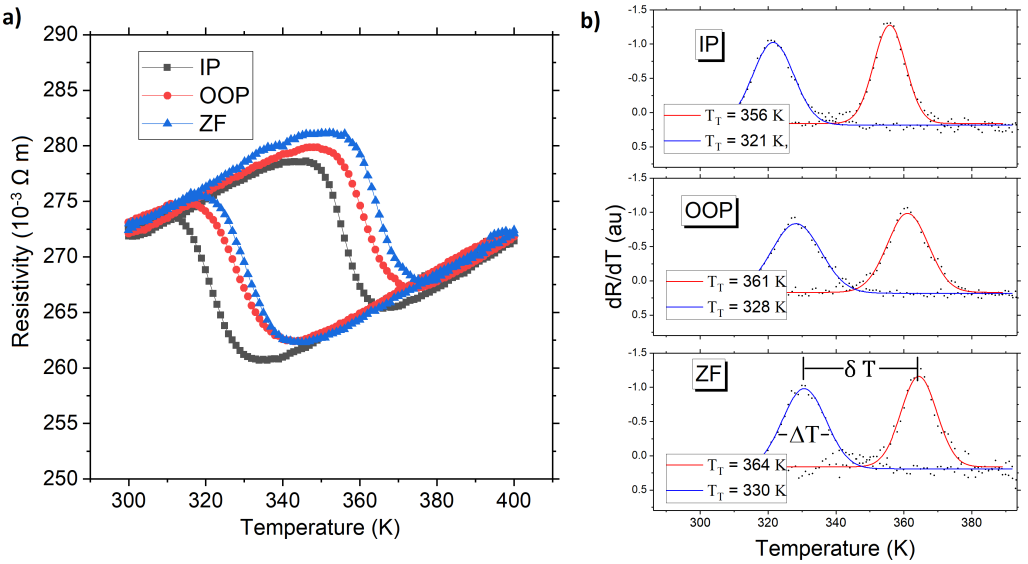

Figure 7.23: a) Resistivity as a function of temperature for FeRh 1 μm wire array. This was performed for 3 magnetic field configurations - ZF, IP, & OOP. b) T_T, ΔT, and δT were extracted in each case by fitting the 1st derivative of the heating (red) and cooling (blue) curves with a Gaussian function.

to the ZF temperature sweep. In the IP configuration, a larger shift in T_T is observed; up to 9 K. Similar shifts in T_T were also observed in 500 nm wires (see Fig. 7.24). However, the data provides no evidence for asymmetric transition behaviour. From Tables 7.4a & 7.4b, the extracted T_T are comparable to that observed in Fig. 7.1a when field and thermal calibration are considered. Knowing T_T is unaffected by the lithography process, the transition mechanism is considered. The width, ΔT, and thermal hysteresis, δT, are comparable across the field orientations with no reduction in the transition width, ΔT, for the IP cooling cycle as predicted by Uhlíř et al. [36]. The electrical transition is symmetric with respect to temperature.

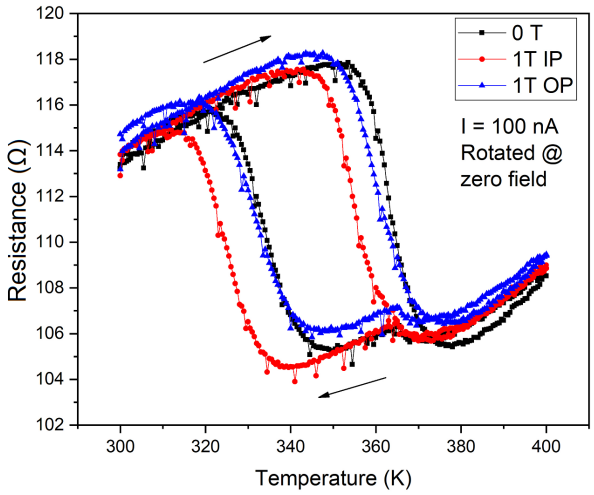

Figure 7.24: Resistance as a function of temperature for FeRh 500 nm wire array. The 'kink' in the cooling cycle at 367 K was investigated further but was not observed when the sample was wire-bonded a second time.

Table 7.4: Extracted transition behaviour from Fig. 7.23 & 7.24.

Field	Cooling - T_T (K)	ΔT (K)	Heating - T_T (K)	ΔT (K)	δT (K)
ZF	330.6 ± 0.1	15.2	364.4 ± 0.2	12.4	33.8 ± 0.2
OOP	328.2 ± 0.1	17.1	361.1 ± 0.1	14.3	32.9 ± 0.2
IP	321.5 ± 0.1	14.3	355.8 ± 0.1	11.1	35.3 ± 0.1

a) 1 μm wires

Field	Cooling - T_T (K)	ΔT (K)	Heating - T_T (K)	ΔT (K)	δT (K)
ZF	333.9 ± 0.1	13.9	363.4 ± 0.1	10.9	29.5 ± 0.1
OOP	331.7 ± 0.1	15.6	360.3 ± 0.2	14.9	28.6 ± 0.2
IP	324.5 ± 0.1	12.6	354.9 ± 0.2	12.6	30.4 ± 0.2

b) 500 nm wires

7.5.1 Influence of Shape Anisotropy on the FeRH MPT

Having discounted transition asymmetry, the internal demagnetisation fields offer an explanation for the changes in transition behaviour. From the demagnetisation factors, the coercive field of the wires can be calculated as a function of angle using Eq. (2.43) [68], see Section 2.3.6.

Shape Anisotropy Calculation

In order to understand how shape anisotropy can affect the demagnetisation fields within wires, and by extension the transition behaviour, the tensor terms of $\mathcal{N}$ are estimated. This is based on the magnetostatic theory presented in Section 2.4.

In the case of individual wires, the Poisson equations are simplified [68] by approximating the shape as slender ellipsoids, $a \gg b \geq c$, whereby the demagnetising

factors, N_x, N_y, and N_z, may be written as [69];

$$\frac{N_x}{4\pi} = \frac{bc}{a^2}\left(\ln\left[\frac{4a}{b+c}\right] - 1\right), \tag{7.11}$$

$$\frac{N_y}{4\pi} = \frac{c}{b+c} - \frac{1}{2}\left(\frac{bc}{a^2}\right)\ln\left[\frac{4a}{b+c}\right] + \frac{bc(3b+c)}{4a^2(b+c)}, \tag{7.12}$$

$$\frac{N_z}{4\pi} = \frac{b}{b+c} - \frac{1}{2}\left(\frac{bc}{a^2}\right)\ln\left[\frac{4a}{b+c}\right] + \frac{bc(b+3c)}{4a^2(b+c)}. \tag{7.13}$$

Applying the above equations to the patterned wire elements of this chapter, the predicted diagonal terms, N_i, in the demagnetisation tensor are presented in Table 7.5. Assuming a coercive field ≈ 45 mT from Fig. 7.7b - and the soft nature of FeRh [14] - saturation along the wire lengths is expected for applied field strengths < 50 mT. In the case of an OOP field, fields in the range 1.2 - 1.3 T are required to saturate the wires. When one considers the field dependence of the FeRh MPT (9 K T^{-1} [114]), it is seen how the difference in applied field direction shifts the T_T by up to 10 K.

This treatment further explains the transient FM signal of Section 7.3.3. Referring to Table 7.5, it is seen that the expected tangential applied field in order to establish the FM order is larger than for axial fields. In the case of the widest wires, fields less than 100 mT should suffice; while for the thinnest wires, fields upwards of 200 mT are required for H_y to exceed the coercive field. The maximum applied field of the quadrupole magnet was ≈ 110 mT (see Section 4.4.1) which demonstrates why weak FM signal is observed for the 2.5 and 1.0 μm wires but not for narrower arrays. In contrast, the film has no in-plane anisotropy with identical behaviour for both orientations [17, 68]. This demonstrates how pattering can introduce a shape anisotropy which influences the FeRh transition behaviour. Extending this argument, the enhanced FM stability observed in the axial configuration could be due to the increased internal field strengths arising from the severe shape anisotropy [36].

For completeness, we consider how patterning increases the nucleation and pinning sites for the FM domains which hinders the FM→AF transition. This has previously been seen to increase coercivity of permalloy samples, both in this project (Fig. 7.8) and in the literature [76, 281]. However, the differences across the range of field orientations confirm that the shape anisotropy is the primary cause. Overall, the most significant change in FeRh transition behaviour is the reduction of T_T when an IP field is applied.

Table 7.5: Demagnetisation factors for the FeRh wire arrays presented in this chapter. These were calculated using Osborn equations and then normalised.

Width (μm)	N_x - Axial	N_y - Tangential	N_z - OOP
2.5	1.03×10^{-5}	0.016	0.9999
1.0	5.15×10^{-6}	0.040	0.9992
0.8	4.33×10^{-6}	0.050	0.9988
0.5	3.02×10^{-6}	0.080	0.9968
0.3	2.05×10^{-6}	0.132	0.9912
Infinite thin film	0	0	1

Conclusions

A method for increasing the Kerr signal from thin film samples is presented with the relevant theory for both longitudinal and polar MOKE set-ups. The effect of dielectric layers is shown to increase the longitudinal MOKE (@45°) signal by up to 280%, indicating resonant enhancement has been achieved.

By sweeping magnetic fields, a method of extracting transient FM signals from FeRh thin films is demonstrated. This is found to emerge more slowly when compared with previously published dipolar Kerr signals in the literature [4, 102], instead following timescales that are more consistent with FM domain growth in FeRh [30, 139]. This transient FM behaviour is found to persist for longer times in nanowire arrays than thin films at axial field strengths of 110 mT. A tangential field induces a measurable Kerr response with reduced FM signal in these same samples. Furthermore, the dipolar Kerr response was observed to relax more quickly under tangential applied fields.

An FEM model is developed using COMSOL® to estimate the sample temperature following laser excitation in both thin films and nanowires. There is no indication that wires have a reduced ability to dissipate heat during these pumped laser experiments. Having discounted heat dissipation dynamics as an explanation for the behaviour of the FeRh nanowires, it is likely a change in the transition behaviour is instigated when the FeRh thin films are patterned. Based on these findings and the static electrical characterisation, it can be hypothesised that internal magnetic fields influence the FM

phase dynamics in patterned nanowires. No significant shift in thermal dissipation or T_T was observed that would explain the behaviour. The field orientation dependence of T_T in FeRh nano-wires suggests that the FM phase stability is a manifestation of shape-imposed anisotropy. Estimation of the effective fields within wire and thin film samples predict a difference of up to 0.8 T can be established depending on the relative sample and axis orientations. This offers a method of controlling the T_T by up 10 K at a constant field strength, with differences also observed in the transition dynamics.

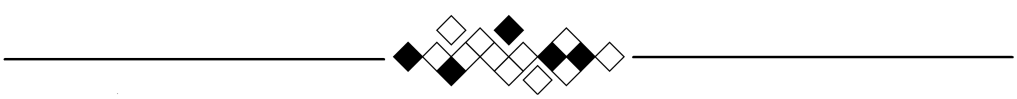

Chapter 8

Conclusions

Now a magnifying glass is a better thing, because you can look at it and what you see when you look is a third thing altogether

Flann O'Brien, *The Third Policeman*

Progress in the understanding the FeRh MPT has relied upon continued development of probes into the electronic, lattice, and magnetic systems [21]. The results presented in this thesis provide new insight to the structural and magnetisation dynamics of FeRh thin films and nano-patterned structures where static and dynamic measurements are reported in each regard. The techniques used to evaluate these properties were: non-resonant magnetic scattering to investigate the evolution of the magnetic sub-lattice of the AF phase, TR-XRD to evaluate the fluence dependence of the structural dynamics of FeRh films when locally heated by laser excitation, TR-MOKE as the field is swept across thin film and patterned FeRh arrays allowing the evolution of surface magnetisation to be probed. Resistivity measurements on these samples quantify the transition behaviour both as a function of applied field and temperature. This experimental approach was complemented by numerical simulations of the transition dynamics with COMSOL multi-physics software, VAMPIRE atomistic software, and Python based ODE solvers. The conclusions drawn from these investigations are summarised in the following sections, and the scope for future work is outlined.

8.1 Non-resonant Magnetic Scattering

The investigation described in Chapter 5 demonstrated the validity of probing the magnetic sub-lattice of FeRh using non-resonant x-rays, with a shift in x-ray polarisation confirming the photon-spin interaction. Optimisation of this weakly scattering technique was achieved by investigating the energy and grazing incidence dependence of the scattering efficiency. The intensities of the AF Bragg peaks were probed as a function of temperature, disappearing as the MPT progresses. The coherence length of AF ordering was found to correlate with that extracted from Bragg peaks due to conventional charge scattering indicating AF domains are limited in size by the structure off thin films. We further demonstrated that the magnetic Bragg peaks are detectable throughout the transition, allowing for a investigation of anti-parallel Fe spin ordering close to and around the transition point. This probe offers insight into the magnetic properties [33] of the AF phase which remain under explored in the literature due to the difficulty of interacting with such materials. This work was recently published in AIP Advances [37].

8.2 Time-resolved X-ray Diffraction

An experiment was undertaken at SACLA, Japan to investigate the time evolution of the FeRh lattice constant via pump-probe XRD. Following laser excitation, the (-101) FeRh peaks exhibit a reduction of intensity which can be related to the increasing lattice temperature via the DWF; and a peak shift which can track the rate of volumetric expansion via Bragg's law. The results at high laser fluences are not consistent with the three-temperature model [84] which has been used previously to track the mechanism of the FeRh MPT [117]. By evaluating these results in the context of quasi-static XRD undertaken as a function of temperature up to 1023 K, we deduce that the system may access the PM phase [116] far beyond T_T of FeRh (355 K). In order to explain such temperatures on short timescales, we provide simulation results derived from an extension to the three-temperature model [145]. This would imply the existence of a transient lattice state, where a subset of the phonon modes couple more strongly to the electron system [3]. As a result of the sub-ps temporal resolution, the lattice dynamics are now described on a similar timescale to the well-understood transformations of the electronic valence-band structure [34]. The results and analysis from this beamtime are included in a manuscript recently published in Scientific Reports [38].

8.3 Evolution of Magnetisation in Patterned FeRh

TR-MOKE was performed on FeRh samples to investigate the time evolution of magnetisation. By sweeping magnetic fields at fixed laser probe delays a method of extracting transient FM signals from MOKE experiments on FeRh thin films was demonstrated. This is found not to correlate with previously reported TR-MOKE results [4, 102], instead following timescales that are more consistent with FM domain growth in FeRh [30]. This transient FM behaviour persists at time intervals > 2.5 ns in nanowire arrays when axial fields of up to 110 mT are applied. A similar tangential field induces a measurable Kerr response with reduced FM character in these same samples. COMSOL simulations were performed that discounted the hypothesis that differences in thermal dissipation would account for the behaviour. By examining the resistivity of the wire arrays as a function of field and temperature, we conclude that the shape anisotropy of the wires is causing the orientation dependant behaviour. This effective field is a more accurate predictor of the behaviour than colossal asymmetry demonstrated by Uhlir et al. [36], when averaged across multiple wires in an array. A manuscript is in preparation detailing this investigation into the static and dynamic properties of FeRh wire arrays. Further electrical characterisation data is being analysed to better understand the influence of shape anisotropy on the FeRh MPT.

8.4 Future and Ongoing Work Resulting from this PhD

This project has demonstrated an x-ray probe of magnetic Bragg peaks, as well as structural dynamics of similar charge peaks with 200 fs resolution. There is scope to perform TR experiments using non-resonant x-ray scattering as a probe of AF ordering. This is motivated by the optimisation of magnetic diffraction presented in Chapter 5 and x-FEL operation experience stemming from work reported in Chapter 6. Such an experiment would be capable of monitoring how FeRh evolves following laser excitation in terms of both the lattice expansion and the long-range ordering of the magnetic sub-lattice [248]. Spin and lattice transformations can be extracted from such measurements for direct comparison of the competing dynamics. By simultaneously monitoring charge and magnetic Bragg peaks, the evolution of the FM state can be probed with sub-ps temporal resolution to definitively determine if the lattice expansion is driving the spin re-orientation or vice versa. As such, the lattice-spin coupling of FeRh as a function of laser fluence and ambient temperature may be explored.

Furthermore, similar analysis to that described in Chapter 6 can be applied to the magnetic Bragg peaks to determine if the first order transition assumption also applies to the evolution of the FM state through the mixed phase [112]. The limitations of x-FEL studies have also been demonstrated in Chapter 6, namely the ablation of deposited films. However, this can be overcome by beam collimation and attenuation in combination with single-photon counting schemes [230].

The results of Chapter 6 demonstrate the non-triviality of electron-phonon coupling in FeRh. The nature of highly coupled phonons could not be extracted from the data obtained here. We speculate in Chapter 6 that the optical modes are more readily coupled to the electron system. This was based on the assumption that a Fe $\rightarrow$ Rh charge transfer process occurs shortly after laser excitation [34] which would predict Fe-Rh vibrations being highly coupled to the electronic structure. Other experiential techniques such as coherently excited phonons or electron diffraction could help resolve the precise nature of the transient lattice mode [282, 283]. A recent paper described an experiment that demonstrated angular momentum is transferred to polarised phonons within 1 ps [284]. It was seen using ultrafast electron diffraction that a non-equilibrium population of anisotropic high-frequency phonons appears within 150-750 fs in excited nickel samples. Tauchert et al. [284] further demonstrated the direction of anisotropy in relation to the initial magnetisation as well as the amplitude of atomic oscillations [284]. A similar study applied to the FeRh MPT would be instructive in quantifying the energy dependence of the electron-phonon coupling.

We are currently analysing a series of field sweeps carried out at fixed temperatures on the wire arrays described in Chapter 7. This will determine the field strength at which the FM phase is induced for a particular field orientation, allowing for an estimation of the internal fields acting on the wires. This can be used to describe quantitatively how the shape anisotropy of the FeRh nanostructures affects the MPT in terms of the micromagnetic energies. Further exploration could take the form of monitoring the in-plane angular dependence of transition behaviour. In-plane scans as a function of angle about the surface normal could reveal more information about the transition mechanism. If maintained at a field strength and temperature where an AF/FM mixed phase is predicted [112], the field orientation dependence described here would suggest a sudden decrease in the resistivity when external field aligns along the wire length, and vice versa [36].

Finally, further studies are required to fully explain the pump-probe results from thin films and nanowires presented Chapter 7. Using a similar approach to Chapter 6, it would be instructive to explore the fluence dependence of the FM signal. The chosen fluence corresponds to the minimum energy that would promote FM behaviour within the entire pumped volume. Increased (and reduced) laser excitation could reveal whether the observed time delay is a fixed entity or is dependent on the degree of energy transfer via electron-spin coupling. Such an experiment would help demonstrate the influence of the PM phase through the MPT under high laser fluence. The goals outlined at the outset of the thesis have been answered with the ultimate aim of the optimising and understanding the limitations of laterally confining FeRh for memory storage devices [11, 25].

Bibliography

[1] Martin, J. D. When condensed-matter physics became king. *Physics Today* **72**, 30 (2019). URL https://doi.org/10.1063/PT.3.4110.

[2] Zhang, G. P., Hübner, W., Lefkidis, G., Bai, Y. & George, T. F. Paradigm of the time-resolved magneto-optical Kerr effect for femtosecond magnetism. *Nature Physics* **5**, 499–502 (2009). URL www.nature.com/naturephysics.

[3] Johnson, S. L. *et al.* Watching ultrafast responses of structure and magnetism in condensed matter with momentum-resolved probes. *Structural Dynamics* **4**, 61506 (2017). URL https://doi.org/10.1063/1.4996176.

[4] Radu, I. *et al.* Laser-induced generation and quenching of magnetization on FeRh studied with time-resolved x-ray magnetic circular dichroism. *Physical Review B* **81**, 104415 (2010). URL https://link.aps.org/doi/10.1103/PhysRevB.81.104415.

[5] Weller, D. *et al.* High K_u materials approach to 100 Gbits/in. *IEEE Transactions on Magnetics* **36**, 10–15 (2000).

[6] Pál, L., Zimmer, G., Picoch, J. C. & Tarnóczi, T. The magnetic field dependence of the antiferromagnetic-ferromagnetic transition temperature in FeRh. *Acta Physica Academiae Scientiarum Hungaricae* **32**, 135–140 (1972). URL https://link.springer.com/article/10.1007/BF03157301.

[7] Fallot, M. Les alliages du fer avec les métaux de la famille du platine. *Annales de Physique* **11**, 291–332 (1938). URL https://www.annphys.org/articles/anphys/abs/1938/10/anphys19381110p291/anphys19381110p291.html.

[8] Foerster, M. *et al.* Local manipulation of metamagnetism by strain nanopatterning. *Materials Horizons* **7**, 2056–2062 (2020). URL https://pubs.rsc.org/en/content/articlehtml/2020/mh/d0mh00601g.

[9] Costa, P., Costa, C. M. & Lanceros-Mendez, S. *Advanced Lightweight Multifunctional Materials* (Elsevier, 2021).

[10] Lendlein, A. & Trask, R. S. Multifunctional materials: Concepts, function-structure relationships, knowledge-based design, translational materials research. *Multifunctional Materials* **1**, 010201 (2018). URL https://iopscience.iop.org/article/10.1088/2399-7532/aada7b.

[11] Thiele, J. U., Maat, S. & Fullerton, E. FeRh/FePt antiferromagnet/ferromagnet exchange spring media for thermally assisted magnetic recording. *Applied Physics Letters* **82**, 2859 (2003). URL https://doi.org/10.1063/1.1571232.

[12] Peters, S. Multifunctional materials. In *Material Revolution 2*, 122–151 (CRC Press, 2014).

[13] Stoffel, A. M. Magnetic and magneto-optic properties of FeRh and CrO_2. *Journal of Applied Physics* **40**, 1238–1239 (1969). URL https://doi.org/10.1063/1.1657608.

[14] Kouvel, J. S. & Hartelius, C. Anomalous Magnetic Moments and Transformations in the ordered alloy FeRh. *Journal of Applied Physics* **33**, 1343 (1962). URL https://doi.org/10.1063/1.1728721.

[15] Zsoldos, L. Lattice Parameter Change of FeRh Alloys due to Antiferromagnetic-Ferromagnetic Transformation. *physica status solidi (b)* **20**, 25–28 (1967). URL http://doi.wiley.com/10.1002/pssb.19670200148.

[16] Correia, D. M., Martins, P., Tariq, M., Esperança, J. M. & Lanceros-Méndez, S. Low-field giant magneto-ionic response in polymer-based nanocomposites. *Nanoscale* **10**, 15747–15754 (2018). URL https://pubs.rsc.org/en/content/articlehtml/2018/nr/c8nr03259a.

[17] Coey, J. M. D. *Magnetism and Magnetic Materials* (Cambridge University Press, Cambridge, 2010).

[18] Fassbender, J., Ravelosona, D. & Samson, Y. Tailoring magnetism by light-ion irradiation. *Journal of Physics D* **37**, 179–196 (2004). URL https://doi.org/10.1088/0022-3727/37/16/R01.

[19] Mei, A. B. *et al.* Magnetic Patterning: Local Photothermal Control of Phase Transitions for On-Demand Room-Temperature Rewritable Magnetic Patterning. *Advanced Materials* **32**, 2070168 (2020). URL https://onlinelibrary.wiley.com/doi/abs/10.1002/adma.202070168.

[20] Le Graët, C. *et al.* Sputter Growth and Characterization of Metamagnetic B2-ordered FeRh Epilayers. *Journal of Visualized Experiments* **80**, 1–8 (2013). URL https://dx.doi.org/10.3791/50603.

[21] Lewis, L. H., Marrows, C. H. & Langridge, S. Coupled magnetic, structural, and electronic phase transitions in FeRh. *Journal of Physics D* **49**, 323002 (2016). URL https://doi.org/10.1088/0022-3727/49/32/323002.

[22] Garcia-Sanchez, F., Chubykalo-Fesenko, O., Mryasov, O., Chantrell, R. W. & Guslienko, K. Y. Exchange spring structures and coercivity reduction in FePtFeRh bilayers: A comparison of multiscale and micromagnetic calculations. *Applied Physics Letters* **87**, 1–3 (2005). URL https://doi.org/10.1063/1.2051789.

[23] Fullerton, E. E., Jiang, J. S., Grimsditch, M., Sowers, C. H. & Bader, S. D. Exchange-spring behavior in epitaxial hard / soft magnetic bilayers. *Physical Review B* **58**, 193–200 (1998). URL https://doi.org/10.1103/PhysRevB.58.12193.

[24] Stöhr, J. *et al.* Images of the antiferromagnetic structure of a NiO(100) surface by means of X-ray magnetic linear dichroism spectromicroscopy. *Physical Review Letters* **83**, 1862–1865 (1999). URL https://journals.aps.org/prl/abstract/10.1103/PhysRevLett.83.1862.

[25] Marti, X. *et al.* Room-temperature antiferromagnetic memory resistor. *Nature Materials* **13**, 367–374 (2014). URL https://doi.org/10.1038/nmat3861. 0402594v3.

[26] Jungwirth, T., Marti, X., Wadley, P. & Wunderlich, J. Antiferromagnetic spintronics. *Nature Nanotechnology* **11**, 231–241 (2016). URL https://link.aps.org/doi/10.1103/RevModPhys.90.015005. 1606.04284.

[27] Griggs, W. *et al.* Polarized neutron reflectometry characterization of interfacial magnetism in an FePt/FeRh exchange spring. *Physical Review Materials* **6**, 024403 (2022). URL https://doi.org/10.1103/PhysRevMaterials.6.024403.

[28] Vedmedenko, E. Y. *et al.* The 2020 magnetism roadmap. *Journal of Physics D: Applied Physics* **53**, 453001 (2020). URL https://iopscience.iop.org/article/10.1088/1361-6463/ab9d98.

[29] Temple, R. C. *et al.* Antiferromagnetic-ferromagnetic phase domain development in nanopatterned FeRh islands. *Physical Review Materials* **104406**, 1–9 (2018). URL https://journals.aps.org/prmaterials/pdf/10.1103/PhysRevMaterials.2.104406. 1806.07321.

[30] Ünal, A. A. *et al.* Laser-driven formation of transient local ferromagnetism in FeRh thin films. *Ultramicroscopy* **183**, 104–108 (2017). URL https://doi.org/10.1016/j.ultramic.2017.03.024.

[31] Mariager, S. O. *et al.* Structural and magnetic dynamics of a laser induced phase transition in FeRh. *Physical Review Letters* **108**, 087201 (2012). URL https://link.aps.org/doi/10.1103/PhysRevLett.108.087201. 1111.6435.

[32] Pellegrini, C. X-ray free-electron lasers: From dreams to reality. *Physica Scripta* **2016**, 014004 (2016). URL https://doi.org/10.1088/1402-4896/aa5281.

[33] Blume, M. & Gibbs, D. Polarization dependence of magnetic x-ray scattering. *Physical Review B* **37**, 1779–1789 (1988). URL https://link.aps.org/doi/10.1103/PhysRevB.37.1779.

[34] Pressacco, F. *et al.* Subpicosecond metamagnetic phase transition in FeRh driven by non-equilibrium electron dynamics. *Nature Communications* **12**, 5088 (2021). URL https://www.nature.com/articles/s41467-021-25347-3. 2102.09265.

[35] Derlet, P. M. Landau-Heisenberg Hamiltonian model for FeRh. *Physical Review B* **85**, 174431 (2012). URL https://journals.aps.org/prb/abstract/10.1103/PhysRevB.85.174431.

[36] Uhlíř, V., Arregi, J. A. & Fullerton, E. E. Colossal magnetic phase transition asymmetry in mesoscale FeRh stripes. *Nature Communications* **7**, 13113 (2016). URL http://www.nature.com/doifinder/10.1038/ncomms13113. 1605.06823.

[37] Grimes, M. *et al.* X-ray investigation of long-range antiferromagnetic order in FeRh. *AIP Advances* **12**, 035048 (2022). URL https://doi.org/10.1063/9.0000320.

[38] Grimes, M. *et al.* Determination of sub-ps lattice dynamics in FeRh thin films. *Scientific Reports* **12**, 8584 (2022). URL https://doi.org/10.1038/s41598-022-12602-w.

[39] Kittel, C. *Introduction to solid state physics* (Wiley, Singapore, 2005).

[40] Dresselhaus, M., Dresselhaus, G., Cronin, S. B. & Filho, A. G. S. *Solid State Properties - From Bulk to Nano* (Springer, Heidelberg, 2018).

[41] Warren, B. E. *X-ray diffraction* (Dover Publications, 1969).

[42] Crystallography. The symmetry of crystals. Representation of Bravais lattices. URL https://www.xtal.iqfr.csic.es/Cristalografia/parte_03_4-en.html.

[43] Thomson, J. J. On the Structure of the Atom: an Investigation of the Stability and Periods of Oscillation of a number of Corpuscles arranged at equal intervals around the Circumference of a Circle; with Application of the Results to the Theory of Atomic Structure. *Philosophical Magazine* **7**, 237–265 (1904).

[44] Griffiths, D. J. *Introduction to quantum mechanics* (Cambridge University Press, Cambridge, 2018).

[45] Bragg, W. H. & Bragg, W. L. The reflection of X-rays by crystals. *Proceedings of the Royal Society of London* **88**, 428–438 (1913). URL https://royalsocietypublishing.org/doi/abs/10.1098/rspa.1913.0040.

[46] Bragg, W. L. & Williams, E. J. The effect of thermal agitation on atomic arrangement in alloys. *Proceedings of the Royal Society of London* **145**, 699–730 (1934). URL https://royalsocietypublishing.org/doi/abs/10.1098/rspa.1934.0132.

[47] Scherrer, P. Bestimmung der inneren Struktur und der Größe von Kolloidteilchen mittels Röntgenstrahlen. *Nachrichten von der Gesellschaft der Wissenschaften zu Göttingen, Mathematisch-Physikalische Klasse* **1918**, 98–100 (1918).

[48] Blume, M. Magnetic scattering of x rays . *Journal of Applied Physics* **57**, 3615 (1985). URL https://doi.org/10.1063/1.335023.

[49] Gibbs, D. *et al.* Polarization and resonance studies of x-ray magnetic scattering in holmium. *Physical Review B* **43**, 5663–5681 (1991). URL https://doi.org/10.1103/PhysRevB.43.5663.

[50] Rackham, H. & Pliny. *Pliny the Elder, Historia naturalis*. Loeb classical library (Harvard University Press, Cambridge Mass., 1938).

[51] Schmidl, P. S. Two Early Arabic Sources on the Magnetic Compass. *Journal of Arabic and Islamic Studies* 81–132 (1996). URL https://journals.uio.no/JAIS/article/view/4547.

[52] Gilbert, W. *De Magnete* (Peter Short, London, 1600). URL https://www.gutenberg.org/files/33810/33810-h/33810-h.htm.

[53] Faraday, M. *Experimental Researches In Electricity* (The University of London, London, 1849). URL https://www.gutenberg.org/files/14986/14986-h/14986-h.htm.

[54] Clerk Maxwell, J. A dynamical theory of the electromagnetic field. *Royal Society* 459–512 (1864). URL https://royalsocietypublishing.org/doi/pdf/10.1098/rstl.1865.0008.

[55] Bohr, N. On the Constitution of Atoms and Molecules. *Philosophical Magazine Series* **6**, 1–25 (1913). URL http://dbhs.wvusd.k12.ca.us/Chem-History/Bohr/Bohr-1913a.html.

[56] Cullity, B. D. & Graham, C. D. *Introduction to Magnetic Materials* (John Wiley & Sons, Inc., Hoboken, NJ, USA, 2008).

[57] Dirac, P. *The Principles of Quantum Mechanics* (Oxford University Press, Oxford, 1930).

[58] Brodsky, S. J. *et al.* A nonperturbative calculation of the electron's magnetic moment. *Nuclear Physics B* **703**, 333–362 (2004). URL https://doi.org/10.1016/j.nuclphysb.2004.10.027.

[59] Shull, C. G., Strauser, W. A. & Wollan, E. O. Neutron Diffraction by Paramagnetic and Antiferromangetic Substances. *American Physical Society* **83**, 333–345 (1951). URL https://doi.org/10.1103/PhysRev.83.333.

[60] Mohn, P. *Magnetism in the Solid State: Introduction* (Springer, Berlin, 2005).

[61] Anderson, P. W. Localized Magnetic States in Metals. *Physical Review* **124**, 41 (1961). URL https://journals.aps.org/pr/abstract/10.1103/PhysRev.124.41.

[62] Gilbert, T. A Lagrangian formulation of the gyromagnetic equation of the magnetic field. *Physical Review* **100**, 1243 (1955).

[63] Gilbert, T. L. A phenomenological theory of damping in ferromagnetic materials. *IEEE Transactions on Magnetics* **40**, 3443–3449 (2004). URL https://doi.org/10.1109/TMAG.2004.836740.

[64] Heisenberg, W. Zur Theorie des Ferromagnetismus. *Zeitschrift für Physik* **49**, 619–636 (1928). URL https://link.springer.com/article/10.1007/BF01328601.

[65] Heusler, F. Über die Synthese ferromagnetischer Manganlegierungen. *Verhandlungen der Deutschen physikalischen Gesellschaft* **12**, 219–223 (1903).

[66] Neel, L. Magnetic properties of ferrites; ferrimagnetism and antiferromagnetism. *Annales de Physique* **3**, 137–198 (1948). URL http://garfield.library.upenn.edu/classics1984/A1984TA22100001.pdf.

[67] Dubowik, J. Shape anisotropy of magnetic heterostructures. *Physical Review B* **54**, 1088 (1996). URL https://journals.aps.org/prb/abstract/10.1103/PhysRevB.54.1088.

[68] Stoner, E. C. & Wohlfarth, E. P. A mechanism of magnetic hysteresis in heterogeneous alloys. *Philosophical Transactions of the Royal Society of London* **240**, 599–642 (1948). URL https://royalsocietypublishing.org/doi/abs/10.1098/rsta.1948.0007.

[69] Osborn, J. A. Demagnetizing factors of the general ellipsoid. *Physical Review* **67**, 351–357 (1945). URL https://journals.aps.org/pr/abstract/10.1103/PhysRev.67.351.

[70] Landau, L. D. & Lifshits, E. M. *Electrodynamics of Continuous Media*, vol. 8 (Butterworth-Heinemann, 1982).

[71] Herak, M. Cubic magnetic anisotropy of the antiferromagnetically ordered Cu_3TeO_6. *Solid State Communications* **151**, 1588–1592 (2011). URL https://doi.org/10.1016/j.ssc.2011.07.024.

[72] Hrkac, G. *et al.* The role of local anisotropy profiles at grain boundaries on the coercivity of $Nd_2Fe_{14}B$ magnets. *Applied Physics Letters* **97**, 232511 (2010). URL https://doi.org/10.1063/1.3519906.

[73] Bennett, A. & Cooper, B. Origin of the Magnetic "Surface Anisotropy" of Thin Ferromagnetic Films. *Physical Review B* **3**, 1642 (1971). URL https://doi.org/10.1103/PhysRevB.3.1642.

[74] Bhatia, E., Barber, Z. H., Maasilta, I. J. & Senapati, K. Domain wall induced modulation of low field H-T phase diagram in patterned superconductor-ferromagnet stripes. *AIP Advances* **9**, 045107 (2019). URL https://aip.scitation.org/doi/abs/10.1063/1.5087925.

[75] Lewis, L. H. & Jiménez-Villacorta, F. Perspectives on permanent magnetic materials for energy conversion and power generation. *Metallurgical and Materials Transactions A* **44**, 2–20 (2013). URL https://doi.org/10.1007/s11661-012-1278-2.

[76] Shull, R. D., Kabanov, Y. P., Gornakov, V. S., Chen, P. J. & Nikitenko, V. I. Shape critical properties of patterned Permalloy thin films. *Journal of Magnetism and Magnetic Materials* **400**, 191–199 (2016). URL https://www.ncbi.nlm.nih.gov/pmc/articles/PMC4778257/.

[77] Pandya, N. Y., Mevada, A. D. & Gajjar, P. N. Lattice dynamical and thermodynamic properties of $FeNi_3$, FeNi and Fe_3Ni invar materials. *Computational Materials Science* **123**, 287–295 (2016). URL https://doi.org/10.1016/j.commatsci.2016.07.001.

[78] Scholl, A. *et al.* Observation of antiferromagnetic domains in epitaxial thin films. *Science* **287**, 1014–1016 (2000). URL https://doi.org/10.1126/science.287.5455.1014.

[79] Marrows, C. H. Spin-polarised currents and magnetic domain walls. *Advances in Physics* **54**, 585–713 (2007). URL https://doi.org/10.1080/00018730500442209.

[80] Slonczewski, J. C. Current-driven excitation of magnetic multilayers. *Journal of Magnetism and Magnetic Materials* **159**, L1–L7 (1996). URL https://doi.org/10.1016/0304-8853(96)00062-5.

[81] Berger, L. Emission of spin waves by a magnetic multilayer traversed by a current. *Physical Review B* **54**, 9353 (1996). URL https://doi.org/10.1103/PhysRevB.54.9353.

[82] Kittel, C. On the Theory of Ferromagnetic Resonance Absorption. *Physical Review* **73**, 155 (1948). URL https://journals.aps.org/pr/abstract/10.1103/PhysRev.73.155.

[83] Griffiths, J. H. Anomalous High-frequency Resistance of Ferromagnetic Metals. *Nature* **158**, 670–671 (1946). URL https://www.nature.com/articles/158670a0.

[84] Beaurepaire, E., Merle, J. C., Daunois, A. & Bigot, J. Y. Ultrafast spin dynamics in ferromagnetic nickel. *Physical Review Letters* **76**, 4250–4253 (1996). URL https://journals.aps.org/prl/abstract/10.1103/PhysRevLett.76.4250.

[85] Kaganov, M., Lifshitz, I. & Tanatarov, L. Relaxation between Electrons and the Crystalline Lattice. *Zhurnal Eksperimental'noi i Teoreticheskoi Fiziki* **31**, 232 (1957).

[86] Schoenlein, R. W., Lin, W. Z., Fujimoto, J. G. & Eesley, G. L. Femtosecond studies of nonequilibrium electronic processes in metals. *Physical Review Letters* **58**, 1680–1683 (1987). URL https://journals.aps.org/prl/pdf/10.1103/PhysRevLett.58.1680.

[87] Koopmans, B. *et al.* Explaining the paradoxical diversity of ultrafast laser-induced demagnetization Demagnetization by spin-flip scattering. *Nature Materials* **9**, 259–265 (2010). URL https://www.nature.com/articles/nmat2593.

[88] Ju, G. *et al.* Ultrafast time resolved photoinduced magnetization rotation in a ferromagnetic/antiferromagnetic exchange coupled system. *Physical Review Letters* **82**, 3705–3708 (1999). URL https://journals.aps.org/prl/abstract/10.1103/PhysRevLett.82.3705.

[89] Onuki, A. *Phase Transition Dynamics* (Cambridge University Press, 2002).

[90] Ju, G. *et al.* Ultrafast generation of ferromagnetic order via a laser-induced phase transformation in FeRh thin films. *Physical Review Letters* **93** (2004). URL https://doi.org/10.1103/PhysRevLett.93.197403.

[91] Kren, E., Pal, L. & Szabo, P. Neutron diffraction investigation of the antiferromagnetic-ferromagnetic transformation in the FeRh alloy. *Physics Letters* **9**, 297–298 (1964). URL https://doi.org/10.1016/0031-9163(64)90369-5.

[92] Kouvel, J. S. Unusual nature of the abrupt magnetic transition in FeRh and its pseudobinary variants. *Journal of Applied Physics* **37**, 1257–1258 (1966). URL https://doi.org/10.1063/1.1708424.

[93] Richardson, M. J., Melville, D. & Ricodeau, J. A. Specific heat measurements on an Fe Rh alloy. *Physics Letters A* **46**, 153–154 (1973). URL https://doi.org/10.1016/0375-9601(73)90071-6.

[94] Ricodeau, J. A. & Melville, D. Model of the antiferromagnetic-ferromagnetic transition in FeRh alloys. *Journal of Physics F* **2**, 337–350 (1972). URL https://doi.org/10.1088/0305-4608/2/2/024.

[95] Ricodeau, J. & Melville, D. High field magnetostriction in a meta-magnetic FeRh alloy. *Journal de Physique* **35**, 149–152 (1974). URL https://hal.archives-ouvertes.fr/jpa-00208138.

[96] Annaorazov, M. P. *et al.* Alloys of the FeRh system as a new class of working material for magnetic refrigerators. *Cryogenics* **32**, 867–872 (1992). URL https://www.sciencedirect.com/science/article/pii/001122759290352B.

[97] Navarro, E., Multigner, M., Yavari, A. R. & Hernando, A. The spin glass state of metastable fcc FeRh. *Europhysics Letters* **35**, 307–312 (1996). URL http://stacks.iop.org/0295-5075/35/.

[98] Ohtani, Y. & Hatakeyama, I. Features of broad magnetic transition in FeRh thin film. *Journal of Magnetism and Magnetic Materials* **131**, 339–344 (1994). URL https://doi.org/10.1016/0304-8853(94)90278-X.

[99] Thiele, J. U., Maat, S., Robertson, J. L. & Fullerton, E. E. Magnetic and structural properties of FePt-FeRh exchange spring films for thermally assisted magnetic recording media. In *IEEE Transactions on Magnetics*, vol. 40, 2537–2542 (2004).

[100] Yuasa, S., Katayama, T., Murata, K., Usukura, M. & Suzuki, Y. Epitaxial growth and magnetic properties of B2-type ordered FeRh alloys. *Journal of Magnetism and*

Magnetic Materials **177-181**, 1296–1298 (1998). URL https://doi.org/10.1016/S0304-8853(97)00951-7.

[101] Doerner, M. F. *et al.* Microstructure and thermal stability of advanced longitudinal media. *IEEE Transactions on Magnetics* **36**, 43–47 (2000).

[102] Thiele, J.-U. U., Buess, M. & Back, C. H. Spin dynamics of the antiferromagnetic-to-ferromagnetic phase transition in FeRh on a sub-picosecond time scale. *Applied Physics Letters* **85**, 2857–2859 (2004). URL https://doi.org/10.1063/1.1799244.

[103] Suzuki, I., Koike, T., Itoh, M., Taniyama, T. & Sato, T. Stability of ferromagnetic state of epitaxially grown ordered FeRh thin films. *Journal of Applied Physics* **105**, 07E501 (2009). URL http://aip.scitation.org/doi/10.1063/1.3054386.

[104] Kumar, H. *et al.* Strain effects on the magnetic order of epitaxial FeRh thin films. *Journal of Applied Physics* **124**, 085306 (2018). URL https://aip.scitation.org/doi/abs/10.1063/1.5020160.

[105] Bordel, C. *et al.* Fe spin reorientation across the metamagnetic transition in strained FeRh thin films. *Physical Review Letters* **109**, 117201 (2012). URL https://journals.aps.org/prl/abstract/10.1103/PhysRevLett.109.117201.

[106] Fina, I. *et al.* Flexible Antiferromagnetic FeRh Tapes as Memory Elements. *ACS Applied Materials and Interfaces* **12**, 15389–15395 (2020). URL https://dx.doi.org/10.1021/acsami.0c00704.

[107] Sandratskii, L. M. & Mavropoulos, P. Magnetic excitations and femtomagnetism of FeRh: A first-principles study. *Physical Review B* **83**, 174408 (2011). URL https://link.aps.org/doi/10.1103/PhysRevB.83.174408.

[108] Stamm, C. *et al.* Antiferromagnetic-ferromagnetic phase transition in FeRh probed by x-ray magnetic circular dichroism. *Physical Review B* **77**, 184401 (2008). URL https://journals.aps.org/prb/pdf/10.1103/PhysRevB.77.184401.

[109] Jiménez, M. J., Schvval, A. B. & Cabeza, G. F. Ab initio study of FeRh alloy properties. *Computational Materials Science* **172**, 109385 (2020). URL https://doi.org/10.1016/j.commatsci.2019.109385.

[110] Oshima, R., Hori, F., Kibata, Y., Komatsu, M. & Kiritani, M. Defect structures and phase transitions of FeRh alloys deformed at high speed deformation. *Materials Science and Engineering: A* **350**, 139–144 (2003). URL https://doi.org/10.1016/S0921-5093(02)00715-3.

[111] Bennett, S. P. *et al.* Magnetic order multilayering in FeRh thin films by He-Ion irradiation. *Materials Research Letters* **6**, 106–112 (2018). URL https://www.tandfonline.com/doi/full/10.1080/21663831.2017.1402098.

[112] Massey, J. R. *et al.* Phase boundary exchange coupling in the mixed magnetic phase regime of a Pd-doped FeRh epilayer. *Physical Review Materials* **4**, 024403 (2020). URL https://journals.aps.org/prmaterials/abstract/10.1103/PhysRevMaterials.4.024403. 1807.01615.

[113] Chung, J.-C. *et al.* Investigating the mechanism of magnetic phase transition temperature of FeRh thin films by doping copper impurities. *Materials Chemistry and Physics* **275**, 125252 (2022). URL https://doi.org/10.1016/j.matchemphys.2021.125252.

[114] Nam, N., Lu, W. & Suzuki, T. Temperature Dependence of Magnetic Properties in Epitaxial FePt/FeRh Bilayer. *IEEE Transactions on Magnetics* **45**, 2531–2533 (2009). URL http://ieeexplore.ieee.org/document/4957764/.

[115] Zarkevich, N. A. & Johnson, D. D. FeRh groundstate and martensitic transformation. *Physical Review B* **97**, 014202 (2018). URL https://arxiv.org/pdf/1710.04199.pdf. 1710.04199v2.

[116] Ibarra, M. R. & Algarabel, P. A. Giant volume magnetostriction in the FeRh alloy. *Physical Review B* **50**, 4196–4199 (1994). URL https://journals.aps.org/prb/abstract/10.1103/PhysRevB.50.4196.

[117] Pressacco, F. *et al.* Laser induced phase transition in epitaxial FeRh layers studied by pump-probe valence band photoemission. *Structural Dynamics* **5**, 034501 (2018). URL http://aca.scitation.org/doi/10.1063/1.5027809. 1803.00780.

[118] Wolloch, M. *et al.* Impact of lattice dynamics on the phase stability of metamagnetic FeRh: Bulk and thin films. *Physical Review B* **94**, 174435 (2016). URL https://link.aps.org/doi/10.1103/PhysRevB.94.174435. 1608.04268.

[119] Belov, M. P., Syzdykova, A. B. & Abrikosov, I. A. Temperature-dependent lattice dynamics of antiferromagnetic and ferromagnetic phases of FeRh. *Physical Review B* **101**, 134303 (2020). URL https://journals.aps.org/prb/abstract/10.1103/PhysRevB.101.134303.

[120] Xie, Y. *et al.* Electric field control of magnetic properties in FeRh/PMN-PT heterostructures. *AIP Advances* **8**, 055816 (2018). URL http://aip.scitation.org/doi/10.1063/1.5003435.

[121] Bennett, S. P., Currie, M., van 't Erve, O. M. J. & Mazin, I. I. Spectral reflectivity crossover at the metamagnetic transition in FeRh thin films. *Optical Materials Express* **9**, 2870 (2019). URL https://doi.org/10.1364/OME.9.002870.

[122] Fox, M. *Optical properties of solids* (Oxford University Press, 2001).

[123] Awari, N. *et al.* Monitoring laser-induced magnetization in FeRh by transient terahertz emission spectroscopy. *Applied Physics Letters* **117**, 122407 (2020). URL https://aip.scitation.org/doi/abs/10.1063/5.0019663.

[124] Barker, J. & Chantrell, R. W. Higher-order exchange interactions leading to metamagnetism in FeRh. *Physical Review B* **92**, 1–5 (2015). 1405.3043.

[125] Aschauer, U., Braddell, R., Brechbühl, S. A., Derlet, P. M. & Spaldin, N. A. Strain-induced structural instability in FeRh. *Physical Review B* **94**, 014109 (2016). URL https://journals.aps.org/prb/abstract/10.1103/PhysRevB.94.014109. 1603.01827.

[126] Gu, R. Y. & Antropov, V. P. Dominance of the spin-wave contribution to the magnetic phase transition in FeRh. *Physical Review B* **72**, 012403 (2005). URL https://link.aps.org/doi/10.1103/PhysRevB.72.012403.

[127] Baldasseroni, C. *et al.* Effect of capping material on interfacial ferromagnetism in FeRh thin films. *Journal of Applied Physics* **115**, 43919 (2014). URL http://dx.doi.org/10.1063/1.4862961.

[128] Xie, Y. *et al.* Effect of epitaxial strain and lattice mismatch on magnetic and transport behaviors in metamagnetic FeRh thin films. *AIP Advances* **7**, 056314 (2017). URL https://aip.scitation.org/doi/pdf/10.1063/1.4976301.

[129] Bull, C. *et al.* PNR study of the phase transition in FeRh thin films. *APL Materials* **7**, 101117 (2019). URL https://aip.scitation.org/doi/abs/10.1063/1.5120622.

[130] Ostler, T. A., Barton, C., Thomson, T. & Hrkac, G. Modeling the thickness dependence of the magnetic phase transition temperature in thin FeRh films. *Physical Review B* **95**, 1–7 (2017). URL https://doi.org/10.1103/PhysRevB.95.064415.

[131] Barton, C. W. *et al.* Substrate Induced Strain Field in FeRh Epilayers Grown on Single Crystal MgO (001) Substrates. *Scientific Reports* **7**, 44397 (2017). URL http://dx.doi.org/10.1038/srep44397.

[132] Griggs, W. *et al.* Depth selective magnetic phase coexistence in FeRh thin films. *APL Materials* **8**, 121103 (2020). URL https://aip.scitation.org/doi/abs/10.1063/5.0032130.

[133] Kinane, C. J. *et al.* Observation of a temperature dependent asymmetry in the domain structure of a Pd-doped FeRh epilayer. *New Journal of Physics* **16**, 113073 (2014). URL https://doi.org/10.1088/1367-2630/16/11/113073. 1407.2154.

[134] Eggert, B. *et al.* Magnetic response of FeRh to static and dynamic disorder. *RSC Advances* **10**, 14386–14395 (2020). URL https://pubs.rsc.org/en/content/articlehtml/2020/ra/d0ra01410a. 1911.11256.

[135] Chappert, C. *et al.* Planar patterned magnetic media obtained by ion irradiation. *Science* **280**, 1919–1922 (1998). URL https://doi.org/10.1126/science.280.5371.1919.

[136] Warren, J. L., Barton, C. W., Bull, C. & Thomson, T. Topography dependence of the metamagnetic phase transition in FeRh thin films. *Scientific Reports* **10**, 4030 (2020). URL https://www.nature.com/articles/s41598-020-60767-z.pdf.

[137] Almeida, T. P. *et al.* Direct visualization of the magnetostructural phase transition in nanoscale FeRh thin films using differential phase contrast imaging. *Physical Review Materials* **4**, 034410 (2020). URL https://journals.aps.org/prmaterials/abstract/10.1103/PhysRevMaterials.4.034410.

[138] De Vries, M. A. *et al.* Asymmetric " melting" and " freezing" kinetics of the magnetostructural phase transition in B2-ordered FeRh epilayers. *Applied Physics Letters* **104** (2014). URL https://doi.org/10.1063/1.4883369.

[139] Baldasseroni, C. *et al.* Temperature-driven nucleation of ferromagnetic domains in FeRh thin films. *Applied Physics Letters* **100**, 262401 (2012). URL http://aip.scitation.org/doi/10.1063/1.4730957.

[140] Baldasseroni, C. *et al.* Temperature-driven growth of antiferromagnetic domains in thin-film FeRh. *Journal of Physics: Condensed Matter* **27**, 256001 (2015). URL https://doi.org/10.1088/0953-8984/27/25/256001.

[141] Wörnle, M. S. *et al.* Coexistence of Bloch and Néel walls in a collinear antiferromagnet. *Physical Review B* **103**, 094426 (2021). URL https://journals.aps.org/prb/abstract/10.1103/PhysRevB.103.094426. 2009.09015.

[142] Donnelly, C. *et al.* Three-dimensional magnetization structures revealed with X-ray vector nanotomography. *Nature* **547**, 328–331 (2017). URL https://www.nature.com/articles/nature23006.

[143] Boutet, S. & Yabashi, M. X-Ray Free Electron Lasers and Their Applications. In *X-ray Free Electron Lasers*, 1–21 (Springer, Cham, 2018).

[144] Togashi, T. *et al.* Femtosecond Optical Laser System with Spatiotemporal Stabilization for Pump-Probe Experiments at SACLA. *Applied Sciences* **10**, 7934 (2020). URL https://www.mdpi.com/2076-3417/10/21/7934/htm.

[145] Mansart, B. *et al.* Temperature-dependent electron-phonon coupling in $La_{2-x}Sr_xCuO_4$ probed by femtosecond x-ray diffraction. *Physical Review B* **88**, 054507 (2013). URL https://journals.aps.org/prb/abstract/10.1103/PhysRevB.88.054507.

[146] Polesya, S., Mankovsky, S., Ködderitzsch, D., Minár, J. & Ebert, H. Finite-temperature magnetism of FeRh compounds. *Physical Review B* **93**, 024423 (2016). URL https://doi.org/10.1103/PhysRevB.93.024423.

[147] Menarini, M., Medapalli, R., Fullerton, E. E. & Lomakin, V. Micromagnetic simulation of THz signals in antiferromagnetic FeRh by sub-picosecond thermal pulses. *AIP Advances* **9**, 035040 (2019). URL https://doi.org/10.1063/1.5080170.

[148] Oura, K., Katayama, M., Zotov, A. V., Lifshits, V. G. & Saranin, A. A. *Surface Science*. Advanced Texts in Physics (Springer, Heidelberg, 2003).

[149] Tsui, R. T. Calculation of Ion Bombarding Energy and Its Distribution in rf Sputtering. *Physical Review* **168**, 107 (1968). URL https://journals.aps.org/pr/abstract/10.1103/PhysRev.168.107.

[150] Mubrarak, A., Hamzah, E. & Toff, M. REVIEW OF PHYSICAL VAPOUR DEPOSITION (PVD) TECHNIQUES FOR HARD COATING. *Jurnal Mekankikal* **20**, 42–51 (2005).

[151] Markov, I. & Kaischew, R. Influence of the supersaturation on the mode of film growth. *Kristall und Technik* **11**, 685–697 (1976). URL https://doi.org/10.1002/crat.19760110702.

[152] Thompson, C. V. Solid-State Dewetting of Thin Films. *Annual Review of Materials Research* **42**, 399–434 (2012). URL http://www.annualreviews.org/doi/10.1146/annurev-matsci-070511-155048.

[153] Stepanova, M. & Dew, S. *Nanofabrication: Techniques and principles* (Springer, Vienna, Vienna, 2014).

[154] Christensen, M. *Epitaxy, thin films and superlattices*. Ph.D. thesis, Technical University of Denmark (1997).

[155] Perry, S. S., Kim, H. I., Imaduddin, S., Lee, S. M. & Merrill, P. B. Generation of atomically flat MgO(100) surfaces: Influence of ambient gas composition during high temperature anneals. *Journal of Vacuum Science & Technology A* **16**, 3402–3407 (1998). URL http://avs.scitation.org/doi/10.1116/1.581493.

[156] Collins, R. A., Krier, A. & Abass, A. K. Optical properties of lead phthalocyanine (PbPc) thin films. *Thin Solid Films* **229**, 113–118 (1993). URL https://doi.org/10.1016/0040-6090(93)90417-N.

[157] Botha, J. *et al.* A Novel Technology for Complex Rheological Measurements. In *Annual Waste Management Conference (WM2016): Education & Opportunity in Waste Management* (Pheonix, Arizona, 2016). URL http://eprints.whiterose.ac.uk/94813/.

[158] Knözinger, E., Jacob, K. H., Singh, S. & Hofmann, P. Hydroxyl groups as IR active surface probes on MgO crystallites. *Surface Science* **290**, 388–402 (1993). URL https://doi.org/10.1016/0039-6028(93)90721-U.

[159] Cao, J. *et al.* Magnetization behaviors for FeRh single crystal thin films. *Journal of Applied Physics* **103**, 07F501 (2008). URL http://aip.scitation.org/doi/10.1063/1.2828812.

[160] Madou, M. J. *Fundamentals of Microfabrication* (CRC Press, 2018).

[161] Odian, G. *Principles of Polymerization* (John Wiley & Sons, Inc., 2004).

[162] Rai-Choudhury, P. *Handbook of Microlithography, Micromachining, and Microfabrication, Volume 2: Micromachining and Microfabrication* (SPIE PRESS, 1997).

[163] Broers, A. N., Hoole Andrew, A. C. & Ryan, J. M. Electron beam lithography - Resolution limits. *Microelectronic Engineering* **32**, 131–142 (1996). URL https://doi.org/10.1016/0167-9317(95)00368-1.

[164] Ivin, V. V. *et al.* The inclusion of secondary electrons and Bremsstrahlung X-rays in an electron beam resist model. In *Microelectronic Engineering*, 343–349 (Elsevier, 2002).

[165] Smits, F. M. Measurement of Sheet Resistivities with the Four-Point Probe. *Bell System Technical Journal* **37**, 711–718 (1958). URL https://onlinelibrary.wiley.com/doi/10.1002/j.1538-7305.1958.tb03883.x.

[166] Uhlir, A. The Potentials of Infinite Systems of Sources and Numerical Solutions of Problems in Semiconductor Engineering. *Bell System Technical Journal* **34**, 105–128 (1955). URL https://onlinelibrary.wiley.com/doi/10.1002/j.1538-7305.1955.tb03765.x.

[167] Foner, S. Versatile and sensitive vibrating-sample magnetometer. *Review of Scientific Instruments* **30**, 548–557 (1959). URL https://doi.org/10.1063/1.1716679.

[168] Robinson, C. C. Longitudinal Kerr Magneto-Optic Effect in Thin Films of Iron, Nickel, and Permalloy. *Journal of the Optical Society of America* **53**, 681–689 (1963). URL https://doi.org/10.1364/JOSA.53.000681.

[169] Hunt, R. P. Magneto-Optic Scattering from Thin Solid Films. *Journal of Applied Physics* **38**, 1652 (1967). URL https://doi.org/10.1063/1.1709738.

[170] You, C. Y. & Shin, S. C. Derivation of simplified analytic formulae for magneto-optical Kerr effects. *Applied Physics Letters* **69**, 1315–1317 (1996). URL https://doi.org/10.1063/1.117579.

[171] Reim, W. & Schoenes, J. Magneto-optical spectroscopy of f-electron systems. In *Handbook of Ferromagnetic Materials*, 133–236 (Springer, 1990).

[172] Moreno, I., Araiza, J. J. & Avendano-Alejo, M. Thin-film spatial filters. *Optics Letters* **30**, 914 (2005). URL https://doi.org/10.1364/OL.30.000914.

[173] Downer, M. C. & Shank, C. V. Ultrafast heating of silicon on sapphire by femtosecond optical pulses. *Physical Review Letters* **56**, 761–764 (1986). URL https://journals.aps.org/prl/abstract/10.1103/PhysRevLett.56.761.

[174] Shank, C. V., Yen, R. & Hirlimann, C. Time-Resolved Reflectivity Measurements of Femtosecond-Optical-Pulse-Induced Phase Transitions in Silicon. *Physical Review Letters* **50**, 454 (1983). URL https://journals.aps.org/prl/abstract/10.1103/PhysRevLett.50.454.

[175] Sabbah, A. J. & Riffe, D. M. Femtosecond pump-probe reflectivity study of silicon carrier dynamics. *Physical Review B* **66**, 165217 (2002). URL https://doi.org/10.1103/PhysRevB.66.165217.

[176] Savitzky, A. & Golay, M. J. Smoothing and Differentiation of Data by Simplified Least Squares Procedures. *Analytical Chemistry* **36**, 1627–1639 (1964). URL https://pubs.acs.org/doi/abs/10.1021/ac60214a047.

[177] Evans, R. F. *et al.* Atomistic spin model simulations of magnetic nanomaterials. *Journal of Physics Condensed Matter* **26**, 103202 (2014). URL https://doi.org/10.1088/0953-8984/26/10/103202. 1310.6143.

[178] Saidl, V. *et al.* Investigation of magneto-structural phase transition in FeRh by reflectivity and transmittance measurements in visible and near-infrared spectral region. *New Journal of Physics* **18**, 083017 (2016). URL https://iopscience.iop.org/article/10.1088/1367-2630/18/8/083017.

[179] COMSOL Multiphysics® v. 5.5. URL www.comsol.com.

[180] Polyak, B. T. *Introduction to optimization* (Optimization Software, Publications Division, 1987).

[181] Hestenes, M. R. & Stiefel, E. Methods of Conjugate Gradients for Solving Linear Systems. *Journal of Research of the National Bureau of Standards* **49**, 409–436 (1952). URL https://doi.org/10.6028/jres.049.044.

[182] Chirkova, A. *et al.* Giant adiabatic temperature change in FeRh alloys evidenced by direct measurements under cyclic conditions. *Acta Materialia* **106**, 15–21 (2016). URL http://dx.doi.org/10.1016/j.actamat.2015.11.054.

[183] Cooke, D. W. *et al.* Thermodynamic measurements of Fe-Rh alloys. *Physical Review Letters* **109**, 255901 (2012). URL https://link.aps.org/doi/10.1103/PhysRevLett.109.255901.

[184] On a new kind of rays. *Nature* **53**, 274–276 (1896). URL https://doi.org/10.1038/053274b0.

[185] Yabashi, M., Tanaka, H. & Ishikawa, T. Overview of the SACLA facility. *Journal of Synchrotron Radiation* **22**, 477–484 (2015). URL https://doi.org/10.1107/S1600577515004658.

[186] Skarzynski, T. Collecting data in the home laboratory: evolution of X-ray sources, detectors and working practices. *Acta Crystallographica Section D* **69**, 1283 (2013). URL https://www.ncbi.nlm.nih.gov/pmc/articles/PMC3689531/.

[187] Ayers, J. & Ladell, J. Spectral widths of the Cu K-α lines. *Physical Review A* **37**, 2404 (1988). URL https://journals.aps.org/pra/abstract/10.1103/PhysRevA.37.2404.

[188] Inaba, K. & Suhiko. X-ray thin-film measurement techniques I. Overview. *The Rigaku Journal* **24**, 10–15 (2008). URL https://www.rigaku.com/journal/summer-2008-volume-24-no-1/10-15.

[189] Wang, H. W. *et al.* Standing [111] gold nanotube to nanorod arrays via template growth. *Nanotechnology* **17**, 2689–2694 (2006). URL https://doi.org/10.1088/0957-4484/17/10/041.

[190] Cramer, S. P. X-ray Optics and Synchrotron Beamlines. In *X-Ray Spectroscopy with Synchrotron Radiation*, 69–105 (Springer, Cham, 2020).

[191] Macgillavry, C. H. & Strijk, B. Determination of Order Parameters from the X-Ray Diffraction Effect. *Nature* **157**, 135–136 (1946). URL https://www.nature.com/articles/157135a0.

[192] Momma, K. & Izumi, F. VESTA 3 for three-dimensional visualization of crystal, volumetric and morphology data. *Journal of Applied Crystallography* **44**, 1272–1276 (2011). URL https://onlinelibrary.wiley.com/doi/full/10.1107/S0021889811038970.

[193] Cullity, B. D. *Elements of X-ray diffraction* (Addison-Wesley Publishing Company, 1956).

[194] Hardy, R. J. & Day, M. A. Correlated Einstein model for the equilibrium properties of solids. *Physical Review B* **29**, 4108 (1984). URL https://doi.org/10.1103/PhysRevB.29.4108.

[195] Debye, P. Interferenz von Röntgenstrahlen und Wärmebewegung. *Annalen der Physik* **348**, 49–92 (1913). URL https://doi.org/10.1002/andp.19133480105.

[196] Waller, I. Zur Frage der Einwirkung der Wärmebewegung auf die Interferenz von Röntgenstrahlen. *Zeitschrift für Physik* **17**, 398–408 (1923). URL https://doi.org/10.1007/BF01328696.

[197] Horning, R. D. & Staudenmann, J. The Debye–Waller factor for polyatomic solids. Relationships between X-ray and specific-heat Debye temperatures. The Debye–Einstein model. *Acta Crystallographica Section A* **44**, 136–142 (1988). URL https://doi.org/10.1107/S0108767387009322.

[198] Klug, H. & Alexander, L. *X-ray diffraction procedures: for polycrystalline and amorphous materials* (Wiley, 1974).

[199] Daillant, J. & Gibaud, A. *X-ray and Neutron Reflectivity. Principles and Applications*. Lecture Notes in Physics (Springer, Berlin, Heidelberg, 2009).

[200] Björck, M. & Andersson, G. GenX: An extensible X-ray reflectivity refinement program utilizing differential evolution. *Journal of Applied Crystallography* **40**, 1174–1178 (2007). URL https://doi.org/10.1107/S0021889807045086. 1503.07163.

[201] Kiessig, H. Untersuchungen zur Totalreflexion von Röntgenstrahlen. *Annalen der Physik* **402**, 715–768 (1931). URL http://doi.wiley.com/10.1002/andp.19314020607.

[202] Schlomka, J. P. *et al.* X-ray diffraction from Si/Ge layers: Diffuse scattering in the region of total external reflection. *Physical Review B* **51**, 2311–2321 (1995). URL https://journals.aps.org/prb/abstract/10.1103/PhysRevB.51.2311.

[203] Ulyanenkov, A., Omote, K. & Harada, J. The genetic algorithm: refinement of X-ray reflectivity data from multilayers and thin films. *Physica B* **283**, 237–241 (2000). URL https://doi.org/10.1016/S0921-4526(99)01972-9.

[204] Parratt, L. G. Surface studies of solids by total reflection of x-rays. *Physical Review* **95**, 359–369 (1954). URL https://link.aps.org/doi/10.1103/PhysRev.95.359.

[205] Pape, I., Hase, T., Tanner, B. & Wormington, M. Analysis of grazing incidence X-ray diffuse scatter from Co-Cu multilayers. *Physica B* **253**, 278–279 (1998). URL https://doi.org/10.1016/S0921-4526(98)00395-0.

[206] McElreath, R. *Statistical Rethinking* (Chapman and Hall, 2020).

[207] Fewster, P. F. Reciprocal space mapping. *Critical Reviews in Solid State and Materials Sciences* **22**, 69–110 (1997). URL http://link.springer.com/10.1007/978-1-4615-5879-8_19.

[208] Taylor, J. R. J. R. *An introduction to error analysis: the study of uncertainties in physical measurements* (University Science Books, Sausalito, California, 1982).

[209] Hughes, I. & Hase, T. *Measurements and their uncertainties: a practical guide to modern error analysis* (Oxford University Press, 2010).

[210] Wilson, E. J. N. Fifty years of synchrotrons. In *5th European Particle Accelerator Conference*, 135–139 (Barcelona, 1996). URL https://cds.cern.ch/record/339572.

[211] Courant, E. D., Livingston, M. S. & Snyder, H. S. The strong-focusing synchroton - A new high energy accelerator. *Physical Review* **88**, 1190–1196 (1952). URL https://journals.aps.org/pr/abstract/10.1103/PhysRev.88.1190.

[212] Chao, A. W., Mess, K. H., Tigner, M. & Zimmermann, F. *Handbook of accelerator physics and engineering* (World Scientific Publishing Co., 2013).

[213] Christou, C. & Kempson, V. C. Operation of the diamond light source injector. In *Proceedings of the IEEE Particle Accelerator Conference*, 1112–1114 (2007).

[214] Christou, C. & Kempson, V. C. The Diamond Light Source booster RF system. In *Proceedings of EPAC 2006* (Edinburgh, 2006).

[215] Lichtenberg, A. J. Optimization of particle injection into a synchrotron. *Review of Scientific Instruments* **34**, 1196–1199 (1963). URL https://doi.org/10.1063/1.1718175.

[216] Haensel, R. ESRF and the third generation of synchrotron radiation sources. In *AIP Conference Proceedings*, vol. 258, 665–672 (American Institute of Physics, 2008). URL https://aip.scitation.org/doi/abs/10.1063/1.42488.

[217] Courant, E. D. & Snyder, H. S. Theory of the alternating-gradient synchrotron. *Annals of Physics* **3**, 1–48 (1958). URL https://doi.org/10.1016/0003-4916(58)90012-5.

[218] Motz, H., Thon, W. & Whitehurst, R. N. Experiments on radiation by fast electron beams. *Journal of Applied Physics* **24**, 826–833 (1953). URL https://aip.scitation.org/doi/abs/10.1063/1.1721389.

[219] Chubar, O., Elleaume, P. & Snigirev, A. Phase analysis and focusing of synchrotron radiation. *Nuclear Instruments and Methods in Physics Research, Section A* **435**, 495–508 (1999). URL https://doi.org/10.1016/S0168-9002(99)00581-1.

[220] Kraft, P. *et al.* Performance of single-photon-counting PILATUS detector modules. *Journal of Synchrotron Radiation* **16**, 368–375 (2009). URL https://doi.org/10.1107/S0909049509009911.

[221] Willmott, P. R. *et al.* The Materials Science beamline upgrade at the Swiss Light Source. *Journal of Synchrotron Radiation* **20**, 667–682 (2013). URL https://doi.org/10.1107/s0909049513018475.

[222] Bruckel, T. *et al.* Antiferromagnetic order and phase transitions in GdS as studied with X-ray resonance-exchange scattering. *European Physical Journal B* **19**, 475–490 (2001). URL https://link.springer.com/article/10.1007/s100510170293.

[223] Image Gallery - I16 - Diamond Light Source (2020). URL https://www.diamond.ac.uk/Instruments/Magnetic-Materials/I16/Image-Gallery.html.

[224] You, H. Angle calculations for a '4S+2D' six-circle diffractometer. *Journal of Applied Crystallography* **32**, 614–623 (1999). URL https://onlinelibrary.wiley.com/doi/full/10.1107/S0021889899001223.

[225] Rogers, T. H. High-intensity radiation from beryllium-window X-ray tubes. *Radiology* **48**, 594–603 (1947). URL https://pubs.rsna.org/doi/abs/10.1148/48.6.594.

[226] Kurahashi, M., Honda, K., Goto, M., Inari, Y. & Katayama, C. Multimode high-angular-resolution powder diffractometer. *Journal of Applied Crystallography* **24**, 61–63 (1991). URL https://doi.org/10.1107/S0021889890008780.

[227] Barrett, H. H. & Myers, K. J. *Foundations of Image Science.* (Wiley, 2013).

[228] Turecek, D., Jakubek, J., Kroupa, M. & Soukup, P. Energy calibration of pixel detector working in time-over-threshold mode using test pulses. In *IEEE Nuclear Science Symposium Conference Record*, 1722–1725 (Institute of Electrical and Electronics Engineers Inc., 2011). URL https://doi.org/10.1109/NSSMIC.2011.6154668.

[229] Tono, K. *et al.* Beamline, experimental stations and photon beam diagnostics for the hard x-ray free electron laser of SACLA. *New Journal of Physics* **15**, 083035 (2013). URL https://iopscience.iop.org/article/10.1088/1367-2630/15/8/083035.

[230] Kameshima, T. *et al.* Development of an X-ray pixel detector with multi-port charge-coupled device for X-ray free-electron laser experiments. *Review of Scientific Instruments* **85**, 033110 (2014). URL https://aip.scitation.org/doi/abs/10.1063/1.4867668.

[231] O'Shea, P. G. & Freund, H. P. Free-electron lasers: Status and applications. *Science* **292**, 1853–1858 (2001). URL http://www.ncbi.nlm.nih.gov/pubmed/11397938.

[232] Malvestuto, M., Ciprian, R., Caretta, A., Casarin, B. & Parmigiani, F. Ultrafast magnetodynamics with free-electron lasers. *Journal of Physics: Condensed Matter* **30**, 053002 (2018). URL https://doi.org/10.1088/1361-648X/aaa211.

[233] McNeil, B. W. J. & Thompson, N. R. X-ray free-electron lasers. *Nature Photonics* **4**, 814–821 (2010). URL https://doi.org/10.1038/nphoton.2010.239.

[234] Feldhaus, J., Arthur, J. & Hastings, J. B. X-ray free-electron lasers. *Journal of Physics B* **38**, S799 (2005). URL https://doi.org/10.1088/0953-4075/38/9/023.

[235] Huang, Z. & Lindau, I. Free-electron lasers: SACLA hard-X-ray compact FEL. *Nature Photonics* **6**, 505–506 (2012). URL https://www.nature.com/articles/nphoton.2012.184.

[236] Savelyev, E. *et al.* Jitter-correction for IR/UV-XUV pump-probe experiments at the FLASH free-electron laser. *New Journal of Physics* **19**, 043009 (2017). URL https://iopscience.iop.org/article/10.1088/1367-2630/aa652d.

[237] Kaneko, S. *et al.* Large constriction of lattice constant in epitaxial magnesium oxide thin film: Effect of point defects on lattice constant. *Journal of Applied Physics* **107**, 073523 (2010). URL https://aip.scitation.org/doi/abs/10.1063/1.3361482.

[238] Ayoub, J. P., Gatel, C., Roucau, C. & Casanove, M. J. Structure and chemical order in FeRh nanolayers epitaxially grown on MgO(001). *Journal of Crystal Growth* **314**, 336–340 (2011). URL https://www.sciencedirect.com/science/article/pii/S0022024810011085.

[239] NIST X-ray Form Factor. URL https://physics.nist.gov/PhysRefData/FFast/html/form.html.

[240] Chen, C. T. *et al.* Experimental confirmation of the x-ray magnetic circular dichroism sum rules for iron and cobalt. *Physical Review Letters* **75**, 152–155 (1995). URL https://journals.aps.org/prl/abstract/10.1103/PhysRevLett.75.152.

[241] Chase, M. NIST-JANAF Thermochemical Tables, Fourth Edition. *Journal Physical Chemistry Reference Data, Monograph 9* 1–1951 (1998). URL https://janaf.nist.gov/.

[242] Busing, W., Levy, H. & IUCr. Angle calculations for 3- and 4-circle X-ray and neutron diffractometers. *Acta Crystallographica* **22**, 457–464 (1967). URL https://doi.org/10.1107/S0365110X67000970.

[243] Ament, L. J., Van Veenendaal, M., Devereaux, T. P., Hill, J. P. & Van Den Brink, J. Resonant inelastic x-ray scattering studies of elementary excitations. *Reviews of Modern Physics* **83**, 705–767 (2011). URL https://journals.aps.org/rmp/abstract/10.1103/RevModPhys.83.705. 1009.3630.

[244] Gilmore, K. *et al.* Description of Resonant Inelastic X-Ray Scattering in Correlated Metals. *Physical Review X* **11**, 031013 (2021). URL https://journals.aps.org/prx/abstract/10.1103/PhysRevX.11.031013. 2011.04509.

[245] Kim, J. W. *et al.* Surface influenced magnetostructural transition in FeRh films. *Applied Physics Letters* **95**, 222515 (2009). URL https://aip.scitation.org/doi/abs/10.1063/1.3265921.

[246] Henke, B. L., Gullikson, E. M. & Davis, J. C. X-ray interactions: Photoabsorption, scattering, transmission, and reflection at E = 50-30, 000 eV, Z = 1-92. *Atomic Data and Nuclear Data Tables* **54**, 181–342 (1993). URL https://doi.org/10.1006/adnd.1993.1013.

[247] Almeida, T. P. *et al.* Quantitative Differential Phase Contrast Imaging of the Magnetostructural Transition and Current-driven Motion of Domain Walls in FeRh Thin Films. *Microscopy and Microanalysis* **24**, 936–937 (2018). URL https://doi.org/10.1017/S1431927618005172.

[248] Giorgianni, F. *et al.* Melting of magnetic order in $NaOsO_3$ by femtosecond laser pulses. *Physical Review B* **105**, 155147 (2022). URL https://doi.org/10.1103/PhysRevB.105.155147.

[249] Arregi, J. A., Caha, O. & Uhlíř, V. Evolution of strain across the magnetostructural phase transition in epitaxial FeRh films on different substrates. *Physical Review B* **101**, 174413 (2020). URL https://journals.aps.org/prb/abstract/10.1103/PhysRevB.101.174413.

[250] Als-Nielsen, J. & McMorrow, D. *Elements of modern X-ray physics* (Wiley, 2011).

[251] Hatsui, T. Developments of X-ray Imaging Detectors at SACLA/SPring-8: Current Status and Future Outlook. *Synchrotron Radiation News* **27**, 20–23 (2014). URL https://www.tandfonline.com/doi/abs/10.1080/08940886.2014.930805.

[252] Baral, A., Vollmar, S., Kaltenborn, S. & Schneider, H. C. Re-examination of the Elliott-Yafet spin-relaxation mechanism. *New Journal of Physics* **18**, 023012 (2016). URL https://iopscience.iop.org/article/10.1088/1367-2630/18/2/023012/meta. 1505.01432.

[253] Koenig, C. Self-consistent band structure of paramagnetic, ferromagnetic and antiferromagnetic ordered FeRh. *Journal of Physics F* **12**, 1123–1137 (1982). URL https://iopscience.iop.org/article/10.1088/0305-4608/12/6/013/pdf.

[254] Bergman, B. *et al.* Identifying growth mechanisms for laser-induced magnetization in FeRh. *Physical Review B* **73**, 060407 (2006). URL https://link.aps.org/doi/10.1103/PhysRevB.73.060407.

[255] Beaud, P. *et al.* A time-dependent order parameter for ultrafast photoinduced phase transitions. *Nature Materials* **13**, 923–927 (2014). URL https://www.nature.com/articles/nmat4046.

[256] Perfetti, L. *et al.* Ultrafast electron relaxation in superconducting $Bi_2Sr_2CaCu_2O_{8+\delta}$ by time-resolved photoelectron spectroscopy. *Physical Review Letters* **99**, 197001 (2007). URL https://journals.aps.org/prl/abstract/10.1103/PhysRevLett.99.197001.

[257] Kubli, M. *et al.* Kinetics of a phonon-mediated laser-driven structural phase transition in $Sn_2P_2Se_6$. *Applied Sciences* **9**, 525 (2019). URL https://doi.org/10.3390/app9030525.

[258] scipy.integrate.odeint — SciPy v1.7.1 Manual. URL https://docs.scipy.org/doc/scipy/reference/generated/scipy.integrate.odeint.html.

[259] Chen, L.-Y. *Optical properties of metals and alloys: Au, Ag, FeRh, $AuAl_2$, and $PtAl_2$*. Ph.D. thesis, Iowa State University, Ames (1987). URL https://lib.dr.iastate.edu/rtd/8624/.

[260] Nikitin, S. A. *et al.* Giant elastocaloric effect in FeRh alloy. *Physics Letters A* **171**, 234–236 (1992). URL https://doi.org/10.1016/0375-9601(92)90432-L.

[261] Lin, Z., Zhigilei, L. V. & Celli, V. Electron-phonon coupling and electron heat capacity of metals under conditions of strong electron-phonon nonequilibrium. *Physical Review B* **77**, 075133 (2008). URL https://doi.org/10.1103/PhysRevB.77.075133.

[262] Allen, P. B. Theory of thermal relaxation of electrons in metals. *Physical Review Letters* **59**, 1460–1463 (1987). URL https://journals.aps.org/prl/abstract/10.1103/PhysRevLett.59.1460.

[263] Reimer, L. *Scanning Electron Microscopy*. Springer Series in Optical Sciences (Springer, Berlin, Heidelberg, 1998).

[264] Bigot, J.-Y. Down to the nanometre scale. *Nature Materials* **12**, 283–284 (2013). URL http://www.nature.com/articles/nmat3605.

[265] Qiu, Z. Q. & Bader, S. D. Surface magneto-optic Kerr effect (SMOKE). *Journal of Magnetism and Magnetic Materials* **200**, 664–678 (1999). URL https://doi.org/10.1063/1.1150496.

[266] Feil, H. & Haas, C. Magneto-optical kerr effect, enhanced by the plasma resonance of charge carriers. *Physical Review Letters* **58**, 65–68 (1987). URL https://journals.aps.org/prl/abstract/10.1103/PhysRevLett.58.65.

[267] Holiday, L. F. & Gibson, U. J. Improved longitudinal magneto-optic Kerr effect signal contrast from nanomagnets with dielectric coatings. *Optics Express* **14**, 13007 (2006). URL https://www.osapublishing.org/oe/abstract.cfm?uri=oe-14-26-13007.

[268] Qureshi, N., Schmidt, H. & Hawkins, A. R. Cavity enhancement of the magneto-optic Kerr effect for optical studies of magnetic nanostructures. *Applied Physics Letters* **85**, 431–433 (2004). URL http://aip.scitation.org/doi/10.1063/1.1774276.

[269] Roychowdhury, T., Shah, D., Hilfiker, J. N. & Linford, M. R. Polymethyl methacrylate: Optical properties from 191 to 1688 nm (0.735-6.491 eV) by spectroscopic ellipsometry. *Surface Science Spectra* **27**, 016002 (2020). URL https://avs.scitation.org/doi/abs/10.1116/1.5095422.

[270] Tikuišis, K. K. *et al.* OPTICAL AND MAGNETO-OPTICAL PROPERTIES OF PERMALLOY THIN FILMS IN 0.7–6.4 eV PHOTON ENERGY RANGE. *Materials & Design* **114**, 31–39 (2017). URL https://doi.org/10.1016/j.matdes.2016.10.036.

[271] Riahi, H. *et al.* Optimizing magneto-optical effects in the ferromagnetic semiconductor GaMnAs. *Journal of Magnetism and Magnetic Materials* **395**, 340–344 (2015). URL https://linkinghub.elsevier.com/retrieve/pii/S0304885315303875.

[272] Philipp, H. R. Optical properties of non-crystalline Si, SiO, SiO_x and SiO_2. *Journal of Physics and Chemistry of Solids* **32**, 1935–1945 (1971). URL https://doi.org/10.1016/S0022-3697(71)80159-2.

[273] Nuida, T., Yamauchi, T. & Ohkoshi, S. I. Light-induced change in magnetization-induced second harmonic generation of $Fe_{0.52}Rh_{0.48}$ films. *Journal of Applied Physics* **110**, 063516 (2011). URL http://aip.scitation.org/doi/10.1063/1.3634114.

[274] Oblak, E. *et al.* Ultrasensitive transverse magneto-optical Kerr effect measurements by means of effective polarization change detection. *Journal of Physics D* **50**, 23–24 (2017). URL https://doi.org/10.1088/1361-6463/aa6df2.

[275] Li, S. *et al.* Coercivity dynamics and origin of time-delayed magneto-optical hysteresis loops in pump-probe Kerr spectroscopy. *Journal of Applied Physics* **113**, 53913 (2013). URL https://doi.org/10.1063/1.4790390.

[276] Hu, P. *et al.* Femtosecond laser micro-milling dental glass ceramics: An experimental analysis and COMSOL finite element simulation. *Ceramics International* **46**, 22146–22153 (2020). URL https://doi.org/10.1016/j.ceramint.2020.05.291.

[277] Liu, Y. *et al.* Large reversible caloric effect in FeRh thin films via a dual-stimulus multicaloric cycle. *Nature Communications* **7**, 11614 (2016). URL https://dx.doi.org/10.1038%2Fncomms11614.

[278] Humaish, H. Evaluating a line heat source method using a COMSOL® multiphysics axisymmetric 2D model. In *IOP Conference Series: Materials Science and Engineering* (2020). URL https://doi.org/10.1088/1757-899X/671/1/012088.

[279] Humaish, H. Effect of porosity on thermal conductivity of porous materials. In *IOP Conference Series: Materials Science and Engineering* (2020). URL https://doi.org/10.1088/1757-899X/737/1/012185.

[280] Casimir, H. Note on the conduction of heat in crystals. *Physica* **5**, 495–500 (1938). /doi.org/10.1016/S0031-8914(38)80162-2.

[281] Malec, C. E., Bennett, B. R. & Johnson, M. B. Detection of ferromagnetic domain wall pinning and depinning with a semiconductor device. *Journal of Applied Physics* **118**, 234501 (2015). URL https://doi.org/10.1063/1.4936783.

[282] Fechner, M. *et al.* Magnetophononics: Ultrafast spin control through the lattice. *Physical Review Materials* **2** (2018). URL https://doi.org/10.1103/physrevmaterials.2.064401. 1707.03216.

[283] Disa, A. S. *et al.* Polarizing an antiferromagnet by optical engineering of the crystal field. *Nature Physics* **16**, 937–941 (2020). URL https://doi.org/10.1038/s41567-020-0936-3. 2001.00540.

[284] Tauchert, S. R. *et al.* Polarized phonons carry angular momentum in ultrafast demagnetization. *Nature* **602**, 73–77 (2022). URL https://www.nature.com/articles/s41586-021-04306-4.

[285] Jenkins, S., Chantrell, R. W., Klemmer, T. J. & Evans, R. F. Magnetic anisotropy of the noncollinear antiferromagnet $IrMn_3$. *Physical Review B* **100**, 220405 (2019). URL https://journals.aps.org/prb/abstract/10.1103/PhysRevB.100.220405.

Appendix A

VAMPIRE Code

VAMPIRE is an simulation software that models magnetic materials through the interactions between spins located at fixed atomic sites [177]. Such simulations are implemented using material, unit cell, and input files. The material file defines the atomic species and known physical properties of the investigated system. The unit cell file describes the crystal structure and interactions between atoms in the structure. The input file defines the simulation. In this project, the laser heating of FeRh was modelled. Simulation results are presented in Fig. A.1, showing the transient changes in electron and lattice temperatures for a range of laser excitation powers.

Material File - AF FeRh

For G-type AF materials, the .mat file includes 3 species of atoms [285]; one for each of the Fe sub-lattices with anti-parallel spins, and another describing the 'non-magnetic' Rh. The values of the exchange interactions, damping constant, uniaxial anisotropy constant, and atomic moments are found from *ab initio* and DFT studies of the material [35, 108, 109, 115, 125, 178].

```
# FeRh antiferromagnetic state
#-------------------------------------
material:num-materials=3
#-----------------------------------
# FeRh 1st Fe sublattice
#-----------------------------------
material[1]:material-name="Fe"
```

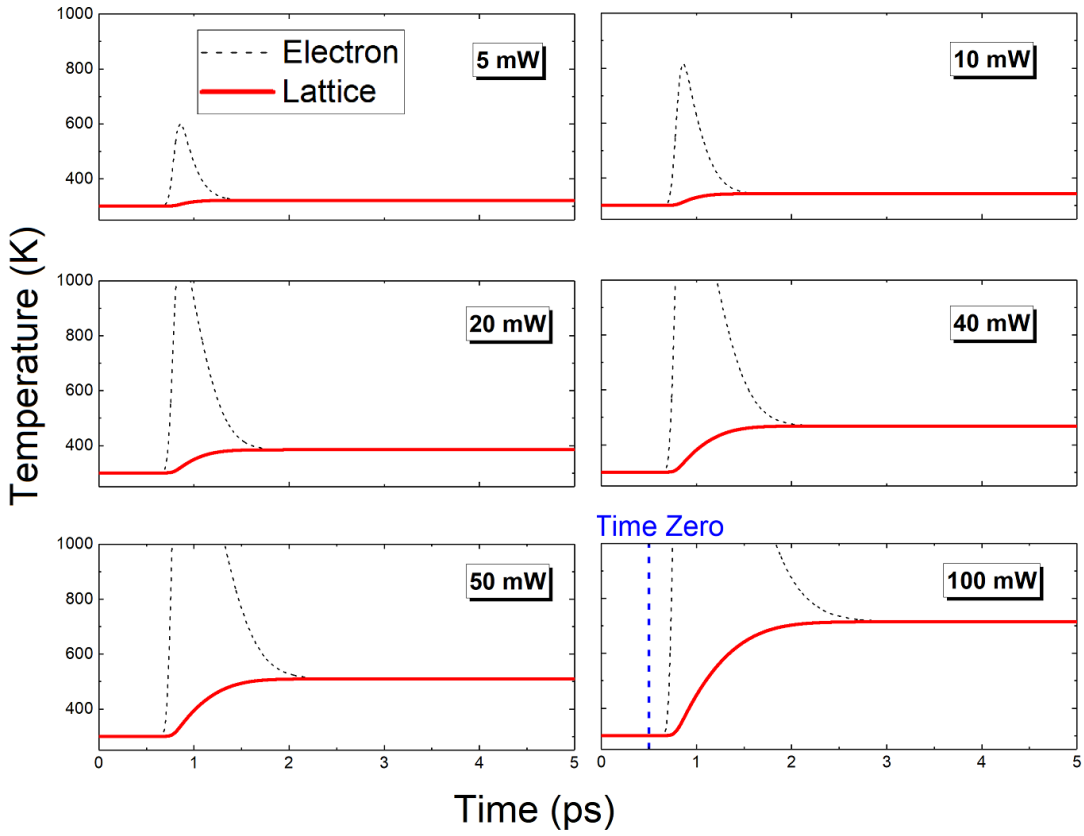

Figure A.1: Results of a VAMPIRE simulation demonstrating the lattice and electronic temperature of an unstrained 20 nm FeRh film when excited by laser pulses of various powers. 10 mW corresponds to $\approx$ 1 mJ cm^{-2}. Time zero refers to the midpoint of the Gaussian heat packet used to simulate the laser heating. This model ignores heat dissipation to the surrounding lattice.

```
material[1]:damping-constant=0.0013
material[1]:atomic-spin-moment=3.15 !muB
material[1]:exchange-matrix[1]=0.4e-21
material[1]:exchange-matrix[2]=-2.75e-21
material[1]:uniaxial-anisotropy-constant=1.404e-23
material[1]:uniaxial-anisotropy-direction = 0,0,1
material[1]:initial-spin-direction=0,0,1
#-------------------------------------
# FeRh 2nd Fe sublattice
#-------------------------------------
material[2]:material-name="Fe"
material[2]:damping-constant=0.0013
material[2]:atomic-spin-moment=3.15 !muB
material[2]:exchange-matrix[1]=-2.75e-21
material[2]:exchange-matrix[2]=0.4e-21
material[2]:uniaxial-anisotropy-constant=1.404e-23
material[2]:uniaxial-anisotropy-direction = 0,0,-1
material[2]:initial-spin-direction=0,0,-1
#-------------------------------------
# Material 3 - Rh
#-------------------------------------
material[3]:material-name="Rh"
material[3]:non-magnetic
```

Unit Cell File - AF FeRh

The unit cell file defines the positions and interactions between each of the atoms in the simulated material. In the case of AF FeRh, we use a cell double the size of the original unit cell to model the 2 magnetic sub lattices. A minimum of 144 interactions are included to entirely model the system. This describes all possible atomic positions, the interactions with each of the nearest neighbours (6 pairs), and the next-nearest neighbours (12 pairs) to give a total of 288 which is divided by 2 to prevent double counting [177]. The system of interactions can be generated using a python script [285].

```
#unit cell size
```

```
5.98    5.98    5.98
#unit cell vectors
1       0       0
0       1       0
0       0       1
#Atoms
#Co-ordinate position of each atom,
#0-Fe spin-up, 1-Fe spin-down, 2-Rh
16      3
0       0       0       0       0       0       0
1       0       0       0.5     1       0       0
2       0.5     0       0       1       0       0
3       0.5     0       0.5     0       0       0
4       0       0.5     0       1       0       0
5       0       0.5     0.5     0       0       0
6       0.5     0.5     0       0       0       0
7       0.5     0.5     0.5     1       0       0
8       0.25    0.25    0.25    2       0       0
9       0.75    0.25    0.25    2       0       0
10      0.25    0.75    0.25    2       0       0
11      0.25    0.25    0.75    2       0       0
12      0.75    0.75    0.25    2       0       0
13      0.75    0.25    0.75    2       0       0
14      0.25    0.75    0.75    2       0       0
15      0.75    0.75    0.75    2       0       0
#interactions
144     normalised-isotropic
0       0       1       0       0       0       1
1       0       2       0       0       0       1
2       0       4       0       0       0       1
3       0       1       0       0       1       1
4       0       4       0       1       0       1
5       0       2       1       0       0       1
6       1       0       0       0       -1      1
7       1       0       0       0       0       1
```

```
8       1       3       0       0       0       1
9       1       5       0       0       0       1
10      1       5       0       1       0       1
11      1       3       1       0       0       1
12      2       0       -1      0       0       1
13      0.75    0.25    0.75    2       0       0
14      0.25    0.75    0.75    2       0       0
15      0.75    0.75    0.75    2       0       0
#interactions
144     normalised-isotropic
0       0       1       0       0       0       1
1       0       2       0       0       0       1
2       0       4       0       0       0       1
3       0       1       0       0       1       1
4       0       4       0       1       0       1
5       0       2       1       0       0       1
6       1       0       0       0       -1      1
7       1       0       0       0       0       1
...
...
141     7       1       0       0       0       1
142     7       2       0       0       0       1
143     7       4       0       0       0       1
```

Input File - Ultrafast Laser Heating

The parameters describing the simulated system are included in the input file by calling the material (.mat) and unit cell files (.ucf) defined above. The following simplified code describes the effect of sudden heating with a 40 mW laser pulse of pulse length 100 fs in a constant field strength of 0.1 T (with the Neél vector aligned parallel to this field). A 10 x 10 x 10 nm^3 system is modelled, where periodic boundary conditions are implemented in all directions along x, y, z. As such, it describes the transient changes of FeRh systems with an ambient temperature of 300 K. The time steps are 0.1 fs over a 5 ps timespan. Precondition steps are required to model the thermal equilibration of the spin system at the investigated temperatures. The outputted electron and lattice

temperature can be found in Fig. A.1. The orientation of the atomic moments at each time step can also be found from the outputted 'config' file.

```
#-----------------------------------------
# Sample vampire input file to perform
# benchmark calculation for v3.0
#-----------------------------------------
#-----------------------------------------
# Creation attributes:
#-----------------------------------------
#create:crystal-structure=fcc
create:periodic-boundaries-x
create:periodic-boundaries-y
create:periodic-boundaries-z
#-----------------------------------------
# System Dimensions:
#-----------------------------------------
#dimensions:unit-cell-size = 3.524 !A
dimensions:system-size-x = 10 !nm
dimensions:system-size-y = 10 !nm
dimensions:system-size-z = 10 !nm
#-----------------------------------------
# Material Files:
#-----------------------------------------
material:file=FeRh.mat
material:unit-cell-file=FeRh.ucf
#-----------------------------------------
# Simulation attributes:
#-----------------------------------------
sim:temperature = 300.0
sim:equilibration-temperature = 300.0
sim:temperature-increment=25
sim:time-steps-increment=1
sim:preconditioning-steps = 1000
sim:equilibration-time-steps=5000
sim:total-time-steps=50000
```

```
sim:time-step=1.0E-16
sim:applied-field-strength = 0.1 !T
sim:laser-pulse-power = 40.0
sim:laser-pulse-temporal-profile=two-temperature
sim:laser-pulse-time=1.0e-13
#----------------------------------------
# Program and integrator details
#----------------------------------------
sim:program=laser-pulse
sim:integrator=llg-heun
#----------------------------------------
# data output
#----------------------------------------
output:real-time
output:electron-temperature
output:phonon-temperature
output:material-magnetisation
config:atoms
```